



HAL
open science

Rheology of concentrated suspensions of sphere-fiber mixtures in view of applications to reinforced cementitious materials

Mounir Meloussi

► **To cite this version:**

Mounir Meloussi. Rheology of concentrated suspensions of sphere-fiber mixtures in view of applications to reinforced cementitious materials. Mechanics [physics]. Université Côte d'Azur; Université M'hamed Bougara de Boumerdès (Algérie), 2022. English. NNT : 2022COAZ4068 . tel-04107103

HAL Id: tel-04107103

<https://theses.hal.science/tel-04107103>

Submitted on 26 May 2023

HAL is a multi-disciplinary open access archive for the deposit and dissemination of scientific research documents, whether they are published or not. The documents may come from teaching and research institutions in France or abroad, or from public or private research centers.

L'archive ouverte pluridisciplinaire **HAL**, est destinée au dépôt et à la diffusion de documents scientifiques de niveau recherche, publiés ou non, émanant des établissements d'enseignement et de recherche français ou étrangers, des laboratoires publics ou privés.

THÈSE DE DOCTORAT

Rhéologie des suspensions concentrées des mélanges sphères-fibres en vue d'applications aux matériaux cimentaires renforcés

Mounir MELOUSSI

Institute de physique de Nice (INPHYNI) / Laboratoire dynamique des moteurs
et vibroacoustique (LDMV)

**Présentée en vue de l'obtention
du grade de docteur en Physique
de l'Université Côte d'Azur
et de docteur en Génie mécanique
de l'Université de M'Hamed BOUGARA
Boumerdes.**

Dirigée par : Pavel KUZHIR / Salah AGUIB
Soutenue le : 24/11/2022

Devant le jury, composé de :

Examineur : Georges BOSSIS,
CNRS DR2 émérite, UCA / INPHYNI

Président : Abdelkader NOUR,
Professeur, UMBB / FT, Boumerdes

Rapporteur : Julien FÉRÉC,
Professeur, Université Bretagne Sud- IRDL

Rapporteur : Moussa HADDAD,
Professeur, Ecole Militaire Polytechnique, Alger

Membre invité : Pascal Boustingorry,
Docteur / ingénieur, société Chryso - Paris

Abstract

Discontinuous shear thickening (DST) in dense non-Brownian suspensions is a well-documented phenomenon in scientific research, however its origins and effects are still under discussion nowadays. Not being able to recognize the direct cause of the phenomenon represents a point of weakness in many industrial fields, especially in the field of concrete and fiber reinforced concrete production.

In this thesis, we will study experimentally as well as theoretically the DST in a suspension of calcium carbonate microparticles loaded with rigid polyamide and glass fibers. The rheology of this suspension simulates the behavior of fiber-reinforced concrete. We reproduce on a reduced scale different types of flows occurring in the concrete placement process, such as double-helix mixing, pumping through tubes, jet flow at the tube outlet, and we derive fundamental rheological behaviors applicable to any type of "sphere-fiber" mixtures. Using "mixing" type rheometry (double helix tools adapted to the rotational rheometer), we will first show that the addition of fibers shifts the DST transition to lower critical shear rates, which is explained by an increase in the viscosity of the suspension, so that the shear rate to reach the DST onset stress decreases. However, the mixture jams at a fiber volume fraction greater than or equal to 4% vol which is interpreted in terms of the percolation threshold of the fiber network in the shear thickening matrix of calcium carbonate. We will show in a second stage that the rheological behavior in a flow induced by a pressure gradient through a capillary remains quite similar to that in a simple shear but only at low fiber volume fractions $\varphi_f \leq 1$ % vol, and if the Mouney-Rabinowitch correction is correctly applied. Above this volume fraction, the flow curves in the capillary rheometry become very different from those measured in simple shear likely because of microstructural difference in two different flow geometries. The theoretical model based on the homogenization approach allows to reproduce at least semi-quantitatively the flow curves in the "mixing" type and capillary rheometry at low fiber volume fractions but fails to capture microstructural changes at higher volume fractions. Finally, the instabilities of the calcium carbonate suspension jet under gravity with and without polyamide fibers will be studied. This instability is manifested by strong lateral oscillations of the axial symmetry axis of the jet accompanied by a slight undulation of the jet surface. We will perform for the first time a two-dimensional direct Fourier transform (2D DFT) analysis of the spatiotemporal variation of the jet diameter and the lateral deflection of the jet in the DST regime. We will show that the addition of polyamide fibers at different concentrations in the suspension allows for jet stability and promotes jet fractures. A theoretical explanation for the onset of jet lateral instability and the stabilizing effect of the fibers will then be developed based on the evaluations of tensile stresses and the lower and upper thresholds of the DST.

Keywords: Rheology; Discontinuous shear thickening; Concentrated suspensions; Calcium carbonate particles; Fibers.

Résumé

Le rhéoépaississement discontinu « DST » dans les suspensions denses non browniennes est un phénomène bien documenté dans la recherche scientifique, cependant ses origines et ses effets sont toujours en discussion aujourd'hui. Ne pas reconnaître la cause directe du phénomène représente un point de faiblesse dans de nombreux domaines industriels, en particulier dans le domaine de la production de béton et de béton renforcé de fibres.

Dans ce travail de thèse, nous étudierons expérimentalement ainsi que théoriquement le DST dans une suspension de microparticules de carbonate de calcium chargée de fibres rigides de polyamide et de verre. La rhéologie de cette suspension simule le comportement de béton renforcé par des fibres. Nous reproduisons à l'échelle réduite différents types d'écoulements ayant lieu dans le procédé de mise en place du béton, tels que malaxage par double hélice, pompage au travers des tubes, écoulement du jet en sortie du tube, et nous en tirons des comportements rhéologiques fondamentales applicables à tout type de mélanges « sphères-fibres ». En utilisant la rhéométrie de type « malaxage » (outils double hélice adapté au rhéomètre rotationnel), nous montrerons d'abord que l'ajout de fibres déplace la transition DST vers des taux de cisaillement critiques plus faibles, ce qui s'explique par une augmentation de la viscosité de la suspension, de sorte que le taux de cisaillement pour atteindre la contrainte de début de DST diminue. Cependant, le mélange se bloque à une fraction volumique de fibres supérieure ou égale à 4% vol ce qui est interprété en terme du seuil de percolation du réseau de fibres dans la matrice rhéoépaississante du carbonate de calcium. Nous monterons dans un deuxième temps que le comportement rhéologique dans un écoulement induit par un gradient de pression au travers un capillaire reste assez semblable à celui dans un cisaillement simple, mais uniquement aux faibles concentrations de fibres, $\varphi_f \leq 1\%$ vol, et à condition d'appliquer correctement la correction de Mouney-Rabinowitch. Au-dessus de cette concentration les courbes d'écoulement dans la rhéométrie capillaire deviennent très éloignées de celles mesurées en cisaillement simple probablement à cause de la différence microstructurelle dans ces deux géométries. Le modèle théorique basée sur l'approche d'homogénéisation permet de reproduire au moins semi-quantitativement les courbes d'écoulement dans les géométries de type « malaxage » et capillaire à faible fraction volumique des fibres mais ne donne pas de bonnes prédictions au-delà de cette concentration. Enfin, les instabilités du jet sous gravité de la suspension de carbonate de calcium avec et sans fibres de polyamide seront étudiées. Cette instabilité se manifeste par de fortes oscillations latérales de l'axe de symétrie axiale du jet accompagnées par une légère ondulation de la surface du jet. Nous réaliserons pour la première fois une analyse bidimensionnelle par transformée de Fourier directe (2D DFT) de la variation spatiotemporelle du diamètre du jet et de la déviation latérale du jet en régime DST. Nous montrerons que l'ajout de fibres de polyamide à différentes concentrations dans la suspension permet la stabilité du jet et favorise les fractures de celui-ci. Une explication théorique de l'apparition de l'instabilité latérale du jet et de l'effet stabilisateur des fibres sera ensuite développée à partir des évaluations des contraintes extensionnelles et des seuils inférieur et supérieur du DST.

Mots clés : Rhéologie; Rhéoépaississement discontinu; Suspensions concentrées; Particules de Carbonate de calcium; Fibres.

ملخص

التثخين المتقطع للقص (الاختصار الدولي العلمي هو « DST ») في مستعلقات غير براونية كثيفة ظاهرة موثقة جيداً في البحث العلمي ومع ذلك ، لا تزال أصولها وتأثيراتها قيد المناقشة في الوقت الحاضر. عدم القدرة على التعرف على السبب المباشر للظاهرة يمثل نقطة ضعف في العديد من المجالات الصناعية، وخاصة في مجال إنتاج الخرسانة المدعمة بالألياف. في هذه الأطروحة، سوف ندرس تجريبياً وكذلك نظرياً التثخين المتقطع للقص في مستعلق مكون من جزيئات كربونات الكالسيوم ومحملة بألياف البولي أميد الصلبة والألياف الزجاجية. تحاكي ريولوجيا هذا التعليق سلوك الخرسانة المدعمة بالألياف. نعيد محاكات في تجاربنا على نطاق مخفض، أنواع مختلفة من التدفقات التي تحدث في عملية صب الخرسانة ، مثل الخلط الحلزوني المزدوج ، والضخ من خلال الأنابيب ، والتدفق النفاث عند مخرج الأنبوب ، ونشتق السلوكيات الريولوجية الأساسية التي تنطبق على أي نوع من هذه المخاليط "الألياف-الكرويات". باستخدام قياس التيار من النوع "الخلاط" (أدوات اللولب المزدوج المكيّفة لمقياس التيار الدوراني) ، سنبين أولاً أن إضافة الألياف تُغيّر انتقال التثخين المتقطع للقص إلى معدلات قص حرجة أقل ، وهو ما يفسره زيادة لزوجة المستعلق ، لذلك أن معدل القص للوصول إلى بداية التثخين المتقطع للقص ينخفض. ومع ذلك ، فإن الخليط يتكدس عند نسبة ألياف أكبر من أو يساوي 4٪ والذي يتم تفسيره من حيث عتبة الترشيح لشبكة الألياف في مصفوفة كربونات الكالسيوم.

سنبين في مرحلة ثانية أن السلوك الريولوجي في التدفق الناجم عن تدرج الضغط عبر الانابيب يظل مشابهاً الى حد ما لذلك في القص البسيط، ولكن فقط بتركيزات ألياف منخفضة $\phi_f \leq 1\%$ بشرط أن يتم تطبيق تصحيح-Mouney Rabinowitch بشكل صحيح. فوق هذا التركيز، تصبح منحنيات التدفق في ريولوجيا الانابيب مختلفة تماماً عن تلك التي تم قياسها في القص البسيط على الأرجح بسبب الاختلاف في البنية المجهرية في هذين الشكلين. يسمح النموذج النظري القائم على نهج التجانس بإعادة إنتاج منحنيات التدفق شبه كمياً على الأقل في مجسمات من نوع "الخلاط" والانابيب مع تركيزات ألياف منخفضة، ولكنها لا تعطي تنبؤات جيدة تتجاوز هذا التركيز.

أخيراً، سيتم دراسة عدم استقرار نفاث مستعلق كربونات الكالسيوم تحت الجاذبية مع وبدون ألياف البولي أميد. يتجلى عدم الاستقرار هذا من خلال التذبذبات الجانبية القوية لمحور التناظر المحوري للنفاث المصحوبة بتموج طفيف للسطح النفاث. سنقوم لأول مرة بإجراء تحليل فورييه المباشر ثنائي الأبعاد (2D-DFT) الزماني المكاني لقطر النفاث والانحراف الجانبي للنفاث في التثخين المتقطع للقص. سنبين أن إضافة ألياف البولي أميد بتركيزات مختلفة في التعليق يسمح بثبات النفاثات ويعزز الكسور في النفاث. سيتم بعد ذلك تطوير تفسير نظري لبداية عدم الاستقرار الجانبي للنفاث وتأثير الألياف الاستقراري بناءً على تقييمات الضغوطات والعتبات الدنيا والعليا للتثخين بالقص.

الكلمات المفتاحية: ريولوجيا؛ التثخين المتقطع للقص؛ المستعلقات المدعمة؛ جزيئات كربونات الكالسيوم؛ اللألياف.

Dedication

I dedicate this work to you father, you always wanted to see me crowned with the title of doctor. Today you will not be present in the room to encourage me, but you will always be present in my heart.

I miss you a lot.

This project is dedicated to my dear parents for their love.

To MALAK and NOUNA. To Oussama and Younes

Acknowledgment

All praise and thanks to God the most powerful and most merciful who has given me the strength and patience to accomplish this work.

*I would express First my special gratitude to my two supervisors. My supervisor **Pavel KUZHIR**, who encouraged me by all means. I appreciate his involvement in the research work. His wealth of knowledge in the field has been extremely helpful. He has been a great advisor and mentor who was always available without being bothered to discuss and support all the technical problems and he always provides a very pleasant research environment and always provides a solution to a physical problem! I benefitted a lot from his guidance and knowledge not only in the academic life but also in the common everyday life. Thank you again **M. Pavel** for accepting my scientific weakness and for sharing your precious knowledge with me. Thank you for all the support you have given me during these last three years...*

*I would like to express my sincere thanks (with an honorary bow) to my supervisor **Salah AGUIB** for his patient guidance and unfailing support throughout my PHD study. His immense knowledge, professional suggestions, and constructive comments were essential to this thesis. He was always by my side, asking me every time if something is in need, unconditionally and without me even asking him! I cannot thank him enough for his support, and I know that without him I would never be in this situation and this thesis project would never have happened.*

*Special thanks to **Mr. Georges BOSSIS** who always guided me in my experiences. A great thanks to **Mrs. Olga VOLKOVA** for all her help during the rheometry experiments as well.*

Thanks to the rapporteurs and to the members of the jury for having accepted to read and to criticize my thesis work.

*I also thank my friends and colleagues at the INPHYNI. Thanks to **Lee and Sumeyra**, thanks to both of you for all the fun moments and beautiful memories together. I already miss our gatherings...! I also thank **Jordy**, for all his precious help when needed during my experiments in the lab and for the friendly discussions. Without forgetting all the special people in my life who have believed and supported me... Thanks to all of you.*

*Last and not least, I would like to thank a man that I respect a lot. Today, I will not thank you as a teacher but as an older brother who has always encouraged me. Thank you **Chemsedine RAHMOUNE**.*

Table of contents

List of Figures	1
List of Tables.....	8
List of Nomenclatures.....	9
Chapter 1: Basic concepts of rheology. Shear thickening. Thesis objectives	14
1.1 Macroscopic rheological behaviors	14
1.1.1 Stress tensor	14
1.1.2 Simple shear and normal stress differences	15
1.1.3 Non-Newtonian behaviors	16
1.2 Suspension rheology	17
1.2.1 Viscosity and volume fraction	17
1.2.2 Particles migration	19
1.2.3 Particles sedimentation	21
1.2.4 Normal stress differences.....	22
1.3 Shear thickening in concentrated suspensions	23
1.3.1 General framework	23
1.3.2 Shear thickening in industrial applications	24
1.3.3 Shear thickening physical origins	26
1.3.4 Shear thickening in particle mixtures	34
1.3.5 Extensional and free surface flows of shear thickening fluids.....	35
1.4 Unresolved problems and general purpose of the thesis	37
Chapter 2 : Material used and Methods employed.....	39
2.1 Materials used in the preparation of the suspension.....	39
2.1.1 Calcium carbonate particles	39
2.1.2 The superplasticizer	43
2.1.3 The fibers	46
2.1.4 Suspension preparation	49
2.2 Experimental methods employed	50
2.2.1 Drag flows in shear rotational rheometry	50
2.2.2 Pressure-driven flows in capillary rheometry	61
2.2.3 Extensional flows withing a free-falling jet.....	64

Chapter 3: Drag flows of sphere-fiber mixtures in a mixer-type geometry	68
3.1 Sigmodal flow curve.....	69
3.2 Thixotropic behavior	71
3.3 Effect of fiber-to-particle diameter ratio	73
3.4 Effect of fibers concentration	75
3.5 Controlled-rate versus controlled-stress response	78
3.6 Reduced shear rate versus homogenization approach. Comparison with experiments	80
3.7 Jamming behavior.....	86
3.8 Conclusion	89
3.9 Appendices.....	91
Chapter 4: Pressure driven flow of sphere-fiber mixtures through a capillary	105
4.1 Transient behavior in capillary flow.....	106
4.2 Shear rheometry in cylindrical Couette geometry	110
4.2.1 Flow curves	110
4.2.2 H-model predictions.....	112
4.3 Capillary rheometry	115
4.3.1 Flow curves	115
4.3.2 H-model predictions.....	118
4.4 Conclusion	121
Chapter 5 : Jet flow and jet instability of sphere-fiber mixtures.....	123
5.1 Qualitative observations	124
5.1.1 Effect of the jet length.....	124
5.1.2 Effect of the PA volume fraction	125
5.2 Quantitative analyses of jet dynamics	126
5.2.1 Variation of the jet diameter	126
5.2.2 Lateral oscillations	131
5.3 Theoretical insight	138

Table of contents

5.3.1 Stress profile along the jet.....	138
5.3.2 Effect of fibers on jet stability.....	143
5.3.3 Break-up length.....	149
5.4 Conclusion	151
5.5 Appendix: a concept of the jet extensional rheometry	153
Conclusion and perspectives	155
References.....	158

List of Figures

CHAPTER 1

Figure 1. 1 Simple shear rheology test. The fluid is located between two continuous plates. The upper plate is driven by a force F and is moving at a speed V	15
Figure 1. 2 Flow curves for different types of fluids. (a): Stress vs shear rate. (b): Viscosity vs shear rate.	17
Figure 1. 3 Relative shear viscosity as a function of volume fraction of particles. From [14]	19
Figure 1. 4 (a): Particles volume fraction profile (in arrow direction) for increasing shear stresses and a constant confining pressure; (b): Velocity profiles for increasing shear stresses of the Couette cell (in arrow direction) and a constant pressure- From Lagrée and Lhuillier [23].	20
Figure 1. 5 Local particles volume fraction as function of the channel distance for different suspension concentrations-from Frank et al. [26].	21
Figure 1. 6 Evolution of viscosity as a function of the volume fraction of the particles in a suspension. Curves extracted from (a): the article by Seto et al [57], (b): article by Zhongcheng Pan et al [58] and (c): article by Mewis and Wagner [59].	24
Figure 1. 7 Pictures of modern concrete light structures. At the right : A museum in Marseille-France “Musée des civilisations de l'Europe et de la Méditerranée”. At the left: The Sheikh Zayed Bridge in Abu Dhabi.	25
Figure 1. 8 Suspension dilation observed in a rheometer shear test using a parallel plate geometry; ω : angular speed of the rotating plate. (b): Representation of the evolution of rheology curves in $\eta = f(\tau)$ versus volume fraction. the shear thickening regime is limited between the stress interval τ_{\min} and τ_{\max} . a non-zero slope value corresponds to shear thickening while a slope value of 1 corresponds to DST. From Brown and Jaeger [89]......	27
Figure 1. 9 Observation of different hydroclusters (different colors) in shear thickening regime for a Brownian suspension. From Cheng et al. (2011) [95].	28
Figure 1. 10 Lubricated contact (left panel) and frictional contact (right panel) between suspension particles.	29
Figure 1. 11 Lubricated and frictional contact regimes in the suspension. At the left, when the shear rate is increased the contact regime between particles changes from frictionless to frictional between the two curves. Figure adapted from [109].	30
Figure 1. 12 Relative viscosity against the particles volume fraction, different friction coefficient at different shear rate. From Mari and Seto 2014 [103].	31
Figure 1. 13 Representation of contact network evolution as a function of applied shear rate. Adapted from Mari and Seto 2014 [103].	32
Figure 1. 14 (a): Shear thickening phase diagram; (b): The prediction of Wyart and Cates model for different flow regimes depending on the volume fraction of the particles and the dimensionless pressure ratio. From Wyart and Cates [107].	33

Figure 1. 15 Viscoelastic behavior of: (a). a suspension of cornstarch [123]. (b). a suspension of PMMA [125]..... 36

CHAPTER 2

Figure 2. 1 Microphotography of allotropic forms of calcium carbonate, (a): calcite; (b): aragonite; (C): vaterite. From Kammoie [136]..... 40

Figure 2. 2 SEM picture of CC-particles [134]. 41

Figure 2. 3 CC- particles size distribution curves using light scattering (L.S) and by classification of particles above 1 μm from MEB pictures [134]. 42

Figure 2. 4 Effect of superplasticizer - dispersant of cement suspension particles..... 43

Figure 2. 5 Sketch of the chemical composition of the PCP polymer [134]. 44

Figure 2. 6 Adsorption isotherm of PCP-45 on C- microparticles [133]. 46

Figure 2. 7 Optical microscopy snapshots of: (a)- the polyamide (PA) fibers and (b)- glass fibers dispersed in deionized water. The width of the images (a) and (b) corresponds to 1500 and 700 μm respectively. 47

Figure 2. 8 Histogram of the length distribution of PA and glass fibers..... 48

Figure 2. 9 Plate-Plate geometry. 51

Figure 2. 10 Mixer-type rheometric geometry: the double helix rotor (a); streamlines of Newtonian fluid flow induced by the double-helix rotation inside a cylindrical cuvette with the arrows showing the direction of possible flow-induced particle migration (b); cylindrical Couette analogy of the mixer type geometry (c). 53

Figure 2. 11 Cylindrical Couette geometry in (a) and its descriptive scheme in (b). 56

Figure 2. 12 Controlled shear stress test for degassed and non-degassed 64% CC-suspensions. 59

Figure 2. 13 Controlled shear stress test for degassed and water completed 64% CC- suspension against non-degassed 64% CC-suspension. 61

Figure 2. 14 Descriptive sketch of the imposed pressure homemade capillary rheometer. 63

Figure 2. 15 Fast camera device for recording jets of the CC-PA mixtures extending from the tube outlet to the experimental table (a). Geometric notations are introduced in (b). 65

CHAPTER 3

Figure 3. 1 Flow curves of isotropic shaped particle (CC) suspensions at different volume fractions ϕ_p of CC particles measured for the ascending branch of the 1st stress ramp in mixer type geometry. The arrows show definition of the critical shear rate and shear stress in the stress-controlled rheometry. Labels “apparent” in the titles of axes recall that the reported shear rate and shear stress values stem from approximate rheometric conversions of the raw rheological data [Section 2.2.1.2]. 70

Figure 3. 2 Effect of the flow history on the shape of experimental flow curves of the isotropic shape particle (CC) suspensions at CC particle volume fraction $\varphi_p = 0.68$ measured in mixer type (a) and plate-plate (b) geometries. All the reported flow curves correspond to the ascending branch of either the 1st or the 2nd stress ramp. Flow curves obtained during the 1st ramp in both rheometric geometries are compared in figure (c). 72

Figure 3. 3 Effect of the ratio D/d of rod – to CC particle diameter on the experimental flow curves of mixtures of isotropic-shaped (CC) particles and PA fibers (red curves) or glass fibers (blue curves) measured in mixer type geometry for CC particle volume fraction $\varphi_p = 0.64$ and at different fiber volume fractions φ_f . The D/d ratio is 3.1 for PA fibers and 1.4 for glass fibers. Figures (a) and (b) correspond to the ascending branch of the flow curve during the 1st and the 2nd stress ramps, respectively. The black curves on both graphs stand to the flow curves of CC suspensions without rods..... 75

Figure 3. 4 Effect of the fiber volume fraction on the flow curves of the mixtures of isotropic-shaped (CC) particles and PA fibers measured in the mixer type geometry for the ascending branch of the 1st stress ramp at different CC volume fractions. The first, the second and the third rows correspond to the CC volume fraction $\varphi_p = 0.64$; 0.66 and 0.68, respectively. Experimental flow curves on the left and right columns are identical for the each row. Simulated flow curves using RSR and H-model and assuming isotropic fiber orientation ($A_{1212} = 1/15$) are plotted on the left and right columns, respectively. Thin dashed color curves correspond to experimental flow curves; thick solid black lines to predictions of both models [Section. 3.6], thick solid green line – to cubic spline interpolation of the experimental flow curve at $\varphi_f = 0$. Labels “apparent” in the titles of axes recall that the reported shear rate and shear stress values stem from approximate rheometric conversions of the raw rheological data [Chapter 2, section 2.2.1.2-A] 77

Figure 3. 5 Effect of the rheometric mode (stress- or rate-controlled) on the experimental flow curves of the mixtures of isotropic (CC) particles and PA fibers measured in the mixer type geometry for PA volume fraction $\varphi_f = 0.02$ and for the CC particle volume fraction $\varphi_p = 0.64$ (a, b) and 0.68 (c, d). The left and the right columns of figures correspond to the ascending branches of the flow curve during the 1st and the 2nd stress or rate ramps, respectively. The insets on each graph show the flow curves in extended stress scale. The arrows in (a) and (c) show the definition of the critical shear rate and critical shear stress for the rate-controlled mode. 79

Figure 3. 6 Comparison of experimental (thin dashed blue line) and simulated (thick solid red, blue and green lines) flow curves of the mixtures of isotropic (CC) particles and PA fibers for the ascending branch of the 1st stress ramp in the mixer type geometry for PA volume fraction $\varphi_f = 0.02$ and for the CC particle volume fraction $\varphi_p = 0.66$. The predictions of the RSR- and H-models are presented in (a) and (b), respectively. Abbreviations “LH”, “Iso” and “CA” in the figure legend stand for the fiber orientations aligned with the flow ($A_{1212} \approx 0.011$), random ($A_{1212} = 1/15$) and aligned along the compression axis ($A_{1212} = 1/4$), respectively. Thin dashed red and thick black solid curves are respectively experimental flow curve at $\varphi_f = 0\%$ vol, $\varphi_p = 0.66\%$ vol and its cubic spline interpolation. The shaded region in (a) and (b) corresponds to the domain between the lower and upper bounds of the prediction of each model. 82

Figure 3. 7 Simulated and experimental dependencies of the critical shear rate (a) and the critical shear stress (b) of the DST transition on the rod volume fraction. Experimental data are drawn from the ascending branch of the 1st ramp of CC-PA mixtures, measured in stress

controlled (triangles) and strain controlled (squares) modes. Continuous and dashed black lines correspond to the prediction of the RSR- and H-models, respectively, for the isotropic orientation distribution in all mixtures ($A_{1212} = 1/15$). The error bars correspond to the standard deviation of a few measurements realized for each given value of φ_p and φ_f 85

Figure 3. 8 Experimental flow curves of the CC-PA mixtures at fiber volume fraction $\varphi_f = 0.035$ and at different CC particle volume fractions φ_p for the ascending branch of the 1st (thin lines) and the 2nd (thick lines) stress ramps (a). To explain jamming behavior of the CC-rod mixtures at the rod volume fractions $\varphi_f \geq 0.04$, a hypothetical flow curve of the CC-rod mixture is schematically presented in (b) by a solid line. The flow curve of the pure CC suspension at the same CC volume fraction is schematically presented by a dashed line in (b). The critical shear rate $\dot{\gamma}_c$ in the concentrated CC-PA mixture is evaluated to be much lower than that, $\dot{\gamma}_{c0}$, in the pure CC suspension; while the yield stress σ_Y [Eq. (3.27)] of the CC-PA mixture is related to a specific value of the local stress in the gap between fibers, tentatively assigned to the upper critical stress σ' of the DST transition in pure CC suspension..... 87

Figure 3. 9 Relative viscosity η_r of the suspension of PA fibers dispersed in a Newtonian solvent (glycerin) as function of the fiber volume fraction φ_f . Points correspond to the experiment using in the mixer type geometry, solid lines to the predictions of Phan- Thien & Graham model [Eq. (3.14)] and Batchelor model..... 93

Figure 3. 10 Flow curves of isotropic shaped particle (CC) suspensions at different volume fractions φ_p of CC particles measured in mixer type geometry. Dotted curves correspond to experiments; solid curves – to the fit of the experimental flow curves by the WC model applied to $\varphi_p = 0.66$. Notice that the black dashed line partially masks the upper branch (solid green curve) of the theoretical fit of the flow curve at $\varphi_p = 0.66$ 100

Figure 3. 11 Effect of the fiber volume fraction on the flow curves of the mixtures of isotropic-shaped (CC) particles and PA fibers measured in the mixer type geometry for the ascending branch of the 2nd stress ramp at different CC volume fractions. The first, the second and the third rows correspond to the CC volume fraction $\varphi_p = 0.64$; 0.66 and 0.68, respectively. Experimental flow curves on the left and right columns are identical for each row. Simulated flow curves using RSR and H-model and assuming isotropic fiber orientation ($A_{1212} = 1/15$) are plotted on the left and right columns, respectively. Thin dashed color curves correspond to experimental flow curves; thick solid black lines – to predictions of both models [Section. 3.6], thick solid green line – to cubic spline interpolation of the experimental flow curve at $\varphi_f = 0$. Labels “apparent” in the titles of axes recall that the reported shear rate and shear stress values stem from approximate rheometric conversions of the raw rheological data (see Chapter 2, Section 2.2.1.2-A) 101

Figure 3. 12 Effect of the fiber volume fraction φ_f on the flow curves of the mixtures of isotropic-shaped (CC) particles and glass fibers at CC volume fraction $\varphi_p = 0.64$. The flow curves were measured in the mixer-type geometry in the stress-controlled mode and both ascending branch of the 1st stress ramp (a) or the 2nd ramp (b) are presented..... 102

CHAPTER 4

Figure 4. 1 Mass versus time experimental dependencies for a flow of the CC-suspension at CC volume fraction of 68% vol and without PA-fibers..... 107

Figure 4. 2 Rotational rheometry test of CC-suspensions at $\varphi_p = 68 \%$ vol without PA-fibers: freshly prepared suspension against the suspension previously tested in the capillary rheometer. 108

Figure 4. 3 Time response to an applied stress of a CC-suspension at 68% without PA-fibers. 110

Figure 4. 4 Experimental flow curves of CC-PA fiber mixtures in comparison with the theoretical predictions of the H-model: (a): Isotropic fibers orientation $A_{1212} = 1/15$; (b) A_{1212} being adjustable parameter (see Table 4.1). The solid yellow line is the fit of the experimental flow curve of the CC-suspension without PA-fibers, the solid black lines correspond to the theoretical predictions by the H-model to every corresponding fiber concentration. The horizontal and vertical black arrows indicate the critical shear rate and the critical stress of the experimental flow curve of the CC suspension without PA-fibers..... 112

Figure 4. 5 Variation of the critical shear rate and the critical stress as a function of fiber volume fraction. The red markers correspond to the experimental results. The blue markers (triangles) and the black dotted line represent the theoretical predictions of the H-model with respect to fibers orientation parameter A_{1212} . The error bars correspond to the theoretically evaluated standard deviation. 114

Figure 4. 6 (a-d): Capillary rheometry in comparison with shear rheometry results and with the macroscopic model for CC-suspensions at different PA-fibers concentrations. (e): Capillary rheometry results in comparison with the macroscopic model for all fibers volume fractions. 116

Figure 4. 7 Flow curves in capillary geometry of CC-PA fiber mixtures predicted by the H-model in comparison with experiments. (a): $A_{1212} = 1/15$, isotropic fibers orientation. (b): The values of A_{1212} is adjustable and reported in Table 4.1 for each PA-fiber concentration. The diamonds points represent the capillary experiments, and the colored solid lines are the theoretical predictions by the H-model. 118

Figure 4. 8 Critical shear rate and critical stress as a function of fiber volume fraction obtained in capillary rheometry versus theoretical predictions by the H-model. The error bars correspond to standard deviation of experimental data..... 120

CHAPTER 5

Figure 5. 1 Snapshots of falling CC-suspension jet without PA fibers: stable viscous jet (a); jet subject to coiling instability (b); jet subject to lateral oscillations (c). The average length-to-diameter ratio is $L/D_0 \approx 4.0, 8.0$ and 30 for the jets shown in (a), (b c). The average length-to-diameter ratio is $L/D_0 \approx 4.0, 8.0$ and 30 for the jets shown in (a), (b)..... 125

Figure 5. 2 Snapshots of the suspension jets at different PA fiber concentrations. (a) CC suspension without PA- fibers. The jet is completely unstable showing a wavy pattern along its length. (b) CC-PA mixture at $\varphi_f = 0.6\%$ vol. The jet is still unstable and presents some fractures in the bottom section. (c) CC-PA mixture at $\varphi_f = 1.6\%$ vol. The jet is stable against lateral oscillations with frequent fractures occurring at the bottom section of the jet. (d) CC-PA mixture at $\varphi_f = 2\%$ vol. The jet is completely stable against lateral oscillations with frequent fractures all along the jet length. 126

Figure 5. 3 Jet diameter $\langle d \rangle$ averaged over observation time (a) and the jet break-up probability (b) as function of the axial position z for CC-PA mixtures at different PA volume fractions listed in the figure legend. 128

Figure 5. 4 Spatiotemporal diagrams of the jet diameter deviation $\Delta d(t, z)$ (in mm, parts (a), (c), (e), (g)) and jet lateral drift $x(t, z)$ (in mm, parts (b), (d), (f), (h)) for CC-PA mixtures at different PA fiber volume fractions: $\varphi_f = 0$ (CC suspension in absence of fibers) (a) and (b); 0.6% vol (c) and (d), 1.2 % vol (e) and (f), 2% vol (g) and (h). The inset on the right of (a) and (b) shows an enlarged view of a rectangular region of the $\Delta d(t, z)$ -map (a) delimited by the dashed line. Thin yellow bands and thick bands delimited by inclined dashed curves are distinguished on this inset. 129

Figure 5. 5 Contour plots of the Fourier amplitude $D(\omega, k)$ (in mm) of the jet instantaneous diameter $d(t, z)$ of the CC-PA mixtures at different PA volume fractions: $\varphi_f = 0$ % vol (a), 0.2 % vol (b), 0.5% vol (c) and 0.7% vol (d). The dashed lines in (a) and (c) are guides for eye to follow either a single wave speed (a) or two different wave speeds (c). The color bars of (a) and (c) are similar to those of (b) and (d). The sampling rates were fixed to the values $\omega_{up} \approx 1060$ rad/s and $k_{up} \approx 3200$ m⁻¹ slightly larger than twice the highest observable ω and k values (cf. section 2.2.3). The lowest non-zero ω and k values are fixed by the film duration (14.86 s) and the observed jet length (~145 mm) that gives $\omega_{down} \approx 0.423$ rad/s and $k_{down} \approx 43.3$ m⁻¹. 130

Figure 5. 6 Fourier amplitude $X(\omega, k)$ (in mm) of the jet lateral drift $x(z, t)$ of the CC-PA mixtures at different PA volume fractions: surface plot (a), 3D scatter plot of the second quadrant ($\omega \leq 0, k \geq 0$) after sign inversion of ω (b) and contour plot (c) for $\varphi_f = 0$ (CC suspension without PA fibers); contour plots for $\varphi_f = 0.6$ % vol (d), 0.7% vol (e) and 0.8% vol (f). The red lines in (b) correspond to the gaussian fit of each vertical slice (along the lines $k = \text{const}$) of the 3D scatter plot. The black dashed lines in (c) are guides for eye helping one to follow the forward and backward wave crests. The sampling rates were fixed to the values $\omega_{up} \approx 530$ rad/s and $k_{up} \approx 860$ m⁻¹ slightly larger than twice the highest observable ω and k values (cf. section 2.2.3). The lowest non-zero ω and k values are fixed by the film duration (14.86 s) and the observed jet length (~145 mm) that gives $\omega_{down} \approx 0.423$ rad/s and $k_{down} \approx 43.3$ m⁻¹. 133

Figure 5. 7 Effect of the fiber volume fraction on the forward/backward wave speeds v_1 of the jet lateral oscillation and on the blob-and-neck propagation speed v_s . Here, we use the highest of two v_s values for comparison with v_1 135

Figure 5. 8 Dependency of the crest height on the crest length for the lateral oscillations at different PA fibers volume fractions (indicated in the legends) and for forward waves (a) or backward waves (b). 137

Figure 5. 9 Theoretical stress profile (in log-log scale) along the jet of the CC particle suspension in terms of the dimensionless tensile stress as function of the dimensionless jet speed (a). Theoretical flow curves for the extensional rheology of the CC particle suspension (b). Both plots (a) and (b) are made for the Newtonian jet (red solid line) and for the DST WC rheological model (dashed lines) with different values of $\sigma_{E,c}$ and Λ parameters. 141

Figure 5. 10 Theoretical stress profiles along the jet in terms of the tensile stress as a function of the axial position along the jet for the CC suspension without fibers and CC-PA mixtures at $\varphi_f = 1$ % vol and two different fiber orientations. 145

Figure 5. 11 Theoretical phase diagram of the jet stability with the hatched region indicating jet instability against lateral oscillations (DST regime) and non-hatched regions standing for stable jets (stable steady-state flow) (a). Experimental dependencies of the RMS amplitude and RMS transverse speed (left ordinate axes) on the fiber volume fraction compared to the semi-empirical dependency of the DST stress range (right ordinate axis) on the fiber volume fraction (b). 147

Figure 5. 12 Experimental and evaluated break-up length as function of the fiber volume fraction. The red horizontal line stands for the jet length. 150

List of Tables

CHAPTER 2

Table 2. 1 Characteristics of the different allotropes of calcium carbonate [135]..... 39

Table 2. 2 Physical and physicochemical parameters of CC-particles [133, 134]..... 42

Table 2. 3 Chemical properties (molar masses) of PCP-45 Superplasticizer [133]..... 44

Table 2. 4 Geometrical and physical properties of fibers. 48

CHAPTER 4

Table 4. 1 Adjustable values of the fibers orientation parameter A_{1212} corresponding to each Fibers concentration. 112

CHAPTER 5

Table 5.1 Parameters of the CC-PA mixtures related to the tensile stress calculations..... 144

List of Nomenclatures

Acronyms

DST	Discontinuous shear thickening
CST	Continuous shear thickening
CC	Calcium carbonate
PA	Polyamide
PP	Plate-Plate
DH	Double helix
DFT	Discrete Fourier transform
UCA	University Cote d'Azur
SEM	Scanning Electron Microscopy
SLS	Static light scattering
POE	Polyoxyethylene
WC	Wyart and Cates
RMS	Root mean square
RSR	Reduced shear rate

Symbols

σ_{ij}	Cauchy stress tensor
p	Pressure
$\boldsymbol{\tau}$	Viscous stress tensor
\mathbf{e}	Deformation tensor
t	Time
S	Fibers effective stiffness
σ	Shear stress
σ_a	Apparent shear stress
σ_{c0}	Critical stress of the DST transition
σ_{loc}	Local shear stress
σ_w	Shear stress at the capillary walls
$\sigma_E = \sigma_{zz} - \sigma_{rr}$	Tensile stress
σ_{zz}	Axial component of the normal stress
σ_{rr}	Radial component of the normal stress

σ_{bulk}	Characteristic bending stress
$\tilde{\sigma}_{E,c}$	Normalized characteristic stress of the DST transition in extension
σ_Y	Yield stress
$\sigma_{E,l}$	Lower DST threshold tensile stress
$\sigma_{E,u}$	Upper DST threshold tensile stress
$\dot{\gamma}$	Shear rate
$\dot{\gamma}_{c0}$	Critical shear rate of the DST transition
$\dot{\gamma}_R$	Shear rate at the periphery of Plate-Plate geometry disks
$\dot{\gamma}_{a,w}$	Apparent shear rate at the capillary walls for a Newtonian fluid
$\dot{\gamma}_w$	Real shear rate at the capillary walls
$\dot{\gamma}_{loc}$	Local shear rate
$\dot{\gamma}_m$	Reduced shear rate in the matrix
N_1	First normal stress difference
N_2	Second normal stress difference
η	viscosity
η_f	Suspending fluid viscosity
η_s or η_r	Relative shear viscosity
η_0	Average low-shear viscosity
η_m	Non-Newtonian matrix viscosity
η_E	Extensional suspension viscosity
$\eta_{E,r}$	Relative extensional viscosity of the non-Newtonian CC suspension
μ	Microscopic friction coefficient
φ	Volume fraction
φ_P	Particles volume fraction
φ_f	Fibers volume fraction
φ_m	Maximum volume fraction
φ_c	Critical volume fraction
φ_{DST}	DST-particles volume fraction
φ_{fm}	Maximum packing fraction of fibers
φ_{fr}	Packing volume fraction for frictional contacts
φ_p^{true}	True volume fraction of CC particles
φ_{dead}	Volume fraction of the dead zones

φ_{perc}	Fibers volume fraction at percolation threshold
$\Phi_{contact}$	Volume fraction of contact regions
φ_j	Jamming volume fraction
φ_{lub}	Packing volume fractions of particles in purely lubricated regime.
ρ_f	Density of the fluid
ρ_p	Density of the particles
F^R	Repulsion force of the particles
F^f	Hydrodynamic force
\dot{I}	Dimensionless ratio of hydrodynamic to repulsion force
P^P	Particle pressure
P^R	Repulsive pressure
P	Dimensionless ratio of particle pressure to repulsive pressure
f	the fraction of frictional contacts
r	Mean aspect ratio of fibers
E	Young's Modulus of fibers
ζ	Zeta potential
k	wave number
C_{ads}	Concentrations of PCP-45 molecules adsorbed on the surface of CC-particles
$C_{plateau}$	Total concentration of the adsorption sites on the CC particle surface
C_{fluid}	Concentration of free non-adsorbed PCP-45 molecules remaining in the fluid
K_{eq}	Equilibrium reaction constant in Langmuir equation
L	Fiber mean length or jet length
D	Fiber mean diameter
d	CC particle diameter
D_0	Jet diameter at the tube outlet
$\Delta d(t, z)$	Jet diameter deviation
$d(t, z)$	Instantaneous jet diameter
$\langle d \rangle(z)$	Jet diameter averaged over time
R	Radius of the rheometric geometries or jet radius
R_i	Inner cylinder radius

R_e	External cylinder radius
V_p	Volume of the CC dry particles
V_m	Volume of the CC aqueous suspension in water
V_f	Fiber solid phase volume
V	Total volume of the mixture
Γ	Torque
ω	Angular speed or angular frequency
α	Proportionality factor between the torque and the rotational speed
r^*	Optimal radius position
N	Rotational speed
$A ; M$	Rheometric conversion factors
L_g	Gap
Q_m	Mass flow rate
Q	Volume flow rate
ΔP	Applied air pressure in the Capillary geometry
u_0	Mean velocity averaged over the tube cross-section
A	Matrix of complex values of Fourier DFT transform
X	Matrix of the Fourier spectrum amplitudes
x_{RMS}	Root mean square amplitude of the lateral drift
v_{RMS}	Root mean square transverse speed of the jet
A_{1212}	Fibers orientation parameter
A_{1212}^{LH}	Orientation parameter for fibers nearly aligned with the flow
A_{1212}^{Iso}	Orientation parameter for isotropic orientation distribution
A_{1212}^{CA}	Orientation parameter for fibers aligned along the compressive axis
Γ_m	Compaction parameter
Z	Minimal number of contacts per fiber at the percolation threshold
$f_1; f_2$	Scalar invariants depending on fiber orientation distribution
$\tau_{migration}$	Characteristic time of the shear-induced migration
Π	Break-up probability
L_b	Critical break-up jet length
λ	Surface undulation or lateral drift wavelength
u	Jet speed

v_l	Wave speed of the lateral drift
v_s	Wave speed for diameter undulation or sedimentation velocity of a particle in a fluid
Λ	Stretching exponent
ψ_S, ψ_E	Shear and extensional components of the 4 th rank fiber orientation tensor.
$\dot{\epsilon}(z)$	Extension rate along the jet

CHAPTER 1

1 Basic concepts of rheology. Shear thickening. Thesis objectives

In this chapter, we provide an overview of some macroscopic rheological laws, suspension rheology, and focus on shear thickening in dense suspensions. In particular, we first introduce the concept of shear thickening and discuss some of its applications, focusing on the discontinuous shear thickening (DST) observed in concentrated suspensions. We also discuss on the origin of this physical behavior, providing a detailed history of the different approaches that can explain its occurrence in dense non-Brownian suspensions, from the hydrodynamic forces approach to frictional contact forces between particles, and also discuss the differences between these two approaches. The review of the recent literature on the DST will allow us to reveal important lacks of rheological understanding of some particular DST systems, which in its turn, will allow us to formulate the objectives of the present work in view of the new physical insights and application to cement-based materials.

1.1 Macroscopic rheological behaviors

1.1.1 Stress tensor

Continuum mechanics expresses the law that defines the behavior of the fluid and its motion, or in other words the relationship between applied stress fields and deformations undergone in a tensorial form. The surface forces exerted by the fluid are generally represented by the Cauchy stress tensor, $\boldsymbol{\sigma}$ written in component form as σ_{ij} . The diagonal terms σ_{ii} are the normal stresses and are responsible for compression and elongation, whereas the terms σ_{ij} ($i \neq j$) are the tangential stresses and are responsible for shear within the fluid, i and j being subscripts representing the direction of the stress and the surface of application of the stress, this means that the stress σ_{ij} is the stress applied in the direction i on a surface normal to j . Its general expression in the (1,2,3) reference frame representing the directions of flow, velocity gradient, and vorticity is given by:

$$\boldsymbol{\sigma} = \begin{bmatrix} \sigma_{11} & \sigma_{12} & \sigma_{13} \\ \sigma_{21} & \sigma_{22} & \sigma_{23} \\ \sigma_{31} & \sigma_{32} & \sigma_{33} \end{bmatrix} \quad (1.1)$$

Without flow, the stresses are normal, identical, and opposite to the pressure applied on the fluid (mainly hydrostatic stresses). The stress tensor can then be reduced to a part representing the exerted pressure $p = -\frac{1}{3}\sigma_{ii}$ (here summation over repeated subscripts is performed) and a part representing the viscous stress tensor $\boldsymbol{\tau}$, which appears when the fluid is in motion.

$$\boldsymbol{\sigma} = \boldsymbol{\tau} - p\boldsymbol{\delta} \quad (1.2)$$

where $\boldsymbol{\delta}$ is the Kronecker delta ($\delta_{ij} = 1$ if $i = j$ and $\delta_{ij} = 0$ if $i \neq j$). By convention, the negative sign of the pressure p indicates that the liquid is in compression.

1.1.2 Simple shear and normal stress differences

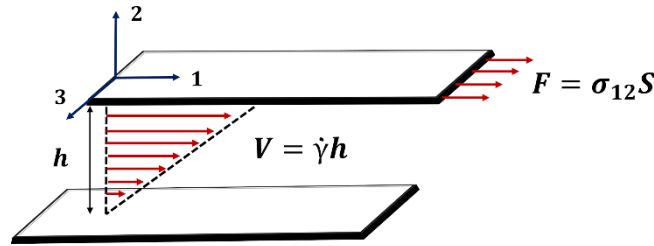


Figure 1.1 Simple shear rheology test. The fluid is located between two continuous plates. The upper plate is driven by a force F and is moving at a speed V .

Simple example of a shear test of a fluid is the flow between two continuous plates [Figure 1.1]. In such case the upper surface moves with a velocity \mathbf{V} by an applied force and drags along the fluid between the plates. This creates a velocity gradient otherwise known as a shear rate $\dot{\gamma}$ which is defined as the derivative of the velocity in the normal direction of the flow (direction 2) and is equal to the ratio of the maximum velocity (that of the upper surface) to the distance h .

$$\dot{\gamma} = \frac{\partial u}{\partial y} = \frac{V}{h} \quad (1.3)$$

The fluid being sheared by a force \mathbf{F} , it naturally undergoes a deformation. The rate of this deformation is expressed by the deformation tensor \mathbf{e} :

$$\mathbf{e} = \frac{1}{2} \begin{bmatrix} 0 & \dot{\gamma} & 0 \\ \dot{\gamma} & 0 & 0 \\ 0 & 0 & 0 \end{bmatrix} \quad (1.4)$$

The stress tensor $\boldsymbol{\sigma}$ is then written as follows:

$$\boldsymbol{\sigma} = \boldsymbol{\tau} - p\boldsymbol{\delta} = \begin{bmatrix} -p & \eta\dot{\gamma} & 0 \\ \eta\dot{\gamma} & -p & 0 \\ 0 & 0 & -p \end{bmatrix} \quad (1.5)$$

knowing that in the case of a Newtonian fluid the viscous stress tensor is directly related to the deformation tensor by the fluid viscosity η_f :

$$\boldsymbol{\tau} = 2\eta_f \mathbf{e} \quad (1.6)$$

In this case only $\sigma_{12} = \sigma_{21} = \eta\dot{\gamma}$ and $\sigma_{11} = \sigma_{22} = \sigma_{33} = -p$ are non-zero applied stresses values, other stresses: $\sigma_{13}, \sigma_{23}, \sigma_{31}$ and σ_{32} are zero.

In the case of non-Newtonian fluids, the viscosity can be dependent on the shear rate. The viscosity expressions are then non-linear, also for such fluids it is not possible to differentiate the pressure p from the normal viscous stresses τ_{ii} [1, 2]. We then try to get rid of the contribution of the isotropic pressure p , which is done by estimating the normal stresses differences N_1 (first normal stress difference) and N_2 (second normal stress difference).

$$N_1 = \sigma_{11} - \sigma_{22} \quad (1.7)$$

$$N_2 = \sigma_{22} - \sigma_{33} \quad (1.8)$$

For a Newtonian fluid the normal stresses differences are nil. The existence of normal stress differences in certain non-Newtonian liquids is the cause of spectacular phenomena such as the Weissenberg effect and the “die swell”. To observe the former effect, one can immerse a rod in this liquid and make it rotate, the liquid can be seen going up along the rod. On the contrary, in a Newtonian liquid, it collapses around the rod by inertia [3].

1.1.3 Non-Newtonian behaviors

In non-Newtonian fluids, the viscosity depends strongly on the applied deformation, more precisely on the shear rate. Therefore, its value is not constant as in the case of Newtonian fluids, this is mainly due to the link between the microstructure of the fluid and the flow, which causes the non-linearity. There are three main types of behavior (see Figure 1.2). The first one is shear-thinning where the viscosity of the fluid decreases with the shear rate. Simple examples of shear-thinning fluids are ketchup or shampoo. The second type is shear thickening where the viscosity increases with the shear rate; as an example, the famous mixture of cornstarch with water if stirred at high speed, solidifies. And the third type corresponds to the yield stress fluids where below a threshold stress, the viscosity is infinite regardless of the applied stress and the fluid does not flow. Above this value the fluid can flow.

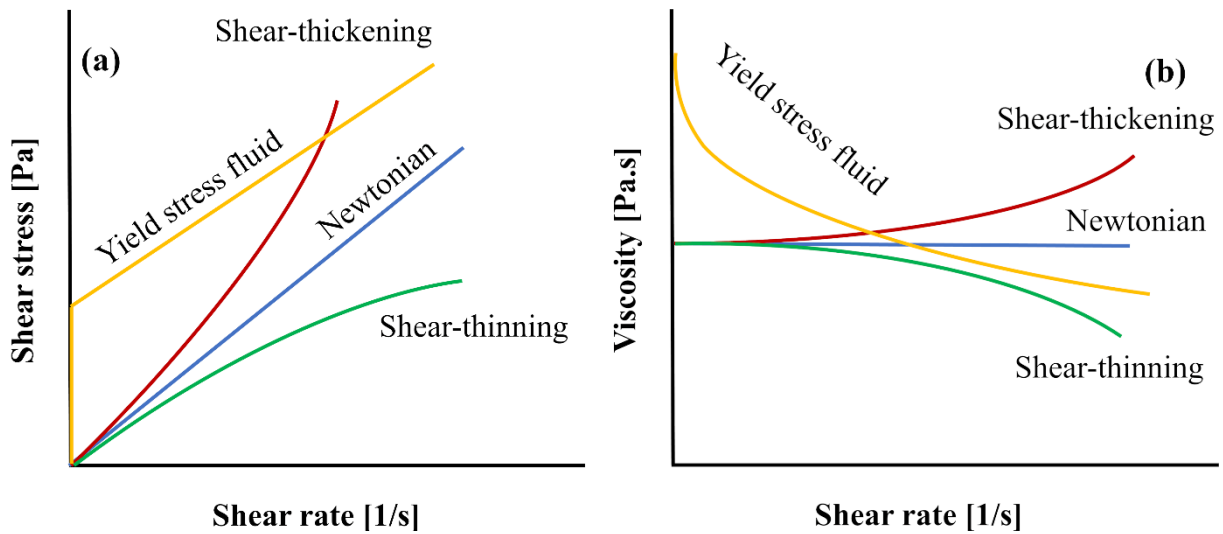


Figure 1.2 Flow curves for different types of fluids. (a): Stress vs shear rate. (b): Viscosity vs shear rate.

In our thesis, we are focusing more on the shear thickening type of non-Newtonian fluids.

1.2 Suspension rheology

1.2.1 Viscosity and volume fraction

Consider a suspension of hard particles dispersed in a Newtonian fluid of viscosity η_f . It has been reported that when the volume fraction φ of the particles in the volume is increased, the rheological behavior of the suspension becomes very strongly related to it, being able to change the Newtonian nature of the suspension flow to a shear thickening nature. For a simple shear test of this suspension (see Figure 1.1), the viscosity η is a function of the suspending fluid viscosity η_f and a relative shear viscosity η_s , a function of the volume fraction φ of the particles.

$$\eta = \eta_f \eta_s(\varphi) \quad (1.9)$$

Numerous studies show the dependence of the viscosity on the volume fraction. Einstein in 1906 [4] proposed the first theoretical model for a diluted regime.

$$\eta_s = 1 + 2.5\varphi \quad (1.10)$$

This law applies to spherical particles whose interactions are neglected. This assumes very low concentrations $\varphi \leq 0.03$ to avoid hydrodynamic interactions and above this value, it is mandatory to consider the interactions between particles. For higher volume fractions, in the semi-dilute regime $\varphi = 0.15$, Batchelor and Green [5] extended Einstein's theoretical formula for a rapid increase in viscosity since hydrodynamic interactions and Brownian forces in the

suspension must be taken into account. The formula found contains a second order term φ^2 highlighting pairwise hydrodynamic interactions between particles implying a faster increase in viscosity as a function of volume fraction.

$$\eta_s = 1 + 2.5\varphi + 6.5\varphi^2 \quad (1.11)$$

Beyond this volume fraction, viscosity divergence occurs at concentrations close to the maximum volume fraction and there is no analytical model to well describe the viscosity divergence. To take into account this divergence it is necessary to consider the contact forces, lubrication, possibly colloidal interactions [6-8], and this becomes a very complex matter. Thus, empirical models along with experimental and numerical studies were involved trying to determine the rheology of suspensions (see Figure 1.3) [9-11]. However, the diversity of the studied systems gives great differences in the different laws. The Eilers model [9] was the first to predict the divergence of the viscosity for volume fractions near the maximum volume fraction φ_m :

$$\eta_s = \left[1 + \frac{1.25 \varphi}{\left(1 - \frac{\varphi}{\varphi_m}\right)} \right]^2 \quad (1.12)$$

Later, Maron-Pierce [10], proposed another model in 1956:

$$\eta_s = \left(1 - \frac{\varphi}{\varphi_m} \right)^{-2} \quad (1.13)$$

After that, in 1957 Krieger and Dougherty [11] developed a model, which became the most popular in the rheologists community :

$$\eta_s = \left(1 - \frac{\varphi}{\varphi_m} \right)^{-[\eta]\varphi_m} \quad (1.14)$$

Notice that a small variation in φ in the high-volume fraction range can lead to a large variation in η . For spherical particles, the maximum packing fraction, or the random close packing (RCP), is agreed to be 0.635 ± 0.005 [7], otherwise for high aspect ratio r of fibers, $\varphi_m = 5.4/r$ corresponding to the upper granular limit of colloidal rods [12].

Other viscosity formulas for $\eta(\varphi)$ exist, such as the one proposed by Morris et Boulay [13] in 1999:

$$\eta_s = 1 + 2.5\varphi \left(1 - \frac{\varphi}{\varphi_m} \right)^{-1} + 0.1 \left(\frac{\varphi}{\varphi_m} \right)^2 \left(1 - \frac{\varphi}{\varphi_m} \right)^{-2} \quad (1.15)$$

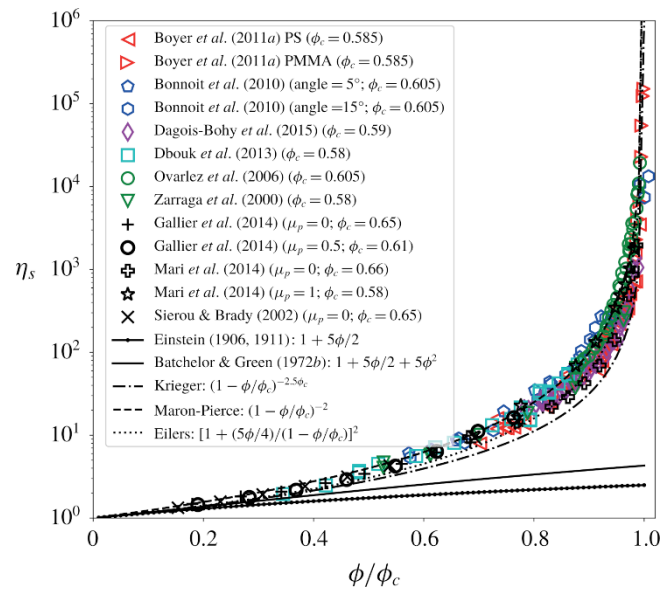


Figure 1.3 Relative shear viscosity as a function of volume fraction of particles. From [14] with kind permission

1.2.2 Particles migration

The flow of a suspension of hard particles is very complex and does not lack physical effects that have been the subject of several studies. In pioneering works on particle migration, it has been found that when a suspension flows through a channel, particles accumulate in the center and agglomerate in the low shear zones leading to a plug flow. This heterogeneity leads to completely blocked zones where the shearing is the weakest. Gadala-Maria and Acrivos [15] observed a decrease in the measured viscosity of the suspension after shear experiments conducted in a Couette cell with concentrated suspensions of spheres due to a diffusion of the particles induced by shear, this is known as particles migration. There are more interactions between particles near the rotating cylinder than near the fixed cylinder, due to the high shear rate. Therefore, the particles subjected to this high shear rate move and migrate towards the regions where the interactions are less frequent. This migration thus generates a gradient of particle concentration, and this gradient itself generates a flow of particles that counterbalances the migration. Furthermore, since viscosity is related to particle concentration, the concentration gradient creates a viscosity gradient within the suspension [16-19]. Since then, several studies have shown similar results in different systems [20-22]. Lagrée and Lhuillier [23], proposed a theoretical model of a continuous medium of the concentrated suspension subjected to a steady shear in a Couette cell geometry, in two different situations: constant confining pressure, and constant average volume fraction (or constant volume of the fluid). The model predicts the profiles of velocity and concentration of the particles. In this model, the pressure exerted along the radial direction (called granular pressure) is the result of the various particle spatial

arrangements, the inter-particle impacts, and the fluid pressure. Because of Reynolds dilatancy [24], shearing of the medium at constant average volume fraction leads to an increase in granular pressure and, shearing of the medium at constant pressure leads to a decrease in average volume fraction. Therefore, at constant mean volume fraction, the volume fraction near the rotating inner cylinder decreases while the volume fraction near the fixed outer cylinder increases. Therefore, whether at constant pressure or constant volume, they highlight two important properties of a volume fraction profile in the Couette cell. The first one is that the local volume fraction increases toward the fixed outer cylinder because of the low shear rate zone, and the local volume fraction near the rotating inner cylinder decreases as the shear increases (see Figure 1.4).

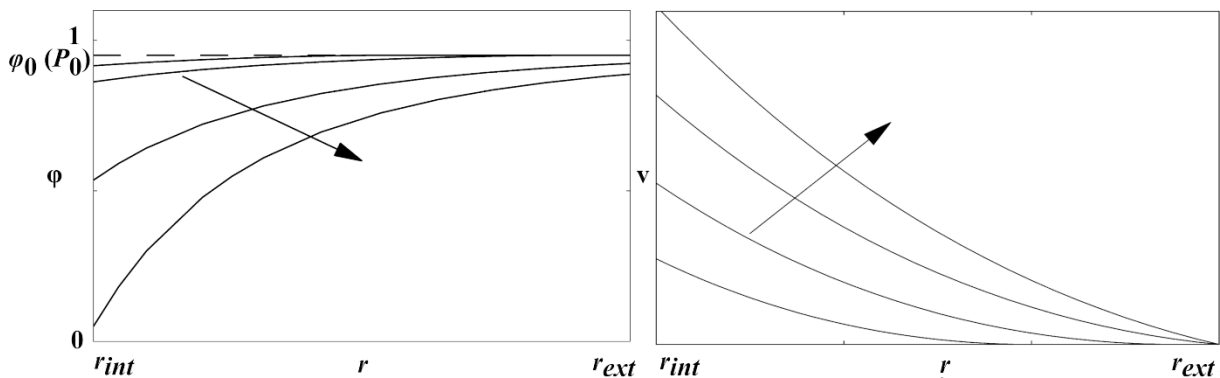


Figure 1.4 (a): Particles volume fraction profile (in arrow direction) for increasing shear stresses and a constant confining pressure; (b): Velocity profiles for increasing shear stresses of the Couette cell (in arrow direction) and a constant pressure- From Lagr e and Lhuillier [23] with kind permission.

Other works investigated the particles migration of non-Brownian [25] and Brownian suspensions [26] in channels of rectangular shapes. They found in such case that the particles tend to migrate to the lower shear zone, which is the center of the channel (see Figure 1.5).

Otherwise, in 1985 Leighton and Acrivos [17] confirmed the clear effect of migration of particles on the decrease of the effective viscosity of a non-Brownian suspension. Their experiment was motivated by the strange observations in the previous study in 1980 conducted by Gadala-Maria and Acrivos [16] when a decrease in the viscosity was observed for a suspension of large diameter polystyrene spheres (40 – 50 μm) suspended in silicone oil at high particles volume fraction ($\varphi > 0.4$), when the suspension underwent a long period of shear. The viscosity after decreasing reached a time independent value after some period of shearing. The comments raised by Leighton and Acrivos about the previous study [16] were that first the suspending fluid was Newtonian, showing no degradation under the experimental conditions and second the particles were large enough (40 – 50 μm) to rule out significant

influence of Brownian and electro-viscous forces. After repeating the experiment with their thin-gap Couette viscometer, Leighton and Acrivos characterized particles migration by a variable frequency of interparticle interactions and variable effective viscosity. They showed that during shear, particles migrate to a reservoir containing a stagnant part of the suspension, thus to a low-shear region, and as in concentrated suspensions, the viscosity is a function that increases very quickly with the particle concentration; its measured value can be therefore strongly impacted by even small variations of the particle concentration during migration.

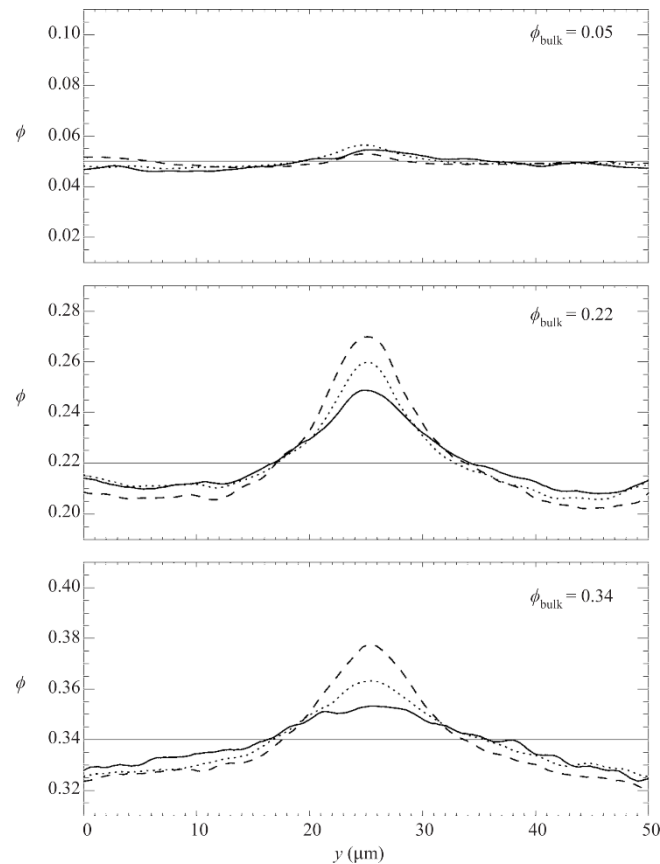


Figure 1.5 Local particles volume fraction as function of the channel distance for different suspension concentrations—from Frank et al. [26] with kind permission.

1.2.3 Particles sedimentation

In a non-Brownian concentrated suspension, the particles of the suspension sediment under gravity. Sedimentation has also an impact on the viscosity of the suspension and the later may increase considerably with the sedimentation of the particles in the suspension. The sedimentation is due to three main forces, particles weight (particles density higher than suspending fluid in the suspension), buoyancy (Archimedes' force) and friction between particles. For dilute suspensions, $\varphi < 1\%$, the sedimentation velocity of a particle in a fluid is given by [27]:

$$v_s = \frac{9(\rho_p - \rho_f)gR^2}{2\eta_f} \quad (1.16)$$

where R is the particle radius, ρ_f is the density of the fluid, ρ_p is the density of the particles and η_f is the suspending fluid viscosity. For more concentrated suspensions, the particle sedimentation velocity will be strongly affected by the hydrodynamic interactions of neighboring particles. Richardson and Zaki [28] considered the impact of the volume fraction in their evaluation of the sedimentation velocity:

$$\langle v \rangle = v_s(1 - \varphi)^{4.65} \quad (1.17)$$

The sedimentation velocity significantly decreases with the increase of the particles volume fraction.

1.2.4 Normal stress differences

In the case of simple shear of a Newtonian fluid, the normal stresses remain isotropic and only the tangential stress σ_{12} is influenced by the flow, however in the case of concentrated suspensions, the shear induces an anisotropy and leads eventually to a difference between normal stresses (see equations 1.7 and 1.8). Numerous studies [29-33] have been conducted on suspensions to determine the normal stress differences N_1 and N_2 . However, whether the normal stresses of the particle phase or of the whole suspension are measured remains open. In previous works, normal stress differences have been expressed as a function of shear stress τ or as a function of shear rate.

Studies on the measurement of N_1 and N_2 for suspensions are few compared to those on polymers. Therefore, recently, various studies have focused on measuring normal stress differences in suspensions [34].

Dbouk et al. [35], conducted an experimental study to evaluate the first and second normal stresses N_1 and N_2 for a suspension of non-Brownian hard spheres. In their study, as expected, the second normal stress N_2 , is a negative value and is much larger than N_1 . This is in agreement with other experimental and numerical studies [30, 31, 36-38] However, in their study, Dbouk et al. reported a small but positive value of the first normal stress N_1 , which contrasts with other experimental studies such as Zarraga et al. and Dai et al, [30], [38] who reported a negative value for N_1 . It is interesting to note through the previous studies that the sign of the difference in the first normal stress is elusive and difficult to assign, some have stated that the value is too small to be identified as positive or negative or even null [31]. The influence of particle volume

fraction on normal stress differences was also investigated in the work of Dbouk et al. [35] it was found that, the second normal stress difference N_2 varies with particle concentration and its value increases rapidly when the particle concentration is greater than 0.2 .

1.3 Shear thickening in concentrated suspensions

1.3.1 General framework

Shear thickening behavior of concentrated suspensions has long been the preoccupation of many studies [39-49]. One of the simplest examples of shear thickening behavior is the mixture of cornstarch polydisperse particles with water, the so-called cornstarch suspension. At low concentrations of cornstarch particles, the viscosity of this mixture is Newtonian, which means that it does not depend on the imposed shear rate or imposed shear stress, but when the particles are put in the suspension at high concentrations, the later becomes shear thickening. This means that its viscosity is no longer a constant and increases as a function of the shear rate (or stress). There are two types of shear thickening: CST or continuous shear thickening where the viscosity increases gently with the shear rate and DST or discontinuous shear thickening, where the viscosity of the fluid increases sharply (see Figure 1.6). The reason for the transition from CST to DST is the high concentration of particles in the mixture, when the particles concentration is sufficiently high, the viscosity of the suspension presents a transition (a divergence) at a critical shear rate, noted $\dot{\gamma}_c$ (or shear stress σ_c). This DST effect has allowed people to run on a pool of cornstarch because the shear is very high and the suspension is enough concentrated, so the viscosity is large enough to support the weight of the person running. The DST behavior is universal for various suspensions; however, its physical origin has always been an open question [50-56].

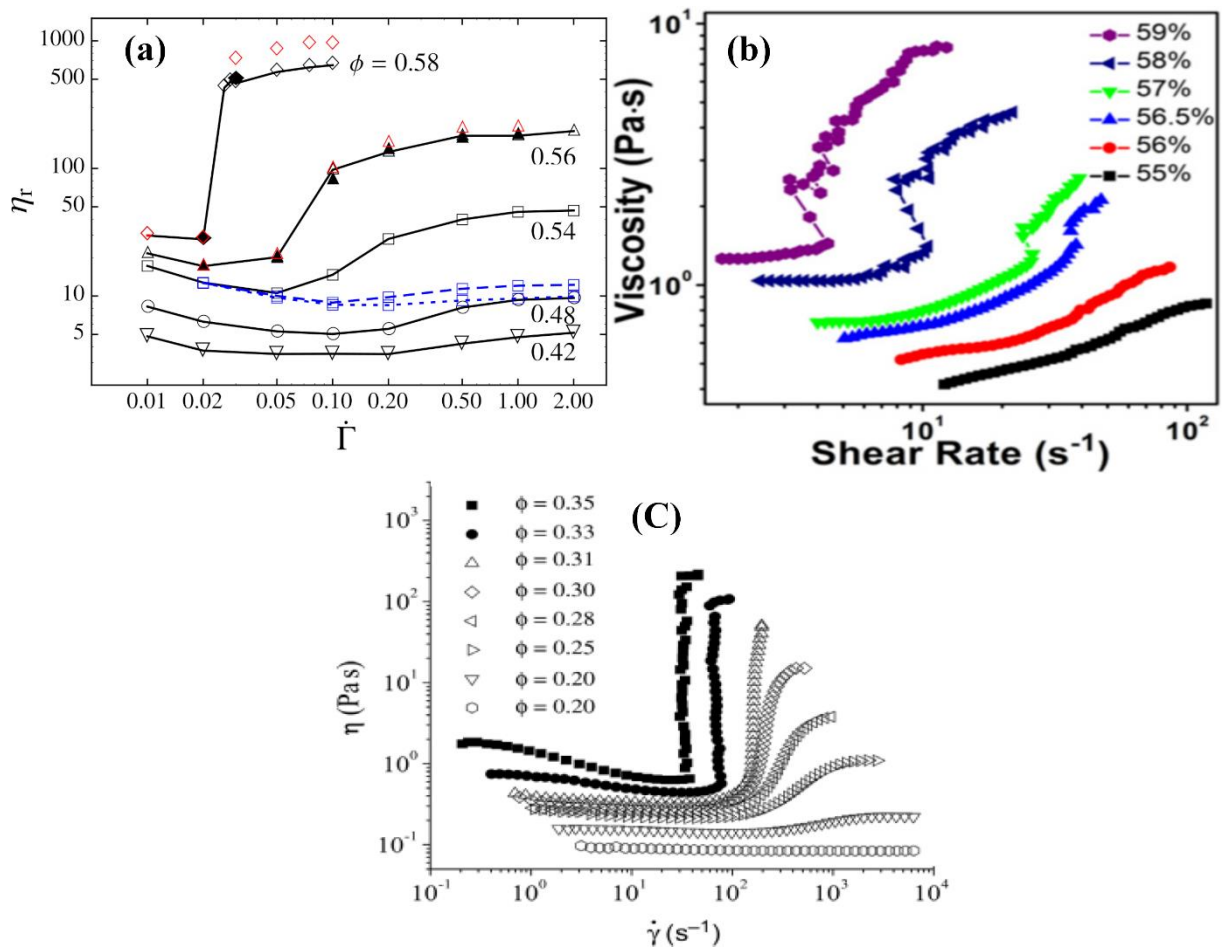


Figure 1.6 Evolution of viscosity as a function of the volume fraction of the particles in a suspension. Curves extracted from (a): the article by Seto et al [57], (b): article by Zhongcheng Pan et al [58] and (c): article by Mewis and Wagner [59], with kind permissions.

1.3.2 Shear thickening in industrial applications

In many applications, producing industries want to prevent shear thickening behavior or at least reduce its effects [60], especially discontinuous shear thickening. A dramatic viscosity rises of a fluid or a suspension under shear can cause several problems leading to damage tools/materials, like mixers for cement pasts or transporting pipes [61]. However, shear thickening can find many useful applications in various industrial fields, such as protective body armors which showed promise for enhanced protection and flexibility [62-67], as well as in food industry [68, 69], in smart structures like smart viscoelastic damper to obtain adaptive stiffness and damping structures/devises [70-72]. Shear thickening can also find a major and important use in the cement industry and reinforced concrete, our thematic work is more related to this field of use, since our studied shear thickening suspension, which is the calcium carbonate (CC) suspension, represent a good model for a cementitious paste. It is a great challenge to obtain a strong dry concrete yet easy to work with in the fresh state due to the high packing fraction of the particles. Keeping good fluidity in a high compaction fraction has been

the subject of vigorous research [73-78], and for a long time, the limited knowledge of concrete forced engineers to give a building a linear shape to ensure a solid structure. The search into the physics and chemistry of concrete has enabled to design self-compacting high-performance concrete allowing more complex shapes of the structure and more spectacular buildings to be built. To achieve this, researchers studied the physicochemical nature of concrete and analyzed it on a microscopic scale. Fresh standard concrete meets all the durability and solidity requirements, but it is often extremely hard and viscous and difficult to work with. A natural physical phenomenon lies at the root of this problem, cement particles in concrete are irreversibly stacked to each other when mixed with water and produce particles agglomeration. Thus, the viscosity of the concrete will eventually increase and the concrete will be hard to work with. To produce concrete with great fluidity and workability without adding more water, researchers have developed technology based on the use of dispersed additives commonly known as superplasticizers [79]. A superplasticizer is a molecule that physically separates the cement particles. This molecule temporarily neutralizes the forces of attraction between cement particles, and this gives the concrete a much more liquid consistency. By taking it in a closer look, it can be seen that superplasticizer molecules are made up of long chains grafted to the cement particle surface and pointing out from the particle surface toward the solvent. Thus, the superplasticizer adsorbs to the cement particles. The quality of the raw material used to manufacture the cement can influence this adsorption process. The later generations of superplasticizers take this cement variation into account. They possess high adsorption energy and cover all the particles regardless of their type. The superplasticizer chains are long enough to separate the particles and fluidize the mixture; this is known as steric repulsion. The science of additives opens up greater opportunities for architects who, thanks to self-compacting, solid and long-lasting concrete, can design more sophisticated buildings with ever more ambitious structures [Figure 1.7].



Figure 1.7 Pictures of modern concrete light structures. At the right : A museum in Marseille- France “Musée des civilisations de l'Europe et de la Méditerranée”. At the left: The Sheikh Zayed Bridge in Abu Dhabi.

1.3.3 Shear thickening physical origins

In the earlier studies [80-82] shear thickening behavior has often been confused with dilatancy. Described as a characteristic of dense granular flows in which, under shear, particles attempt to bypass each other but often cannot take a direct path, so their packing volume is stretched [7], [24], but this misunderstanding soon was dismissed after the confirmation in Metzner and Whitlock's work [81] that dilatancy can be observed without shear thickening in some suspensions. It is important to mention that there are still some studies which came after and reconsidered dilatancy as a mechanism that may lead to discontinuous shear thickening (DST) [83-88]. Brown and Jager [89] carried out experiments in a rheometer with two geometries: a parallel plates geometry where the suspension is confined between the two plates by the liquid-air surface tension and another modified geometry similar to a Couette geometry where the suspension is completely confined by solid walls all around so that the particles cannot penetrate this liquid-air interface. The idea was that when the dense suspension is sheared, it dilates and is soon frustrated by the boundaries of the confining geometry walls. Normal stresses are therefore generated against the confining walls which in turn generate opposite reaction forces transmitted fictionally by particles and build a frictional contact chain proportional to the normal force applied to the confining walls, this allows the shear stress to increase dramatically with the shear rate associated with the DST [Figure 1.8]

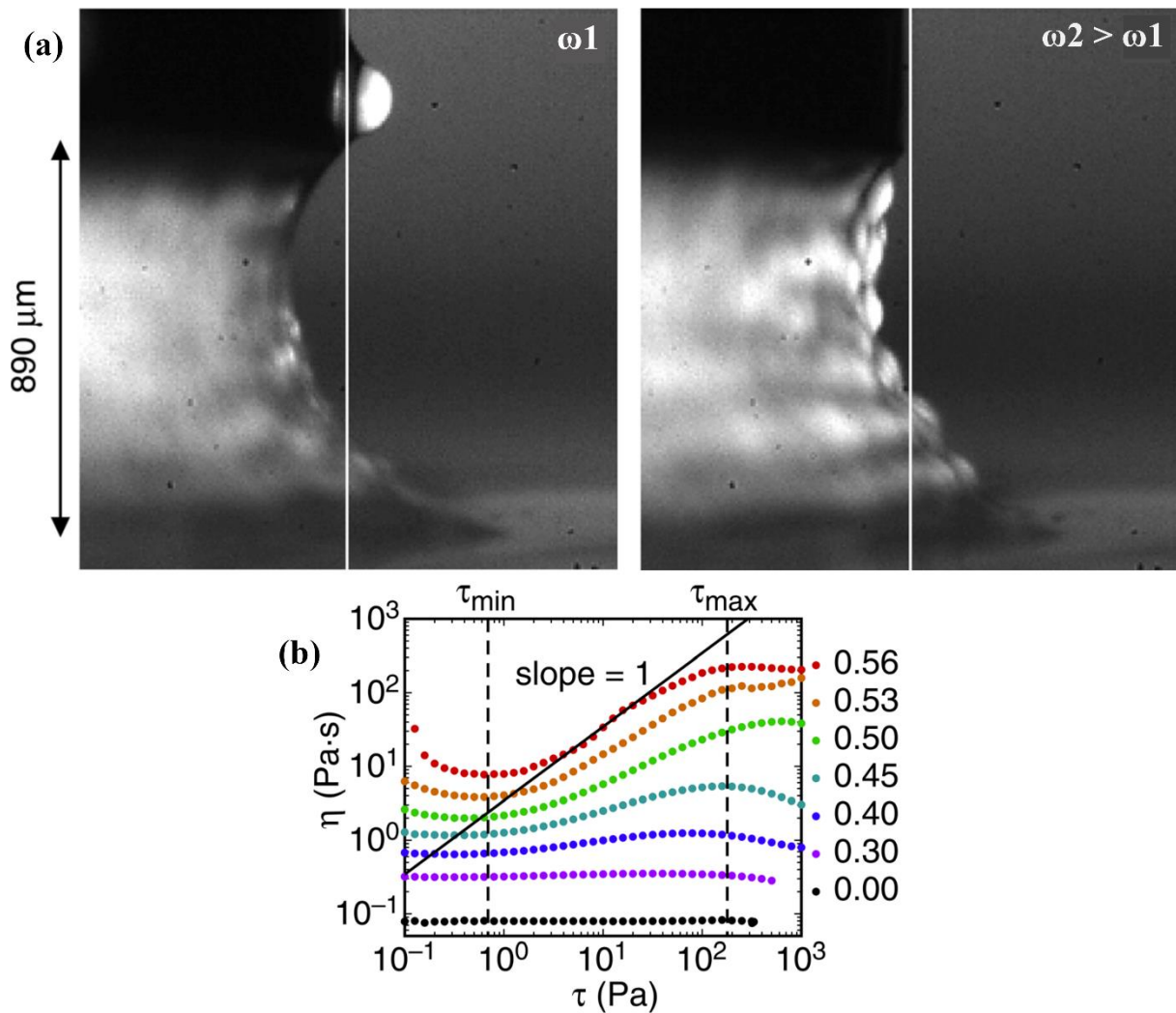


Figure 1.8 Suspension dilation observed in a rheometer shear test using a parallel plate geometry; ω : angular speed of the rotating plate. (b): Representation of the evolution of rheology curves in $\eta = f(\tau)$ versus volume fraction. the shear thickening regime is limited between the stress interval τ_{min} and τ_{max} . a non-zero slope value corresponds to shear thickening while a slope value of 1 corresponds to DST. From Brown and Jaeger [89], with kind permission.

We can see that the frictional contact between particles was involved in the first efforts to explain the shear thickening and DST. However, the mechanism involving hydroclusters became more popular for some period of time.

1.3.3.1 Hydrodynamic forces approach

After studies that attempted to relate shear thickening to dilatancy, in the last eighties, a new mechanism was proposed to describe shear thickening behavior. This mechanism is based only on the hydrodynamic forces (viscous-drag friction and lubrication force) exerted between particles immersed in a Newtonian fluid. Basically, the particles are prevented from collisions with each other by hydrodynamic lubrication forces that diverge when two particles come very close to each other. Brady and Bossis [90] were the first to introduce this mechanism in 1985. Due to the large increase in hydrodynamic lubrication forces between the vicinity of the

particles, at some critical shear, the particles can form what we can call hydrocluster (see Figure 1.9) and when the hydrocluster of the particles become large, this will increase the effective viscosity producing a shear thickening behavior. However, this mechanism based of hydrodynamic forces and particles hydroclustering has only been linked to a soft regime of shear thickening or what we call continuous shear thickening, especially for colloidal suspensions (suspensions with small size particles between 1 nm and 1 μm) [91-94]. As it can only rise the viscosity of the suspension to a factor of 2, way too far from the viscosity magnitude observed experimentally for discontinuous shear thickening.

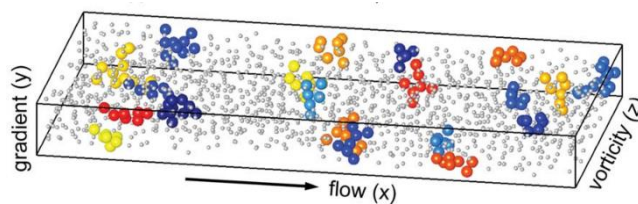


Figure 1.9 Observation of different hydroclusters (different colors) in shear thickening regime for a Brownian suspension. From Cheng et al. (2011) [95], with kind permission.

1.3.3.2 Order disorder transition

A mechanism to explain the DST in suspensions known as «the order-disorder transition" was introduced by Hoffman [39, 40], where the idea was that the DST is the result of a change in the microstructure of the suspension. Basically, during shear, the flow transits from a stable ordered state at low shear rate where it can flow easily to an unstable disordered state that restricts the flow to high shear rate.

This mechanism was able to predict the onset of DST and has also been validated [96], however, other studies [97-99], have shown that DST is not necessarily the result of this transition and can be observed in other contexts. Therefore, DST may coincide with a change in the microstructure of a suspension but not necessarily the product of it.

1.3.3.3 Frictional force approach

Until a decade ago, there was no solid evidence of the origin of shear thickening. the approach of hydrodynamic lubrication forces with the formation of hydroclusters could only explain the weak form of shear thickening or CST, on the other hand this mechanism was far from explaining the strong form of shear thickening or DST. For non-Brownian suspensions the case was even more complex, the models based on hydrodynamic forces all failed to predict DST [100]. Recently the notion of frictional contact has been brought back into consideration [101], and since then a growing number of works have also highlighted the importance of frictional contact between particles in suspension rheology in general [102] and for the onset of

DST in particular [57], [103 -107]. In the following, we will detail some of proposed theoretical model of frictional transition since it is often compared in our work.

A. General framework

The principle behind the frictional transition model can be explained with a simple diagram of two spherical solid particles in a suspension with particles volume fraction φ suspended in a Newtonian fluid (see Figure 1.10). The relevant parameter of the suspension flow is the repulsive force denoted F^R , which is the force that allows the particles to remain in lubricated contact. This force comes for example from a layer of polymer adsorbed on the surface of the particles [108].

During the flow, the fluid exerts a hydrodynamic force denoted F^f , the competition between the two forces allows to define the nature of the flow, either lubricated or frictional:

- If $F^R > F^f$ the flow is lubricated and no frictional contact between particles is established.
- If $F^R < F^f$ the repulsion force of the particles cannot counterbalance the hydrodynamic force and the contact between particles becomes frictional beyond their lubrication layer.

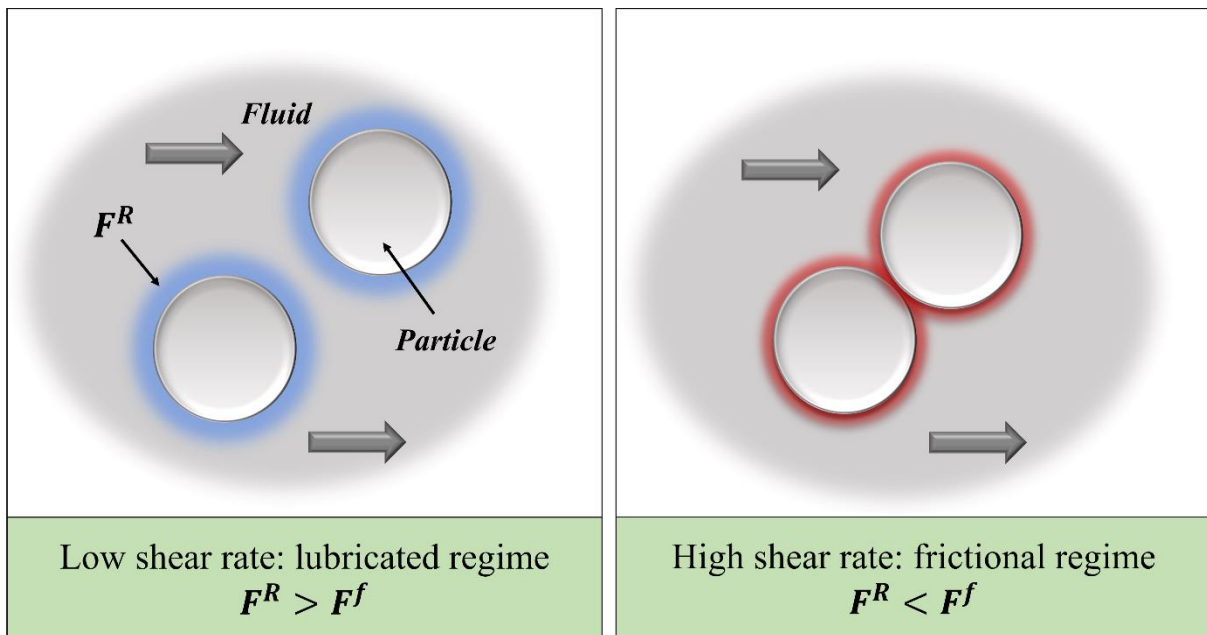


Figure 1.10 Lubricated contact (left panel) and frictional contact (right panel) between suspension particles.

This shear dependent transition of regimes (lubricated at low shear rate (or shear stress) to a frictional non-lubricated at high shear rate (or shear stress)) allows to introduce a dimensionless ratio between the two forces which control the transition:

$$\dot{\Gamma} = \frac{F^f}{F^R} \tag{1.18}$$

The viscosity of the suspension η however, strongly depend on the flow regime (frictionless/frictional) and the particles volume fraction φ . Two case scenarios are then noted (see Figure 1.11):

- For low $\dot{\gamma}$: The flow regime is frictionless and $\eta = \eta_1$ that diverge at φ_c^1 .
- For high $\dot{\gamma}$: The flow regime is frictional and $\eta = \eta_2 > \eta_1$ that diverge at $\varphi_c^2 < \varphi_c^1$

We can then notice the different regimes for shear thickening according to particles volume fraction as the following:

- If $\varphi < \varphi_c^2$, then for low values of φ , the shear thickening is qualified as continuous CST and for high values of φ , the shear thickening is then discontinuous DST.
- If $\varphi_c^2 < \varphi < \varphi_c^1$, in that case, continuous stable flow can only occur in the lubricated regime. If the shear rate is suddenly increased, the regime quickly becomes frictional and the suspension jams.

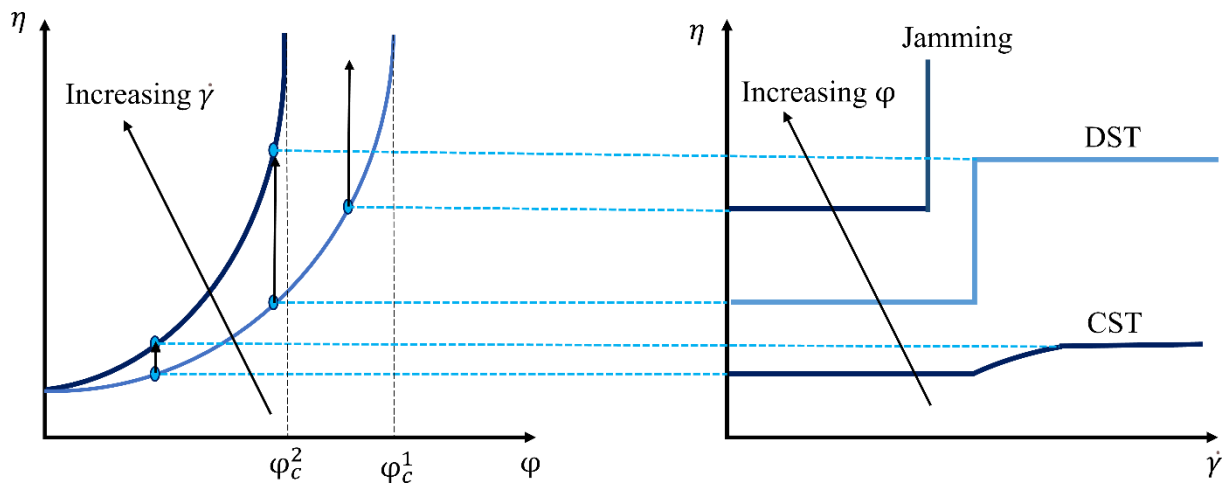


Figure 1.11 Lubricated and frictional contact regimes in the suspension. At the left, when the shear rate is increased the contact regime between particles changes from frictionless to frictional between the two curves. Adapted from [109].

The viscosity of the suspension is now a function of the particles volume fraction as well as the shear rate (compared to Eq. 1.9).

$$\eta = \eta_f \eta_s(\varphi, \dot{\gamma} \text{ or } \dot{\Gamma}) \quad (1.19)$$

B. Simulations studies

Seto et al [57] in 2013, followed by another work of Mari and Seto [103] in 2014, proposed a simulation where they consider the frictional contacts between particles. In their

simulation, the flow is governed by the set of hydrodynamic forces acting between the particles, namely, lubrication force between particles and drag force between the fluid and the particle. The flow is also governed by the frictional contact forces taking into consideration the repulsion force F^R between two particles. The frictional contact in their study [57], [103] was characterized by the microscopic friction coefficient μ and the DST regime is clearly governed by frictional forces.

As Figure 1.12 shows, the regime is qualified as frictionless at low shear rate (the viscosity evolution is slow). However, at high shear rates, the viscosity curve diverges at a critical volume fraction $\phi_j^{\mu > 0}$ (j index stands for jamming).

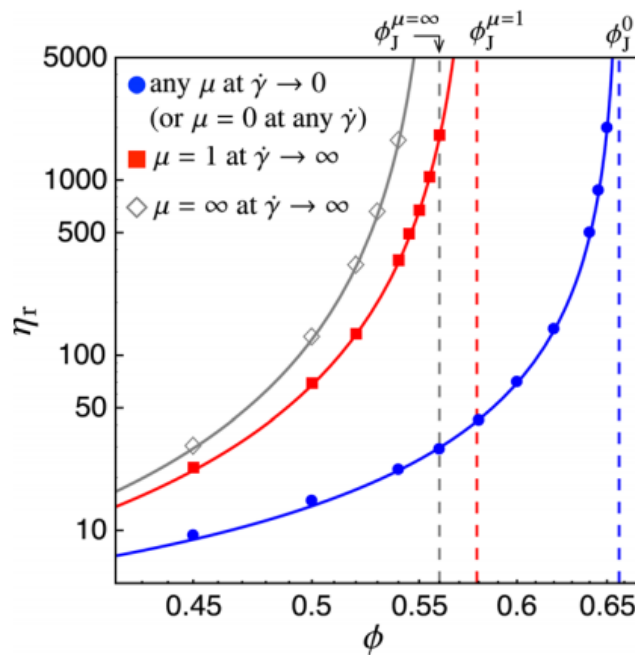


Figure 1.12 Relative viscosity against the particles volume fraction, different friction coefficient at different shear rate. From Mari and Seto 2014 [103], with kind permission.

Figure 1.13 shows that during the flow of a suspension a contact network between particles is formed and depends substantially on the shear rate. In fact, in both cases the contact network increases with the shear rate. In the case of a CST the number of contacts at a given shear rate is stable in time. In the case of a DST the number of contacts varies with time at the critical shear rate. It is stable at low and high shear rates.

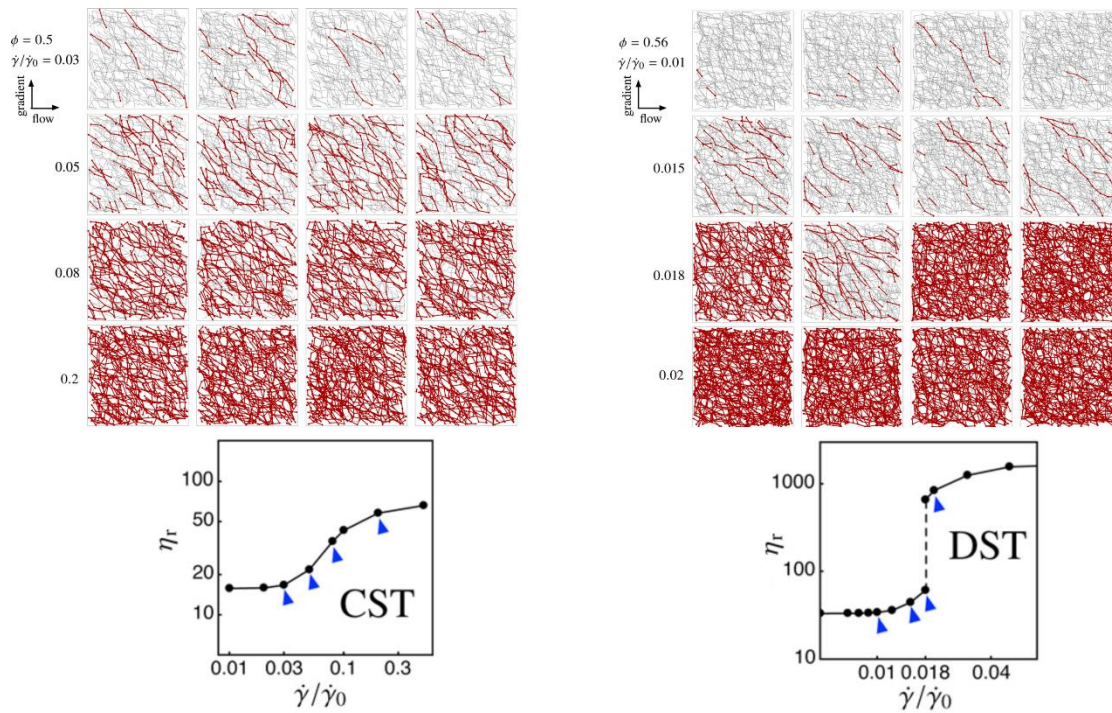


Figure 1.13 Representation of contact network evolution as a function of applied shear rate. Adapted from Mari and Seto 2014 [103], with kind permission.

C. Theoretical studies

A theoretical model was proposed by Wyart and Cates [107] in 2014. According to this model for a suspension of non-Brownian solid particles, the transition from the CST to the DST flow regime is established by frictional contact between the particles of the suspension. Therefore, they introduced a ratio that allows to predict the type of contacts between particles (lubricated or frictional), this ratio is between two pressures, the particle pressure P^P and the repulsive pressure $P^R = F^R/R^2$ (R is the particles radius). This ratio can be resumed in a dimensionless number $P = P^P/P^R$.

- If $P \ll 1$, the contact between particles is lubricated.

-If $P \gg 1$, the acting pressure on the particles is much higher than the pressure that keeps the contact between particles lubricated. The contact between particles is then frictional.

Two critical particle volume fractions of viscosity divergence can then be distinguished according to their model:

- ϕ_c^1 when the regime is qualified as totally lubricated and can never be blocked below this volume fraction, this is for low particle pressure $P \ll 1$.

- ϕ_c^2 when the regime is qualified as totally frictional and will always be blocked above this volume fraction value, this is for low particle pressure $P \gg 1$.

A formula has been suggested for all intermediate critical volume fractions which represents the area where the suspension will be able to partially flow at low shear rates and be blocked at high shear rates. This will capture the volume fraction ϕ_{DST} of the transition between CST and DST.

$$\phi_c(P) = f(P)\phi_c^2 + (1 - f(P))\phi_c^1 \quad (1.20)$$

where f is the fraction of frictional contact function of P and giving by:

$$f(P) = 1 - \exp(-P) \quad (1.21)$$

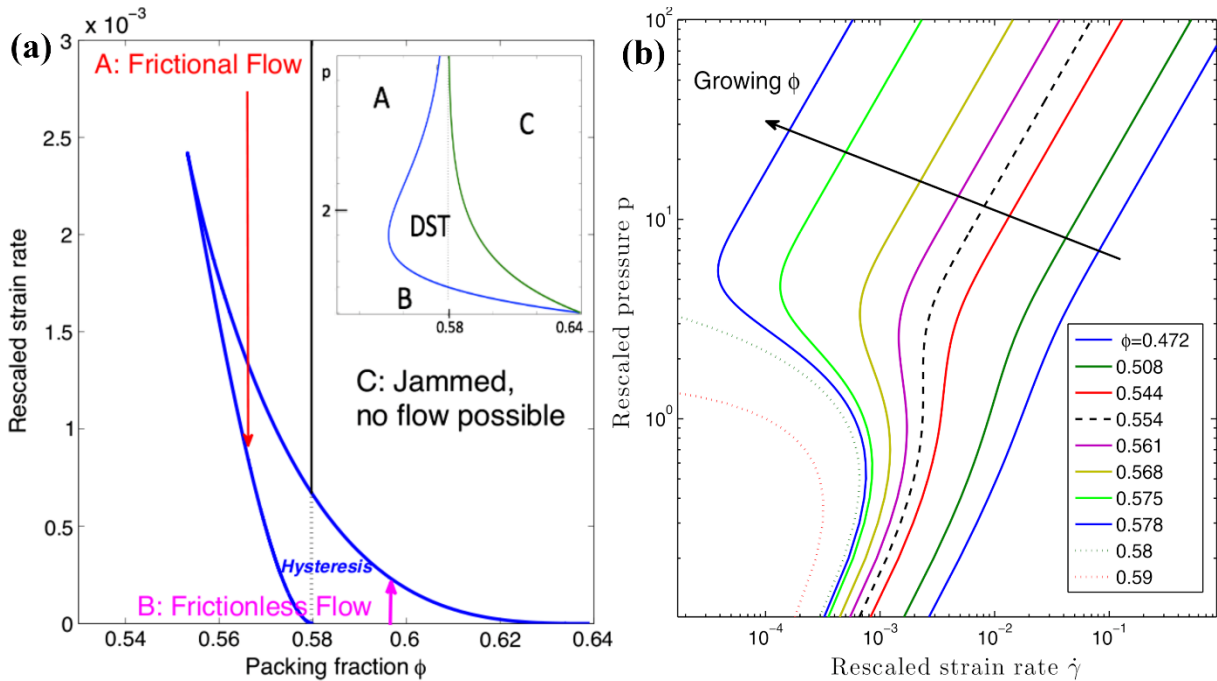


Figure 1.14 (a): Shear thickening phase diagram; (b): The prediction of Wyart and Cates model for different flow regimes depending on the volume fraction of the particles and the dimensionless pressure ratio. From Wyart and Cates [107], with kind permission.

For volume fraction lower than ϕ_c^1 the flow is continuous with a slight curvature between two straight segments exhibiting two Newtonian plateaus, then at a volume fraction of the particles $\phi_{DST} = 0.554$, the two straight segments are then connected by a curvature characterized by an infinite slope and the complete curve has an S shape. The suspensions in this case can flow in either the lower or the upper straight segment with low or high viscosity respectively.

The suspension is completely jammed for high pressures applied above a volume fraction ϕ_c^2 . The Figure 1.14 represents the different flow phases and the jammed section.

In contrast to the model based only on hydrodynamic forces [90], the Wyart and Cates model provided a robust explanation of the origin of shear thickening and the transition CST to DST, which once could not be explained without the involvement of frictional forces between particles. Several experimental works [43, 58, 110, 111] afterwards started to confirm this transition and observed this S-shaped pattern that connects in the flow curve a first straight quasi-Newtonian line, sign to CST regime to a second straight quasi-Newtonian line above the transition, sign to DST. However, the contact forces of the particles in the shear thickening phases have not yet been measured, but studies have reported the role of frictional interactions between particles on the suspension rheology [6, 102].

1.3.4 Shear thickening in particle mixtures

It has already been shown that adding large spherical particles to a concentrated cornstarch suspension shifts the DST transition to lower shear rates. This can be related to the two following effects: (a) appearance of highly sheared regions between the large particles in which the shear thickening matrix (cornstarch suspension) exhibits local DST transition at lower global shear rates as compared to the cornstarch suspensions without addition of large particles [112]; (b) local enhancement of the cornstarch concentration due to the excluded-volume shell surrounding the large particles [113]. The first effect can be simply seen as follows: the addition of large particles increases the viscosity of the bimodal particle mixture, therefore, the shear rate to reach the onset stress of DST becomes lower, under condition that this stress is independent (or slightly dependent) of the large particle volume fraction. Such interpretation, particularly relevant for the stress-controlled rheology, stems from the seminal work of Ohl and Gleissle [114], who supposed that, at the fixed shear stress, the shear rate in particulate suspension is reduced by a factor equal to the suspension relative viscosity. More recently, this approach has been successfully applied to describe CST in non-Brownian suspensions of spherical or cubic particles dispersed in shear thickening colloidal matrix [115, 116]. These last works report a possibility of the enhancement of CST by local confinements of the colloidal matrix in the spaces between suspended large particles.

In the case of a particle mixtures suspension, when large rod-like particles are dispersed in a shear thickening matrix composed of small isotropic-shaped particles dispersed in a Newtonian liquid, similar effects are expected of the rods on the DST of the composite mixture. However, the DST transition is believed to be governed not only by the concentration ratio of the large and small particles but also by orientation state of the rods since it should affect both the local shear rates in the space between rods and the excluded volume and local confinement effects

by tuning the size of the pores formed by the rods (see chapter 3). From a general perspective, the rheology of shear thickening mixtures of isotropic-shaped particles and fibers is expected to show behaviors reminiscent for shear thickening fluids and fiber suspensions, especially concerning the effects of the aspect ratio and the fiber orientation distribution on the suspension viscosity – see helpful reviews by Larson [117]; Petrie [118] and Bulter and Snook [119]. It is worth noticing that the DST transition has already been discovered in concentrated suspensions of relatively short (length-to-diameter ratio $1 \leq L/D \leq 9$) non-Brownian polyethylene glycol rods and has been found to share similar qualitative features with DST in spherical particle suspensions without focusing on the effect of the rod orientation distribution [120].

1.3.5 Extensional and free surface flows of shear thickening fluids

Extensional flows of the DST fluids have been studied to a lesser extent. Filament stretching (FiSER) and capillary break-up (CaBER) extensional rheometry was employed in experiments and have shown qualitatively similar behavior to those observed in shear rheometry: a nearly constant extensional viscosity at low strain rates followed by an abrupt increase above a critical strain rate [121, 122]. However, quantitative comparison between shear and extensional rheology of DST suspensions remains delicate because of transient character and complexity of the flows in FiSER and CaBER experiments. Viscoelastic pinch-off experiments in the work of Roché et al. [123] allowed finding the ratio of extensional-to-shear viscosities close to 3 (Trouton ratio for Newtonian fluids) above DST transition at small particle size-to-filament diameter ratios (weak confinements). This is consistent with particle level simulations of the work conducted by Seto et al. [124] showing similar energy dissipation in shear and extensional flows of bi-disperse suspensions at a ratio of big-to-small particle size higher than 1.4. These simulations have revealed an anisotropic particle microstructure under extension with the contact network (tested through a pair correlation function) somewhat diffused around the compression axis. In what concerns surface phenomena accompanying extensional flow experiments, brittle fracture of filaments reminiscent to glassy states has been typically observed above the DST transition in the works of White et al. [121] and the work of Andrade et al [122]. For pinch-off experiments, the authors have reported relatively strong undulation of the filament surface before the break-up related to a sequence of jammed and fluid states, as well as filament bending along its fluid parts after the break-up [123, 125] (see Figure 1.15).

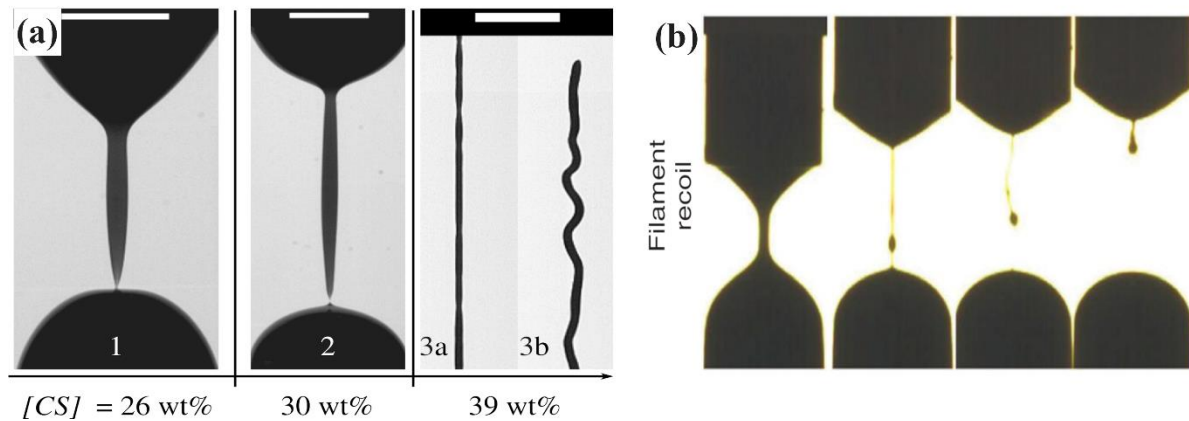


Figure 1.15 Viscoelastic behavior of: (a). a suspension of cornstarch from [123]. (b). a suspension of PMMA from [125], with kind permissions.

Free surface phenomena of DST fluids have been mainly studied for vibrating DST layers exhibiting surface instabilities in form of holes and fingers, as well as in the context of the impact resistance with a special accent on propagation of cracks, an important topic for body armor application – see the review by Brown and Jaeger [100]. A recent work of Darbois Texier et al. [126] reports another type of the surface instability observed in a film flow down an inclined plane. Surface waves emerging during this flow have visual resemblance with classical roll waves, but they arise without inertia due to the S-shape of the flow curve of DST fluids.

Falling viscous jets combine extensional and free surface flows and offer an alternative way to test the extensional rheology. However, only a few recent publications have considered jet flows of DST concentrated suspensions. Liard et al. [127] has studied a free-falling jet of a DST aqueous silica suspension. At high particle concentrations, the jet is shown to develop a new type of instability manifested through rapid transverse oscillations (somewhat similar to filament bending in Roché et al. experiments [123]) accompanied by break-up events above some critical length. The instability has been fully ascribed to stress oscillations within the jet above the DST transition. Following the motion of wave maxima, the authors have measured a distribution of forward and backward wave speeds and found that the waves are not advected by the falling jet but the average wave speed is close to the one of a vibrating solid string under gravitational stretching. Wang et al. [128, 129] has studied the primary break-up of aqueous cornstarch jets by an annular air jet and the secondary break-up of the DST drops by a transverse air jet, in the context of the spray atomization process. The authors report so-called “hardened” primary break-up, when, under strong shear imposed by a surrounding air jet, the suspension jet exhibits lateral oscillations and fractures into large fragments at the inflection points. They

also observed a hardened secondary drop break-up manifested through a hemispherical droplet shape atypical for this phenomenon.

However, it is worth mentioning that in the existing literature works, direct relationship between the suspension rheology and transverse jet oscillations is still lacking, while different important wave characteristics, like dispersion relation, frequency spectra, root mean square (RMS) amplitude, have not yet been reported.

1.4 Unresolved problems and general purpose of the thesis

The analysis of the state of the art of the DST phenomenon presented in section 1.3 reveals a few important aspects that have received little attention and need further and deeper investigations:

1. The DST transition in mixtures of spherical and rod-like (fibers) particles have been studied only scarcely and, to the best of our knowledge, the effect of the fiber addition on the DST transition has never been reported despite of high practical relevance of this effect in mixing, pumping and handling of fiber-reinforced concentrated cement pastes.
2. The effect of flow geometry on the DST response of shear thickening suspensions has also received a little attention, especially nothing is known how confinement of fibers in sphere-fiber mixtures will affect the suspension rheology in drag shear (simple shear or mixer-type) flows and pressure-driven flows through narrow channels – this question being also of crucial importance for cement industry.
3. Finally, little is known about extensional flows and/or free surface flows of DST fluids without any information about behaviors of sphere-fiber mixtures in these flows. Free falling jet flow is an example of high practical relevance for mortar spraying or cement jet grouting. Jet flow instabilities that may occur above the DST transition (perturbing the cement application) should somehow depend on the content of fibers in the sphere-fiber mixture but this remains completely unknown.

The above stated lacking knowledge on the DST behavior of sphere-fiber mixtures allow us to formulate the objectives of the present thesis work. **The general aim of this thesis** is to study the phenomenon of DST in the sphere-fiber mixtures and to analyze the effect of the fiber addition on the suspension rheology. We use a dense non-Brownian suspension of the calcium carbonate CaCO_3 (CC) particles loaded with fibers. The choice of our suspension is dictated by possible application of our results to the flows of concentrated cement pastes loaded with fibers.

As justified in section 2.1.1.1, the aqueous dispersion of CC particles is an excellent experimental model of a cement paste before hardening. The reinforcement of cementitious materials (CM) by fibers improves their mechanical strength and ductility [130-132], however, the manufacture of CMs highly loaded with fibers is problematic because of their low fluidity, heterogeneity, and poor workability. As we have seen, superplasticizers (polymers adsorbed on the surface of cement particles) improve the fluidity but the fiber content remains very limited due to the localized shear thickening phenomenon in the vicinity of the contacts between fibers.

In this thesis we will clarify the effect of fibers on the rheology of shear thickening "particles-fibers" mixtures both experimentally and theoretically. We will first present in chapter 2 with detail the ingredients of our suspension, the method of its preparation, and the experimental equipment that we have used. In three subsequent chapters (3-5), we handle the suspension flows, which simulate different stages of the cement paste processing: mixing, pumping and spaying. In particular, in chapter 3, we will make a shear rheological study for our suspension in order to simulate the shear that undergoes a cement paste during its mixing. This will allow us to make the point on the suspension rheology and analyze the critical parameters that can influence its DST behavior. In chapter 4, we will study the flow of our suspension through a cylindrical channel at imposed pressure, the situation simulating concrete pumping in construction sites. We will compare then the suspension shear rheology against the capillary one in DST flow regime. Finally in chapter 5, the jet under gravity of a shear thickening suspension loaded with fibers will be investigated to evaluate the rheology in extension of this type of dense and fiber loaded mixtures, DST will be linked to suspension jet instabilities and the advantage of fibers addition will be discussed. From application perspective, this part of the study simulates to some extent the concrete or mortar spraying when it flows out of the pumping lines. Finally, at the end of the manuscript we will present general conclusions with some prospects for future work.

CHAPTER 2

2 Material used and Methods employed

2.1 Materials used in the preparation of the suspension

In the present work, the suspensions were constituted of calcium carbonate (CC) particles, polyamide (PA) or glass fibers and a superplasticizer PCP-45, all dispersed in a deionized water at desired proportions. The CC particles and PCP-45 were extensively characterized in the previous works of the hosting team at UCA [133, 134]. Thus, the results of their characterizations are briefly reviewed in sections 2.1.1 and 2.1.2. Then, PA and glass fibers are characterized in detail in section 2.1.3, while the protocol of the suspension preparation is provided in section 2.1.4.

2.1.1 Calcium carbonate particles

With the chemical formula CaCO_3 , calcium carbonates (CC) are one of the most abundant non-toxic minerals.

There are three allotropic forms of calcium carbonate summarized in Table 2.1 and depicted in Figure 2.1.

Table 2.1 Characteristics of the different allotropes of calcium carbonate [135].

CC form	Microscopic shape	Stability
Calcite	Rhombohedral	Very stable
Aragonite	Orthorhombic	Fairly stable, obtained at high temperature and pressure.
Vaterite	Hexagonal	Unstable under normal temperature and pressure conditions

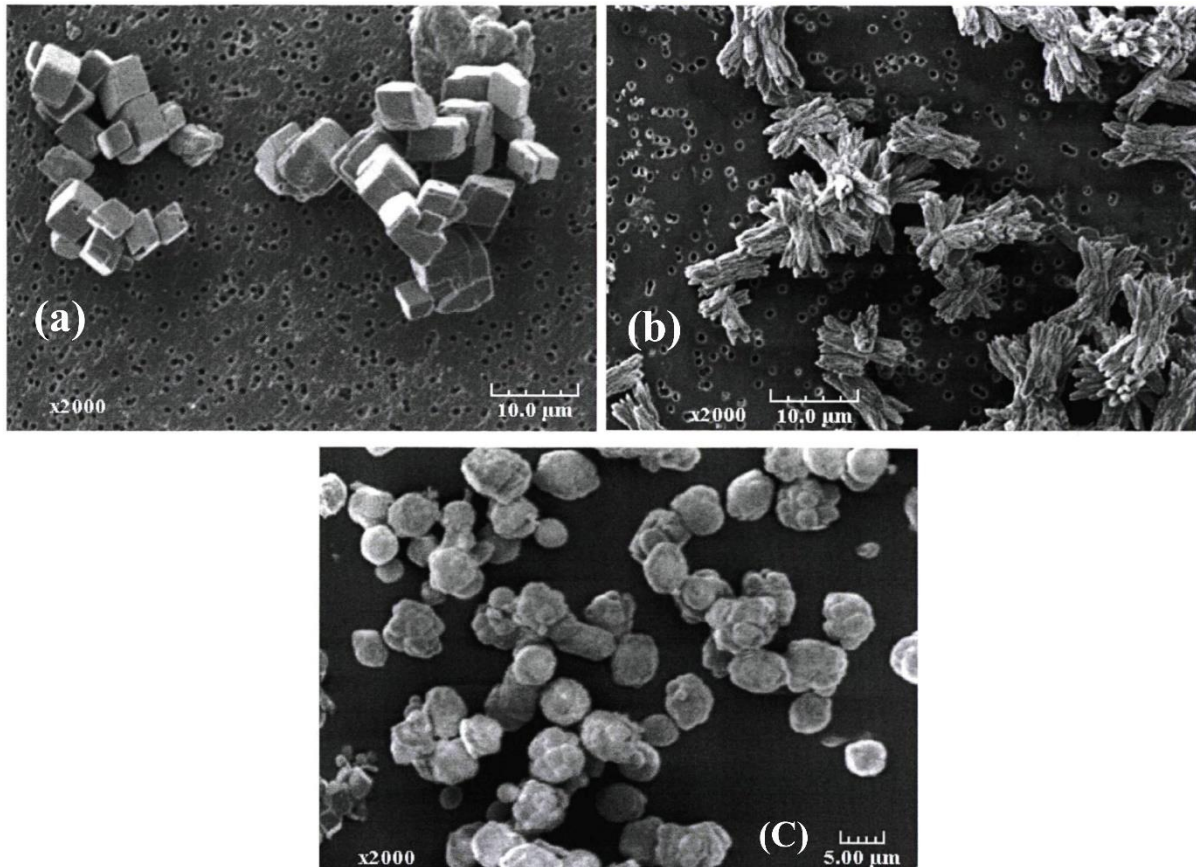


Figure 2.1 Microphotography of allotropic forms of calcium carbonate, (a): calcite; (b): aragonite; (C): vaterite. From Kammoe [136]

2.1.1.1 Why CC-particles suspension is a good model for cement paste?

In our doctoral thesis we studied the CC-suspension as the best representative and closest model to a cement paste. This point can be justified in the literature by several works, [137-143]. We recall the exhaustive work of Mikanovic [144] where the authors have experimentally compared a Portland cement with five minerals that can be used as a model for a cement paste, among which carbonate calcium. The tests with the cement were all conducted in the handling phase before hardening, or the workability phase. The results were all in favor of calcium carbonate for a better model to describe the cement paste and this because they have a similarity in properties:

- The zeta potential in aqueous medium and the isoelectric point (the pH of an aqueous solution in which a solid exists under a neutral electric potential) are the closest to cement in case of CC.
- The same packing density was observed with CC-suspension in a sedimentation test.
- Rheological conservation and dissipation moduli in rheological oscillation tests were the closest for CC compared with the cement.

2.1.1.2 Characterization of CC-particles used in the present work

The CC-particles and the adsorbed superplasticizers used in the present manuscript are the same that were used in previous PHD work of Romain Morini [133]. CC-particles were supplied by the Swiss company OMYA, a world producer of white minerals. The commercial name of the product is BL 200 and it is obtained by mechanical crushing. The shape of the CC microparticles is depicted in Figure 2.2 using SEM (Scanning Electron Microscopy) and it is rhomboidal and considered isotropic insofar as their size is approximately equal in all directions, (see Figure 2.2). Their size distribution was obtained by the static light scattering (SLS) with the help of the Master Sizer device from Malvern coupled to a Hydro2000S module, this device allows to determine the intensity of the light that the CC-particles scatter with the help of several light sensors which are located at different positions encompassing all the light beam of the particles and capturing the scattered intensity. Nevertheless, this device has some limitations: the shape of the particles must be relatively spherical, the size of the particles must not be smaller than 10 nm because the smaller the particle, the more light it scatters with a large angle, and the volume concentration must not be high in order to avoid a multiple scattering.

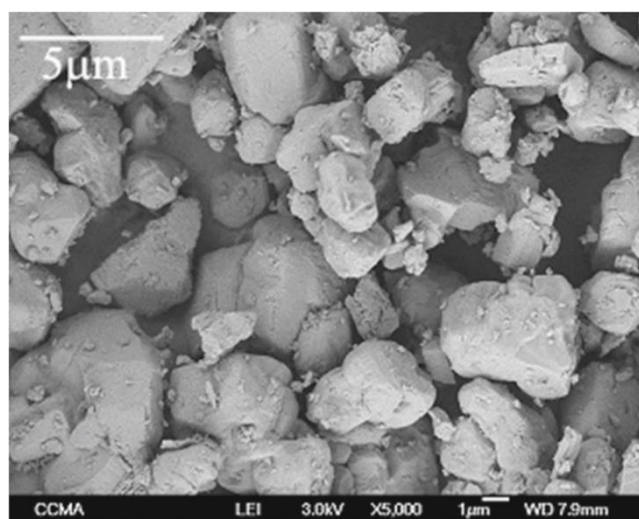


Figure 2.2 SEM picture of CC-particles from [134], with kind permission.

Figure 2.3 represent the results of the volume size distribution of CC obtained by SLS (empty triangles) and by direct geometrical measurements of the particles above 1 μm using SEM pictures (filled diamonds) [134].

The measurement of the specific surface developed by one gram of CC-particles has been carried out with great precision by BET analysis (adsorption of nitrogen gas on the surface of the particles) [133]. the zeta potential and conductivity of the CC-suspension were estimated using Malvern Zeta sizer ZS apparatus.

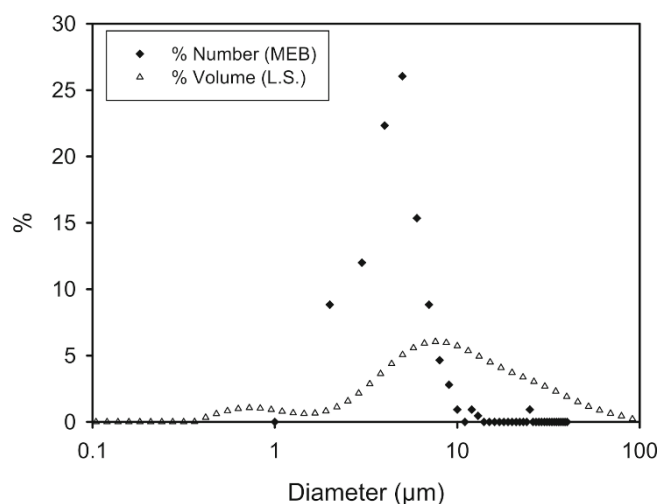


Figure 2.3 CC- particles size distribution curves using static light scattering (SLS) and by classification of particles above 1 μm from SEM pictures, from [134], with kind permission.

Several physical and physicochemical parameters are summarized in Table 2.2

Table 2.2 Physical and physicochemical parameters of CC-particles [133, 134].

Particles	Mean diameter D [μm]	Density ρ [kg/m^3]	specific surface S_0 [m^2/g]	Zeta potential ζ [mV]
CaCO_3	5.5	2525	0.88	8.3

It is important to notice that we have used two series of the same kind of particles. Both series corresponded to two different bags containing the particles. Both series had very close physicochemical parameters with slightly different particle size distribution (the Table 2.2 show the characterization results of the 1st series). However, we got quite different rheometric results for both series: the 1st series showed lower critical shear rates of the DST onset as compared to the 2nd series. This discrepancy is tentatively explained by the fact that a very slight difference in size distribution generates a slight difference in the maximum packing fraction φ_m of particles, which is sufficient to provide relatively large rheological differences, provided that the suspension viscosity diverges as $\eta \sim (1 - \varphi_p/\varphi_m)^{-2}$ and the CC particle volume fraction φ_p was always close to φ_m . Unfortunately, we were unable to conduct all the measurements of this work with the same series of particles. For this reason, the rheometric results obtained in mixer type and plate-plate geometries (1st series, chapters 3 and 5) cannot be safely compared to those obtained in cylindrical Couette and capillary geometries (2nd series, chapter 4). However, both particle series showed very similar qualitative behaviors.

2.1.2 The superplasticizer

The superplasticizers are organic polyelectrolytes. In the concrete industry, the superplasticizer plays the role of an additive that is introduced into a concrete mortar, shortly before its implementation, ensuring as main function the maximum increase of the workability of the mixture by allowing to reduce the water amount, which leads to an increase of the strength and the compactness. This is mainly done by neutralizing the electric charges present on the surface of the cement particles, known as steric repulsion, which makes it possible to separate the particles from each other, thanks to the very long molecular chains of the superplasticizer (see Figure 2.4). Therefore, the suspending fluid that once was trapped by the particle flocs is free again for the workability of the concrete. Superplasticizers are also sometimes used to delay the setting of concrete, but they also depend on the characteristics of the cement and the composition of the concrete or mortar.

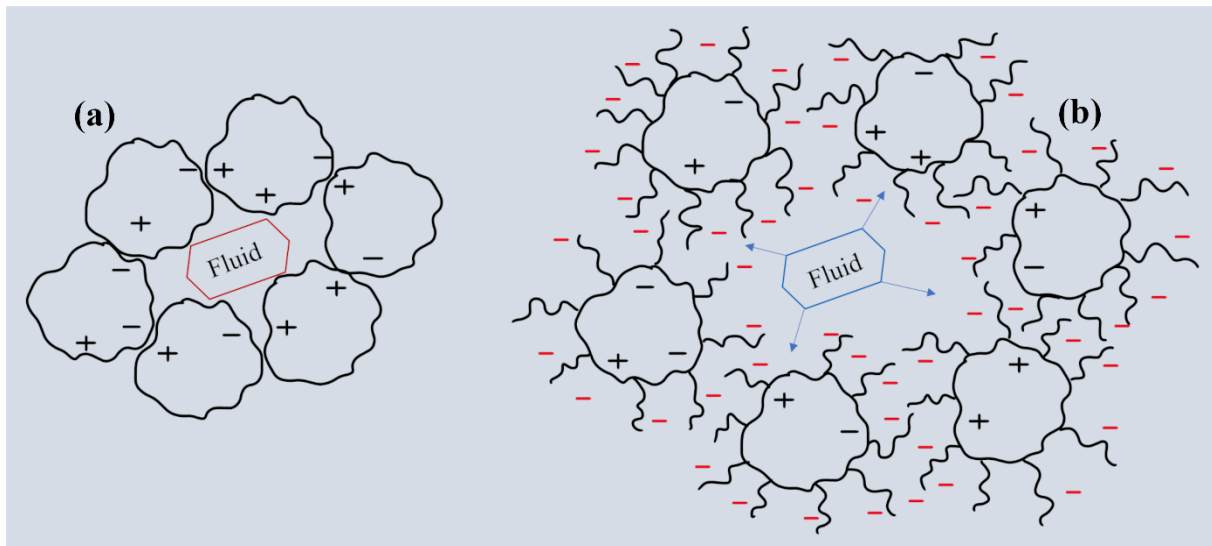


Figure 2.4 Effect of superplasticizer - dispersant of cement suspension particles

The superplasticizers are of different families and the Polyoxyethylene Carboxylate family otherwise known as PCP, was first introduced in the 1990's. It consists of one or more chains of polyethylene glycols grafted onto carboxylic anionic groups of a polymethacrylate skeleton and it is the one we are using as a superplasticizer in our CC-suspension.

2.1.2.1 Characterization of the PCP superplasticizer

Since in our experiments we are working with CC-suspension, which is a good model of a cement suspension, it is necessary to add superplasticizer to the mixture. The molecules of the superplasticizer are grafted on the surface of the CC-particles separating the particles and lubricating them by neutralizing the attractive colloidal forces between particles.

The superplasticizer we are using in our experiments have been supplied by the French company of additives for building materials Chryso and it is known under the “PCP” abbreviation. PCP are polymethacrylates grafted with polyoxyethylene chains (POE) (see Figure 2.5). These molecules have $P = 45$ ethylene oxide units in the PEO chain grafted in $n = 10$ segments composed of $N = 5$ carboxylate functions.

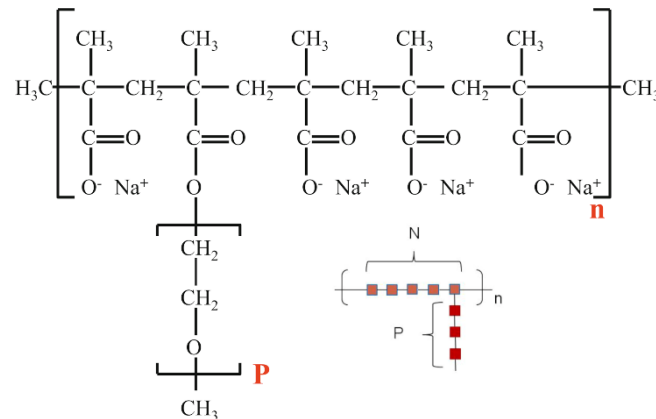


Figure 2.5 Sketch of the chemical composition of the PCP polymer, from [134], with kind permission.

Table 2.3 Chemical properties (molar masses) of PCP-45 Superplasticizer [133].

Superplasticizer	M_{bac} [kg/mol]	M_{ch} [kg/mol]	M_{seg} [kg/mol]	M_{PCP} [kg/mol]
PCP-45	5.310	18.040	2.335	23.350

The chemical properties of the PCP-45 superplasticizer have been provided by Chryso company and are summarized in table 2.3, where M_{bac} , M_{ch} , M_{seg} , M_{PCP} are respectively the molar masses of the whole methacrylate backbone constituting the molecule, the whole POE chain unit, of a segment of the molecule having four carboxylic functions and a POE chain and the molar mass of the PCP-45 molecule [133].

The PCP-45 is 59.3 wt % aqueous solution of polymers. The zeta potential and conductivity for the PCP-45 solution are respectively: $\zeta = -15.6$ mV and $k = 2.26$ mS/cm at pH = 6,96. The zeta potential for the superplasticizer is a negative value meaning its charge is negative at a considered pH, which will provide electrostatic attraction between positively charged CC-particles and negatively charged PCP-45 superplasticizer, allowing an easy adsorption of PCP-45 onto CC surface.

2.1.2.2 Adsorption isotherms of PCP-45 on CC-microparticles

An adsorption isotherm is the curve relating the activity of the adsorbate contained in a given and known atmosphere to the quantity of adsorbate adsorbed on a solid in equilibrium

with this atmosphere. It allows to evaluate the adsorption affinity of different molecules for the same surface by giving the maximum number of molecules that can be adsorbed. In our case, it will allow to determine the maximum concentration of molecules of the superplasticizer PCP-45 that can be adsorbed on the surface of CC-particles. By modeling these isotherms, one can also trace the adsorption energies, thus the intensity of the bonds between the anchoring functions of the molecules on the surface. It is also possible to identify the difference between adsorbed and simply coagulated molecules in the presence of certain ions present in the suspension.

Langmuir isotherm model is the simplest of the adsorption models in which four conditions are assumed:

- Each free site in the solid surface of the adsorbent can bind only one molecule of the adsorbate, so the adsorption takes place in a monomolecular layer.
- All the sites are identical.
- The existence of a dynamic equilibrium between the molecules fixed on the surface of the adsorbent and those leaving the surface means that there is adsorption and desorption of molecules at the same time.
- There is no interaction between adsorbent molecules.

The model consists in writing the third condition of equilibrium between the rate of adsorption and desorption of the molecules. At equilibrium, the Langmuir equation is giving by:

$$C_{ads} = C_{plateau} \left(\frac{K_{eq} C_{fluid}}{1 + K_{eq} C_{fluid}} \right) \quad (2.1)$$

where: C_{ads} , $C_{plateau}$, C_{fluid} , are respectively the concentrations of the molecules adsorbed on the surface, the total concentration of the adsorption sites on the adsorbent surface and the concentration of free non-adsorbed molecules remaining in the fluid; K_{eq} is an equilibrium reaction constant.

Morini in his PhD work [133] measured the adsorption isotherms of PCP-45 on the surface of CC particles using the Total Organic Carbon analyzer TOC-VCSH from Shimadzu.

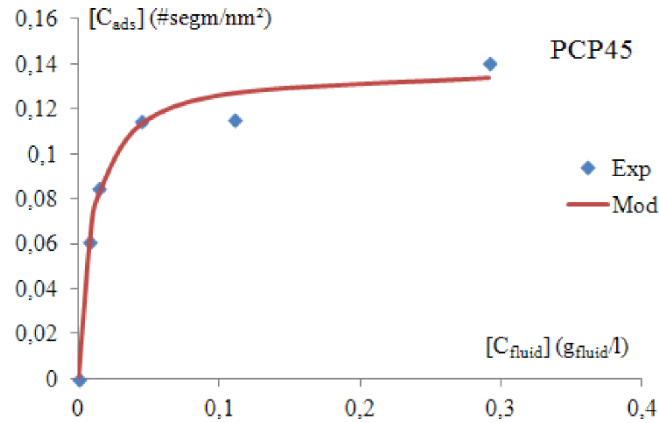


Figure 2.6 Adsorption isotherm of PCP-45 on CC microparticles [133].

Figure 2.6 represent the adsorption isotherm of PCP-45 expressed as the number of adsorbed PCP-45 molecule segments per square nanometer (nm^2) of CC surface against the quantities of PCP-45 superplasticizer remaining in the solvent ($\text{g}_{\text{fluid}} / \text{l}$), where the blue points are experimental data, and the red line is the modeling by the Langmuir model. The slope of the first linear part at the origin of the isotherm gives information on the adsorption affinity of the PCP molecule for the surface, while the adsorption plateau gives information on the saturation of the surface of the CC particles and allows to determine the maximum quantity of adsorbed superplasticizer. We see that the adsorption plateau is approximately achieved at the concentration of free (non-adsorbed) PCP, $C_{\text{fluid}} \approx 0.4 \frac{\text{g of PCP}}{\text{L of water}}$. At adsorption plateau, the free PCP concentration is close to the total concentration of PCP added to the suspension: $C_{\text{fluid}} \approx C_0$. In our CC suspensions of a density $\rho \approx 2000 \text{ g/L}$ at particle volume fraction, $\varphi_p = 0.64 - 0.68$, the amount of PCP that should be added to the suspension by unit mass of CC particles is evaluated as $\frac{C_{\text{fluid}}}{\rho} \approx 0.002 \frac{\text{g of dry PCP}}{\text{g of dry CC}}$. This quantity is used all along the current work for the suspension preparation.

2.1.3 The fibers

In the current work, we try to model the fiber reinforced concrete by the suspension of CC-particles mixed with rigid fibers in order to study the DST phenomenon in dense concentrated suspensions. Since a long time, fibrous substances of micron-to-millimetric sized metallic (steel) fibers, or mineral (glass or carbon) fibers, or polymeric (polyamide, polyethylene or polypropylene) fibers have been added to concrete in the cement industry in order to improve its physical and mechanical qualities. Indeed, reinforcements, such as steel [145], polymer [130], glass [131, 132], or carbon fibers [146], are commonly used to prevent the occurrence and propagation of cracks. The addition of fibers to concrete helps to restrain

cracks and reduce potential problems such deterioration due to water infiltration. Fiber-reinforced concrete also outperforms ordinary concrete in terms of higher tensile strength, and ductile tensile behavior and it covers areas requiring extreme mechanical and environmental loads. Several studies have considered the addition of polyamide fibers (PA) as a reinforcement for concrete and have characterized its physical and mechanical properties [147-149]. PA-fibers are synthetic fibers are generally derived from the chemical reaction of difunctional monomers containing amine and carboxylic groups. PA-fibers have several mechanical properties, first of all they are light in weight, that is why they have been chosen for concrete reinforcement in order to guarantee a good workability of the reinforced concrete in the construction site. They also have a low water absorbance, a high resistance to humidity and a good resistance to traction and abrasion. These and other properties make PA-fibers an ideal choice for fiber reinforced concrete [150, 151]. In our work we considered mainly and most of the part the use of PA-fibers in the CC-suspension (in chapters 3, 4 and 5) and also the use of glass fibers with CC-suspension in shear rheological tests in chapter 3, in order to compare the rheological behavior, especially the DST, in the presence of two types of rigid fibers in a shear thickening CC-suspension of.

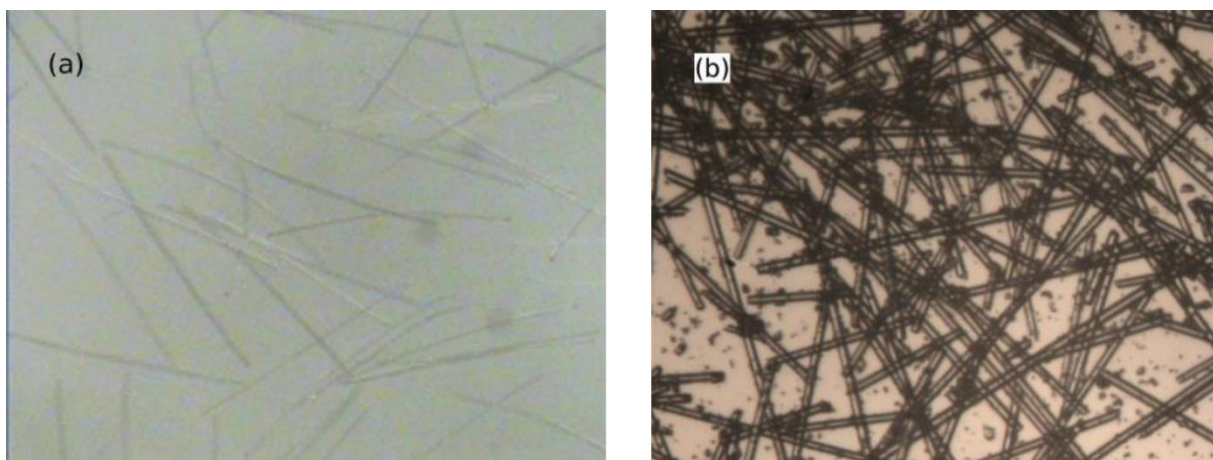


Figure 2.7 Optical microscopy snapshots of: (a)- the polyamide (PA) fibers and (b)- glass fibers dispersed in deionized water. The width of the images (a) and (b) corresponds to 1500 and 700 μm respectively.

The fibers used in our suspension are considered as anisotropic particles of axisymmetric geometry, with cylindrical shape, of mean length L , mean diameter D and mean aspect ratio $r = L/D \gg 1$. The physical and geometrical properties are summarized later in Table 2.4. The PA fibers were supplied by the producer of textile additives, Pinfloc French company. The fibers were used without any additional treatment, although we checked their monodispersity from several collected and analyzed images (see Figure 2.7). The glass fibers (studied only in chapter 2) were purchased from the Arkema company in France initially supplied with an

average size of 5 mm and were manually grinded in a ceramic mortar and seeded through a series of sieves in order to adapt the average aspect ratio to that of the PA fibers. Figure 2.7 shows optical microscopy snapshots of the two types of fibers dispersed in deionized water. The snapshot (a) shows a fairly good monodispersity of the PA fibers, while both snapshots (a) and (b) do not reveal any strong aggregation of two types of fibers.

From the optical microscopy snapshots, we could measure the length distribution of the fibers, which is represented as a histogram in Figure 2.8.

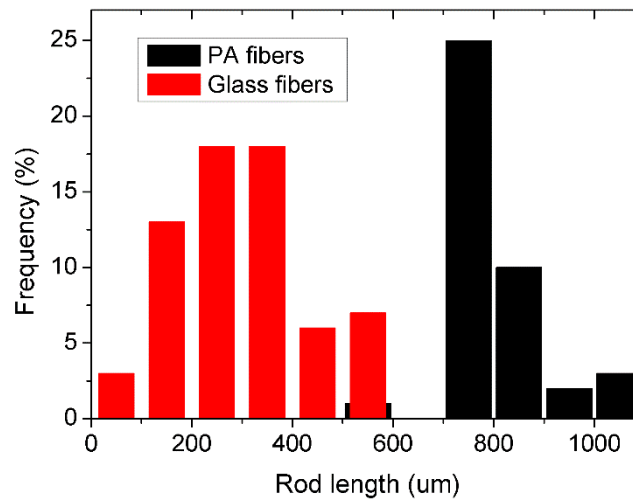


Figure 2.8 Histogram of the length distribution of PA and glass fibers.

The PA and glass fibers show a relatively narrow and wide length distribution, respectively, and a narrow diameter distribution for both types of fibers. The measured geometric and physical properties are summarized in Table 2.4 for both fiber types.

Table 2.4 Geometrical and physical properties of fibers.

Fibers	Mean length L [μm]	Mean diameter D [μm]	Mean aspect ratio $r = L/D$	fiber to CC part. D/d ratio	Density ρ [$\frac{\text{kg}}{\text{m}^3}$]	Young's Modulus E [GPa]
PA	800	17	47	3.1	1140	4.56
Glass	300	7.5	40	1.4	2600	80

It is assumed that we are in the case of a scale separation between the PA-fibers and the CC-suspension. Indeed, the PA-fibers have a diameter three times larger than the diameter of the CC-particles ($\sim 5.5 \mu\text{m}$) so the fibers see the suspension as an effective medium while the

diameter ratio is much smaller ($D/d = 1.4$) and the diameters are almost identical for the glass fibers and the calcium carbonate. The effective stiffness of both fiber types was estimated based on the experimental values of characteristic shear (σ) or tensile (σ_E) stresses developed, respectively, in shear or jet flows. The effective stiffness in the shear and jet flow tests is given by [152, 153]:

$$S = \frac{\sigma_{bulk}}{\{\sigma \text{ or } \sigma_E\}} \approx 1.2 \frac{E \ln(2r)}{r^4 \{\sigma \text{ or } \sigma_E\}} \quad (2.2)$$

where σ_{bulk} is the characteristic bending stress corresponding to the buckling instability, E is the fiber Young modulus (Table 2.4). Both the PA and glass fibers are considered as rigid in our study since the effective stiffness S is found to be larger than unity in both conducted shear and jet flow tests. In particular, for the shear and capillary flows considered in chapters 3 and 4, the values of S are 51 and 1.6×10^3 for PA and glass fibers respectively at the characteristic applied shear stress $\sigma = 100$ Pa in most of experiments. However, in the jet flow considered in chapter 5, the profile of the applied tensile stress σ_E depends on the axial and radial components of the normal stresses σ_{zz} and σ_{rr} . For an evaluated tensile stress at DST in jet flow of $\sigma_E \leq 143$ Pa, the value of effective stiffness S is 35 for PA fibers.

2.1.4 Suspension preparation

In this section we will mention the steps we followed for the preparation of our CC-suspension with different concentration of CC-particles and different concentration of PA/glass fibers. We will also include the step of degassing the suspension to remove the air bubbles present in the mixture and we will discuss later if this step is necessary and sensitive in the preparation of our suspension.

As mentioned above, our suspension consists of a shear thickening CC matrix at different CC-particles concentrations, and which contains PA/glass fibers dispersed at different concentrations. The preparation of the suspension is carried out in the following steps:

The first step consists of the preparation of the CC suspension without fibers and with a desired volume fraction of the CC particles:

$$\varphi_P = \frac{V_p}{V_m} \quad (2.3)$$

where, the concentration of the CC particles is equal to the ratio of the volume of the CC dry particles V_p to the volume of the CC aqueous suspension in water V_m . After that, the necessary quantity of superplasticizer PCP-45 solution is prepared and mixed with the weighed quantity

of CC particles. For this purpose, the solution of PCP-45 is mixed with deionized water (resistivity of 18.2 MΩ cm) to reach the desired concentration of superplasticizer. The whole (CC dry particles + PCP-45 solution) is quickly mixed and weighed in a balance, and the lacking weight is completed with the necessary amount of dry CC particles to reach the final weight of the CC suspension. The ingredients must be well mixed to ensure adsorption of the superplasticizer PCP-45 on the surface of the CC particles, so we proceed to a 5 min agitation in a vortex mixer, followed by 5 min treatment in an ultrasonic bath to ensure a better homogeneity and distribution of particles, followed by another 5 min in the vortex mixer. After the preparation of CC suspension, we prepare the quantity of the fibers according to the wanted concentration (0.2 to 4% vol). The concentration of the fibers is defined as the ratio of the fiber solid phase volume V_f to the whole volume V of the mixture of CC shear thickening matrix with the PA or glass fibers,

$$\varphi_f = \frac{V_f}{V} = \frac{V_f}{V_f + V_m} \quad (2.4)$$

The fibers are added to the CC suspension and the mixture is stirred and sonicated as the same protocol followed before. Finally, after stirring/sonication, we put the suspension to rest for 3 hours at 4°C to achieve thermodynamic equilibrium of different species (polymers and ions). Before proceeding to the shear tests the suspension is again well mixed and sonicated and degassed for a 30 min with the use of a vacuum pump which allows to remove the air bubbles trapped in the suspension. The 30 min degassing is divided in two ramps of 15 min separated also by mixing and sonication of the suspension.

2.2 Experimental methods employed

2.2.1 Drag flows in shear rotational rheometry

The shear rheology of CC suspensions and CC-fibers mixtures was measured mainly by Anton Paar Physica MCR 301 rheometer using a mixer type geometry and a homemade cylindrical Couette geometry. In some cases, measurements were performed by Thermo Haake RheoStress 600 rheometer using plate-plate geometry. Sample expulsion from the rheometer gap at the applied stresses above DST threshold, particle sedimentation and water evaporation encountered in plate-plate configuration did not allow reliable and reproducible measurements of the samples containing rods; only CC suspensions without rods using a single stress ramp gave reliable results. On the contrary mixer type and cylindrical Couette configurations was found to be free of the above artefacts thanks to continuous sample mixing and low sample free surface – to volume ratio, at the expense of a complex flow field and stress distribution within

the sample. Below, we describe in detail the three rheometric tools and associated measurement protocols.

2.2.1.1 Plate-Plate geometry

A. General description

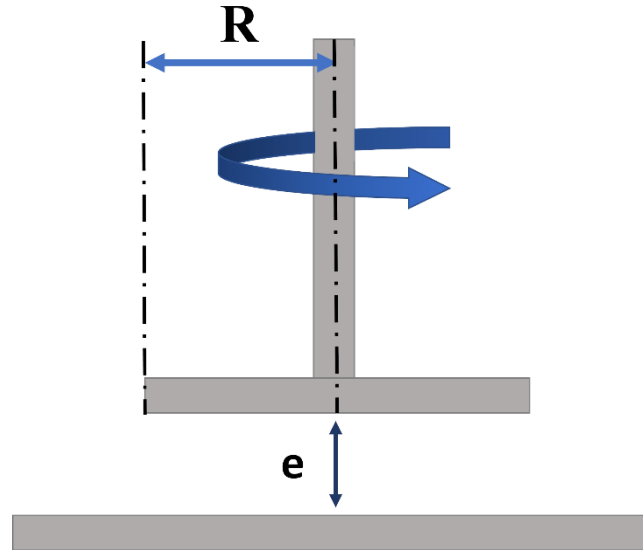


Figure 2.9 Plate-Plate geometry.

The use of a rough geometry (sandpaper glued on the upper and the lower rheometer plates) allows to limit the problems of sliding on the walls. It consists of two parallel plates where the rotating plate has a radius R , separated by a variable air gap, noted e (Figure 2.9). The latter is adjustable depending on the particle size of the used suspensions. The measuring cell is composed of a fixed bottom part (stator) and an upper rotating part (rotor) linked to the rotating shaft of the rheometer spinning at an angular speed ω . The suspension is confined in the space between the rotor and the stator (air gap). Moreover, the shear gradient is not uniform. Indeed, there is no shear rate at the center (close to the axis) and it is maximum at the edges of the discs. The relationship between the shear rate at the edge of the disk and the rotational speed is written as follows [154]:

$$\dot{\gamma} = \dot{\gamma}_R = \frac{\omega R}{e} \quad (2.5)$$

The equation giving the stress as a function of the torque Γ applied by the tool during rotation for a given shear rate $\dot{\gamma}_R$ at the periphery of the disks is as follows [154]:

$$\sigma = \sigma(\dot{\gamma}_R) = \frac{\Gamma}{2\pi R^3} \left[3 + \frac{d \ln \Gamma}{d \ln \dot{\gamma}_R} \right] = \sigma_a \left[\frac{3}{4} + \frac{1}{4} \frac{d \ln \Gamma}{d \ln \dot{\gamma}_R} \right] \quad (2.6)$$

with

$$\sigma_a = \frac{2\Gamma}{\pi R^3} \quad (2.7)$$

being so-called apparent shear stress at the disk edge, i.e. the shear stress that would have been developed in a Newtonian liquid at a given applied torque Γ . The right-hand side of Eq. (2.6) allows relating the true shear stress in a non-Newtonian fluid to the apparent shear stress σ_a typically reported by the rheometer. This relationship is known under the name of the Mooney correction.

B. Measuring protocol

The plate-plate geometry of the RheoStress 600 rheometer is characterized by the upper plate diameter of 60 mm and rheometer gap set to 1.8 mm. To decrease wall slip, a sandpaper of an r.m.s. roughness of 40 μm was glued to both rheometer plates. In order to decrease water evaporation, after placing a sample (CC suspension without rods, 1st series of particles – cf. note at the end of Section 2.1.1.2) into the rheometer gap, a home-made water trap (Plexiglas cylinder with wetted washcloth fitted to inner surface of the cylinder) was placed around the upper plate and the temperature at the level of the lower plate was fixed to 14°C by a refrigerated circulating bath. A linearly increasing stress ramp was applied to the sample from $\sigma_a = 0$ Pa to $\sigma_a = 100$ Pa with a rate of the stress increase of 0.33 Pa/s and the measured shear rate was recorded with a sample rate of 2 points per second. Once the maximum stress was achieved, a linearly decreasing stress ramp was applied from $\sigma_a = 100$ Pa to $\sigma_a = 0$ Pa at the same rate. In some cases, a second increasing-decreasing (up-and-down) stress ramp was applied to check how the sample expulsion affected the rheological measurements. Once the flow curves were measured, the imposed apparent shear stress σ_a was converted to the real shear stress σ using Mooney correction [154]. This correction was subjected to substantial errors above the DST transition related to the numerical derivation of strongly oscillating σ_a versus $\dot{\gamma}$ dependencies. However, it neither changed the qualitative appearance of the flow curves, nor the average amplitude of shear rate oscillations above the DST.

2.2.1.2 Mixer type geometry

A. General description

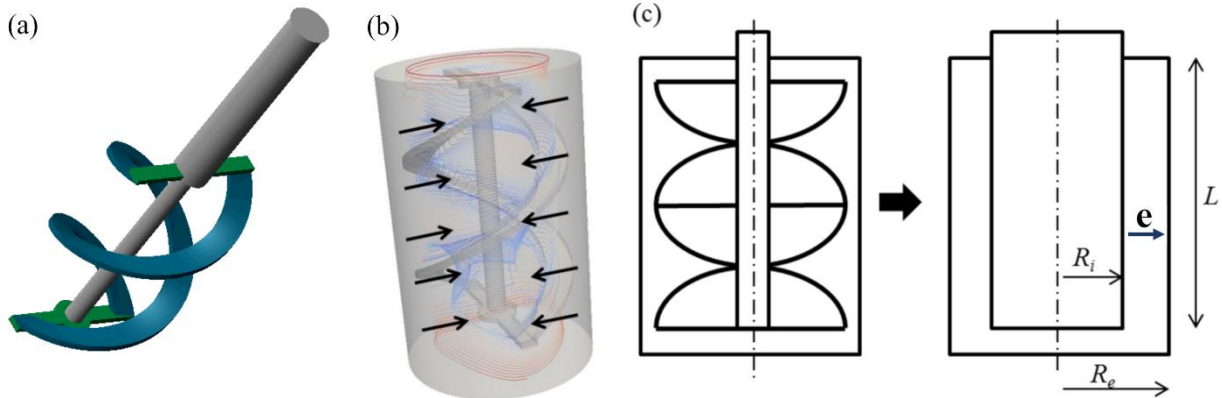


Figure 2.10 Mixer-type rheometric geometry: the double helix rotor (a); streamlines of Newtonian fluid flow induced by the double-helix rotation inside a cylindrical cuvette with the arrows showing the direction of possible flow-induced particle migration (b); cylindrical Couette analogy of the mixer type geometry (c).

This geometry prevents problems due to sedimentation of CC- particles by applying a vertical mixing motion in addition to the classical shear motion. It also has the advantage of reproducing good measurements and the use of this specific cylindrical cuvette allows to work with a large rheometer gap for the longest fibers with a ratio of the gap to the length of the fibers which is equal or higher than 3. However, this geometry is not a conventional one. Indeed, to obtain the viscosity of a fluid from this geometry, an analogy based on the classical cylindrical Couette geometry is performed.

The assembly consists of a double helix rotating in a cylindrical cuvette separated by a space called the air gap, denoted by e , (see Figure 2.10c). The conversions between the quantities measured by the rheometer (applied torque Γ in N.m and rotational speed ω in rad/s of the double helix) and the effective rheological quantities (shear stress σ and shear rate $\dot{\gamma}$) are defined according to the work of Aït-Kadi et al. [155]. The complex flow in the mixer type geometry is represented by a simple shear flow between two concentric cylinders of the radii R_e (for the real external cylinder) and R_i (for the imaginary internal cylinder), as shown in Figure 2.10c. The equivalent radius R_i of the inner cylinder is evaluated by equating the torque developed in the concentric cylinder geometry to the torque measured in the mixer type geometry with a Newtonian calibration liquid of a known viscosity η_0 :

$$R_i = R_e \left[1 + \frac{4\pi \eta_0 L R_e^2}{\alpha} \right]^2 \quad (2.8)$$

where L is the inner cylinder length, taken to be equal to double helix length and α (in $\text{N} \times \text{m} \times \text{s}$) is the proportionality factor between the torque Γ and the rotational speed

ω experimentally determined for the calibration liquid. The shear rate in the gap between cylinders depends on the radial position r and on the rheological behavior of the measured non-Newtonian sample. It has been shown that for power-law rheological behavior, $\sigma \propto \dot{\gamma}^n$, there exists a so-called optimal position $r = r^*$ where the shear rate does not depend on the exponent n . In original paper of Aït-Kadi et al. [155], this position is defined by equating the shear rate at two different rheological exponents $n \neq 1$ and $n' = 1$, with the final result for r^* being almost independent of n . In our case, instead of using an arbitrary value of n , we evaluate r^* in the limit $n \rightarrow n' = 1$ by developing in Taylor series the original result of Aït-Kadi et al. around vanishing values of $n - n'$:

$$r^* \approx R_e \exp \left[\frac{1}{2} - \frac{\left(\frac{R_e}{R_i}\right)^2}{\left(\frac{R_e}{R_i}\right)^2 - 1} \ln \frac{R_e}{R_i} \right] \quad (2.9)$$

Taking advantage of independency of the shear rate on the power-law rheological behavior of the sample at optimal position r^* , the stress and the shear rate are evaluated at this position as for a Newtonian liquid:

$$\sigma = \sigma(r^*) = \frac{\Gamma}{2\pi r^{*2} L} = A \times \Gamma \quad (2.10)$$

$$\dot{\gamma} = \dot{\gamma}(r^*) = \frac{2\omega}{r^{*2}(R_i^{-2} - R_e^{-2})} = M \times N \quad (2.11)$$

where N is the rotational speed imposed (in turns per second) of the tool such that $\omega = 2\pi N$, then it is only necessary to determine the conversion factors A and M using Eqs. (2.10), (2.11). These factors were checked and corrected by calibration using two Newtonian fluids of known viscosity.

We note that these rheometric conversions are valid for shear thinning power-law rheology but have not been validated for shear thickening rheology. Thus, the shear stress and shear rate measured in the double helix geometry will be hereinafter, labeled as ‘‘apparent’’ quantities in all relevant figures but not in the text for the sake of easier reading. Notice also that in a complex flow field, possible extensional components of the rate-of-deformation fields could lead to the alignment of the rods along the extension axis and that lead to significant stress levels; however, this effect is believed to be relatively weak because the viscosity of the suspension of fibers dispersed in a Newtonian solvent perfectly fits to classical shear rheology models. We believe therefore that the proposed rheometric conversions can be used for at least semi-qualitative

comparison of rheological response of different bimodal mixtures considered in the present study.

The double helix rotor tool is made of stainless-steel material (see Figure 2.10a) and has an inner radius of $R_i = 12$ mm, the length of the effective working tool is $L = 37$ mm, the thickness of the blade is 1 mm, and the radius of the central shaft is 1.5 mm. The outer radius of the mixer-type geometry (or the inner radius of the cylindrical cuvette) is $R_e = 14.5$ mm (see Figure 2.10c) and the inner surface of the bowl has horizontal and vertical grooves 0.5 mm wide by deep spaced at a period of 0.5 mm in order to prevent wall slip on the inner surface of the bowl. The gap between the bottom surface of the cylindrical cuvette and the bottom part of the double helix rotor was set at 2 mm.

B. Measuring protocol

The samples (1st series of CC particles – cf. note at the end of Section 2.1.1.2 – mixed or not with PA or glass fibers) were prepared directly in the brass cylindrical cuvette. Before the measurements, the double helix tool was gently introduced into the cuvette and the latter was placed into the rheometer and the gap of 2 mm was adjusted between the cuvette bottom and the bottom part of the double helix. A water trap (wetted washcloth) was placed on the top of the cuvette, the cuvette was thermally isolated from the ambient air and the temperature at the base of the cuvette was adjusted to 14°C by a Peltier element integrated to the rheometer. Increasing-decreasing stress ramps were applied to the sample in a similar way than in the case of plate-plate geometry. Each time at least two up-and-down stress ramps were applied in order to check the effect of possible particle migration on the suspension rheology. To obtain the flow curve from raw rheological data, the applied torque was related to the shear stress and the measured rotational speed by Eqs. (2.10), (2.11).

In some cases, the rheological measurements with double helix geometry were conducted in shear rate-imposed mode [chapter 3, section 3.5]. The rate of increase of the shear rate was adjusted to a value ensuring the same rate of increase of the stress in the stress-controlled mode. All the measurements were repeated a few times in order to check their reproducibility.

2.2.1.3 Cylindrical Couette geometry

A. General description

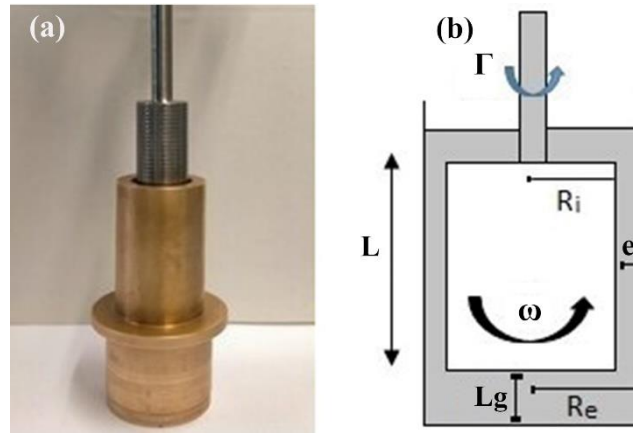


Figure 2.11 Cylindrical Couette geometry in (a) and its descriptive scheme in (b).

The cylindrical Couette geometry that we used is the same as the conventional geometry, although, we made some modification on the rotating tool. Indeed, the geometry is constituted by a cylinder of inner radius $R_i = 12$ mm (rotor) rotating at an angular speed ω . However, this tool has a completely flat base (See Figure 2.11b) contrary to the tapered base in the commercially available Couette tools. The tool is also grooved in order to avoid slipping on its surface. The height of the Couette rotating tool is $L = 37$ mm. The cylindrical cuvette of the Couette geometry is the same as the one used in the double helix case with an inner radius $R_e = 14.5$ mm and it is also grooved on its inner surface in order to prevent the fluid from slipping on the inner surface of the cuvette.

The torque Γ imposed in the rheometer is converted to shear stress σ and the corresponding measured angular speed ω is converted to shear rate $\dot{\gamma}$. In the present case of relatively small rheometer gap ($e = R_e - R_i$) the stress σ and the shear rate $\dot{\gamma}$ vary only slightly across the gap, and their representative values can be taken at the inner cylinder surface. At such condition, the relations between the torque and the shear stress and the angular speed and the shear rate read [154]:

$$\sigma = \sigma(R_i) = \frac{\Gamma}{2\pi R_i^2 L} \quad (2.12)$$

$$\dot{\gamma} = \dot{\gamma}(R_i) = \frac{2\omega}{1 - (R_i/R_e)^2} \quad (2.13)$$

B. Determination of the gap at the measuring position

Since the cylindrical rotating tool has a circular flat base surface, it is necessary to calculate a sufficient gap L_g to apply between the bottom surface of the cuvette and the bottom surface of the rotating cylinder during the shearing of the suspension, this is necessary to minimize the effect of the flat base surface of the measuring tool on the sheared suspension. For such a flat surface, the torque applied by the rotating tool is approximately giving by:

$$\Gamma = \Gamma_{cyl} + \Delta\Gamma \quad (2.14)$$

where Γ_{cyl} is the torque contribution coming from the lateral surface of the rotating cylinder, and $\Delta\Gamma$ is the torque contribution coming from the bottom flat surface of the rotating cylinder. For a Newtonian liquid of a viscosity η_0 , we get:

$$\Gamma = \left[\frac{2\pi R_i^2 L \eta_0 2\omega}{1 - (R_i/R_e)^2} \right] + \left[\frac{\left(\frac{2\pi R_i^3}{4} \right) \eta_0 \omega R_i}{L_g} \right] \quad (2.15)$$

$$\frac{\Delta\Gamma}{\Gamma_{cyl}} = \frac{R_i^2 (1 - (R_i/R_e)^2)}{8L_g L} \quad (2.16)$$

For the following geometrical parameters (see Figure 2.11b):

- Internal radius: $R_i = 12$ mm.
- External radius : $R_e = 14.5$ mm.
- Gap between the cuvette bottom and the rotating cylinder bottom surface $L_g = 10$ mm.
- Rotating tool length: $L = 37$ mm,

we get $\frac{\Delta\Gamma}{\Gamma_{cyl}} = 0.015$, Thus, the effect of the base surface of the rotating cylinder is of the order of 1.5% with the chosen gap of $L_g = 10$ mm. This is considered a very low percentage of the flat effect compared to the torque generated by the lateral surface of the rotating cylinder, such that the shear contribution coming from the energy dissipation in the fluid gap between the cuvette bottom and the rotating cylinder can be neglected.

C. Calibration of the cylindrical Couette tool

The cylindrical Couette measuring tool used is a home-made tool, consequently, it does not carry a recognition microchip as opposed to the standard tools of the Anton Paar Physica 301 rheometer; for this reason, a calibration before starting the shear tests is required.

For the calibration of the tool two main coefficients must be determined to allow the good conversion of the data by the rheometer.

The coefficients are:

- Coefficient of conversion of the applied torque into shear stress noted "A".
- Coefficient of conversion of the rotation speed of the tool into shear rate noted "M".

For a cylindrical Couette tool, the torque-stress relationship is given by:

$$\sigma = A \times \Gamma \quad (2.17)$$

where:

$$A = \frac{1}{2\pi R_i^2 L} \quad (2.18)$$

and the rotation speed-shear rate conversion is giving by:

$$\dot{\gamma} = M \times N \quad (2.19)$$

where:

$$M = \frac{4\pi}{1-(R_i/R_e)^2} \quad (2.20)$$

The values of $A = 29.871 \text{ Pa/mN.m}$ and $M = 6.6467$ evaluated using Eqs. (2.18), (2.20) are theoretical and are needed to be checked and corrected through the calibration procedure. For this purpose, shear tests with a Newtonian silicon oil of known viscosity were conducted in the cylindrical Couette tool and the coefficients A and M were readjusted in order that the slope value of the measured flow curve coincide with the known value of the calibrating oil viscosity.

D. Measuring protocol

In these experiments, we used the 2nd series of CC particles – cf. note at the end of Section 2.1.1.2 – mixed or not with PA fibers. As mentioned before, the bottom surface of the homemade Couette measuring tool is a flat geometric shape, therefore the suspension samples were first prepared in the cylindrical cuvette and then the Couette tool was slowly introduced into the cylindrical cuvette to avoid any suspension jamming artifacts, until the gap 10 mm was adjusted between the Couette tool and the bottom part of the cuvette. The upper surface of the cylindrical cuvette was then closed by a cover pierced in its center to allow free rotation of the Couette tool. The cover allows the insulation of the suspension from the outer atmosphere, thus avoiding any possible evaporation of the water from the samples and helps to keep the adjusted temperature within the cuvette of 14°C. The applied shear stress profile this time was set just to an ascending stress ramp from $\sigma_a = 0 \text{ Pa}$ to $\sigma_a = 500 \text{ Pa}$ with the same rate of the stress increase in the case of Plate-Plate and Mixer type geometries experiments of 0.33 Pa/s. Each time at least two stress ramps for the same sample were applied in order to check the

reproducibility of the results. To obtain the flow curves, the applied torque was related to the shear stress and the measured rotational speed by Eqs. (2.12), (2.13).

2.2.1.4 Evaluation of the effect of air bubbles presence in CC-suspension

We are interested in this section to see the effects that could have the presence of air within the suspension in the form of bubbles during the preparation of the CC-suspension on the rheology of this one. To this purpose, we conducted shear tests in the rheometer using the mixer type geometry for two samples at 64% of CC volume fraction and without fibers. The first sample is degassed according to the protocol mentioned before (see section 2.1.4) and the other one is tested without degassing.

For this shear tests we have chosen the mixer type geometry described in section 2.2.1.2 with the measuring protocol described in section 2.2.1.2-B.

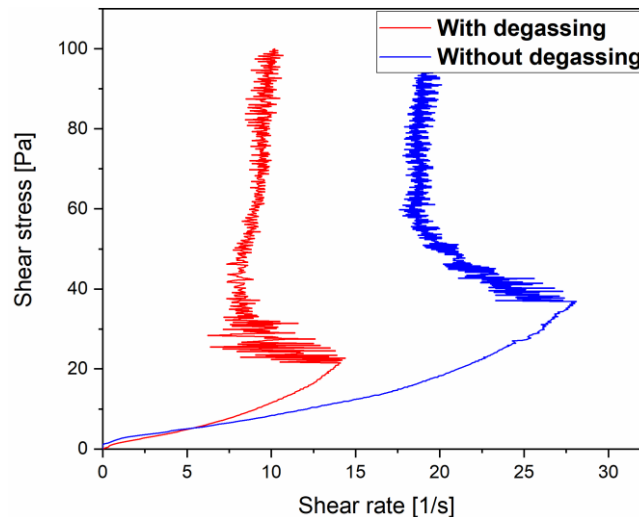


Figure 2.12 Controlled shear stress test for degassed and non-degassed 64% CC-suspensions.

The sample of the suspension prepared with degassing shows a rather remarkable difference in results compared to the sample prepared without degassing. The difference shifts to low shear rate compared to the non-degassed suspension; thus, the degassed suspension represents more shear thickening behavior and therefore a higher suspension viscosity. Since the removal of air bubbles in the prepared suspensions was verified with a second degassing of the suspension (the 30 min degassing is performed in two 15 min ramps in order to ensure that no air is left in the sample), the difference observed in the results can be justified by the change in concentration φ_p of the CC particles in the prepared suspension due to the evaporation of the water during the degassing process.

In order to verify the variation of CC particles concentration in a degassed carbonate calcium suspension, a $\varphi_p = 64\%$ sample was prepared, degassed and weighed before and after degassing process to measure the variation of particle concentration due to possible water evaporation during degassing. The weighing results are: before degassing: $m_1 = 69.1776$ g; after degassing, $m_2 = 68.5590$ g and the mass difference $\Delta m = 0.6186$ g, corresponding to the evaporated water. This allows evaluation of the particle volume fraction ratio before and after degassing:

$$\frac{\varphi_1}{\varphi_2} = \frac{V_p/V_1}{V_p/V_2} = \frac{V_1 - \Delta V}{V_1} = 1 - \frac{\Delta m \rho_1}{m_1 \rho_w} \quad (2.21)$$

where V_1, V_2 are initial and final suspension volumes, ΔV is the volume of the evaporated water, $\rho_1 \approx 2$ g/mL and $\rho_w \approx 1$ g/mL are the densities of the initial suspension and of water, respectively. Evaluation gives $\frac{\varphi_1}{\varphi_2} \approx 0.98 \rightarrow \varphi_2 = 65.3\%$ vol. The concentration of CC - particles in the suspension increased by 1.3% during degassing due to the evaporation of water making the suspension more shear thickening. Notice that such an increase of the volume fraction near the particle packing limit is very significant because the suspension viscosity diverges as $(1 - \varphi_p/\varphi_m)^2$ as φ_p becomes close to φ_m evaluated to be about 0.69 in our experiments (see chapter 3, Appendix C).

To ensure that the difference in behavior observed in the graphs (Figure 2.13) is not due to the presence of air bubbles in non-degassed suspension and that this difference is the result of water evaporation, and consequently to the change in concentration of CC-particles in the suspension, a test with degassed CC-suspension completed with water after degassing (in order to keep the same concentration of CC-particles $\varphi_p = 64\%$ vol) was conducted. The same standard procedures for preparing a CC-suspension are followed but with the weighing of the suspension after degassing and adding water to compensate evaporation during degassing. Also, to avoid water evaporation, we loaded the sample very gently but quickly into the measuring cylinder.

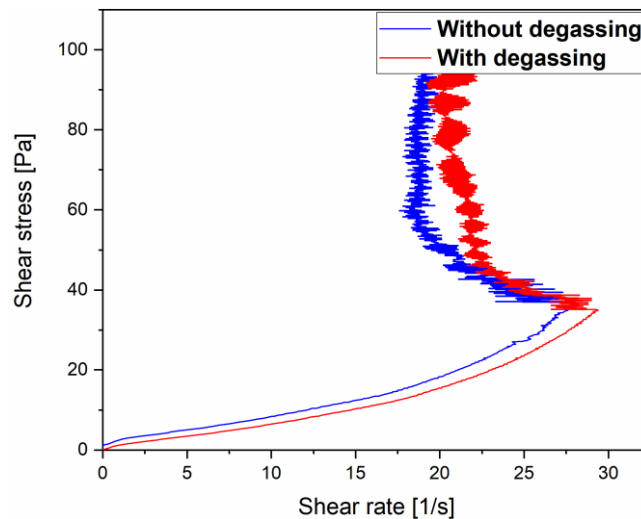


Figure 2.13 Controlled shear stress test for degassed and water completed 64% CC- suspension against non-degassed 64% CC-suspension.

We can observe from Figure 2.14. a reproduction of the results and a very good agreement between curves with a very slight difference that falls within the calculation errors. Completing the degassed suspension with water just after degassing allows to keep the desired concentration of CC-particles in the suspension at $\varphi_P = 64\%$ vol. The slight difference in measurements observed in the graphs is due to errors related to the operation of the experimental equipment and is within the tolerated error range. A decision to prepare CC-suspensions without degassing was taken, given the results obtained, which confirm the fact that, due to the degassing of the suspension, a quantity of the water in the suspension evaporates, thus changing the particle concentration. So, the presence of air bubbles in the suspension does not have a major impact on the obtained results.

2.2.2 Pressure-driven flows in capillary rheometry

A. General description

The basic principle behind the capillary rheometry used in our tube flow tests is depicted in Figure 2.15. It consists of a homemade pressure-imposed rheometer recently developed in the hosting team in UCA [156, 157] and differs from conventional speed-imposed capillary rheometers used in literature [154], in which the flow rate is imposed by a moving piston. The principle of our homemade capillary rheometry consists of applying a compressed air at a desired pressure from an air compressor to a tank containing our suspension, with a pressure control valve (MDG-3 from Selid) and a piezoelectric manometer (LEO 2 from Serv'instrumentation: resolution 10^{-3} bar, maximal applied pressure 3 bars) connected to a 3-port steering valve (SS-43GXS4 from Swagelok). The length and diameter of the plexiglass

tank containing the suspension are $l = 100$ mm and $d = 25$ mm, respectively. A capillary is connected to the bottom of the tank by a union (SS-400-6 for a tube of $\frac{1}{4}$ inch outside diameter or $1/4 \times 2.54$ cm). The capillary has the length $L = 35$ cm and a diameter $D = 0.77$ cm. Under the action of the applied air pressure, the suspension flows out from the capillary on the top of the electronic balance measuring its mass flow rate.

B. Measuring protocol

The experiment starts by aspirating the freshly prepared CC suspension (2nd series of CC particles – cf. note at the end of Section 2.1.1.2) at a specific PA-fibers concentration in the tank by turning the 3-port steering valve towards the venturi vacuum ejector and using the venturi aspiration valve connected to a vacuum pressure gauge through a steering two port valve. Aspirating the suspension to the tank helps degassing the suspension from any trapped air bubbles, that can disrupt or block the flow of the suspension through the capillary. The aspiration pressure was chosen relatively low $\Delta P \geq 0.2$ bar, which corresponds to a wall shear stress σ_w of 62 Pa at capillary walls for 0.33 cm capillary diameter and 150 Pa for 0.77 cm capillary diameter, in order to avoid suspension jamming due to DST behavior of the suspension since the critical DST shear stress for CC-suspension is ranged between 120 Pa for suspension without fibers and 165 Pa for suspension with 2.5% vol PA fibers in shear rheology tests using cylindrical Couette geometry (see chapter 4, section 4.3.1, Figure 4.4). Once the suspension is fully aspirated, a desired air pressure is applied to the confined suspension using the pressure control valve, then the mass flow rate of the suspension flowing out from the capillary is measured using an electronic balance Ohaus STX 2202, programmed to record the amount of the collected suspension every 1 second and store the results in a USB stick.

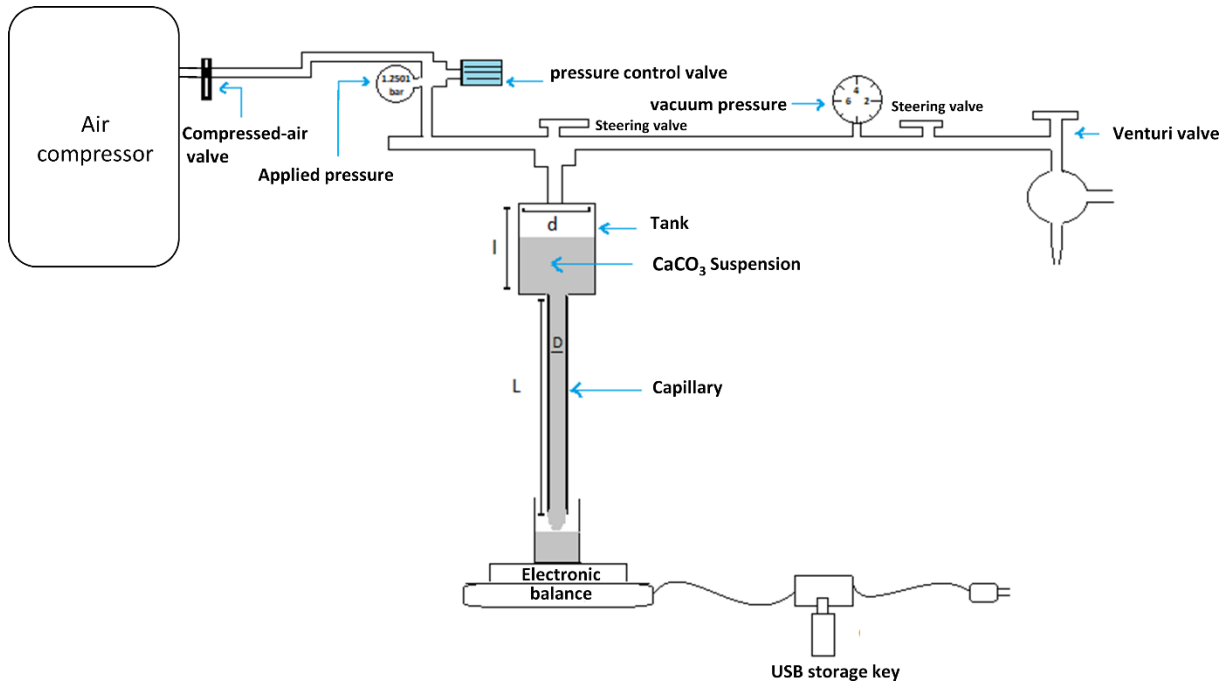


Figure 2.14 Descriptive sketch of the imposed pressure homemade capillary rheometer.

C. Rheometric conversions

By the application of a known and precise pressure value ΔP ($\pm 5 \times 10^{-3}$ bar precision) using pressurized air in a cylindrical plexiglass container where the suspension is located, the mass in grams of the suspension which is evacuated from a capillary connected to this cylindrical container is measured for each instant $t = 1$ s. Therefore, by a linear fit of the amount of suspension evacuated in time t , the mass flow rate of the suspension at the exit of the capillary is estimated. The applied air pressure ΔP and the mass flow rate Q_m are converted respectively to shear stress and shear rate, both evaluated at the capillary wall: [154]

$$\sigma_w = \frac{(\Delta P + \rho g L)R}{2L} \quad (2.22)$$

$$\dot{\gamma}_{a,w} = \frac{4Q_m}{\rho \pi R^3} \quad (2.23)$$

where σ_w is the shear stress at the capillary walls and $\dot{\gamma}_{a,w}$ the apparent shear rate at the capillary walls for a Newtonian fluid. In the case of non-Newtonian, it is mandatory to apply the Mooney-Rabinowitch correction, where the apparent shear rate can be related to the real shear rate at capillary wall of the non-Newtonian fluid [154]:

$$\dot{\gamma}_{a,w}(\sigma) = \frac{4}{\sigma_w^3} \int_0^{\sigma_w} \sigma^2 \dot{\gamma}_w(\sigma) d\sigma \quad (2.24)$$

and the real shear rate $\dot{\gamma}_w$ can be obtained by deriving equation (2.24) with respect to σ_w to give:

$$\dot{\gamma}_w = \dot{\gamma}_{a,w} \left[\frac{3}{4} + \frac{1}{4} \frac{d \ln \dot{\gamma}_{a,w}}{d \ln \sigma_w} \right] \quad (2.25)$$

This expression contains the derivative of $\dot{\gamma}_{a,w}$ with respect to σ_w and gives considerable numerical errors when converting $\dot{\gamma}_{a,w}$ to $\dot{\gamma}_w$ for our fluctuating flow curves obtained in shear rotational rheometry in the DST domain, (see chapter 4, Figure 4.4), therefore we prefer not to make the conversion of the apparent shear rate $\dot{\gamma}_{a,w}$ to the real shear rate $\dot{\gamma}_w$. However, when we compare the results of capillary with rotational rheometer tests (using the cylindrical Couette geometry), we convert the shear rate $\dot{\gamma}$ measured in rotational rheometer tests to the apparent shear rate at the capillary walls $\dot{\gamma}_{a,w}$ using equation (2.24). This will allow to verify to what extent the rheometric geometry affects the DST behavior of our CC-PA mixtures. We will therefore compare the curves of $\dot{\gamma}_{a,w} = f(\sigma)$ obtained in the two geometries, with $\sigma = \sigma_w$ for capillary geometry. $\dot{\gamma}_w$ to $\dot{\gamma}_{a,w}$ conversion in cylindrical Couette geometry is made by first smoothing the corresponding experimental flow curves in order to reduce the shear rate fluctuations in the curves, then a higher order polynomial fit is applied to the curve to get the corresponding polynomial expression $\dot{\gamma}_w = f(\sigma)$ (see Figure 4.7 in chapter 4). Finally, $\dot{\gamma}_{a,w}$ can be obtained in cylindrical Couette geometry using equation (2.24). Results are then presented in form of $\dot{\gamma}_{a,w} = f(\sigma)$ curves in chapter 4.

2.2.3 Extensional flows withing a free-falling jet

2.2.3.1 Experimental setup

The experimental setup of the jet flow experiment is presented in Figure 2.15 and composed by a filling tank, a vertical tube of an internal diameter $D_0 = 2R_0 = 5 \text{ mm}$ and length $h = 215 \text{ mm}$, connected coaxially to the bottom of the tank, a collecting Petri dish and a fast camera Miro C110 (Phantom, US) equipped with a charge-coupled device (CCD) sensor. About 30 mL of the suspension were first poured in the tank (average diameter $D_1 \approx 50 \text{ mm}$, suspension height $h_1 \approx 15 \text{ mm}$). During the filling, the lower tube extremity was maintained open allowing the suspension to fill the tube under gravity. Then the lower extremity was mechanically closed, and the suspension was left at rest inside the tank and the tube for 1 min. At the moment of time $t=0$, the lower extremity was again opened, the suspension started flowing through the tube under gravity at nearly constant flow rate during the whole duration of the experiment (thanks to $D_0 \ll D_1$ and $h_1 \ll h$). The flow through the tube is laminar and the wall shear stress $\sigma_w \approx \rho g R_0 / 2 \approx 25 \text{ Pa}$ (with $\rho \approx 2000 \text{ kg/m}^3$ being the suspension density and $g \approx 10 \text{ m/s}^2$ the gravity acceleration) is believed to be below the DST transition ($\sim 40 \text{ Pa}$) revealed in a plate-plate (PP) shear rheometry (see the blue curve in Figure 3.2 in

chapter 3). Below DST, the CC suspension experiences nearly Newtonian behavior with the average low-shear viscosity $\eta_0 \approx 5 \text{ Pa} \times \text{s}$, corresponding to the linear fit of initial part of the blue flow curve in defined from shear flow curves [Figure 3.2c in chapter 3]. The velocity profile inside the tube is expected to be nearly parabolic and the mean velocity averaged over the tube cross-section is given by

$$u_0 \approx \frac{\rho g R_0^2}{32\eta_0} \quad (2.26)$$

The measured flow rate Q through the tube fits within 13% error to the theoretical value $Q = u_0 \pi R_0^2$. This correlates with the supposed laminar flow regime below DST transition. The stress field in the jet is supposed to be mostly extensional (at least at axial distances a few tube diameters downstream the tube outlet) with the stress levels governed by gravitational forces. All experiments were performed at room temperature of 20°C , controlled by an air conditioner.

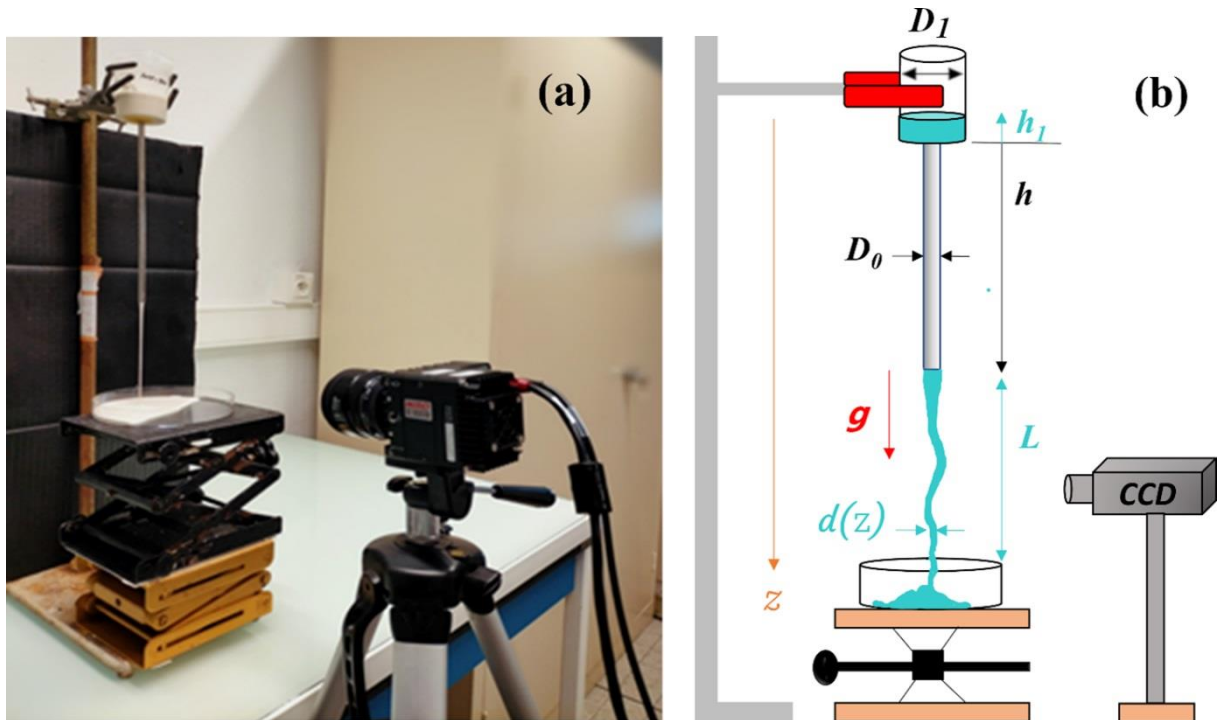


Figure 2.15 Fast camera device for recording jets of the CC-PA mixtures extending from the tube outlet to the experimental table (a). Geometric notations are introduced in (b).

The dynamics of the CC-suspension jet was recorded with a high-speed camera at 336.5 fps (frames per second) and at spatial resolution of 2.6 pixel/mm. This allowed us to follow the falling suspension and enabled capturing the jet diameter $d(t, z)$ (supposing preservation of the jet's axial symmetry) and the deviation $x(t, z)$ of the jet centerline from rectilinear trajectory (hereinafter called lateral drift) at the spatial resolution of 0.39 mm and the temporal resolution of 3.0 ms. To quantify the magnitudes $d(t, z)$ and $x(t, z)$, we developed an image processing

script in MATLAB (MathWorks®). Defining the background intensity with graphical user interface, the script analyzed each frame of the movie. For each frame (each moment of time t), the script detects the jet using a gaussian fit of the intensity profile, to extract its diameter $d(z)$ and its lateral drift $x(z)$ along the vertical axis. In case of the jet break-up, the script also quantifies the properties of each jet segment. The script analyses each frame in a parallel workflow to optimize the computation time (230ms/frame on a 6-core processor).

2.2.3.2 Fourier analysis

Apart from direct analysis of the jet lateral drift $x(t, z)$, we performed a Two-Dimensional Discrete Fourier Transform (2D DFT) of the measured lateral drift $x(t, z)$. To this purpose, we applied the “fft2” built-in function of the MATLAB software to the $m \times n$ matrix of the x values, whose $m = 5000$ rows and $n = 364$ columns correspond to discrete values of t and z , respectively. The “fft2” function returns a $m \times n$ matrix \mathbf{A} of complex values, using the following expression:

$$A_{p+1,q+1} = \sum_{j=0}^{m-1} \sum_{l=0}^{n-1} \exp\left(-\frac{2\pi i}{m} jp - \frac{2\pi i}{n} lq\right) x_{j+1,l+1} \quad (2.27)$$

where $i = \sqrt{-1}$ stands for the imaginary unit, $p = 0, 1 \dots m - 1$ and $q = 0, 1 \dots n - 1$. For the better presentation (see the results in chapter 5), we shifted the zero-frequency component of the matrix \mathbf{A} to the center of the spectrum using “fftshift” built-in MATLAB function. This function swaps the first quadrant of \mathbf{A} with the third, and the second quadrant with the fourth. The components of the matrix \mathbf{X} of the Fourier spectrum amplitudes were then calculated as $X_{j,l} = |A_{j,l}| / (m \cdot n)$, with the rows $j = 1 \dots m$ and columns $l = 1 \dots n$ corresponding to discrete values $\omega_j = 2\pi f_t(j - m/2)/m$ and $k_l = 2\pi f_z(l - n/2)/n$ of the temporal angular frequency ω and wave numbers k , respectively. Here, $f_t = 336.5 \text{ s}^{-1}$ (fps) is temporal sampling rate fixed by the camera speed and $f_z = 2.6 \text{ mm}^{-1}$ (pixel/mm) is the spatial sampling rate fixed by the image resolution. In this way, we obtained a discrete $X(\omega, k)$ dependency of the Fourier amplitude on the temporal and spatial frequencies. The final signal $X(\omega, k)$ allowed evaluation of dominant frequency and wavelength of the jet lateral oscillations, as well as the dispersion relation, which was retrieved as a curve $\omega(k)$ drawn along the crests of the $X(\omega, k)$ surface plots. A similar 2D DFT analysis was applied to the jet diameter $d(t, z)$ with the Fourier spectrum amplitude denoted by $\mathfrak{D}(\omega, k)$ (see the results of the analysis in chapter 5).

Notice that the “instrumental” sampling rates $f_t = 336.5 \text{ s}^{-1}$ and $f_z = 2.6 \text{ mm}^{-1}$ appeared to be too large as compared to maximal observable frequencies in $X(\omega, k)$ and

$\mathfrak{D}(\omega, k)$ -transforms. Thus, prior to Fourier transform, we had to “coarse” the recorded data (by removing appropriate lines and columns of the $x(t, z)$ and $d(t, z)$ -matrices and reducing the $m \times n$ matrix size) to achieve the sampling rates just slightly larger than twice the maximal observable frequency. In this way, the Nyquist limit, was still respected.

For quantitative comparison of the intensity of lateral oscillations, a root mean square (RMS) amplitude x_{RMS} of the lateral drift and RMS transverse speed v_{RMS} of the jet. These parameters are directly defined from the Fourier amplitudes using the Plancherel theorem, as follows:

$$x_{RMS} = \sqrt{\sum_{j=1}^m \sum_{l=1}^n X_{j,l}^2} \quad (2.28)$$

$$v_{RMS} = \sqrt{\sum_{j=1}^m \sum_{l=1}^n (X_{j,l}^2 \omega_j^2)} \quad (2.29)$$

with the summation performed over all elements of the Fourier amplitude matrix \mathbf{X} .

CHAPTER 3

3 Drag flows of sphere-fiber mixtures in a mixer-type geometry¹

This chapter is devoted to the study of the drag shear flows of calcium carbonate CC suspension concentrated with rigid glass and polyamide fibers. Special attention is paid to the effect of fibers on the rheology of the sphere-fiber mixtures and to the mixer-type rheometry allowing one to mimic mixing processes of the fiber-reinforced concretes during their preparation and transport. The physicochemical characterizations, suspension preparation and rheometric protocols are described in detail in chapter 2.

This chapter is organized as follows. First, we will discuss the rheological behaviors that are qualitatively similar for the CC suspensions with and without fibers. These are sigmodal shape of the flow curve [section 3.1] and thixotropic behavior [section 3.2]. Then, we will describe the effect of fibers on the rheology of the mixtures of isotropic-shaped and fiber-like particles, more precisely the effect of the fiber-to-particle diameter [section 3.3] and fiber concentration [section 3.4]. After that, the rheological response at imposed shear stress is compared to the response at imposed shear rate in section 3.5. On the basis of the experimental findings of section 3.1 – 3.5, we propose in section 3.6 two conceptually similar models allowing prediction of the flow curves of the fiber-isotropic particles mixtures. These models are based on the reduced shear rate approach of Ohl and Gleissle [114] and on homogenization approach of

¹ The results of this chapter were obtained with the 1st series of CC particles and can be compared quantitatively to the results of the Chapter 5.

Main results are published in [Sidaoui, N., Arenas Fernandez, P., Bossis, G., Volkova, O., Meloussi, M., Aguib, S., & Kuzhir, P. (2020). Discontinuous shear thickening in concentrated mixtures of isotropic-shaped and rod-like particles tested through mixer type rheometry. *Journal of Rheology*, 64(4), 817-836].

Château et al. [158] with a special attention paid to orientation distribution of fibers. Finally, jamming behavior above some critical volume fraction of fibers is considered in section 3.7.

3.1 Sigmodal flow curve

Experimental flow curves of the CC suspensions without fibers obtained from the increasing branch of the first stress ramp in double helix geometry are shown in Figure 3.1 by dotted lines for four different CC particle volume fractions ($\varphi_p = 0.62, 0.64, 0.66$ and 0.68). The flow curves of the samples containing fibers are qualitatively similar to those shown in Figure 3.1 and will be discussed in detail in sections 3.3 and 3.4. The flow curve of the CC suspension of a particle volume fraction $\varphi_p = 0.62$ shows a monotonic, stronger than linear increase of the stress with shear rate, which is a signature of continuous shear thickening (CST). At higher volume fractions $\varphi_p \geq 0.64$, the flow curves have a sigmodal (S-) shape reminiscent to DST with irregular oscillations above the critical stress. Here, we introduce the critical shear stress σ_{c0} and the critical shear rate $\dot{\gamma}_{c0}$ of the DST as, respectively, the stress and the shear rate at the point where the slope of the flow curve changes from positive one to the negative one, as shown by arrows in Figure 3.1. As expected, the critical shear rates decrease with increasing particle volume fraction as it approaches some maximal value, called jamming volume fraction. There exist different possible mechanisms for the DST transition listed in chapter 1 (section 1.3.3). Strictly speaking, we cannot directly support any of them without precise microstructural information on the spatial organization of particles within the suspension and on polymer conformation on particle surface affected by the applied stress. In what follows, we briefly discuss on several possible origins of the DST transition in our specific case.

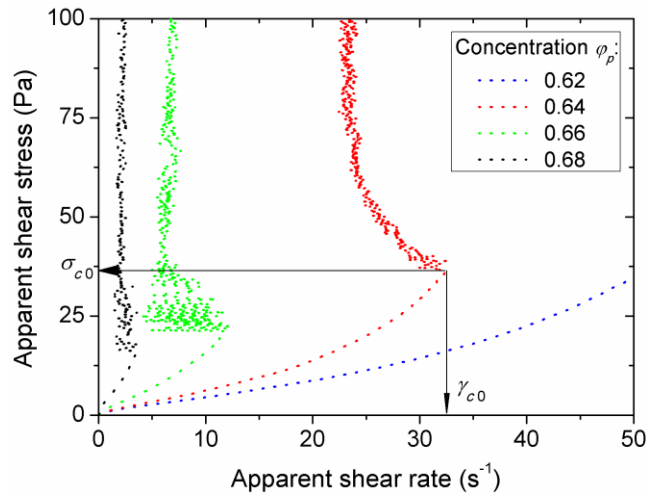


Figure 3.1 Flow curves of isotropic shaped particle (CC) suspensions at different volume fractions ϕ_p of CC particles measured for the ascending branch of the 1st stress ramp in mixer type geometry. The arrows show definition of the critical shear rate and shear stress in the stress-controlled rheometry. Labels “apparent” in the titles of axes recall that the reported shear rate and shear stress values stem from approximate rheometric conversions of the raw rheological data [section 2.2.1.2].

As stated in chapter 1, the DST is often believed to arise due to transition between lubricated and frictional inter-particle contacts building percolated contact network of particles as the applied stress increases. Recent measurements on sliding friction between compressed polymer layers adsorbed on the particle surface find a direct correlation between boundary-to-hydrodynamic lubrication transition on the nanoscale and the DST transition at the macroscopic scale [159]. The macroscopic physics of such a transition is qualitatively captured by the model of Wyart and Cates (WC) [107], which interpolates the suspension rheology between two Newtonian states: the low viscosity state at fully lubricated contacts and high viscosity state at fully frictional contacts. The WC model is detailed in Appendix E of this chapter, and the fit of the flow curves by this model is shown in Figure 3.10 Using different versions of the WC model [106, 160, 161], we did not succeed to reliably fit our flow curves above the critical stress σ_{c0} . The discrepancy is very likely related to the WC assumption of the Newtonian rheology in frictional regime. This assumption likely does not apply to our specific system where attractive colloidal interactions could in principle arise above some critical compression of adsorbed polymer layers, as point out below.

From the microscopic perspective, the DST transition could be related to the collapse of the polymer layers on the particle surface as a result of the compression of these layers when increasing applied shear stress pushes neighboring particles together. This scenario has been considered in more details in the work [134] and seems to not contradict to the macroscopic picture of the WC frictional transition scenario. Nevertheless, the above hypotheses on the

origins of the DST need to be checked by microscale measurements. The value of the critical stress σ_0 related to the polymer layer collapse can be evaluated by balancing the compressive force stemming from the applied shear stress and the repulsive steric force between compressed brushes at critical distance between solid particle surfaces taken to be on the order of equilibrium thickness of the non-deformed polymer layer, $\delta \approx 5.4$ nm. This gives the following scaling behavior [134]:

$$\sigma_0 \sim \frac{k_B T \delta n_c^{3/2}}{d} \quad (3.1)$$

where $k_B T \sim 4 \times 10^{-21}$ J is the thermal agitation energy at ambient temperature, $n_c \approx 0.14$ nm⁻² is the grafting density of the PEG brushes on the CC particle surface [Figure 2.6] and $d \approx 5.5$ μ m is the average CC particle diameter [cf. section 2.1.1]. Evaluation gives $\sigma_0 = O(10^2$ Pa), which is consistent with the order of magnitude of the critical stress σ_{c0} of the DST transition, (see Figure 3.1 for graphical definition of σ_{c0}).

3.2 Thixotropic behavior

Experimental flow curves of the CC suspensions without fibers obtained from ascending and descending branches of several (up to four) consequent stress ramps were analyzed. For the sake of brevity, only the ascending branches of the first and the second stress ramps are shown in Figure 3.2 for the CC suspension at volume fraction $\varphi_p = 0.68$ measured in double helix (Figure 3.2a) and plate-plate (Figure 3.2b) geometries. Remarkably, the sigmodal shape of the flow curve already disappears at the decreasing branch of the first stress ramp in double helix geometry. After that, increasing and decreasing branches of the second stress ramp collapse on the decreasing branch of the first ramp and distinguishable flow curve hysteresis is no longer observed. The same data collapse without hysteresis is observed for the third and the fourth stress ramps (not shown here). On the contrary, the sigmodal shape is always present in increasing and decreasing branches of the first, the second and subsequent (not shown here) ramps in the plate-plate geometry but a noticeable and reproducible flow curve hysteresis is observed for each ramp (Figure 3.2b).

Since evaporation, particle sedimentation and sample expulsion are minimized in double helix geometry, the change of the flow curve shape from S-like to monotonous one could be associated to the particle migration. In previous studies [160], the particle migration has been qualitatively observed using a high torque rheometer with a large diameter double helix geometry. Removing the double helix rotor from the flow cell, one observed a solid-like coaxial

plug confined by the internal face of the double helix, while the rest of the suspension (situated between the double helix rotor and cylinder) showed fluid-like behavior. This observation suggests the particle migration towards the cylinder axis, along the radial direction (shown by arrows in Figure 2.10). The suspension experiences lowest shear rates in the central region of the flow cell. Thus, our observation seems to be consistent with particle migration towards the regions of small shear rates (and consequently smaller normal stresses), as suggested both by shear-induced and normal-stress induced scenarios [13, 16]. These migration mechanisms do not contradict to the stress-controlled rheology or stress-activated percolated network of particles, as long as the coaxial plug can rotate as a solid body together with the double helix being subjected to lower stress levels than those expected in the gap between double helix and external wall. The particle migration changes the concentration and local stress distributions in the double helix geometry, and this certainly affects the “effective” flow curve (obtained from the torque versus rotational speed relationship) measured by the rheometer. However, without direct access to concentration distribution and local rheological properties, it is impossible to predict how the effective flow curve changes as a consequence of particle migration.

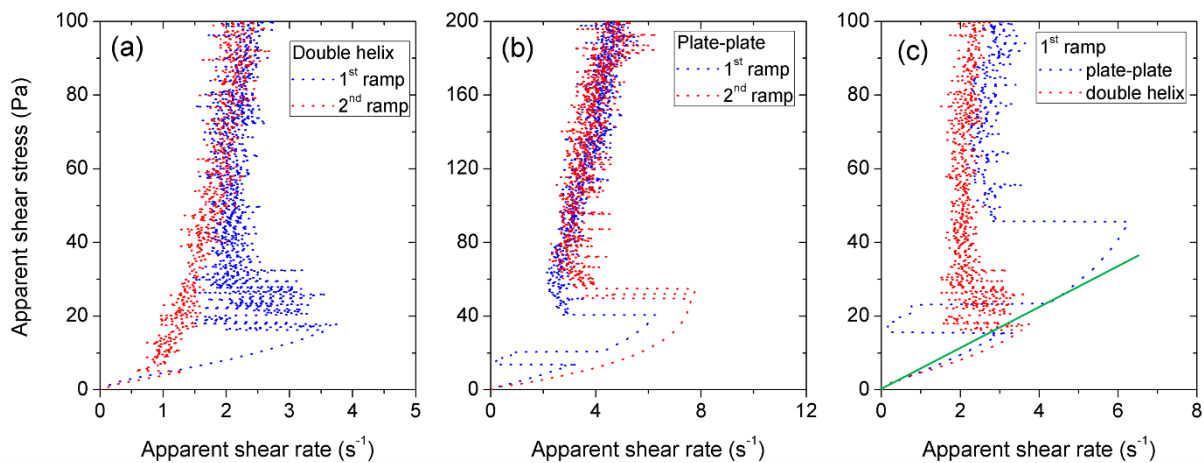


Figure 3.2 Effect of the flow history on the shape of experimental flow curves of the isotropic shape particle (CC) suspensions at CC particle volume fraction $\varphi_p = 0.68$ measured in mixer type (a) and plate-plate (b) geometries. All the reported flow curves correspond to the ascending branch of either the 1st or the 2nd stress ramp. Flow curves obtained during the 1st ramp in both rheometric geometries are compared in figure (c).

Conservation of the S-shape of the flow curves in plate-plate geometry remains poorly understood. On the one hand, this can point out to insignificant particle migration as typically observed for non-shear thickening suspensions in this specific geometry [162, 178]. On the other hand, the particle migration could likely induce unsteady locally oscillating vorticity bands in plate-plate geometry [111, 163]. Such vorticity banding probably slows down the

variation of particle concentration on the scale of the rheometer plate. However, only local concentration measurements under shear can affirm or rule out the above hypotheses.

It is also noticeable that the flow curves measured in both geometries are mainly different in the vicinity of the DST transition which occurs at higher critical shear rates in the plate-plate geometry, as compared to double helix geometry, as is seen in Figure 3.2c where increasing branches of the first ramp are compared for $\varphi_p = 0.68$. However, below the DST transition increasing branches of the first ramps of the flow curves seem to collapse for both geometries within the statistical error of the measurements. These branches correspond to the beginning of the measurements when the particle concentration is expected to be roughly homogeneous. The same conclusions hold for two other volume fractions $\varphi_p = 0.64$ and 0.66 exhibiting DST.

In what follows, we will consider the quantitative effects of the fibers on the rheology of fiber-isotropic particles mixtures starting with the effect of the fiber-to-particle diameter ratio. We will consider only the results obtained in mixer type geometry (because the plate-plate geometry generates numerous artefacts in mixtures with fibers – see section 2.2.1 in chapter 2 and using either increasing branch of the first stress ramp (to access the S-shaped flow curves) or increasing branch of the second ramp (to access monotonic flow curves not showing any hysteresis).

3.3 Effect of fiber-to-particle diameter ratio

The effect of the ratio D/d of the fiber diameter D to the CC particle diameter d , can be monitored by comparing the rheology of the mixtures containing PA or glass fibers of different diameters but roughly similar aspect ratio, recalling that both are considered as rigid in the considered stress range according to the evaluation of the effective stiffness (see chapter 2, section 2.1.3). Physically, the size ratio D/d together with the fiber volume fraction φ_f affects the average size of the pores formed by the fiber network. For the two extreme orientation states of the fibers, the average distance between aligned fibers and the mean pore size of randomly oriented fibers are both roughly equal to

$$h \approx \frac{D}{2} \sqrt{\frac{\pi}{\varphi_f}} \quad (3.2)$$

under the high aspect ratio ($r \gg 1$) and low concentration ($\varphi_f \ll 1$) limits [164, 165]. At the highest fiber volume fraction, $\varphi_f = 0.03$, for which the yield stress is still absent, the ratio

h/d of the average pore size to the CC particle diameter is on the order of 16 for PA fibers and 7 for the glass fibers.

The flow curves of the CC particle- fibers mixtures with addition of either PA or glass fibers are presented in Figure 3.3 for the CC volume fraction $\varphi_p = 0.64$ and for different volume fractions φ_f of fibers (including 0 corresponding to the CC suspension without fibers – black curve). Firstly, the flow curves obtained from the ascending branches of the first (Figure 3.3a) and second (Figure 3.3b) stress ramps are qualitatively similar to those already reported in Figure 3.2a for the suspension without addition of fibers. Second, we observe that the flow curves of the suspensions containing PA and glass fibers (respectively, red and blue curves in Figure 3.3) are quite close to each other and the difference between them falls into the range of the statistical error arising because of flow instability above DST transition. Such quasi-collapse of flow curves for two types of rigid fibers at nearly similar average aspect ratio ($r = 47$ for PA and $r = 40$ for glass fibers) is also observed for other fiber volume fractions (not shown here) and indicates that the DST behavior of CC-fibers mixtures is not considerably affected by the pore – to – particle size ratio, at least in the range $7 < h/d < 16$. This result does not support the hypothesis of Cwalina et al. [116] that the shear thickening enhancement by addition of large particles to a shear thickening matrix composed of small particles comes in part from the confinement of small particles in the space between the large ones. Quantitatively, numerical simulations of Bian et al. [166] predict a mild enhancement of shear thickening at $h/d = 16$ ($L_y = 8$ in their paper) but a substantial enhancement at $h/d = 8$, as inferred from Figure 5 of their paper. This is apparently not the case for our system because the hydrocluster model employed in their simulations is likely less relevant for the DST behavior of our system.

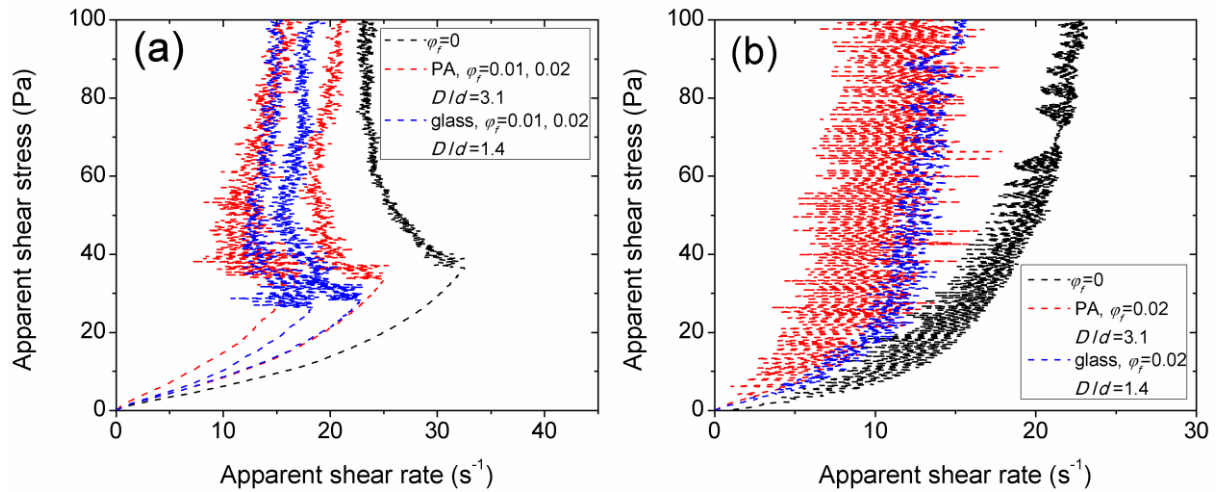


Figure 3.3 Effect of the ratio D/d of fiber – to CC particle diameter on the experimental flow curves of mixtures of isotropic-shaped (CC) particles and PA fibers (red curves) or glass fibers (blue curves) measured in mixer type geometry for CC particle volume fraction $\phi_p = 0.64$ and at different fiber volume fractions ϕ_f . The D/d ratio is 3.1 for PA fibers and 1.4 for glass fibers. Figures (a) and (b) correspond to the ascending branch of the flow curve during the 1st and the 2nd stress ramps, respectively. The black curves on both graphs stand to the flow curves of CC suspensions without fibers.

Since both types of fibers with different size ratios give quantitatively similar behavior, in what follows, we rule out the confinement effects induced by addition of fibers and, unless otherwise specified, focus our attention on the behavior of suspensions containing PA fibers.

3.4 Effect of fibers concentration

The flow curves of the CC-PA mixtures measured in double helix geometry are shown in Figure 3.4 for three CC volume fractions ϕ_p and for the ascending branch of the first stress ramp. For the sake of completeness, the flow curves for the second stress ramp of the CC-PA fiber mixtures are presented in Figure 3.11, while the flow curves for the both ramps on CC-glass fiber mixtures – in Figure 3.12 in Appendix F. Thick solid black lines represent predictions of the reduced shear rate (left column in Figure 3.4) and the homogenization (right column in Figure 3.4) models that will be presented in section 3.6. Extensive discussion on the degree of agreement between the models and experiments will also be presented in section 3.6.

As is seen in Figure 3.4, the flow curves shift to the left with increasing fiber concentration. As a consequence, the critical shear rate $\dot{\gamma}_c$ of the DST transition is progressively shifted to lower values, while the critical shear stress σ_c (see Figure 3.1 for definition of both $\dot{\gamma}_c$ and σ_c) remains roughly constant up to fiber volume fractions $\phi_f = 0.02$ but increases significantly at $\phi_f = 0.02$ for all CC concentrations ϕ_p . The flow curve and $\dot{\gamma}_c$ shift to lower shear rates points out to enhanced energy dissipation with addition of the fibers. As stated in chapter 1, the addition of fibers increases the viscosity of the CC-fiber mixture, therefore, the shear rate to reach the

critical stress of DST becomes lower, provided that this stress is nearly independent of the fiber volume fraction at $\varphi_f < 0.02$. This shift can also be interpreted in terms of local shear rates, as specified below, keeping in mind that both interpretations are essentially similar and consistent with the stress-controlled rheology. In fact, at the fixed shear stress, the local shear rate $\dot{\gamma}_{loc}$ in the shear thickening matrix between fibers is by definition higher than the global shear rate $\dot{\gamma}$ (measured by the rheometer through the rotational speed of the double helix tool). The global shear rate in the CC-fiber mixture is consequently lower than in the CC suspension without fibers at the same applied stress. Applied to the DST threshold, this reasoning stipulates that, if the DST occurs at the same shear stress (at $\varphi_f < 0.02$), it should be shifted to lower global shear rates. A variation of the critical stress with fiber concentration at $\varphi_f > 0.02$, does not change this qualitative conclusion. The quantitative dependencies of the critical shear rate and shear stress on the fibers concentration will be analyzed in detail in section. 3.6 in comparison with the models.

The increasing branch of the second stress ramp (Figure 3.11) gives oscillating but, in average, monotonous flow curves in agreement with the findings of section 3.2. Again, the flow curves are shifted to the left when the fibers concentration increases. Despite an average monotonic increase of these flow curves, they seem to become very steep at the applied stress on the order of $\sigma = 100$ Pa, and the slope increases with the fiber concentration. It is therefore important to check whether or not the suspension stress will diverge at some critical shear rate in rheological experiments conducted at controlled shear rate at the second shear rate ramp. In addition to it, the definition of the critical shear rate $\dot{\gamma}_c$ and critical shear stress σ_c of the DST at the controlled stress experiment (Figure 3.1) is sometimes subjected to uncertainties related to intermittent oscillations of the flow curve below the point where the sign of the flow curve slope changes to negative. It is therefore desirable to get a supplementary definition of $\dot{\gamma}_c$ and σ_c in controlled-rate experiments. These two aspects impose a separate study of the rheological response in controlled-rate mode.

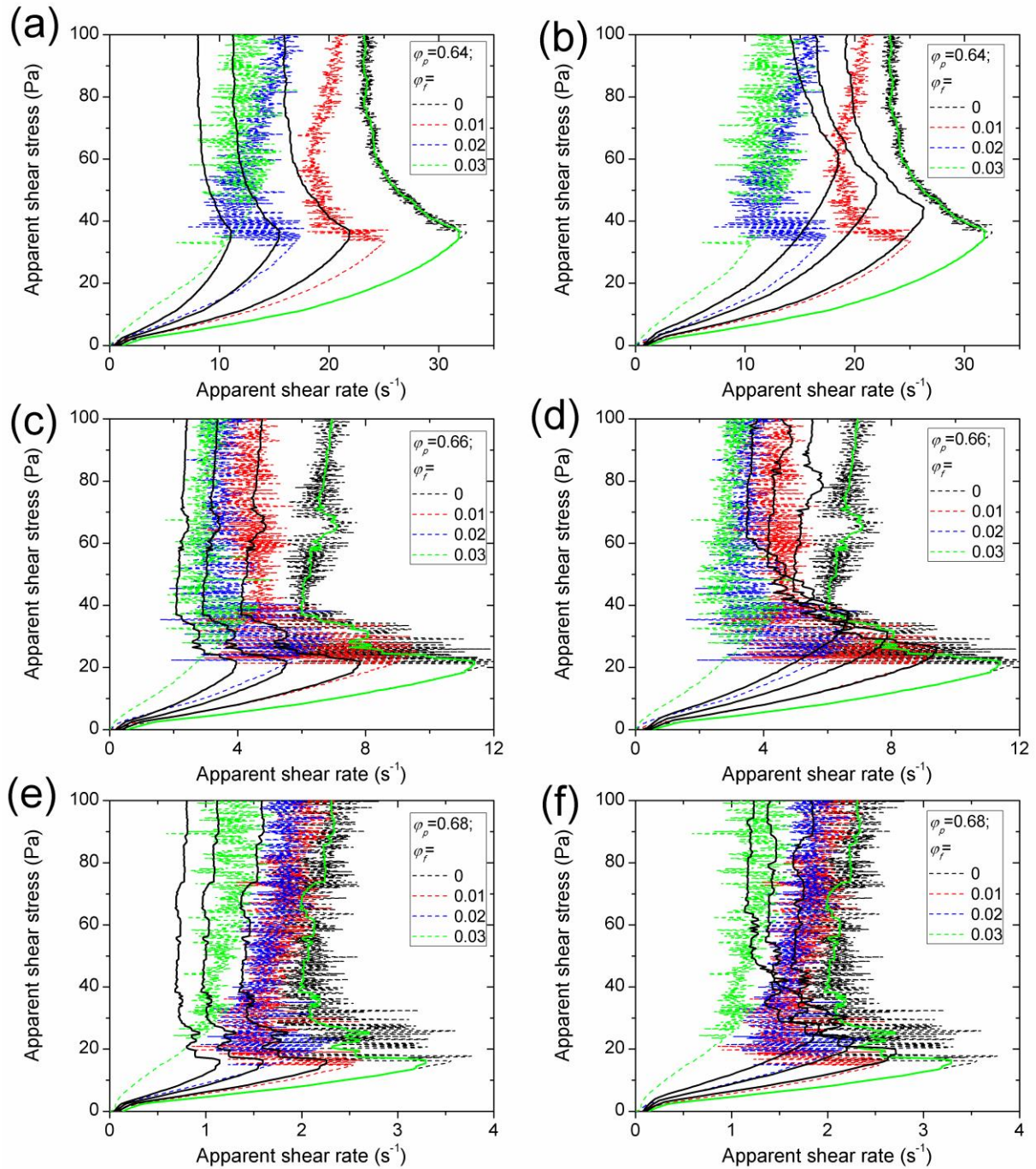


Figure 3.4 Effect of the fiber volume fraction on the flow curves of the mixtures of isotropic-shaped (CC) particles and PA fibers measured in the mixer type geometry for the ascending branch of the 1st stress ramp at different CC volume fractions. The first, the second and the third rows correspond to the CC volume fraction $\phi_p = 0.64$; 0.66 and 0.68 , respectively. Experimental flow curves on the left and right columns are identical for each row. Simulated flow curves using RSR and H-model and assuming isotropic fiber orientation ($A_{1212} = 1/15$) are plotted on the left and right columns, respectively. Thin dashed color curves correspond to experimental flow curves; thick solid black lines to predictions of both models [section 3.6], thick solid green line – to cubic spline interpolation of the experimental flow curve at $\phi_f = 0$. Labels “apparent” in the titles of axes recall that the reported shear rate and shear stress values stem from approximate rheometric conversions of the raw rheological data [chapter 2, section 2.2.1.2-A]

3.5 Controlled-rate versus controlled-stress response

Figure 3.5 compares the flow curves measured at applied shear stress (red curves) and applied shear rate (blue curves) for the suspensions containing PA fibers at volume fraction $\varphi_f = 0.02$ and CC particles at volume fraction $\varphi_p = 0.64$ or 0.68 . First of all, the rheological response stemming from the first and the second shear rate ramp (respectively left and right columns of Figure 3.5) are qualitatively similar and holds for subsequent ramps (not shown here). In particular, starting from some critical shear rate, the mixture exhibits either strong shear stress oscillations [at $\varphi_p = 0.64$, Figures 3.5 (a,b)] or an abrupt increase above the value of 3000 Pa at which the rheometer was ordered to stop the measurements (at $\varphi_p = 0.68$, Figure 3.5c,d). Both these behaviors point out to the DST transition in the rate-controlled mode observed for the first and the second shear rate ramps. Notice that the controlled-rate experiments allowed only ascending branch of the flow curve because strong stress oscillations above the DST transition caused the rheometer to stop once the maximal allowable stress of 3000 Pa was achieved.

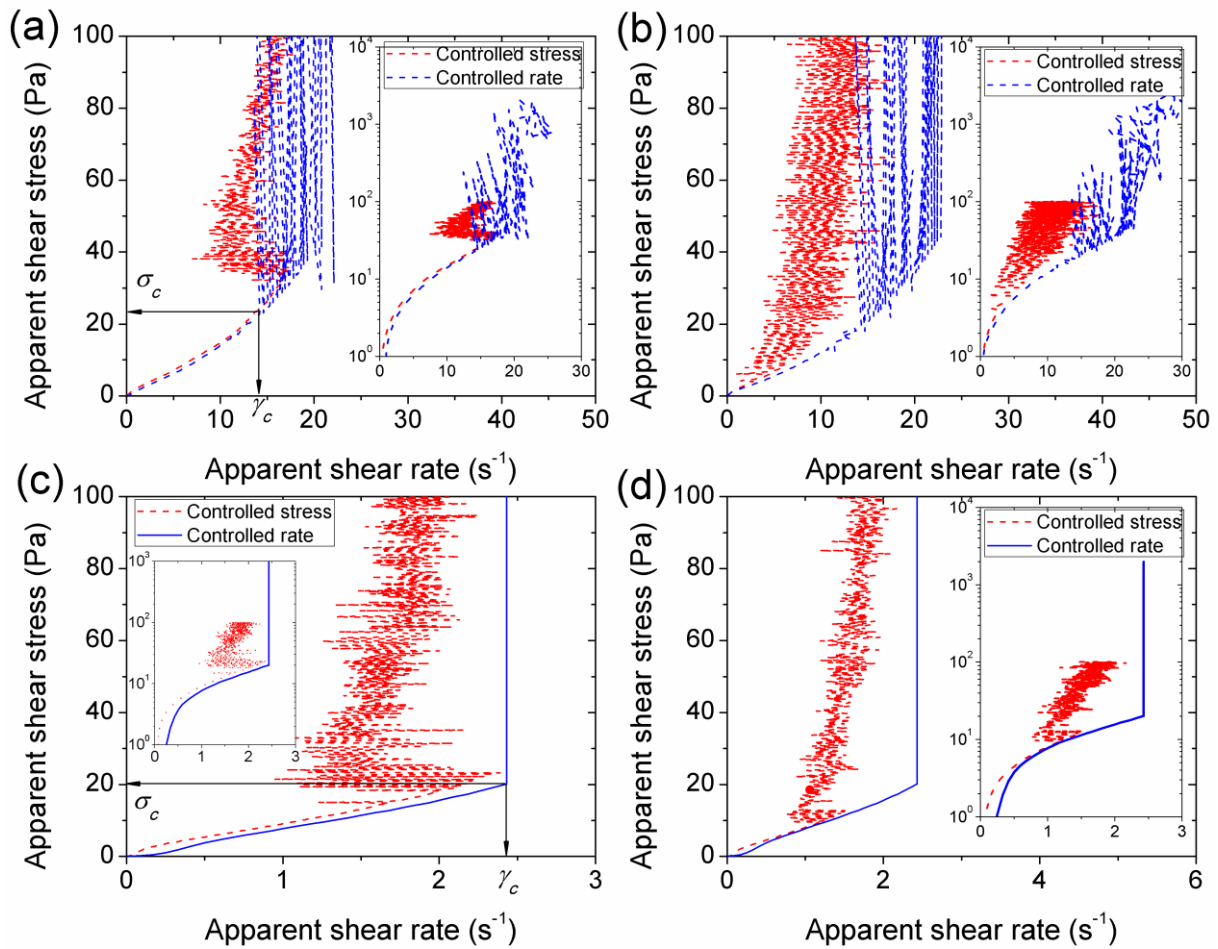


Figure 3.5 Effect of the rheometric mode (stress- or rate-controlled) on the experimental flow curves of the mixtures of isotropic (CC) particles and PA fibers measured in the mixer type geometry for PA volume fraction $\varphi_f = 0.02$ and for the CC particle volume fraction $\varphi_p = 0.64$ (a, b) and 0.68 (c, d). The left and the right columns of figures correspond to the ascending branches of the flow curve during the 1st and the 2nd stress or rate ramps, respectively. The insets on each graph show the flow curves in extended stress scale. The arrows in (a) and (c) show the definition of the critical shear rate $\dot{\gamma}_c$ and critical shear stress σ_c for the rate-controlled mode.

We define the critical shear rate $\dot{\gamma}_c$ and the critical shear stress σ_c for the strain-controlled mode at the point of the first abrupt increase of the shear stress (see arrows in Figures 3.5a and 5c), while $\dot{\gamma}_c$ and σ_c for the stress controlled mode are defined, as previously, at the point of the change of the sign of the flow curve slope (see arrows in Figure 3.1). Interestingly, the flow curves measured in the stress and rate-controlled modes coincide at low shear stress/shear rates, below the DST transition, while the critical values σ_c and $\dot{\gamma}_c$ seem to rather weakly depend on whether the stress or the rate are imposed. A quantitative analysis of the values σ_c and $\dot{\gamma}_c$ as function of CC and fiber concentrations will be presented in section 3.6. At this point, it is important to stress that the Anton Paar Physica MCR 301 rheometer is unable to reliably control the shear rate at fast dynamics of the samples. This results to non-vertical fluctuations of the shear stress above DST, as observed in insets of Figures 5 (a,b). Even though the stress values

above the DST cannot be considered safely, the onset of the DST transition is still reliably measured in the strain-controlled mode.

3.6 Reduced shear rate versus homogenization approach. Comparison with experiments

On the basis of the main experimental findings of section 3.3 and section 3.4, we can now develop models allowing a better and more quantitative understanding of the effect of fiber concentration on the DST transition of the mixtures of fibers with isotropic shaped particles. The objective of the models is to predict the flow curve of the CC-fiber mixtures on the basis of the experimental flow curves for the CC suspensions without fibers.

Assuming a perfect scale separation between CC particles and fibers, we consider that the fibers are dispersed in a shear thickening matrix – aqueous CC suspension – considered as a continuum with the rheology independent of the presence of fibers. Independence (within statistical errors) of the flow curves on the fiber – to – particle diameter ratio D/d is an argument in favor of the scale separation hypothesis, which however will be revisited in section 3.7 in conjunction to the jamming behavior. This hypothesis allows us to adapt the reduced shear rate (RSR) approach of Ohl and Gleissle [114] and the homogenization (H) approach of Château et al. [158], both developed for hard spheres dispersed in a non-Newtonian solvent. Both approaches employ essentially similar basic idea that the addition of particles to a non-Newtonian matrix induces higher local shear rates in the matrix at the same stress, and, consequently lower global shear rates in the suspension. Both models determine the local shear rate as function of the relative viscosity $\eta_r(\varphi)$ of a suspension of the same solid particles but dispersed in a Newtonian matrix at a given volume fraction φ . The models mainly differ in the way how these relationships are postulated. Furthermore, in the present case of CC-fiber mixtures, the relative shear viscosity is the function of both volume fraction φ_f and orientation of fibers, described by the shear component A_{1212} of the fourth-order orientation tensor (subscripts “1” and “2” stand for directions along the velocity and velocity gradient); the quantity A_{1212} is hereinafter called the orientation parameter.

The RSR-model relates the global (“macroscopic”) shear rate $\dot{\gamma}(\sigma)$ in the suspension to the (“reduced”) shear rate in the matrix $\dot{\gamma}_m(\sigma) = \dot{\gamma}(\sigma, \varphi_f = 0)$ through a proportionality factor (shift factor) is simply equal to the relative viscosity [114]:

$$\dot{\gamma}(\sigma) = \frac{\dot{\gamma}_m(\sigma)}{\eta_r(\varphi_f, A_{1212})} \quad (3.3)$$

The H-model relates $\dot{\gamma}(\sigma)$ to $\dot{\gamma}_m(\sigma)$ through the condition that the energy dissipation in the whole suspension is equal to the energy dissipation in the suspending matrix [158]. This approach initially developed for the rate-controlled rheology is adapted to the present case of the stress-controlled rheology. The details of derivation are provided in Appendix A, and the model predicts the following relationship:

$$\dot{\gamma}(\sigma) = \dot{\gamma}_m(\sigma_{loc}) \sqrt{\frac{1-\varphi_f}{\eta_r(\varphi_f, A_{1212})}} \quad (3.4)$$

$$\sigma_{loc} = \frac{\sigma}{\sqrt{(1-\varphi_f)\eta_r(\varphi_f, A_{1212})}} \quad (3.5)$$

where σ_{loc} is the local root mean square (RMS) shear stress in the suspending matrix, which is different from the macroscopic stress σ applied to the suspension boundaries because the applied stress is not uniformly distributed between the solid phase consisting of rigid fibers and the suspending matrix. The principal difference between σ_{loc} and σ is discussed in detail in Appendix G. The definition of the local shear stress is exact if the fibers are dispersed in a Newtonian matrix. Therefore, it is approximately valid for the CC-fibers mixtures below the critical stress of the DST transition, i.e. at $\sigma \leq \sigma_c$, where the matrix (pure CC suspension) shows approximately Newtonian behavior, as inferred from Figure 3.1. However, as shown in Appendix B, equation (3.5) remains approximately valid for the shear thickening matrix even above the DST transition, at $\sigma > \sigma_c$ where the flow curve becomes nearly vertical.

The relative viscosity $\eta_r(\varphi_f, A_{1212})$ of the suspension of fibers dispersed in a Newtonian matrix (glycerol) was measured in the double helix geometry [Appendix A, Figure 3.9]. The concentration behavior of η_r agrees relatively well with the phenomenological equation of Phan-Thien and Graham [167] [Eq. (3.14)] without adjustable parameters and with the fiber orientation nearly aligned with the flow and corresponding to the orientation parameter $A_{1212}^{LH} \approx 0.011$, as evaluated by Leal and Hinch model [168] [Eq. (3.15)].

The flow curves of CC-fiber mixtures can be constructed in parametric form $(\dot{\gamma}(\sigma), \sigma)$ using Eq. (3.3) for the RSR-model and Eq. (3.4) for the H-approach. To plot the flow curves predicted by the RSR model, we proceed as follows. Firstly, we smooth the fluctuations of the experimental flow curves of the CC suspensions ($\varphi_f = 0$) shown in Figure 3.1 using a median smoothing algorithm. Then, we interpolate the smoothed data by a continuous function $\dot{\gamma}_m(\sigma)$ using a cubic spline interpolation. Finally, we insert $\dot{\gamma}_m(\sigma)$ to Eq. (3.3) that allows us to construct theoretical flow curves of CC-fiber mixtures on the basis of an experimental flow

curve of the CC suspension without fibers. A similar procedure is used for the H-model, except that the argument σ in the interpolated function $\dot{\gamma}_m(\sigma)$ should be replaced by σ_{loc} [Eq. (3.5)] in order to get a continuous function $\dot{\gamma}_m(\sigma_{loc})$, which is used in Eq. (3.4).

As an example, in Figure 3.6, we plot experimental and computed flow curves (obtained from the ascending branch of the first stress ramp) of the CC-PA mixture at the CC volume fraction $\varphi_p = 0.66$ and the fiber volume fraction $\varphi_f = 0.02$. The predictions of the RSR- and H-models are presented in Figures 3.6 (a,b) respectively. In both figures, the thin dashed red curve represents experimental flow curve of the CC suspension without fibers at $\varphi_p = 0.66$ and the thick black curve is its cubic spline interpolation. The thin dashed blue curve represents the experimental flow curve of the CC-fiber mixture, while the thick solid red curve corresponds to the prediction of both models. The simulated flow curves appear to be far from the experimental ones but relatively close to the flow curve of the shear thickening matrix. This indicates that in the present form, both models strongly underestimate the viscous dissipation in the CC-fiber mixture.

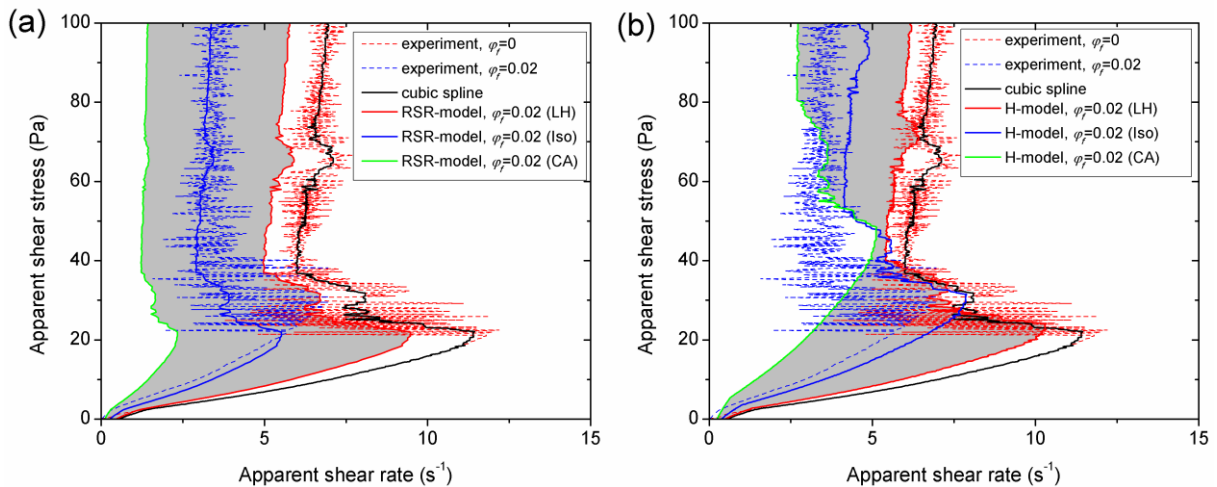


Figure 3.6 Comparison of experimental (thin dashed blue line) and simulated (thick solid red, blue and green lines) flow curves of the mixtures of isotropic (CC) particles and PA fibers for the ascending branch of the 1st stress ramp in the mixer type geometry for PA volume fraction $\varphi_f = 0.02$ and for the CC particle volume fraction $\varphi_p = 0.66$. The predictions of the RSR- and H-models are presented in (a) and (b), respectively. Abbreviations “LH”, “Iso” and “CA” in the figure legend stand for the fiber orientations aligned with the flow ($A_{1212} \approx 0.011$), random ($A_{1212} = 1/15$) and aligned along the compression axis ($A_{1212} = 1/4$), respectively. Thin dashed red and thick black solid curves are respectively experimental flow curve at $\varphi_f = 0\%$ vol, $\varphi_p = 0.66\%$ vol and its cubic spline interpolation. The shaded region in (a) and (b) corresponds to the domain between the lower and upper bounds of the prediction of each model.

The most intuitive reason for this discrepancy is that the orientation distribution of the fibers in the shear thickening matrix is likely very different from the nearly aligned state observed in the Newtonian matrix (like in our experiments with PA fibers suspended in glycerol, cf. Figure 3.9)

and described by Eq. (3.15). It is highly possible that the formation of transient clusters of CC particles below DST and the flow instability above DST strongly affect fiber dynamics and induce more isotropic fiber orientation. In the same vein, the network of frictional contacts between CC particles can make the fibers aligned along the main axis of this network, which is the compression axis of the shear flow, making the angle $-\pi/4$ with the flow direction [57]. The orientation parameter A_{1212} takes the following values for these two particular cases: $A_{1212}^{Iso} = 1/15$ and $A_{1212}^{CA} = 1/4$, where superscripts “*Iso*” and “*CA*” stand for “isotropic” and “compression axis”. The orientation state along the compression axis will be hereinafter denoted by CA-orientation for brevity.

To take into account a correct orientation distribution of fibers in shear thickening matrix, an appropriate value of A_{1212} should be used in Eq. (3.14) for the relative viscosity $\eta_r = f(\varphi_f, A_{1212})$, while computing the CC-fiber flow curve. The simulated flow curves of the CC-fiber mixture corresponding to both isotropic and CA orientation of fibers are added to Figures 3.6a and 3.6b by thick solid blue and green lines, respectively. The flow-aligned orientation provides the lowest relative viscosity η_r and predicts the smallest shift of the flow curve with addition of fibers (thick solid red line), while the CA-orientation provides the highest relative viscosity and the largest flow curve shift (thick solid green line). If the models are correct, the experimental flow curve (thin dashed blue line) should fit into the shaded space between lower and upper bounds of the models corresponding to the two limiting simulated flow curves. This is the case for the RSR-model but not completely true for the H-model (for which the experimental flow curve leaves the shaded region at intermediate stresses), at least for the particular set of volume fractions ($\varphi_p = 0.66$ and $\varphi_f = 0.02$) of the data presented in Figure 3.6.

To ensure the best agreement between the models and experiments, it would be possible to fit the experimental flow curves by adjusting the orientation parameter A_{1212} values in Eq. (3.14) for the relative viscosity $\eta_r(\varphi_f, A_{1212})$. However, we prefer comparing experimental flow curves with the model flow curves all calculated for a single fixed and physically relevant value of the orientation parameter, $A_{1212} = A_{1212}^{Iso} = 1/15$, corresponding to random fiber orientation, without necessity of any adjustable parameter. All the experimental flow curves of the CC-PA fiber mixtures shown in Figure 3.4 and Figure 3.11 are compared with the simulated ones (solid black lines), using the RSR-model (left columns) and the H-model (right columns). Thick solid green lines fitted to the experimental black flow curves of pure CC suspensions

stand for the cubic spline interpolation. The qualitative difference between predictions of both models is that the RSR-model leads to the same critical shear stress of the DST transition independently of the volume fraction of fibers, which is mainly supported by experiments for fiber volume fractions up to 0.02. In general, the RSR-model agrees better with experiments than the H-model at $\varphi_f \leq 0.02$. However, at higher volume fraction, $\varphi_f = 0.03$ it fails to predict substantial increase of the critical shear stress with respect to the one of the shear thickening matrix, while the H-model capture this increase, at least qualitatively. Furthermore, at each particle and fiber concentrations, the H-model provides better prediction of the monotonously growing flow curves measured at the 2nd stress ramp [Figure 3.11].

Let us now focus on the critical values of the shear stress and shear rate at the DST transition. Let σ_{c0} and $\dot{\gamma}_{c0}$ – critical shear stress and shear rate of the CC suspension without fibers. The critical value of $\dot{\gamma}_c$ for both models is obtained from Eqs. (3.3) and (3.4) by replacing $\dot{\gamma}$ by $\dot{\gamma}_c$ and $\dot{\gamma}_m$ by $\dot{\gamma}_{c0}$. The critical shear stress for the RSR-model is equal to that of the shear thickening matrix, since this model postulates only a horizontal shift of the flow curves. The critical shear stress for the H-model is obtained from Eq. (3.5) by expressing the applied global stress σ through the local stress σ_{loc} and then replacing σ_{loc} by σ_{c0} , and σ by σ_c . The final set of expressions covering both models read:

$$\dot{\gamma}_c = \begin{cases} \dot{\gamma}_{c0}/\eta_r(\varphi_f, A_{1212}), & \text{for RSR-model;} \\ \dot{\gamma}_{c0}\sqrt{(1-\varphi_f)}/\eta_r(\varphi_f, A_{1212}), & \text{for H-model;} \end{cases} \quad (3.6)$$

$$\sigma_c = \begin{cases} \sigma_{c0}, & \text{for RSR-model;} \\ \sigma_{c0}\sqrt{(1-\varphi_f)\eta_r(\varphi_f, A_{1212})}, & \text{for H-model.} \end{cases} \quad (3.7)$$

Thus, using the last two equations, the values of σ_c and $\dot{\gamma}_c$ can be calculated as function of the fiber volume fraction φ_f using experimental values of σ_{c0} and $\dot{\gamma}_{c0}$ obtained from controlled stress [section 3.1] or controlled strain [section 3.4] experiments on pure CC suspensions for a given CC volume fraction φ_p . Simulated and experimental dependencies $\dot{\gamma}_c(\varphi_f)$ and $\sigma_c(\varphi_f)$ are shown in Figures 3.7(a,b) respectively. Triangles and squares correspond to experimental values on CC-PA suspensions measured for the ascending branch of the 1st ramp in stress-controlled mode [Figure 3.4] and strain-controlled mode [Figure 3.5], respectively. Continuous and dashed black lines correspond to the prediction of the RSR- and H-models, respectively, for a single value of the orientation parameter $A_{1212} = A_{1212}^{Iso} = 1/15$ corresponding to the isotropic fiber orientation.

Firstly, a relatively good agreement, within the experimental statistical errors, is observed between two experimental modes of definition of the critical values σ_c and $\dot{\gamma}_c$. Secondly, the RSR and H-models give reasonable agreement with experimental values of the critical shear rate. The RSR-model systematically underestimates experimental $\dot{\gamma}_c$ values and the H-model overestimates them. As already mentioned, the RSR-model reproduces the independence of the critical stress on the fiber volume fraction at $\varphi_f \leq 0.02$, while the H-model predicts a continuous growth of σ_c with φ_f because it differentiates the average stress in the suspending matrix (local stress σ_{loc}) from the macroscopic applied stress σ and shifts the flow curves both vertically and horizontally, as clearly seen on the right column of Figure 3.4. However, this trend reverses at the highest considered fiber volume fraction $\varphi_f = 0.03$ for which the experimental values of σ_c are noticeably larger than the corresponding values σ_{c0} in the absence of fibers. The H-model seems to follow this increase, while the RSR-model is unable to capture it. The discrepancy between experiments and RSR-model becomes more dramatic at higher volume fractions, $\varphi_f > 0.03$, for which we observe the behaviors qualitatively different from those reported above. They cannot be reproduced at all by the RSR-model and need a separate analysis.

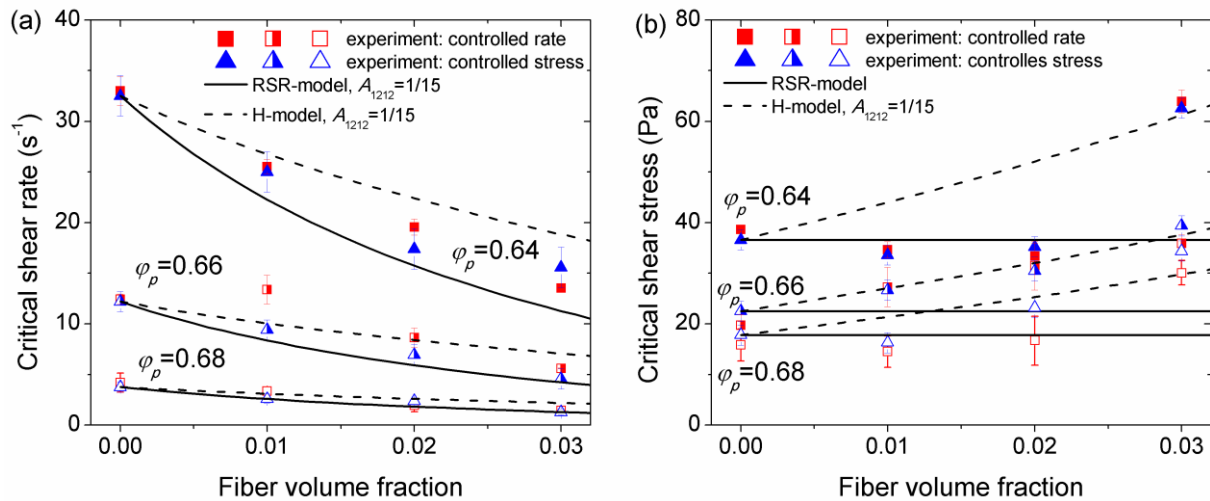


Figure 3.7 Simulated and experimental dependencies of the critical shear rate (a) and the critical shear stress (b) of the DST transition on the fiber volume fraction. Experimental data are drawn from the ascending branch of the 1st ramp of CC-PA mixtures, measured in stress controlled (triangles) and strain controlled (squares) modes. Continuous and dashed black lines correspond to the prediction of the RSR- and H-models, respectively, for the isotropic orientation distribution in all mixtures ($A_{1212} = 1/15$). The error bars correspond to the standard deviation of a few measurements realized for each given value of φ_p and φ_f .

3.7 Jamming behavior

Experimental flow curves of the CC-PA mixtures at fiber volume fraction $\varphi_f = 0.035$ and at different CC particle volume fractions φ_p are shown in Figure 3.8a for the ascending branch of the 1st (thin lines) and the 2nd (thick lines) stress ramps. During the 1st ramp, the flow curves show decreasing slope with increasing stress reminiscent to a shear thinning behavior (except for $\varphi_p = 0.68$), followed by an increasing slope with oscillations (shear thickening). The 2nd ramp is characterized by a threshold stress below which the mixture does not flow, referred to as a yield stress, and by stronger fluctuations above the yield stress as compared to the flow curve fluctuations of the 1st ramp. The subsequent stress ramps show the similar behavior to that of the 2nd ramp. As stated in section 3.2, the difference in behaviors of the 1st and the 2nd stress ramps could be attributed to CC particle migration which changes the rheology on local scale. Notice that, at the fiber volume fraction above $\varphi_f \geq 0.04$, it was impossible to make the CC-PA mixtures flow below the maximal achievable stress $\sigma = 3000\text{Pa}$ in our experiments with mixer type geometry. This indicates a jamming transition of the CC-PA mixtures at a critical fiber concentration $\varphi_f \approx 0.04$ independent of the CC particle concentration within the range $0.64 \leq \varphi_p \leq 0.68$ at which the shear thickening matrix (CC suspension alone) exhibits the DST transition. It is therefore believed that the combination of the yield stress and shear thickening at $\varphi_f = 0.035$ reflects a transient behavior between purely shear thickening behavior at $\varphi_f \leq 0.03$ and jamming behavior at $\varphi_f \geq 0.04$. Notice that the term “jamming transition” should not be confounded with the term “DST transition”, as the first one is hereinafter assigned to the liquid-solid transition at any small applied stress for particle concentrations near the compaction limit, while the second one is related to the liquid-solid transition above some non-zero critical stress at concentrations that can be well below the compaction limit.

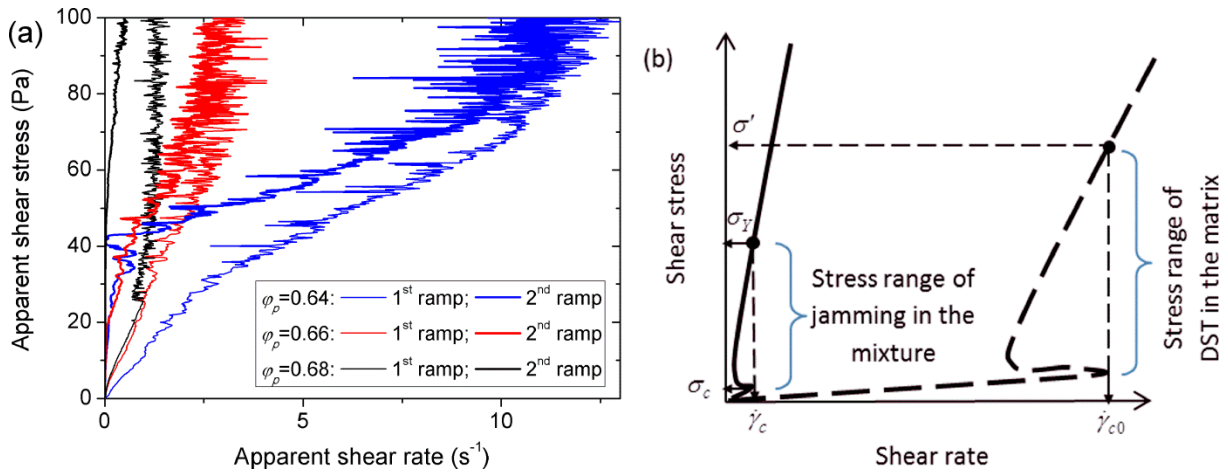


Figure 3.8 Experimental flow curves of the CC-PA mixtures at fiber volume fraction $\varphi_f = 0.035$ and at different CC particle volume fractions φ_p for the ascending branch of the 1st (thin lines) and the 2nd (thick lines) stress ramps (a). To explain jamming behavior of the CC-fiber mixtures at the fiber volume fractions $\varphi_f \geq 0.04$, a hypothetical flow curve of the CC-fiber mixture is schematically presented in (b) by a solid line. The flow curve of the pure CC suspension at the same CC volume fraction is schematically presented by a dashed line in (b). The critical shear rate $\dot{\gamma}_c$ in the concentrated CC-PA mixture is evaluated to be much lower than that, $\dot{\gamma}_{c0}$, in the pure CC suspension; while the yield stress σ_Y [Eq. (3.27)] of the CC-PA mixture is related to a specific value of the local stress in the gap between fibers, tentatively assigned to the upper critical stress σ' of the DST transition in pure CC suspension.

At this point, we try to find a physical mechanism for the jamming behavior at $\varphi_f \geq 0.04$. First, the jamming in a bimodal mixture of particles can simply occur due to a compaction limit imposed by geometrical constraints. Second, since the perfect scale separation between CC particles and PA fibers is not really fulfilled (even though confinement effects seem to be ruled out – cf. section 3.3), the jamming could arise as a result of excluded volume effects, as suggested by Madraki et al. [113] for bidisperse mixtures of spheres. These two effects are analyzed in detail in Appendix C. It is shown that the two scenarios predict that the jamming of the mixture strongly depends both on the particle volume fraction φ_p and on the fiber volume fraction φ_f , while in experiments it only depends on φ_f and independent of φ_p within the range $0.64 \leq \varphi_p \leq 0.68$. The jamming scenario respecting this experimental condition is related to the percolation threshold of the fiber network, which, to the first approximation, is expected to be independent of φ_p .

In more detail, when the fiber concentration achieves the percolation threshold φ_{perc} , the force applied at the boundary is transmitted through the small gaps between fibers (filled with shear thickening matrix). Due to small effective volumes of these gaps, and their small density in the suspensions of fibers as compared to spheres, the local stress in these gaps is expected to be much higher than the global (macroscopic) applied stress, as typically observed for the force chains in granular media [169]. Consequently, the shear thickening matrix can undergo the DST transition locally near the contact points at very small critical values of the global shear stress

σ_c and the global shear rate $\dot{\gamma}_c$ that are probably close to zero, as shown schematically on Figure 3.8b. At $\sigma > \sigma_c \approx 0$, extremely strong local viscosity of the shear thickening matrix between contact points solidifies the percolated fiber network, which hinders any flow. To fluidize the bridges between fibers and therefore to make the mixture flow, the stress level in shear thickening matrix near the inter-fiber contacts should at least overcome the upper critical stress of the DST, σ' , which is the upper stress value corresponding to the critical shear rate $\dot{\gamma}_{c0}$ in the shear thickening matrix [Figure 3.8b]. Thus, for the flow onset, one has to apply some (presumably high) global stress σ_Y (which can be considered as an apparent yield stress) corresponding to the local stress σ' . Below percolation threshold, $\varphi_f < \varphi_{perc}$, the fiber network does not span the rheometer gap facilitating the flow of the shear thickening matrix, while above the percolation threshold, $\varphi_f > \varphi_{perc}$, the fiber network is solidified by the shear thickening matrix leading to the jamming.

Evaluations of the percolation threshold φ_{perc} and of the stress levels σ_c , σ_Y are presented in Appendix D. Firstly, our experimental value of the jamming threshold $\varphi_f \approx 0.04$ fits to the predicted percolation threshold interval $0.015 \leq \varphi_{perc} \leq 0.115$. Secondly, the RSR-model does not differentiate the local and macroscopic stresses and predicts $\sigma_Y = \sigma'$, $\sigma_c = \sigma_{c0}$ and the values of $\dot{\gamma}_c$ going up to 8 s^{-1} at $\varphi_f = 0.04$; thus it cannot capture jamming behavior at $\varphi_f = 0.04$. On the contrary, the H-model is successfully extended to the case when the local stress is mainly concentrated within the gaps between fibers. Thirdly, the modified H-model shows that the critical shear rate and critical shear stress of the DST vary in the ranges $0.04 < \dot{\gamma}_c < 0.37 \text{ s}^{-1}$ and $0.8 < \sigma_c < 1.6 \text{ Pa}$ within the range of CC volume fractions $0.64 \leq \varphi_p \leq 0.68$ and at PA volume fraction $\varphi_f = 0.04$. At such small values of the lower bound of the jammed state, the mixture behaves as a solid with the apparent yield stress σ_Y estimated to be about 5 % of the upper critical stress σ' of the DST in the CC matrix: $\sigma_Y \approx 0.05\sigma'$. Unfortunately, we do not have access to experimental values of σ' [Figure 3.8b] because in most of the cases, the shear rate does not overcome the critical value $\dot{\gamma}_{c0}$ at the maximal achievable stress $\sigma = 3000 \text{ Pa}$. Using a high torque rheometer [170] it has been shown that the stress jump at the DST transition can achieve the values on the order of $\sigma' \sim 10^5 \text{ Pa}^2$. If so, the apparent yield stress can easily

² The upper DST threshold in the flows with free surface is usually defined through a capillary stress pushing the microparticles through the fluid/air interface, as will be explained in chapter 5. However, in the present case of

reach the values above the maximal achievable stress of the Anton Paar rheometer: $\sigma_Y > 3000$ Pa. Detailed experimental and theoretical studies on the mixture behavior near the fiber percolation threshold are required to confirm the above stated trends.

3.8 Conclusion

In this chapter, we have studied the effect of the fibers on the DST transition in the mixtures of isotropic-shaped CC particles and rigid (PA or glass) fibers. The chosen mixer type rheometric geometry provides only approximate conversions of the raw rheological data (torque and angular speed) to the shear stress and the shear rate; both latter quantities are considered as apparent. The mixtures are prepared by mixing the fibers at a desired volume fraction φ_f with the shear thickening matrix, which presents the suspension of micron-sized CC particles dispersed in water at a volume fraction φ_p and coated by a polymer brush of superplasticizer molecules. The DST behavior of the matrix is observed at CC volume fractions $\varphi_p \geq 0.64$ and is accompanied by irregular oscillations of the shear rate above the critical applied shear stress, σ_{c0} . The DST in the considered matrix is believed to be governed by the competition between the applied stress and the repulsive steric forces of the compressed polymer brushes. In mixer type rheometric geometry, the matrix exhibits thixotropic behavior manifested through evolution of the flow curve shape from the S-like to monotonous one likely due to CC particle migration towards the axis of symmetry of the mixer type geometry. Nevertheless, irregular shear rate oscillations persist even on monotonous branches of the flow curve.

The effect of the addition of rigid fibers to the shear thickening matrix can be summarized as follows:

1. Within the concentration range $0.01 \leq \varphi_f \leq 0.03$, the CC-fibers mixtures exhibit qualitatively similar rheological behavior as pure CC suspensions (S-shape of the flow curve, irregular oscillations, thixotropy). However, the DST is shifted to lower values of the critical shear rate $\dot{\gamma}_c$, while the critical shear stress σ_c remains essentially the same at $\varphi_f \leq 0.02$. This effect is explained by the fact that the addition of fibers increases the viscosity of the CC-fiber mixture, therefore, the shear rate to reach the critical stress of DST decreases. Such behavior is satisfactorily reproduced by the reduced shear rate (RSR) approach of Ohl and Gleissle [114]. At the fiber volume fraction, $\varphi_f = 0.03$, the critical shear stress exhibits a noticeable increase

local DST transition in the vicinity of fiber-fiber contact there is no really free surface through which the particles would tend to escape, so the definition of the upper DST threshold from physical grounds remains complicated

with respect to its value for the shear thickening matrix. This effect seems to be correctly reproduced by the homogenization (H) approach of Château et al. [158] adapted here for the stress-controlled rheology. However, more experimental points in the vicinity of the volume fraction $\varphi_f = 0.03$ need to be compared with the predictions of the H-model in order to confirm its performance. The H-model distinguishes the average local stress in the shear thickening matrix from the macroscopic shear stress applied on the suspension boundaries.

2. At higher concentrations of fibers, $\varphi_f = 0.035$, the behavior of the CC-fiber mixtures qualitatively changes and a yield stress, $\sigma_Y \approx 20$ Pa, appears at the descending branch of the 1st stress ramp and persists during ascending and descending branches of subsequent ramps. At $\varphi_f = 0.04$, the suspension is completely blocked and no any distinguishable shear was detected until the upper stress limit, $\sigma = 3000$ Pa, of the rheometer. These behaviors (yielding at $\varphi_f = 0.035$ and complete jamming at $\varphi_f = 0.04$) are independent of the volume fraction of isotropic-shaped particles within the range $0.64 \leq \varphi_p \leq 0.68$, where the matrix exhibits the DST. At such circumstances, the jamming is expected to arise at the percolation threshold of the fiber network, $\varphi_f = \varphi_{perc}$, with $0.7/r \leq \varphi_{perc} \leq \min(5.4/r, 0.35)$ [cf. Appendix D], nearly independent of the CC concentration φ_p . At percolation, any distinguishable global motion of the mixture is expected to lead to the levels of the local stress sufficient to produce DST localized in the vicinity of the contacts between fibers, thus solidifying the percolated fiber network. This idea is qualitatively supported by modified H-model, assuming that viscous dissipation mostly occurs in the vicinity of the contacts, while the RSR-model fails to capture jamming. Similar jamming behavior could be anticipated in bidisperse mixtures of spherical particles at the percolation threshold of large spheres ($\varphi_{perc} \sim 0.35$). However, the percolation network of spheres is likely more fragile than that of fibers because the network of spheres could be more or less easily layered by the applied stress.

3. Comparing predictive capabilities of the RSR and the H-models, it can be summarized that for the 1st stress ramp, the RSR-model gives much better predictions at the fiber volume fractions well below the percolation threshold of the fiber network, and the H-model performs much better near the percolation threshold. For the 2nd and subsequent stress ramps characterized by monotonous flow curves, the H-model gives closer predictions to experiments in the whole studied range of fiber volume fractions. We believe that the predictive capability of the H-model can be further improved by interpolating between two proposed definitions of the local stress [Eqs. (3.5) and (3.25)] at two different scales. However, we have to bear in mind

that none of these definitions, nor their combination is exact because of complex rheology of the shear thickening matrix.

4. It is difficult to conclude about the role of the fiber orientation without being able to control and visualize it. The flow-induced orientation and the DST behavior are expected to mutually affect each other. At this stage, on the basis of two proposed models, it can be anticipated that the critical shear rate of DST can vary in a wide interval depending on the orientation parameter A_{1212} , as long as the latter strongly affects the relative viscosity of the mixture. All the calculations in the present work were conducted for the random orientation state, ensuring semi-quantitative agreement with experiments without adjustable parameters.

5. Within statistical measurement errors and within the range $1.4 \leq D/d \leq 3.1$, the fiber-to-particle diameter ratio D/d seems not to affect the rheological response of the mixtures at nearly similar aspect ratio of PA ($r \approx 47$) and glass ($r \approx 40$) fibers. This allows us to rule out possible scenario of the DST enhancement by confinement of CC particles within the pores formed by the fiber network as the fiber volume fraction increases, as suggested in [116].

From the practical point of view, we have learned about physical limitations of the fluidity in bimodal mixtures. On the basis of the obtained results, standard ratios of the isotropic-shaped particles and fibers in cementitious composites could be revisited. In perspective, shear-induced microstructure of the considered bimodal mixtures has to be extensively studied through X-ray micro-tomography and particle level simulations. This will allow assessing the real fiber orientation distribution in shear thickening matrix, the spatial distribution of the contact network between isotropic-shaped particles and will allow checking the percolation-driven jamming scenario on the microscopic scale.

3.9 Appendices

Appendix A. Homogenization approach for the stress-controlled rheology

According to the original work of Château et al. [158], the suspension viscosity $\eta(\dot{\gamma})$ is assumed to be a product of the non-Newtonian matrix viscosity $\eta_m(\dot{\gamma}_{loc})$ taken at some local shear rate $\dot{\gamma}_{loc}$ and the relative viscosity $\eta_r(\varphi)$ of a suspension of the considered particles dispersed in a Newtonian solvent at particle volume fraction φ . In our case of the stress-controlled rheology, the shear thickening matrix viscosity should be taken at a local shear stress σ_{loc} , which results in

$$\eta(\sigma) = \eta_m(\sigma_{loc})\eta_r(\varphi_f) \quad (3.8)$$

where $\eta_r(\varphi_f)$ is the relative viscosity of a suspension of fibers dispersed in a Newtonian solvent at a given volume fraction φ_f .

By analogy with $\dot{\gamma}_{loc}$ defined in [158, 171], the local shear stress σ_{loc} can be evaluated as a root mean square (RMS) stress arising in a Newtonian solvent when the particle suspension (fibers dispersed in a Newtonian solvent) is subjected to flow of a given shear field. For the sake of simplicity, we assume a simple shear flow at a global shear rate $\dot{\gamma}$ and a global applied shear stress σ , and suppose that the interactions between fibers are solely defined by the rheology of the suspending matrix, while direct contact interactions between fibers are absent. As a consequence, the energy dissipation in the whole volume V of the suspension is equal to the viscous dissipation in the volume V_m of the Newtonian matrix, or rather:

$$\sigma\dot{\gamma}V = \iiint_{V_m} \sigma_{ik}\dot{\gamma}_{ik}dV \quad (3.9)$$

where subscripts “ ik ” denote the components of the local stress and the local rate-of-strain tensors along the coordinate axes $i = 1,2,3$ and $k = 1,2,3$. The global and local shear rates, $\dot{\gamma}$ and $\dot{\gamma}_{ik}$, in a Newtonian suspension of fibers can be related to the corresponding stresses σ and σ_{ik} , through the following obvious formulas:

$$\dot{\gamma} = \frac{\sigma}{\eta_N} = \frac{\sigma}{\eta_0\eta_r(\varphi_f)}; \quad \dot{\gamma}_{ik} \equiv \frac{1}{2} \left(\frac{\partial v_i}{\partial x_k} + \frac{\partial v_k}{\partial x_i} \right) = \frac{\sigma_{ik}}{2\eta_0} \quad (3.10)$$

where η_0 and $\eta_N = \eta_0\eta_r(\varphi_f)$ are viscosities of the Newtonian solvent and the Newtonian suspension of fibers, respectively. Substituting Eq. (3.10) into Eq. (3.9), and dividing by V , we get the following equation:

$$\frac{\sigma^2}{\eta_0\eta_r(\varphi_f)} = \frac{1}{V\eta_0} \iiint_{V_m} \frac{1}{2} \sigma_{ik}\sigma_{ik}dV = \frac{(1-\varphi_f)\sigma_{loc}^2}{\eta_0} \quad (3.11)$$

which gives us the final expression for the local (RMS) shear stress, as follows:

$$\sigma_{loc} \equiv \left(\frac{1}{V_m} \iiint_{V_m} \frac{1}{2} \sigma_{ik}\sigma_{ik}dV \right)^{1/2} = \frac{\sigma}{\sqrt{(1-\varphi_f)\eta_r(\varphi_f)}} \quad (3.12)$$

where we have used the following relationship: $V_m/V = 1 - \varphi_f$.

By putting the global shear stress in Eq. (3.12) equal to $\sigma = \eta_N\dot{\gamma} = \eta_0\eta_r(\varphi_f)\dot{\gamma}$ (as inferred from Eq. (3.10)), we easily check that the local RMS shear stress reduces to $\sigma_{loc} = \eta_0\dot{\gamma}_{loc}$, with the local RMS shear rate given by the following relationship derived in [171]:

$$\dot{\gamma}_{loc} = \dot{\gamma} \sqrt{\eta_r(\varphi_f)/(1 - \varphi_f)} \quad (3.13)$$

Thus, as expected, we obtain the local shear rate larger than the global one ($\dot{\gamma}_{loc} > \dot{\gamma}$). However, according to Eq. (3.12), the local stress is lower than the global one ($\sigma_{loc} < \sigma$). This can be explained by the fact that viscosity η_N appears to increase stronger with the volume fraction φ_f of fibers than the local shear rate $\dot{\gamma}_{loc}$, such that $\sigma_{loc} = \eta_0 \dot{\gamma}_{loc}(\varphi_f) < \sigma = \eta_N(\varphi_f) \dot{\gamma}$. Notice that the tendency reverses for the local shear stress defined on the scale of the small gaps between fibers in the vicinity of their contact points: $\sigma_{contact} > \sigma$ [cf. Eq. (3.25)].

The relative viscosity $\eta_r(\varphi_f)$ of the suspension of fibers dispersed in a Newtonian matrix can be found both experimentally and theoretically. To this purpose, using the mixer type geometry, we have measured the viscosity, η_N , of the suspension of PA fibers dispersed at different volume fractions φ_f in a glycerol ($\eta_0 = 2.41 \text{ Pa}\cdot\text{s}$). In the range of the applied stresses, $\sigma = 0 - 100 \text{ Pa}$, both glycerol and glycerol-fiber suspensions exhibited a Newtonian behavior and the concentration dependency of the relative viscosity $\eta_r(\varphi_f) = \eta_N(\varphi_f)/\eta_0$ is reported in Figure 3.9.

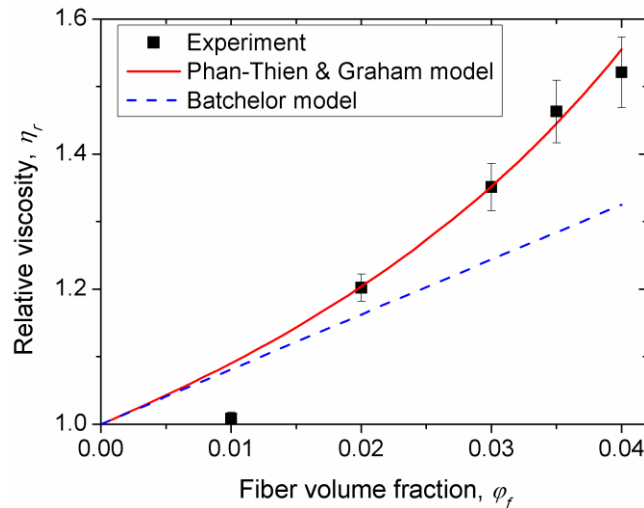


Figure 3.9 Relative viscosity η_r of the suspension of PA fibers dispersed in a Newtonian solvent (glycerin) as function of the fiber volume fraction φ_f . Points correspond to the experiment using in the mixer type geometry, solid lines to the predictions of Phan-Thien & Graham model [Eq. (3.14)] and Batchelor model.

The experimental data were well described by the phenomenological equation of Phan-Thien and Graham [167] without adjustable parameters:

$$\eta_r(\varphi_f) = 1 + 2\varphi_f + \frac{\varphi_f(2-\varphi_f/\varphi_{fm})}{(1-\varphi_f/\varphi_{fm})^2} \frac{f^{II}(r)}{3 \ln(2r)} r^2 A_{1212} \quad (3.14)$$

where $f^{II}(r) = (1 + 0.64\varepsilon)/(1 - 1.5\varepsilon) + 1.659\varepsilon^2$ is a correction factor in the slender body theory of Batchelor [172]; $\varepsilon = 1/\ln(2r)$; $\varphi_{fm} = 5.4/r$ is the maximum packing fraction of fibers taken at the upper concentration limit of granular suspension of fibers [12]; A_{1212} is the

orientation parameter, whose value is taken from the seminal work of Leal and Hinch [168] predicting the fiber orientation distribution nearly aligned with the shear flow under vanishing rotary diffusivity of fibers, $D_r \ll \dot{\gamma}/r^3$ (caused by inter-fiber collisions) and at the high aspect ratio limit $r \gg 1$:

$$A_{1212}^{LH} \approx 0.315/r_e \quad (3.15)$$

where the superscript “LH” stands for Leal and Hinch, and $r_e \approx 1.24r/\ln^{1/2} r$ is equivalent fiber aspect ratio introduced to account for an effect of the blunt shape of the fibers to their dynamics under applied shear [173]. Notice that the original Phan-Thien and Graham’s equation can be recovered replacing the factor $f^H(r)/(3 \ln(2r))$ in Eq. (3.14) by $1/(2(\ln(2r) - 1.5))$. The original Phan-Thien and Graham’s equation has been slightly modified in order to recover the dilute limit viscosity given by Batchelor [172] when keeping only the linear term on φ_f in Eq. (3.14). For the sake of completeness, predictions of these two models are shown in Figure 3.9.

Substituting Eq. (3.14) into Eq. (3.12), we get a complete definition of the local stress σ_{loc} . After that, the shear thickening matrix viscosity can be calculated as $\eta_m(\sigma_{loc}) = \sigma_{loc}/\dot{\gamma}_m(\sigma_{loc})$, where $\dot{\gamma}_m(\sigma_{loc})$ is the local RMS shear rate in a shear thickening matrix. Substituting this expression into Eq. (3.8) and making use of Eq. (3.12) allows us to evaluate the global shear rate of the CC-fiber mixture as function of $\dot{\gamma}_m(\sigma_{loc})$:

$$\dot{\gamma}(\sigma) = \frac{\sigma}{\eta(\sigma)} = \frac{\sigma}{\eta_m(\sigma_{loc})\eta_r(\varphi_f)} = \frac{\sigma\dot{\gamma}_m(\sigma_{loc})}{\sigma_{loc}\eta_r(\varphi_f)} = \dot{\gamma}_m(\sigma_{loc})\sqrt{\frac{1-\varphi_f}{\eta_r(\varphi_f)}} \quad (3.16)$$

Notice that the last equation can be easily obtained from Eq. (3.13) by replacing $\dot{\gamma}_{loc}$ by $\dot{\gamma}_m(\sigma_{loc})$.

Appendix B. Local stress above the DST transition in frames of the H-model

Above the DST transition, the shear rate in the shear thickening matrix usually exhibits relatively small variations, as the experimental flow curves in Figure 3.1 become nearly vertical, at least in the range of the local stress range $\sigma_{c0} < \sigma_{loc} < \sigma'$, with σ' being the upper critical stress of the DST in the matrix [Figure 3.8b]. Therefore, within the considered stress range, the local shear rate in the space between fibers is assumed to be almost constant and equal to the critical value $\dot{\gamma}_{c0}$, while the global shear rate in the whole mixture is also taken to be constant and equal to its critical value $\dot{\gamma} \approx \dot{\gamma}_c$. The dissipated power at nearly constant levels of the rate-of-strain tensor, $|\dot{\gamma}_{ik}| \approx \dot{\gamma}_{c0}$ in the space between fibers, can be very roughly evaluated as

follows: $\iiint_{V_m} \sigma_{ik} \dot{\gamma}_{ik} dV \sim \sigma_{loc} \dot{\gamma}_{c0} V_m$. The dissipated power in the whole mixture at nearly constant global shear rate $\dot{\gamma} \approx \dot{\gamma}_c$ is roughly equal to $\sigma \dot{\gamma}_c V$. Equating both power dissipations, we arrive to the approximate evaluation of the local stress above the DST transition:

$$\sigma_{loc} \approx \frac{\sigma \dot{\gamma}_c}{(1-\varphi_f) \dot{\gamma}_{c0}}, \text{ at } \sigma > \sigma_c \quad (3.17)$$

recalling that $V_m/V = 1 - \varphi_f$. Replacing now the critical shear rate $\dot{\gamma}_c$ by Eq. (3.6), we arrive at the final approximate expression for the local shear stress above DST transition:

$$\sigma_{loc} \approx \frac{\sigma}{\sqrt{(1-\varphi_f) \eta_r(\varphi_f, A_{1212})}}, \text{ at } \sigma > \sigma_c \quad (3.18)$$

which is similar to Eqs. (3.5) and (3.12) derived for the Newtonian matrix.

Appendix C. Geometric compaction limit and excluded volume effect in bimodal mixtures.

In this Appendix we evaluate the two following possible reasons of the jamming behavior in mixtures of isotropic-shaped particles and fibers:

(a) The geometric constraints in bimodal mixtures lead to the compaction limit depending on volume fractions φ_p and φ_f of both types of particles. The “geometric” compaction limit in a bimodal mixture is characterized by a compaction parameter Γ_m , which is the volume fraction of the whole solid phase in the mixture. Under hypothesis of perfect scale separation and using our definition of the volume fractions φ_p [Eq. (2.4)] and φ_f [Eq. (2.5)] this parameter is evaluated as follows [175]:

$$\Gamma_m = \min \left[\frac{\varphi_{fm}}{1-y_2}, \frac{\varphi_{pm}}{1-(1-\varphi_{pm})y_1} \right], \quad y_1 = \frac{\varphi_f}{\varphi_f + \varphi_p(1-\varphi_f)}, \quad y_2 = \frac{\varphi_p(1-\varphi_f)}{\varphi_f + \varphi_p(1-\varphi_f)} \quad (3.19)$$

where φ_{pm} is the maximum packing fraction of isotropic shaped CC particles taken as the packing fraction for frictional contacts $\varphi_{fr} = 0.69$ (as evaluated by fits of the CC suspension rheology to WC model – see Figure 3.10 and Appendix. E for details) and $\varphi_{fm} = 5.4/r$ is the maximum packing fraction of PA fibers taken at the upper concentration limit of granular suspension of fibers [Appendix A]. The compaction parameter Γ_m has to be compared to the experimental values of the concentration parameter $\Gamma_1 = \varphi_f + \varphi_p(1 - \varphi_f)$. It is shown that our experimental values Γ_1 are always below (at least by a value of 0.01) the values Γ_m of the compaction parameter. Thus, the jamming in our case arises at lower concentrations than those predicted by geometric effects.

Another concentration parameter was formulated by Martinie [174] for mixtures of cement particles with fibers: $\Gamma_2 = \varphi_f/\varphi_{fm} + \varphi_p(1 - \varphi_f)/\varphi_{pm}$. It was experimentally shown that high yield stress appeared in fresh cementitious materials at $\Gamma_2 \geq 0.8$, while the material did not exhibit yield behavior at $\Gamma_2 < 0.8$. In our experimental case, the concentration parameter fits to the range $1.0 \leq \Gamma_2 \leq 1.3$ for the CC-PA mixtures not exhibiting any yield stress. It can thus be concluded that the critical value of the parameter Γ_2 for our shear thickening mixtures is well above the value 0.8 for shear thinning cementitious materials. In any case the empirical parameter Γ_2 does not inform us about the nature of the jamming behavior.

(b) The excluded volume effects. They could arise as a result of finite size ratio of isotropic-shaped particles and fibers (imperfect scale separation). In fact, our bimodal mixture can be seen as the fiber network whose pores are filled by the suspension of smaller isotropic-shaped particles. Since the CC-particle size, d , is not infinitely smaller than the PA fiber diameter, D , a part of the pores presents a so-called dead volume non-occupied by CC particles. Thus, the true volume fraction φ_p^{true} of CC particles in the accessible zones of the pores will be higher than the apparent one, φ_p , evaluated by Eq. (2.5). Volume fraction φ_{dead} of the dead zones can be evaluated using the dilute limit ($\varphi_f \ll 1$) expansion of the model of Chatterjee [165]:

$$\varphi_{dead} \approx \varphi_f \left[\left(\frac{d}{D} \right)^2 + 2 \frac{d}{D} \right] \quad (3.20)$$

while the true volume fraction of CC-particles reads:

$$\varphi_p^{true} = \frac{\varphi_p}{1 - \varphi_{dead}} \approx \varphi_p \left[1 + \varphi_f \left(\left(\frac{d}{D} \right)^2 + 2 \frac{d}{D} \right) \right] \quad (3.21)$$

Evaluation shows that the true volume fraction of CC particles in accessible zones is by a factor 1.03 larger than the apparent one for fiber volume fraction $\varphi_f = 0.04$. At $\varphi_p = 0.68$, the true volume fraction $\varphi_p^{true} \approx 0.70$ rises above the packing limit of frictional contacts $\varphi_{fr} \approx 0.69$ (see Appendix. E), however at $\varphi_p = 0.64$ and 0.66, the true volume fraction is respectively $\varphi_p^{true} \approx 0.66$ and 0.68, thus remains well below the packing limit 0.69. Thus, the excluded volume effect introduced by Eqs. (3.20) and (3.21) cannot fully explain the jamming behavior at $\varphi_f = 0.04$.

Appendix D. Percolation threshold and stress levels for the percolated fiber network

The percolation threshold of the fiber network depends on the fiber orientation distribution. Since this distribution is unknown in our case, we consider two limiting cases of

isotropic and aligned fiber orientation. The minimal number Z of contacts per fiber at the percolation threshold has been evaluated by Balberg et al. [175] and is equal to $Z^{Iso} \approx 1.4$ and $Z^A \approx 2.8$ for isotropic and aligned orientation, respectively. An adequate relationship between Z and φ_f has been proposed by Toll [176]:

$$Z = 4\varphi_f \left(\frac{2f_1 r}{\pi} + f_2 + 1 \right) \quad (3.22)$$

where $f_1 = \langle |\sin \theta| \rangle$ and $f_2 = \langle |\cos \theta| \rangle$ are the scalar invariants depending on fiber orientation distribution and θ is the angle between fibers. For the two considered limiting cases, we get $f_1^{Iso} = \pi/4$, $f_2^{Iso} = 1/2$ and $f_1^A = 0$, $f_2^A = 1$. This allows finding the following expressions for the percolation threshold, the first of which is valid for the high aspect ratio limit $r \gg 1$:

$$\varphi_{perc}^{Iso} \approx \frac{0.7}{r} \quad (3.23)$$

$$\varphi_{perc}^A \approx 0.35 \quad (3.24)$$

Notice that Eq. (3.23) is the same as obtained by Philipse and Wierenga [177], while, for our fibers with aspect ratio $r \approx 47$ the concentration threshold given by Eq. (3.24) is higher than the upper concentration limit of granular suspension of fibers $\varphi_{fm} = 5.4/r$ [12]. Thus, the percolation threshold is expected to fit to the interval $0.7/r \leq \varphi_{perc} \leq \min(5.4/r, 0.35)$, that in our case gives $0.015 \leq \varphi_{perc} \leq 0.115$. Our experimental value of the jamming threshold $\varphi_f \approx 0.04$ fits to this interval.

The lower and upper stresses σ_c and σ_Y of the suspension jamming at the percolation threshold can be evaluated using a modified H-model. It is considered that, above the percolation threshold, the most important local stress and rate-of-strain levels arise in some small characteristic volumes $V_{contact}$ around contact points between fibers called hereinafter contact region volumes, while they are almost zero outside these volumes. The local rheology of the shear thickening matrix is supposed to be governed by a local stress $\sigma_{contact}$ averaged over the contact region volumes rather than by the stresses σ_{loc} averaged over the whole matrix volume, nor by the macroscopic applied stress σ . Under these assumptions, the viscous dissipation is mostly concentrated in the contact regions and the energy dissipation equality takes the form of Eq. (3.9), in which the integration domain V_m has to be replaced by $V_{contact}$. This allows us to immediately define the local stress by replacing in Eq. (3.5) the fraction $V_m/V = (1 - \varphi_f)$ of the whole mixture volume filled with the shear thickening matrix by the fraction $V_{contact}/V = \Phi_{contact}$ of the whole volume of the mixture occupied by the contact regions:

$$\sigma_{contact} = \frac{\sigma}{\sqrt{\eta_r(\varphi_f, A_{1212})\Phi_{contact}}} \quad (3.25)$$

Similar reasoning, as the one developed in Appendix B, allows showing that Eq. (3.25) remains approximately valid even above the DST transition within the local stress range, $\sigma_{c0} < \sigma_{contact} < \sigma'$.

Since the CC particles are expected to migrate from highly sheared zones near the solid contact between fibers to the periphery, the DST transition is expected to extend over the space between two fibers delimited by the projected area $D^2/\langle|\sin \theta|\rangle$ of one fiber onto the longitudinal cross-section of the second fiber. The average volume of a single contact region is $V_1 \approx D^3(1 - \pi/4)/\langle|\sin \theta|\rangle$, while the volume fraction of all contacts $\Phi_{contact}$ may be evaluated by multiplying the volume V_1 by the number density of contacts $n_{contact} = n_f^2 DL^2 \langle|\sin \theta|\rangle$ (with $n_f = 4\phi_f/(\pi D^2 L)$ being the number density of fibers) taken at high aspect ratio limit $r \gg 1$ [176], which gives.

$$\Phi_{contact} \approx \frac{16}{\pi^2} \left(1 - \frac{\pi}{4}\right) \varphi_f^2 \approx 0.35 \varphi_f^2 \quad (3.26)$$

As expected, the volume fraction $\Phi_{contact}$ of contact regions is proportional to the fiber volume fraction squared, φ_f^2 , similarly to the contact density $n_{contact}$. However, $\Phi_{contact}$ is independent of the fiber orientation distribution because lower contact density $n_{contact}$ for more aligned orientation is compensated by higher volumes V_1 of the single contact region, at least in high aspect ratio limit, $r \gg 1$. The prefactor at φ_f^2 could be different from 0.35 and its exact value depends on the length scale of the stress variation near the contact point.

Finally, the lower and upper bounds σ_c and σ_Y of the suspension jamming can be evaluated from Eq. (3.25) upon replacing $\sigma_{contact}$ by σ_{c0} or σ' , respectively, while the critical shear rate $\dot{\gamma}_c$ of the DST transition is obtained by dividing σ_c by the viscosity of the mixture. The final expressions for $\dot{\gamma}_c$ and σ_c are given by Eqs. (3.6) and (3.7) upon replacing $(1 - \varphi_f)$ by $\Phi_{contact}$, while the expression for σ_Y takes the following form:

$$\sigma_Y = \sigma' \sqrt{\eta_r(\varphi_f, A_{1212})\Phi_{contact}}, \quad (3.27)$$

where the relative viscosity of the fiber suspension $\eta_r(\varphi_f, A_{1212})$ is evaluated using Eq. (3.14) with the values of the orientation parameter $A_{1212} = A_{1212}^{Iso} = 1/15$ corresponding to the random orientation of fibers.

Appendix E. Wyart and Cates model

According to Wyart and Cates [107], the fraction f of frictional contacts is supposed to be a growing function of the shear stress. Various functional forms $f(\sigma)$ have been reported in literature and our analysis is not restricted to any of them. For the sake of demonstration, we choose the following empirical function $f(\sigma)$ that has been shown to correctly fit the rheological data of CC suspensions [Bossis et al. [160]]:

$$f(\sigma) = \left[1 + \exp\left(-\lambda\left(\frac{\sigma}{\sigma_0} - 1\right)\right) \right]^{-1} \quad (3.28)$$

where λ and σ_0 are two adjustable parameters, the latter of which being a characteristic stress above which the frictional contacts dominate over the lubricated ones. Typically, σ_0 is of the same order of magnitude that the critical stress σ_{c0} . The jamming volume fraction φ_j is supposed to be a sum of the packing fractions of particles in purely lubricated (φ_{Lub}) or purely frictional ($\varphi_{Fr} < \varphi_{Lub}$) regimes, weighed by the fractions $(1-f)$ and f of the lubricated and frictional contacts, respectively:

$$\varphi_j(\sigma) = \varphi_{Fr}f(\sigma) + \varphi_{Lub}(1 - f(\sigma)) \quad (3.29)$$

The suspension viscosity is given by an empirical Maron-Pierce law [10], in which the jamming volume fraction is a function of the applied stress:

$$\eta(\sigma) = \eta^* \left(1 - \frac{\varphi}{\varphi_j(\sigma)} \right)^{-2} \quad (3.30)$$

where η^* is some characteristic viscosity, which is not compulsorily equal to the solvent viscosity η_0 because Eq. (3.30) is only valid for the particle volume fractions φ relatively close to the lowest packing fraction φ_{Fr} ; thus η^* is taken as another adjustable parameter.

The shear rate as a function of the applied stress is finally obtained as $\dot{\gamma}(\sigma) = \sigma/\eta(\sigma)$, allowing simulation of the flow curves σ versus $\dot{\gamma}(\sigma)$. The experimental flow curves of pure CC suspensions shown in Figure 3.10 by dotted lines are fitted to the WC model using the following set of adjustable parameters: $\lambda = 10$, $\varphi_{Fr} = 0.69$, $\varphi_{Lub} = 0.72$, $\eta^* = 10 - 2 \text{ Pa}\cdot\text{s}$ taken the same for all the particle volume fractions φ_p , while distinct values of the characteristic stress were used for each particle volume fraction: $\sigma_0 = 50, 35, 25$ and 20 Pa for $\varphi_p = 0.62, 0.64, 0.66$ and 0.68 , respectively. Notice that the packing fractions as high as $\varphi_{Fr} = 0.69$ and $\varphi_{Lub} =$

0.72 stem from a polydispersity of the CC particles. The fitted flow curves are shown in Figure 3.10 by solid lines.

First, the model predicts that at $\varphi_p < \varphi_{Fr}$, in the whole range of the applied stress, $\sigma \in [0, +\infty)$, the flow curve must fit to an envelope delimited by two straight lines (branches) corresponding to the Newtonian viscosities of the suspension with purely lubricated ($f = 0$) and purely frictional ($f = 1$) inter-particle contacts, as shown by thick dashed lines in Figure 3.10 for $\varphi_p = 0.66$. Second, the theoretical flow curves fit reasonably well the experimental ones only below the DST transition. Above this transition, the WC model qualitatively captures a sigmodal shape of the flow curve but fails to predict the slope of the curve at high stress if a single set of parameters λ , φ_{Fr} , φ_{Lub} and η^* is used for all volume fractions φ_p . In other words, the experimental flow curves always cross the upper branch of the model. Such disagreement persists for any other tested shapes of the $f(\sigma)$ – functions [107,161] and using other variants of the WC model [106, 160]. The discrepancy likely comes from the fact that the granular flow at high shear stress is no longer Newtonian as supposed in the WC model.

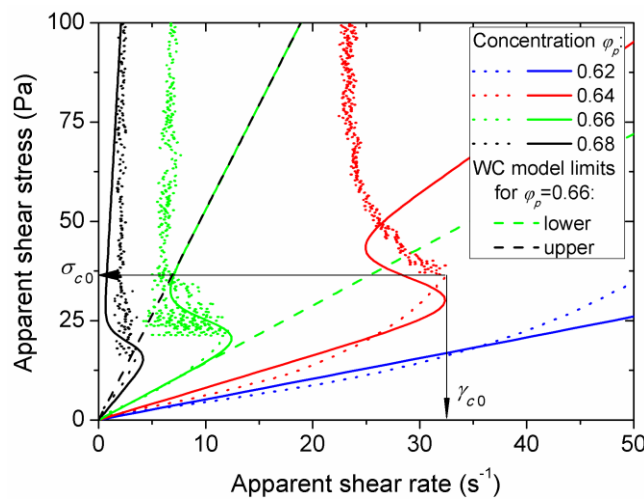


Figure 3.10 Flow curves of isotropic shaped particle (CC) suspensions at different volume fractions φ_p of CC particles measured in mixer type geometry. Dotted curves correspond to experiments; solid curves – to the fit of the experimental flow curves by the WC model applied to $\varphi_p = 0.66$. Notice that the black dashed line partially masks the upper branch (solid green curve) of the theoretical fit of the flow curve at $\varphi_p = 0.66$.

Appendix F. Complementary data on the rheology of the CC-fiber mixtures

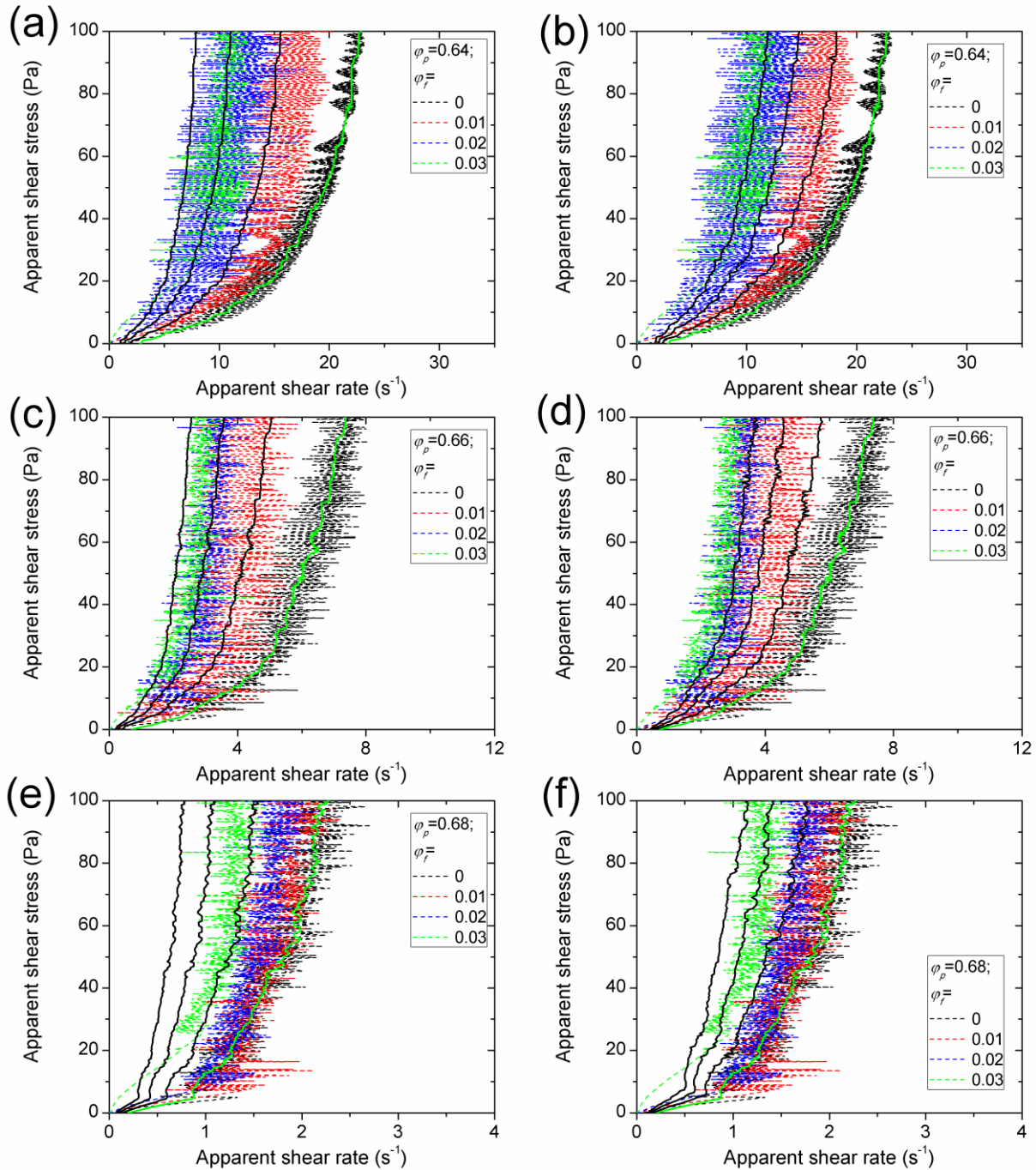


Figure 3.11 Effect of the fiber volume fraction on the flow curves of the mixtures of isotropic-shaped (CC) particles and PA fibers measured in the mixer type geometry for the ascending branch of the 2nd stress ramp at different CC volume fractions. The first, the second and the third rows correspond to the CC volume fraction $\varphi_p = 0.64$; 0.66 and 0.68, respectively. Experimental flow curves on the left and right columns are identical for each row. Simulated flow curves using RSR and H-model and assuming isotropic fiber orientation ($A_{1212} = 1/15$) are plotted on the left and right columns, respectively. Thin dashed color curves correspond to experimental flow curves; thick solid black lines – to predictions of both models [section 3.6], thick solid green line – to cubic spline interpolation of the experimental flow curve at $\varphi_f = 0$. Labels “apparent” in the titles of axes recall that the reported shear rate and shear stress values stem from approximate rheometric conversions of the raw rheological data (see Chapter 2, section 2.2.1.2-A)

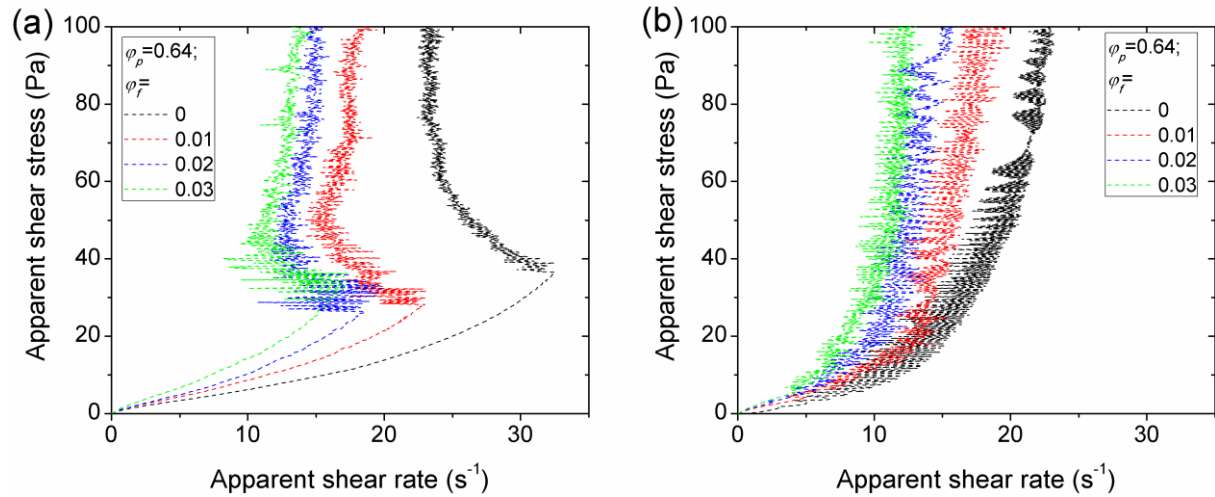


Figure 3.12 Effect of the fiber volume fraction ϕ_f on the flow curves of the mixtures of isotropic-shaped (CC) particles and glass fibers at CC volume fraction $\phi_p = 0.64$. The flow curves were measured in the mixer-type geometry in the stress-controlled mode and both ascending branch of the 1st stress ramp (a) or the 2nd ramp (b) are presented.

Appendix G. Local versus global shear rate and shear stress

In this Appendix, we show a principal difference between local and global shear rate as well as between local and global shear stress. To this purpose we would like first to clarify the strict definition of both the local shear rate and local shear stress independently of whether the stress or the rate are imposed at the boundaries of the system. We take the Batchelor's seminal work [172] as a basis considering the stress levels in a suspension of force-free rigid particles of an arbitrary shape dispersed in a Newtonian solvent at an arbitrary particle volume fraction ϕ (with allowance for hydrodynamic interactions between particles). The volume average of the rate-of-strain tensor $\dot{\gamma}_{ik}$ (global shear rate) is given by

$$\langle \dot{\gamma}_{ik} \rangle = \frac{1}{V} \int_V \dot{\gamma}_{ik} dV = \frac{1}{V} \int_{V_f} \dot{\gamma}_{ik} dV + \frac{1}{V} \sum_n \underbrace{\oint_{S_n} \frac{1}{2} (v_i n_k + v_k n_i) dS}_{=0 \text{ for rigid particles at no slip at particle surface}} = \frac{1}{V} \int_{V_f} \dot{\gamma}_{ik} dV \quad (3.31)$$

where V_f and V stand for the space domains occupied by the solvent and by the whole suspension respectively, the summation is conducted over all particles and the surface integral is taken over the surface S_n of the n 'th particle with \mathbf{n} being the outward unit vector normal to the particle surface and \mathbf{v} – the velocity vector (with respect to the laboratory reference frame) at the particle surface.

One may introduce the local shear rate in different ways. One possibility (not employed in the H-model, section 3.6) is the average shear rate \sum over the solvent volume:

$$\langle \dot{\gamma}_{ik}^{loc} \rangle = \frac{1}{V_f} \int_{V_f} \dot{\gamma}_{ik} dV = \frac{\langle \dot{\gamma}_{ik} \rangle}{1-\varphi} \quad (3.32)$$

Here we have made use of Eq. (3.31) and of the evident formula $V_f/V = 1 - \varphi$.

The volume averaged (global) stress is defined as $\langle \sigma_{ik} \rangle = \frac{1}{V} \int_V \sigma_{ik} dV$, and in simple shear flow (axes 1 and 2 stand for the velocity and velocity gradient directions) is found to be of the form [154]:

$$\langle \sigma_{12} \rangle = 2\eta_0 \langle \dot{\gamma}_{12} \rangle \eta_r(\varphi) \quad (3.33)$$

with $\langle \dot{\gamma}_{12} \rangle = \dot{\gamma}/2$ and $\eta_r(\varphi)$ - the relative viscosity depending on particle volume fraction. The exact correspondence of the volume average quantities $\langle \sigma_{12} \rangle$ and $2\langle \dot{\gamma}_{12} \rangle$ with the global stress $\sigma = F/S$ and global rate $\dot{\gamma} = v/h$ applied through the tangential force F and tangential velocity v on a surface S of a flat channel of a thickness h is easily checked by transformation of the volume integrals into surface integrals and integrating over the closed surface including channel walls.

Let us first define the local shear stress as the average stress over the solvent volume. Using the definition of the global shear rate [Eq. (3.31)], and using Eq. (3.33), we get:

$$\langle \sigma_{12}^{loc} \rangle = \frac{1}{V_f} \int_{V_f} 2\eta_0 \dot{\gamma}_{ik} dV = \frac{2\eta_0 \langle \dot{\gamma}_{12} \rangle}{1-\varphi} = \frac{\langle \sigma_{12} \rangle}{\eta_r(\varphi)(1-\varphi)} \quad (3.34)$$

The formulas (3.32) and (3.34) are exact for Newtonian solvents and for arbitrary particle shape and concentration, under condition of particle infinite rigidity. These formulas clearly show that, for given definitions, the local shear rate is different from the global one and the local shear stress is different from the global one, independently of whether the stress $\sigma = \langle \sigma_{12} \rangle$ or the rate $\dot{\gamma} = 2\langle \dot{\gamma}_{12} \rangle$ are applied on the suspension boundaries. The same conclusion is expected to hold for a non-Newtonian solvent and in the presence of non-hydrodynamic interactions.

Conversely, if the local average stress $\langle \sigma_{12}^{loc} \rangle = 2\eta_0 \langle \dot{\gamma}_{ik}^{loc} \rangle$ were equal to the global stress $\langle \sigma_{12} \rangle$, the relative viscosity of a Newtonian suspension would be always equal to $\eta_r(\varphi) = 1/(1 - \varphi)$, for any particle shapes and concentrations, as it can be easily shown with the help of Eqs. (3.32) and (3.33).

Other definitions of local shear rate and stress are possible. In particular, in their original paper, Château et al. [158] argue that root mean square (RMS) values are more relevant for describing

the local rheology in frames of the H-model. The RMS local shear stress and shear rate are formulated through Eqs. (3.12) and (3.13) and are also different from their global counterparts.

Notice that in many numerical simulations of stress-controlled rheology of shear thickening suspensions, the homogeneous shear stress is applied across the whole suspension and the shear field is retrieved from the relationship between the shear stress (constant over the simulation box) and its spatially varying components corresponding to frictional, hydrodynamic and repulsive interactions [106, 178]. The simulations provide a considerable insight into microscopic physics of the DST transition without real necessity of further improvement. However, from the experimental point of view, a constant (over time) tangential force (or torque) applied at one of the suspension boundaries would be a more relevant boundary condition that would allow for variations of both stress and shear rate over the suspension volume and would conduct to some difference between the local and global shear stress.

CHAPTER 4

4 Pressure driven flow of sphere-fiber mixtures through a capillary³

In this chapter, the DST transition of a CC-PA mixture is experimentally studied in a home-made capillary rheometer under a pressure imposed by compressed air. The description of the capillary geometry used is given in chapter 2 (section 2.2.2), while the suspension characterization and preparation protocol are provided in section 2.1. First, we inspect in section 4.1 whether the flow through a capillary is enough slow for the steady-state regime to be established during the suspension travel time along the capillary. Then, it is quite intuitive to qualitatively compare the rheological results obtained in the capillary rheometer with those previously obtained in a mixer type rheometry in chapter 3. However, as already stated, the flow fields are quite complicated in the double helix (DH) geometry, so comparison with the capillary rheometry results could become delicate (recall that the DH tool was used to avoid various artefacts and mimic the mixing process in cement industry). On the contrary, standardized cylindrical Couette geometry with roughened walls can be a good compromise for the quantitative rheological comparison, since the stress and the shear rate fields are simple and well characterized [see chapter 2, Eqs. (2.12), (2.13)], at the expense of possible particle sedimentation, which is completely ruled out in the DH mixer type geometry. In this context, we present the results of the cylindrical Couette rheometry in section 4.2, followed by the presentation of the capillary rheometry results in section 4.3 completed by the comparison between rheological responses in both rheometric configurations. The comparison of rheological responses in two different geometries allows an implicit check of the difference

³ The results of this chapter were obtained using CC particles of the 2nd series and can be compared with the results of the chapters 3 and 5 only qualitatively.

These results are included into the manuscript: [Meloussi et al. « Pressure-driven pipe flow of discontinuously shear thickening suspensions of isotropic shaped particles mixed with rigid fibers » under preparation]

between flow-induced microstructures developed in these geometries. As in chapter 3, we pay a special attention to the effects of the fiber volume fraction and orientation distribution on the DST transition of the sphere-fiber mixtures. Again, the fiber orientation effect is tested only implicitly through theoretical modeling of the flow curves using the homogenization approach (H-model described in detail in chapter 3) assuming different orientation distributions.

4.1 Transient behavior in capillary flow

In this section, we have to inspect whether at the constant imposed pressure difference the flow rate remains constant or gradually changing with time because of possible water evaporation / filtration / particle migration, or even more fluctuating with time because of the flow instabilities expected above the DST transition.

From the technical point of view, when the suspension is aspirated into the plexiglass cuvette of our imposed pressure capillary rheometer, the suspension is degassed due to the vacuum produced in the cuvette by the air suction process. In theory, if the cylindrical cuvette of the system is well isolated from the external atmosphere, there would be no evaporation of water from the suspension and therefore no change in the concentration of the CC-particles within the suspension tested in the capillary. On the other hand, we have already seen that when degassing the carbonate calcium suspension with a vacuum pump (chapter 2, section 2.2.1.2), an important amount of the water of the suspension evaporated, and this impacted the concentration of the particles in the suspension which increased after degassing and changed the rheology of the prepared suspension.

In our tests conducted in the capillary rheometer at imposed pressure, we have observed an increase of the slope of the collected mass versus time curves for a 68%-CC-suspension without PA-fibers (see Figure 4.1). This means that there is an increase of the mass flow rate through the capillary after a certain moment of time from the beginning of the experiment. This effect is frequently reproduced in the curves with the exception of few cases. This effect has also been observed for low as well as for high pressure applied in the capillary, like in the case represented in Figure 4.1, where $\Delta P = 0.2$ bar is equivalent to the wall shear stress of 62 Pa (see Eq. (2.22) in chapter 2). Therefore, this shear stress is well below the critical stress $\sigma_c = 122$ Pa for DST observed in rotational rheometry using the cylindrical Couette geometry (see Figure 4.2). Also, applied air pressure of $\Delta P = 0.9$ bar is equivalent to the wall shear stress of 222 Pa, well above the critical value $\sigma_c = 122$ Pa. This observed effect of increasing mass flow rate with time cannot in any way be explained by water evaporation, which would increase the particle volume

fraction along with the suspension viscosity and would consequently conduct to a decreasing flow rate with time at a fixed applied pressure.

The first scenario behind an increasing flow rate would suggest a liquid-solid phase separation in the suspension at some point of the experiment where the particles are pressed into the bottom of the cylindrical tank, and the liquid phase of the suspension filtrates through a porous plug formed by the particles immobilized in the tank at the capillary inlet. This is a rather extreme scenario suggesting that only a liquid phase (water) flows out from the capillary. In reality, we would expect a two-phase flow with the liquid phase developing higher average velocity through the capillary than the solid particle phase that is somehow slowed down by geometrical constriction at the capillary outlet (as often reported for granular flows through a funnel [179]). Because of slower convection of particles through the capillary inlet, some particle accumulation would be expected at the tank, which would be compensated by a decrease of the particle concentration in the capillary resulting in a progressive increase of the mass flow rate, as observed in Figure 4.1. Another possible scenario is related to particle migration towards the axis of symmetry of the capillary in the direction opposed to the shear rate gradient, as commonly observed for the shear-induced migration (cf. Sec. 1.2.2).

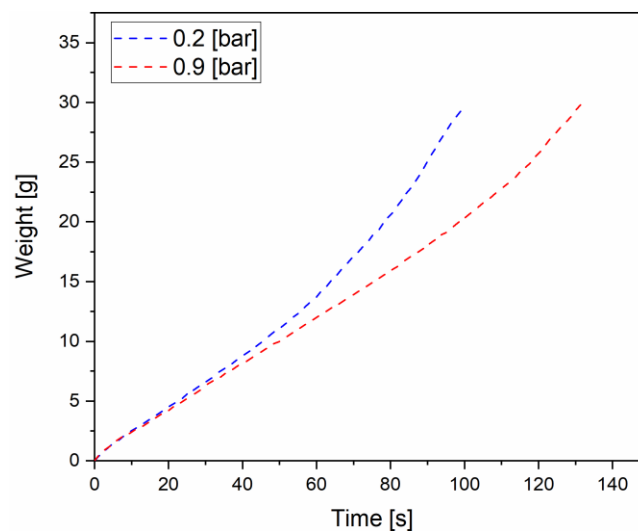


Figure 4.1 Mass versus time experimental dependencies for a flow of the CC-suspension at CC volume fraction of 68% vol and without PA-fibers.

To check the first (phase separation) scenario, we tried first to determine the particle concentration of the suspension flowing out from the capillary through drying it in an oven and weighing the dried particles. Unfortunately, this method was subject to large errors. So, we conducted a rheological experiment with the cylindrical Couette geometry for a CC-suspension

at 68% vol without PA-fibers that had just been flowed out from the capillary and collected on the top of a beaker placed onto the electronic balance.

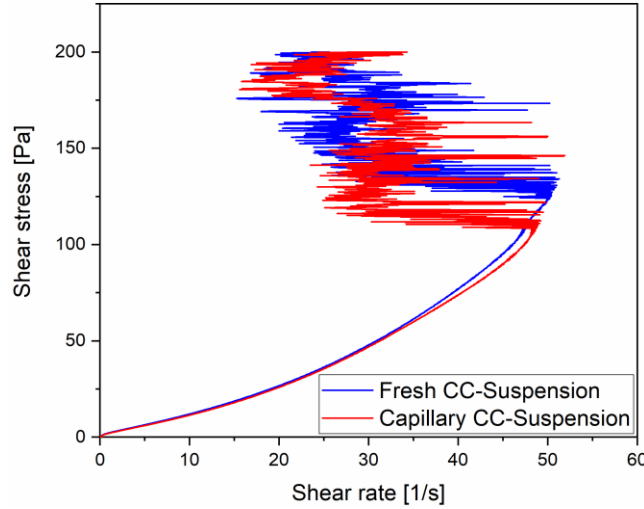


Figure 4.2 Rotational rheometry test of CC-suspensions at $\varphi_p = 68\%$ vol without PA-fibers: freshly prepared suspension against the suspension previously tested in the capillary rheometer.

The concentration test has demonstrated a coincidence (within statistical errors related to flow fluctuations) of both flow curves meaning that the concentration of the CC-suspension previously tested in the capillary rheometer did not change when compared to a freshly prepared one. This presumably excludes the two-phase flow scenario with a decelerated particle convection with the main flow along the tube. Indeed, by comparing two flow curves in Figure 4.2, we can claim that the suspension tested in rotational rheometer after the capillary test at imposed pressure $\Delta P = 1.5$ bar and equivalent wall shear stress $\sigma_w = 360$ Pa, is still of the same particles concentration despite we are well above the critical DST shear stress of 122 Pa.

Unfortunately, we cannot check experimentally the last scenario related to the particle migration. From the theoretical background, Bossis et al. [49], have shown that particle migration toward the capillary axis could significantly increase the flow rate at a constant applied pressure. The typical timescale of the shear-induced migration is on the order of

$$\tau_{migration} \approx \frac{1}{\dot{\gamma}_{a,w}} \left(\frac{D}{d_c} \right)^2, \text{ where } D \text{ and } d_c \text{ are respectively the capillary diameter and the length}$$

scale of the flow-induced particle clusters (or rather a space correlation length of the particle structures formed under shear in shear thickening suspensions). The cluster size is expected to continuously grow with the proportion f of frictional contacts (introduced into the Wyart and Cates model, cf. chapter 3, Appendix E) starting from the individual particle size, $d_c = D_p = 5.5 \mu m$ at $f = 0$ up to the capillary diameter, $d_c = D$ at $f = 1$ meaning complete percolation of the channel in the granular flow regime above DST. Since the proportion of frictional

contacts can already be non-negligible below the DST critical stress (as long as non-zero f values result in continuous shear thickening below the DST transition), d_c is expected to be comparable with D at any applied pressures (except the zero one), and it can be claimed that the characteristic migration time scale can become comparable with the travel time, $\tau_{travel} = \frac{\rho\pi D^2 L}{4Q_m} \approx 30 - 130$ s of the suspension along the capillary tube.

From the first glance, such a physics is expected to produce a stronger migration at higher stresses that would result in a stronger increase of the flow rate (and stronger deviation from linear mass-versus-time dependence) at $\Delta P = 0.9$ bar as compared to $\Delta P = 0.2$ bar. This is in stark contradiction with experimental results presented in Figure 4.1. The discrepancy could be tentatively explained through the fact that the particle migration is likely strongly damped if the particles are gathered to fully percolated contact network, as expected well above the DST transition ($\Delta P = 0.9$ bar) as opposed to non-percolated network below the DST (for $\Delta P = 0.2$ bar). Numerical simulations and X-ray microtomography should be conducted in future to further elucidate the suspension microstructure and better explain the origins of the unsteady flow.

To avoid any artefacts in interpretation of rheological data, we decided to calculate the mass flow rate (and consequently the apparent wall shear rate [see Eq. (2.23) in chapter 2]) as a slope at the origin of the mass versus time experimental curves, precisely at the first 10 collected measurement points corresponding to the first 10s of the experiment (the balance recording time is 1s), assuming a homogeneous particle concentration within the capillary at the beginning of the flow (at time $t = 0$). Flow rate definition at short times (a few seconds) since the moment of the pressure application should not be affected by neither transient rheological response of the suspension (related to the relaxation time of the frictional contacts; notice that the suspension was degassed excluding the transients related to the air bubble compression), nor the time response of the pressure increase in our capillary rheometer, being equal or slightly less than 1s. The time response of the suspension to the stress application was estimated by a supplementary rheometry test conducted in the cylindrical Couette geometry with the CC-suspension at 68% vol. The suspension was subjected to an instantaneous shear stress increase from 0 Pa to 300 Pa (the value above the critical stress $\sigma_c = 122$ Pa) and the characteristic time for the shear rate to reach a steady state value is evaluated to be about 1 s (see Figure 4.3).

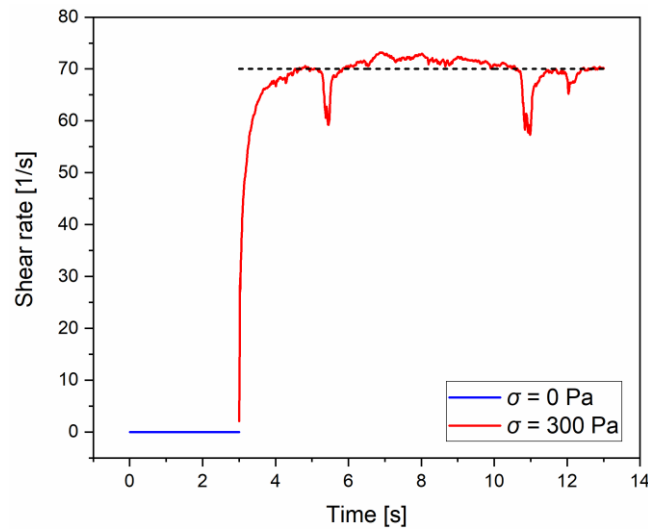


Figure 4.3 Time response to an applied stress of a CC-suspension at 68% vol without PA-fibers.

If the increase of the flow rate observed in Figure 4.1, is related to particles migration scenario, we can deduce that the characteristic time of migration (several dozens of seconds, see Figure 4.1) remains rather higher than the time (~ 1 s) to reach stationary flow regime (Figure 4.3). So, by taking the first 10 seconds (measurement points) of the mass versus time curves in our experiments, we already eliminate the initial transient artifacts but do not reach the migration process yet.

Noteworthy, whatever the applied pressure, the mass versus time dependencies never show any irregular fluctuation that are expected above the DST transition. However, this is not surprising taking into account the discrete nature of these measurements: the mass increment caused by each falling suspension drop (or even a part of a broken unstable jet – see chapter 5 for the details of the jet flows) is too large and “integrates” possible flow rate fluctuations. Thus, the measured mass flow rate and the apparent wall shear rate are some effective magnitudes likely corresponding to their time averaged fluctuating counterparts.

4.2 Shear rheometry in cylindrical Couette geometry

4.2.1 Flow curves

Flow curves of CC-PA fiber mixtures measured using cylindrical Couette geometry in rotational rheometer are depicted in Figures 4.4 (a,b). Flow curves $\sigma = f(\dot{\gamma})$ show a first regime of shear thickening of the suspension, where the slope increases steadily with the shear rate, this is called continuous shear thickening. Here the interparticle contacts of the suspension remain mostly lubricated and direct frictional contacts between particles are less present. The DST regime occurs above a critical value of the shear rate $\dot{\gamma}_C$ and the shear stress σ_C , the

viscosity of the suspension suddenly jumps to much higher values indicating that frictional contacts between suspension particles become dominant. In tribological studies, it is argued that frictional contacts do not always imply dry friction between particles but rather the very local proximity between the particles whose asperities are separated by the lubricating layer. The latter is strongly squeezed, and it loses its Newtonian character at nanoscale and develops a yield stress blocking tangential sliding motion of particles [180]. Thus, the particle-liquid-particle assembly forms an almost solid contact. This DST onset can be also a signature of the formation of a percolated network of particles and fibers, significantly increasing the viscosity of the suspension. After the establishment of the DST, the shear rate of the suspension has a non-zero value that constantly oscillates between a range of close values that can be explained by the effects of inertia of the rotating part of the rheometer [49], or, to a lesser extent, by the inertia of the fluid itself [181].

These flow curves also show an important progressive decrease of the critical shear rate at controlled shear stress with the increase of PA-fiber concentration in the CC-suspension. On the other hand, the critical shear stress slightly increases until the fiber volume fraction $\varphi_f = 2\%$ vol and considerably increases between $\varphi_f = 2\%$ vol and $\varphi_f = 2.5\%$ vol. As already mentioned in section 3.4 in chapter 3, the shift of the critical shear rate $\dot{\gamma}_C$ to lower values can be interpreted by the fact that at the fixed shear stress, the local shear rate $\dot{\gamma}_{loc}$ in the shear thickening matrix (aqueous CC-suspension) between the PA-fibers is higher than the global shear rate $\dot{\gamma}$ (related to the rotational speed of Couette inner cylinder). The global shear rate $\dot{\gamma}$ in the CC-PA fiber mixture is consequently lower than that of the CC-suspension without PA-fibers at the same applied shear stress, as already reported using two different rheometric geometries (double helix and plate-plate, cf. chapter 3).

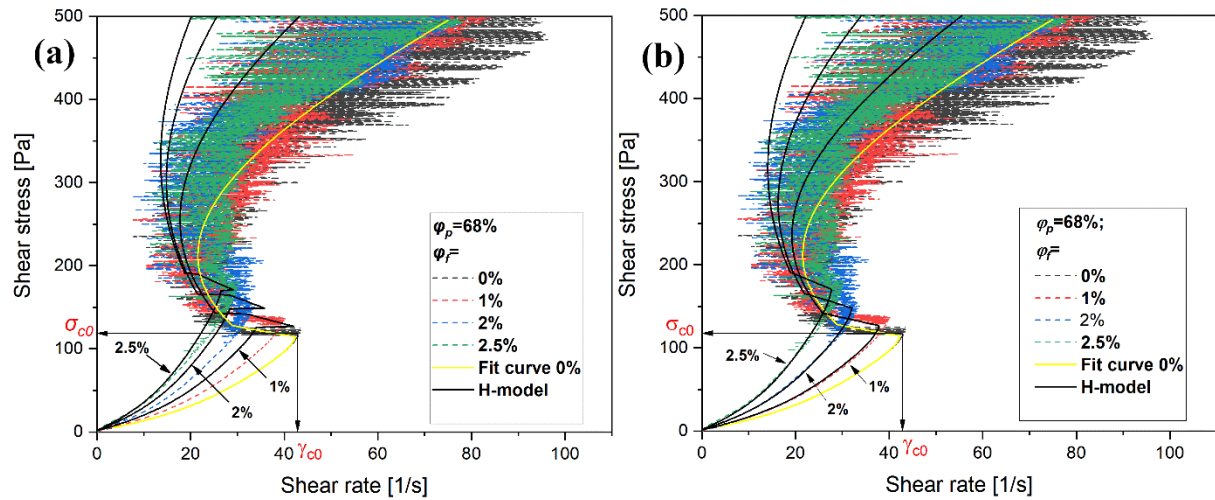


Figure 4.4 Experimental flow curves of CC-PA fiber mixtures in comparison with the theoretical predictions of the H-model: (a): Isotropic fibers orientation $A_{1212} = 1/15$; (b) A_{1212} being adjustable parameter (see Table 4.1). The solid yellow line is the fit of the experimental flow curve of the CC-suspension without PA-fibers, the solid black lines correspond to the theoretical predictions by the H-model to every corresponding fiber concentration. The horizontal and vertical black arrows indicate the critical shear rate and the critical stress of the experimental flow curve of the CC suspension without PA fibers.

Table 4.1 Adjustable values of the fiber orientation parameter A_{1212} corresponding to each fiber concentration.

Fiber concentration, (φ_f)	1%	2%	2.5%
A_{1212}	$1/30$	$1/23$	$1/17$

4.2.2 H-model predictions

We will now use a theoretical approach to predict the flow curves of the CC-PA fibers mixtures and compare them to the experimental curves conducted in the rheometer with the cylindrical Couette geometry. The H-model is based on the homogenization approach of Château et al [158], which has been adapted to the present case of stress-controlled rheology and rod-like particle shape, as detailed in section 3.6 and Appendix A of chapter 3. Recall that the model predicts the flow curves of CC-PA fiber mixtures from the flow curve of the CC-suspension without PA fibers, assuming a perfect scale separation between CC particles and PA fibers. PA fibers are considered to be dispersed in an aqueous CC suspension whose shear thickening rheology is independent of the presence of the fibers.

To plot the curves predicted by the H-model we proceeded by the following steps. First, we smoothed the experimental shear flow curve of the CC suspension without PA fibers, by calculating the arithmetic average using “numpy.mean” function in a Python script to reduce as much as possible the shear-rate fluctuations in the curves above the DST transition. With the data obtained from the smoothing, we made a segmental fit to the experimental curve using

polynomial functions and splitting the curve into three parts according to the applied shear stress profile in Figures 4.4 (a, b). The first region corresponds to the continuous shear thickening where the suspension exhibits nearly Newtonian behavior; the second region corresponds to a narrow stress range, $\sigma_c < \sigma < 1.05 \sigma_c$ in the vicinity of the DST transition, within which an abrupt decrease of the shear rate is observed; and the third region corresponds to the stresses $\sigma > 1.05 \sigma_c$ within which a smooth variation of the time averaged shear rate is observed. In this way, we obtain a continuous smoothed function $\dot{\gamma}_m = f(\sigma)$.

We established then a linear ramp of the stress from $\sigma = 0$ to $\sigma = 500$ Pa to deduce the local stress σ_{loc} as a function of the applied stress σ [see Eq. (3.5) in chapter 3]. Finally, by estimating the matrix shear rate as a function of the local shear stress $\dot{\gamma}_m(\sigma_{loc})$, we can find the global shear rate $\dot{\gamma}(\sigma)$ [Eq. (3.4)] and therefore we can plot the curves corresponding to the theoretical prediction (solid lines in Figure 4.4). As already stated in chapter 3, the fiber orientation distribution is unknown, because we are unable to neither measure it in opaque suspensions, nor predict it through the solution of the Fokker-Planck equation, in which the term corresponding to the interactions between fibers and the frictional contact network of CC particles is undefined. So, the orientation parameter A_{1212} (introduced in section 3.6 of chapter 3) is strictly speaking unknown. In this chapter, we will proceed by two following approaches. First, we will impose an isotropic fiber distribution with $A_{1212} = 1/15$, inspired from chapter 3 with the main argument that the complex flow field within the shear thickening matrix may randomize the fiber orientation. Second, we will fit the experimental flow curves using A_{1212} as an adjustable parameter, chosen within the range $0.315/r_e \leq A_{1212} \leq 1/4$, whose limits correspond to the nearly aligned orientation with the flow as given by Leal and Hinch [168] and the orientation along the compression axis of the shear flow, as suggested in section 3.6 of chapter 3. Recall that $r_e = 1.24r/\ln^{1/2}r$ is the equivalent fiber aspect ratio.

The experimental flow curves are compared to the theoretical ones obtained in Figure 4.4a for a fixed value of $A_{1212} = 1/15$ and in Figure 4.4b for adjustable A_{1212} values (see Table 4.1). We see that the H-Model predictions are in agreement with the experimental flow curves of CC-PA mixtures. However, an important difference can be noticed between the predicted curves where the fibers orientation is isotropic [Figure 4.4a] and the predicted curves where the orientation of the fibers is adjusted [Figure 4.4b]. First, an isotropic orientation of the fibers $A_{1212} = 1/15$, gives a higher relative viscosity in the CST as well as the DST regimes compared to the adjusted orientations and thus induces a shift of the theoretical curves to the left compared to the experimental curves. Secondly, from the observations in Figure 4.4a, it is

obvious that the isotropic orientation of the fibers fails to properly predict the transition zone between the CST and DST regimes which in contrary is not the case with the adjusted orientations. Therefore, we deduce that in our case, the PA-fiber orientation that best fits the experimental flow curves lies between nearly aligned with the flow $A_{1212} = \frac{0.315}{re} \approx 0.011$ and nearly isotropic orientation ($A_{1212} = 1/15$).

Now, we are interested in the variations of the critical shear rate and shear stress of the DST transition as a function of the fibers volume fraction. These variations are shown in Figure 4.5. The critical shear rate $\dot{\gamma}_c$ and shear stress σ_c are evaluated using Eqs. (3.6) and (3.7). (See chapter 3). The critical shear rate $\dot{\gamma}_{c0}$ and critical shear stress σ_{c0} of the DST transition for a CC- suspension without PA-fibers are depicted by horizontal and vertical arrows in Figure 4.4.

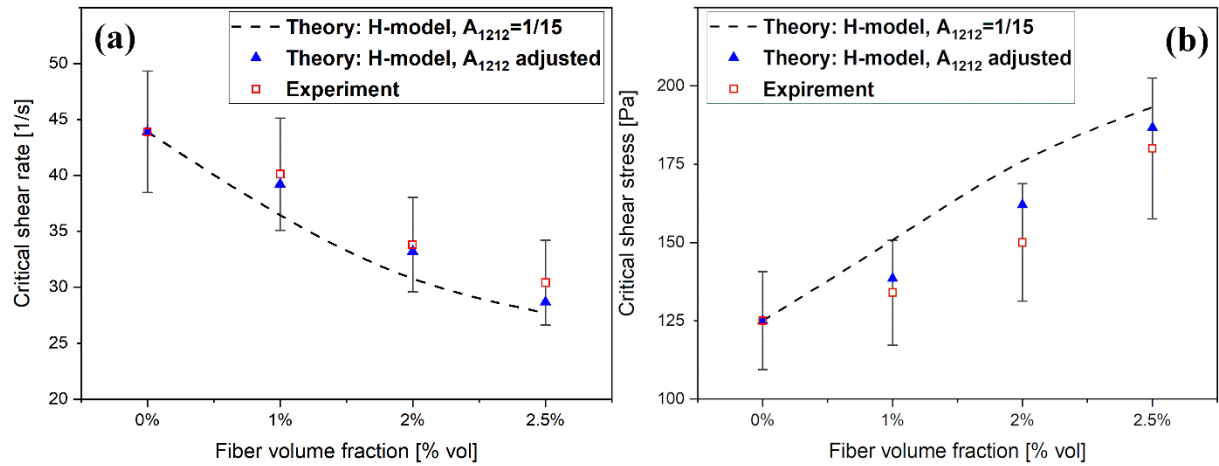


Figure 4.5 Variation of the critical shear rate and the critical stress as a function of fiber volume fraction. The red markers correspond to the experimental results. The blue markers (triangles) and the black dotted line represent the theoretical predictions of the H-model with respect to fiber orientation parameter A_{1212} . The error bars correspond to the standard deviation of experimental results.

The experimental findings in Figure 4.5 are in relative agreement with the theory. The H-model seems to underestimate the values of the critical shear rate and overestimates the critical shear stress for an isotropic fiber orientation $A_{1212} = 1/15$ within the CC-PA mixtures. However, the adjustment of the A_{1212} parameter according to previous mentioned values for the different fiber volume fractions gives a relatively good match with the experimental results. One can notice that in both cases of the experiment and theory, we do have nearly the same progressive decrease of the critical shear rate when increasing fiber volume fraction, in agreement with the interpretation given in section 4.2.1. In the case of the critical shear stress, the H-model predicts a faster increase with the fiber volume fraction, and this discrepancy with experiments is likely due to the very rough effective medium approach of the H-model.

4.3 Capillary rheometry

4.3.1 Flow curves

In this section, we present the results of the capillary rheometry experiments and compare them with the results of the rotational rheometry performed with the cylindrical Couette geometry, both using the same 2nd series sample of CC particles. The results are shown in Figure 4.6. Figures 4.6 (a-d) shows the experimental results of the CC-suspension without and with PA-fibers; these results are represented by solid blue points (diamond shape) for the capillary rheometry and by thin gray lines for the Couette geometry. The solid red line is a polynomial fit of the experimental shear flow curve (gray line) obtained in the cylindrical Couette geometry. In the experimental points of the capillary rheometry, the represented shear rate is the apparent wall shear rate $\dot{\gamma}_{a,w}$ [see Eq. (2.23) in chapter 2], so in order to compare with the rotational Couette rheometry, we had to apply the Mooney correction, i.e. to convert the real shear rate $\dot{\gamma}$ obtained in experiment using the cylindrical Couette geometry to the apparent wall shear rate for the capillary geometry using Eq. (2.24) (See chapter 2). Therefore, the solid green line in Figures 4.6 (a-d) corresponds to the curve $\sigma_w = f(\dot{\gamma}_{a,w})$ in the capillary rheometry obtained by integration of the smoothed experimental flow curve measured in rotational shear rheometry test [see Eq. (2.26) in chapter 2]. This curve is expected to coincide with the experimental flow curve of the capillary rheometry in the case when the capillary geometry does not induce a suspension microstructure different from the one observed in simple shear rheometry with the cylindrical Couette geometry. In what follows, this approach [quantified through Eq. (2.24) in chapter 2] will be referred to as the “macroscopic model”.

Figure 4.6e combines the experimental points of the capillary rheometry of CC- PA fiber mixtures at different volume fractions (from 0% to 2.5% vol) in comparison with the macroscopic model.

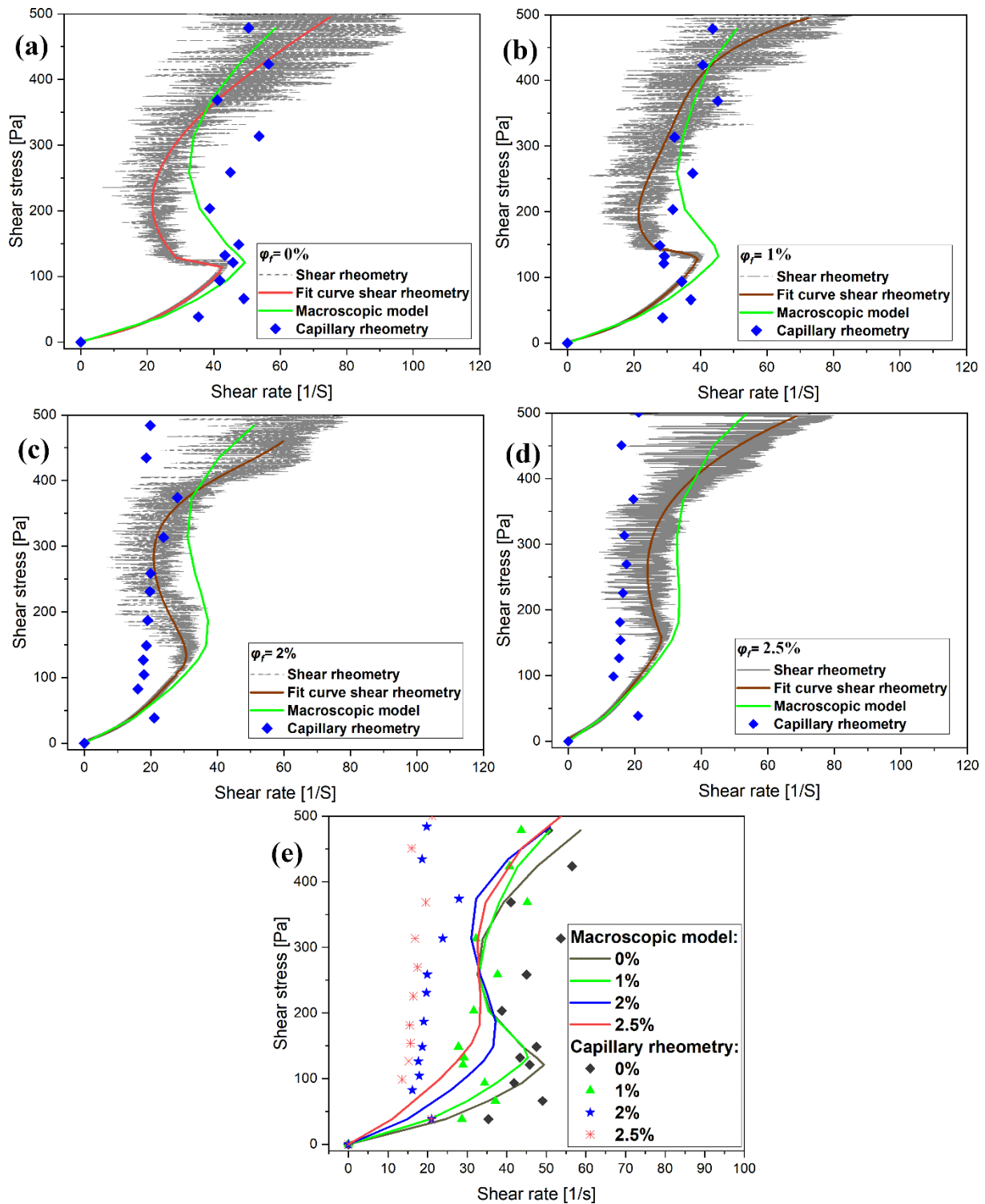


Figure 4.6 (a-d): Capillary rheometry in comparison with shear cylindrical Couette rheometry results and with the macroscopic model for CC-suspensions at different PA-fibers concentrations. (e): Capillary rheometry results in comparison with the macroscopic model for all fiber volume fractions.

The flow curve of the CC-suspension without PA-fibers in capillary rheometry exhibits a relatively similar rheology to that observed in shear rheometry [the sigmodal S-shape, Figure 4.6a]. Before the DST transition (where the regime is qualified as closed to a Newtonian one), the experimental points of the capillary rheometry are in a reasonable agreement with the shear

flow curve. Then we note a DST transition with critical shear stresses and critical shear rates values relatively close for both capillary and shear rheometry. Above the DST transition, strong fluctuations in shear rate are observed in both cases. Due to the very complex aspect of the CC shear thickening suspension after reaching DST domain, it is difficult to predict the behavior of the suspension in two different geometries, but still, it can be seen that the flow curve obtained in the capillary rheometry at $\varphi_f = 0\%$ (blue experimental points in Figure 4.6a) still fits to the fluctuation range of the shear rheometry curve (grey curve). The same statement holds for the fiber volume fraction $\varphi_f = 1\%$ vol, for which the experimental points of the capillary rheometry and the flow curve of the shear rheometry are also close below the DST transition and overlap above the DST transition stress [Figure 4.6b]. Furthermore, the curves of CC-suspension without PA-fibers and of CC-PA suspension at $\varphi_f = 1\%$ vol are close to the curves predicted by the macroscopic model (green lines) with a relatively small offset below the DST [Figures 4.6 (a, b, e)]. These observations suggest that for CC-PA mixtures at $\varphi_f \leq 1\%$ the suspension microstructure (in terms of the geometric and statistical characteristics of the CC-particle contact network and spatial and orientational organization of PA-fibers) likely remains similar in a pressure-driven flow through the capillary and in the drag shear flow between concentric cylinders.

The situation becomes completely different for the CC-PA mixtures at higher fiber volume fractions, $\varphi_f \geq 2\%$ vol. Moreover, for the flow curves at $\varphi_f = 2\%$ vol and $\varphi_f = 2.5\%$ vol, we have a rather different rheology [see Figures 4.6 (c,d)]: sigmodal shapes are not very apparent anymore and a significant difference between the capillary rheometry experiments and the prediction of the macroscopic model can be observed [Figure 4.6e], this difference can even be observed below the DST transition. Furthermore, the DST transition in capillary rheometry happened at a lower critical shear stress and shear rate than that predicted by the macroscopic model and, equivalently in shear rotational rheometry with small fluctuations in shear rate values above the DST transition as the curves appear to be almost vertical. At $\varphi_f \leq 1\%$ vol the difference between capillary rheometry and shear rheometry is rather small and noticeable however, at $\varphi_f \geq 2\%$ vol, this difference becomes very significant. This shift indicates that at a higher fiber volume fraction, the two different geometries imply two different rheological behaviors. Indeed, starting from fiber volume fraction $\varphi_f \geq 2\%$ vol, the microstructure of the suspension (CC-particle distribution, fiber orientation distribution) is different in the capillary flow compared to the shear flow. It is rather difficult to give a direct and clear explanation of the observable differences, but it is also likely that with increasing fiber volume fraction the

size and cohesive strength of the flow-induced cluster in the suspension is expected to increase. Large solid clusters are likely convected through the capillary along its axis of symmetry, their spinning under shear field is obstructed and they give a larger contribution to the energy dissipation as compared to the clusters that have better ability to rotate in the simple shear flow in the Couette geometry. In order to get more information about this observable microstructural difference as well as the flow-induced microstructure in the two considered geometries, an X-ray microtomography experiments for these mixtures must be involved in future works.

4.3.2 H-model predictions

We are going now to apply the homogenization approach to predict the flow curves of the CC-PA fiber mixtures in capillary rheometry from the experimental flow curve obtained in capillary rheometry with CC-suspension without PA-fibers. The same computational procedures described in section 4.2.2 were performed to plot the flow curves, and the obtained results are depicted in Figure 4.7.

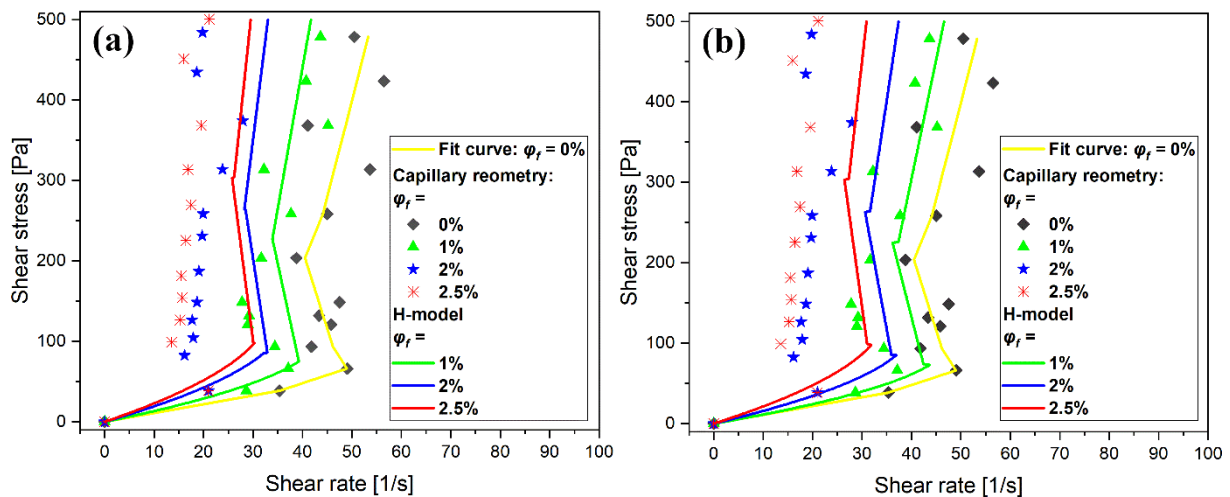


Figure 4.7 Flow curves in capillary geometry of CC-PA fiber mixtures predicted by the H-model in comparison with experiments. (a): $A_{1212} = 1/15$, isotropic fiber orientation. (b): The values of A_{1212} is adjustable and reported in Table 4.1 for each PA-fiber concentration. The diamonds represent the capillary flow experiments, and the colored solid lines are the theoretical predictions by the H-model.

The results of the H-model predictions are divided into two main parts, predictions with isotropic PA fiber orientation distribution ($A_{1212} = 1/15$) in Figure 4.7a and predictions with adjusted PA fiber orientation distribution (distribution between almost aligned with the flow and isotropic) in Figure 4.7b (see Table 4.1 for adjustable A_{1212} values). The curves with the isotropic orientation parameter ($A_{1212} = 1/15$) are smoother and capture the DST transition zone better this time compared to the curves with the adjusted fiber orientation parameter values (see Table 4.1) also the prediction curves with isotropic orientation are the closest to the experimental points of the capillary rheometry.

The theory succeeded very well in predicting the flow curve in the case of $\varphi_f = 1\%$ both before the DST and after the DST transition as we can clearly see that the capillary experimental points are close to the predicted curve in the DST region [Figures 4.7 (a, b)], however a very significant difference can be seen for the case of $\varphi_f \geq 2\%$, the theory fails to predict the flow curves at the DST regime in the case of an isotropic fiber distribution [Figure 4.7a] as well as for an adjustable orientation [Figure 4.7b], while the experimental points of the capillary rheometry for $\varphi_f \geq 2\%$ are scattered to the left of the predicted flow curves. This seems to indicate that the effective medium approach is not able to capture the changes in suspension structure in capillary rheometry induced by the addition of PA-fibers. Note that a strong disagreement of the flow curves with the H-model predictions for a PA-fiber concentration above a critical value of φ_f has already been observed for simple shear in mixing type rheometry [chapter 3, Figure 3.4]. It was explained by the percolation of the fiber network beyond the critical concentration; the shear thickening matrix experienced strong local stresses in the vicinity of the fiber contact and solidified the PA-fiber network even at low global stresses. This percolation threshold was $\varphi_{perc} \approx 4\%$ vol in simple shear. If for some reason, the percolation threshold becomes lower in capillary flow, this could in principle explain the near-vertical appearance of the experimental curves at $\varphi_f = 2\%$ vol and $\varphi_f = 2.5\%$ vol. We can assume that the orientation of the fibers could be more random in capillary flow ($A_{1212} \approx 1/15$) than in simple shear flow ($A_{1212} \approx 1/30$), this would lead to the percolation threshold $\varphi_f \approx 0.7/r = 0.015$ (1.5% vol). This alternative scenario, although does not contradict to the abrupt change in the rheology between $\varphi_f = 1\%$ and $\varphi_f = 2\%$, but leads to very small wall shear rates above the DST transition. Indeed, combining Eqs. (3.6), (3.7) and (3.26), we evaluate the critical shear rate and the critical shear stress for the fiber percolation scenario, as

$$\dot{\gamma}_c = \dot{\gamma}_{c0} \sqrt{\frac{\Phi_{contact}}{\eta_r(\varphi_f, A_{1212})}} \approx \frac{0.6\varphi_f \dot{\gamma}_{c0}}{\sqrt{\eta_r(\varphi_f, A_{1212})}} \quad (4.1)$$

$$\sigma_c = \sigma_{c0} \sqrt{\Phi_{contact} \eta_r(\varphi_f, A_{1212})} \approx 0.6\varphi_f \sigma_{c0} \sqrt{\eta_r(\varphi_f, A_{1212})} \quad (4.2)$$

that gives the critical values $\dot{\gamma}_c \approx 0.4 \text{ s}^{-1}$ and $\sigma_c \approx 2 \text{ Pa}$ at $\varphi_f = 2\%$ vol. These evaluated values appear to be well below the experimental ones. The discrepancy could come from underestimation of the volume fraction $\Phi_{contact}$ of the suspension involved into the “bridging” of neighboring fibers. At this point, it is therefore difficult to affirm any of both scenarios, i.e. whether the abrupt change of the flow curves at $\varphi_f \geq 2\%$ vol comes from microstructural

changes in CC particle network or in PA fiber network. It is very likely that the conformation of both networks is highly correlated at $\varphi_f \geq 2\%$ vol. At such condition, it is not surprising that neither macroscopic model, nor the H-model (assuming scale separation) are unable to correctly predict the rheological response of the mixture.

Let us now inspect the variations of the critical stress σ_c and critical shear rate $\dot{\gamma}_c$ of the DST transition as a function of PA-fiber volume fraction in the case of the capillary rheometry. The results are presented in Figure 4.8 along with the theoretical predictions of the H-model for two cases: an isotropic distribution ($A_{1212} = 1/15$) of the fibers in the mixture and a distribution intermediate between the one almost aligned with the flow and the isotropic orientation. In this second case, A_{1212} values are taken equal to those presented in Table 4.1 for the flow curves obtained in the Couette geometry.

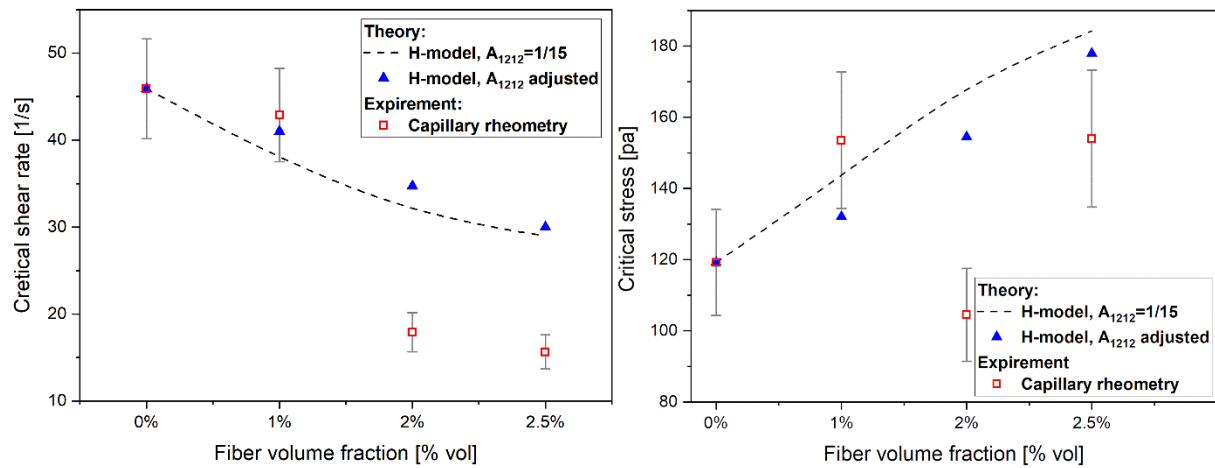


Figure 4.8 Critical shear rate (a) and critical stress (b) as a function of fiber volume fraction obtained in the capillary rheometry versus theoretical predictions by the H-model. The error bars correspond to standard deviation of experimental data.

A correspondence can be observed between the capillary rheometry experiments and the predictions by the H-model for the fiber volume fraction $\varphi_f = 1\%$ vol. However, the H-model overestimates the critical shear rate $\dot{\gamma}_c$ and critical stress σ_c at fiber volume fractions $\varphi_f = 2\%$ vol and $\varphi_f = 2.5\%$ vol. As indicated above, this abrupt change in σ_c and $\dot{\gamma}_c$ between the two PA-fiber volume fractions $\varphi_f = 1\%$ vol and 2% vol may be related to a considerable change of the microstructure of the interpenetrated CC particles and PA fibers networks. We also see the adjusted A_{1212} values do not significantly alter the correspondence between the H-model and experiments at $\varphi_f = 1\%$ vol, as compared to the single value $A_{1212} = 1/15$ used for isotropic fiber orientation.

4.4 Conclusion

In this chapter we have evaluated first the effect of PA-fibers on the DST transition in CC-PA mixtures, in a pressure-driven flow through a capillary and compared it to rotational rheometry using the classical cylindrical Couette geometry.

Qualitatively, in these both rheometric configurations, we have noticed that an increase in the volume fraction of PA-fibers induces a shift in the shear stress vs. shear rate flow curves of the CC-PA fiber mixtures with the critical shear rate of the DST transition decreasing and the critical shear stress increasing with the increase of PA-fiber volume fraction. Quantitatively, the flow curves obtained in the capillary and cylindrical Couette geometries were quite close to each other at zero and low fiber volume fraction, $\varphi_f = 1\%$ vol, which was interpreted in terms of a similar flow-induced microstructure in both geometries. On the contrary, at higher fiber volume fractions, $\varphi_f = 2\%$ vol and 2.5% vol, the flow curves of the capillary rheometry showed a much stronger viscosity (lower shear rates at a given shear stress) than in the drag flow in cylindrical Couette geometry. This difference suggests a strong difference of the suspension microstructure that can be assigned to stronger cohesive strength of the interpenetrated fiber and CC particle networks with possible percolation phenomena. The homogenization approach (H-model) and the macroscopic model (simply based on the integration of the local rheological relationship across the capillary cross-section) gave a correct prediction of the flow curves only at $\varphi_f = 1\%$ vol, the case for which the suspension microstructure was assumed to be independent of the flow geometry. However, both models failed, to a larger extent, to reproduce the experimental flow curves at $\varphi_f \geq 2\%$, without considering microstructural aspects.

For a deeper understanding of the rheological differences observed in both rotational and capillary geometries, it would be necessary to visualize the structure of the suspension under flow. This could in principle be achieved by X-ray microtomography at appropriately chosen spatial and temporal resolutions. A Stokesian dynamics modeling would also be useful to understand the system behavior.

Recall that unfortunately, we cannot provide a quantitative comparison of the rheological results obtained in capillary and Couette geometries (present chapter) with those obtained in double helix and plate-plate geometries (chapter 3) because different series of CC particles were used for these two rheometric pairs. However, the qualitative rheological behaviors remain similar in all the four geometries: the S-shape of the flow curves; shear rate fluctuations above

the DST; the shift of the critical DST shear rate to lower values with addition of fibers; much stronger jamming above a critical volume fraction of fibers tentatively explained in terms of the percolation of the fiber network.

CHAPTER 5

5 Jet flow and jet instability of sphere-fiber mixtures⁴

Shear rheological response of CC-PA mixtures has been reported in detail in chapters 3 and 4. It is time now to inspect the rheological behavior in extensional flow that is done in the present chapter on an example of the free-falling jet of the CC-PA mixtures flowing out from a cylindrical capillary under gravity. We warrant the reader that, in contrast to previous chapters, in the present chapter, we will mostly focus our attention on fluid dynamics aspects of the falling jet (jet instability, wave propagation, ...), as long as they are closely related to the suspension rheology (especially DST transition) and allow, at least, qualitative evaluation of the rheological behavior under extension, while retrieving stress-strain rate relations from the jet flows remains quite uncommon (we present however the concept of the jet extensional rheometry in Appendix – section 5.5). From the application point of view, the jet flow described in this chapter mimics to some extent the flow of the cement paste out of pumping lines and can therefore be important for mortar spraying or cement jet grouting.

Thus, in the present chapter, we conduct a detailed experimental analysis of the jet dynamics of CC-PA mixtures based on qualitative observations of the recorded jet flows (section 5.1) and on spatiotemporal diagrams of the jet lateral drift and jet surface undulation, as well as on two-dimensional (2D) Fourier spectra of these both quantities giving access to the dispersion relations, wave speeds and RMS amplitude and RMS speed of the lateral drift of the unstable jet (section 5.2). Suspension characterizations, the experimental setup and protocols, as well as

⁴ The results were obtained using the 1st series of CC particles, so they can be safely compared to the results of the chapter 3, while only qualitative comparison with the results of chapter 4 is possible.

Main results of this chapter are published in [M. Meloussi, S. Schaub, A. Cifreio, S. Aguib, P. Kuzhir. Jet instability of suspensions of different shaped particles exhibiting discontinuous shear thickening *Journal of Rheology*, 66, 1005 (2022)]

the data processing routines are detailed in chapter 2. As in previous chapters, we inspect the effect of rigid polyamide (PA) fibers addition on the jet dynamics. Finally, theoretical evaluation of the stress profile along the jet provides, if not complete understanding, a physical insight into the origin of the jet instability without fibers and the effect of the fiber addition on the jet dynamics (section 5.3). As in the previously studied case of shear flow in chapters 3 and 4, the fiber orientation distribution is expected to play an important role on the rheology of CC-PA mixtures in extensional flows within the falling jets when the flow-induced fiber alignment could considerably enhance the extensional viscosity [154] and somehow influence the DST transition and thus the jet instability – this effect will be discussed in the present chapter.

5.1 Qualitative observations

In this section, we report the visualization experiments conducted on the jet of the CC-suspension or CC-PA mixtures. First, we consider the CC mixtures without PA fibers and evaluate the effect of the jet length on the jet dynamics [section 5.1.1]. Second, we consider CC-PA mixtures and evaluate the effect of PA fiber addition on the behavior of the jet [subsection 5.1.2].

5.1.1 Effect of the jet length

In this section, we inspect the jets of the CC suspension without addition of PA fibers. At a given flow rate, depending on the jet length different behaviors are observed, as shown on snapshots of Figure 5.1. At the jet length $L < 4$ cm, the jet remains strictly vertical and cannot be distinguished from a Newtonian viscous thread [Figure 5.1a]. Viscoelastic coiling instability (typically reported for honey-like fluids [182]) then takes place at $4 \text{ cm} < L < 6$ cm, when the jet extremity describes circular motion on the experimental table, while the whole jet exhibits precession motion around the tube axis [Figure 5.1b]. These two first regimes have been extensively studied in literature and are out of scope of the present work. Increasing the suspension jet length above $L > 6$ cm suddenly gives place to another form of instability. The falling jet no longer follows a straight vertical trajectory but undergoes lateral drifts (oscillations) with well distinguishable running waves in both downstream and upstream directions [Figure 5.1c]. At $L > 15$ cm and at axial positions $z > 15$ cm we notice periodic rupturing of the jet into solid-like segments, which after falling on the experimental table keep their cylindrical shape for a few seconds before melting to become liquid again. As it was reported, DST state for a shear thickening fluid keeps for a few seconds after applied shear stress removal [183], – duration long enough for the jet to stay in DST state after it breaks and until it hits the experimental table. These observations on the lateral oscillations and

solidification effects agree with previous work of Liard et al. [127] on the jets of silica particle suspension.

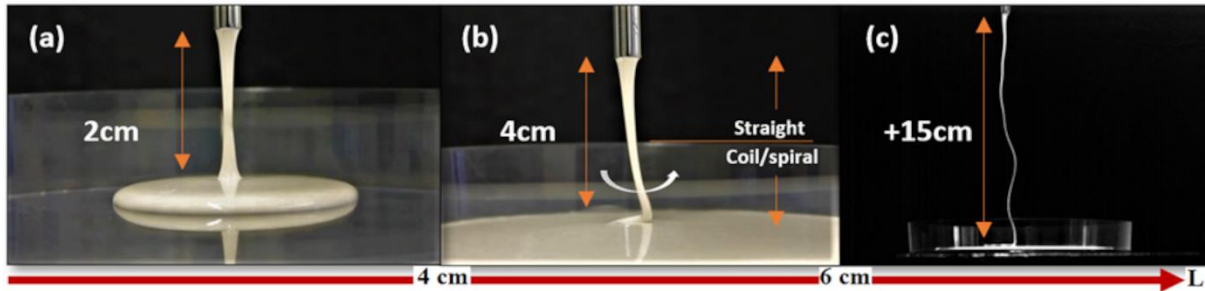


Figure 5.1 Snapshots of falling CC-suspension jet without PA fibers: stable viscous jet (a); jet subject to coiling instability (b); jet subject to lateral oscillations (c). The average length-to-diameter ratio is $L/D_0 \approx 4.0$, 8.0 and 30 for the jets shown in (a), (b) (c). The average length-to-diameter ratio is $L/D_0 \approx 4.0$, 8.0 and 30 for the jets shown in (a), (b)

5.1.2 Effect of the PA volume fraction

Addition of PA fibers to the CC suspension qualitatively changes the jet behavior, and these changes depend on the PA volume fraction. In Figure 5.2, the jet of CC-suspension without PA fibers is compared with jets of CC-suspension with three different concentrations of PA fibers. The jet length is fixed to 15 cm. The jet of CC-suspension without PA fibers [Figure 5.2a] is continuous (with only some rare fracture events), and laterally oscillating all along its length. The generation of these oscillations may be due to stress fluctuations in the jet above a critical stress of DST transition, as typically observed in confined CC-suspension in shear-rheological measurements [100]. Addition of the PA fibers globally decreases the lateral oscillations [Figures 5.2 (b-d)] and stops them completely (i.e. the jet becomes completely vertical) at $\varphi_f \approx 0.7 - 0.8$ % vol. This effect will be explained and quantitatively evaluated later in section 5.3.2. However, with increasing fiber concentration, the break-up events become more frequent and occur at shorter distances L_b from the tube outlet called hereinafter the break-up length. It is possible that with increasing PA volume fraction, PA fibers form larger flocs inside the jet, whose size likely becomes comparable to the jet diameter leading to the jet break-up, as it occurs with the jet of concentrated suspension of spheres [184]. This point will be inspected in section 5.3.3 along with quantitative evaluation of the break-up length.

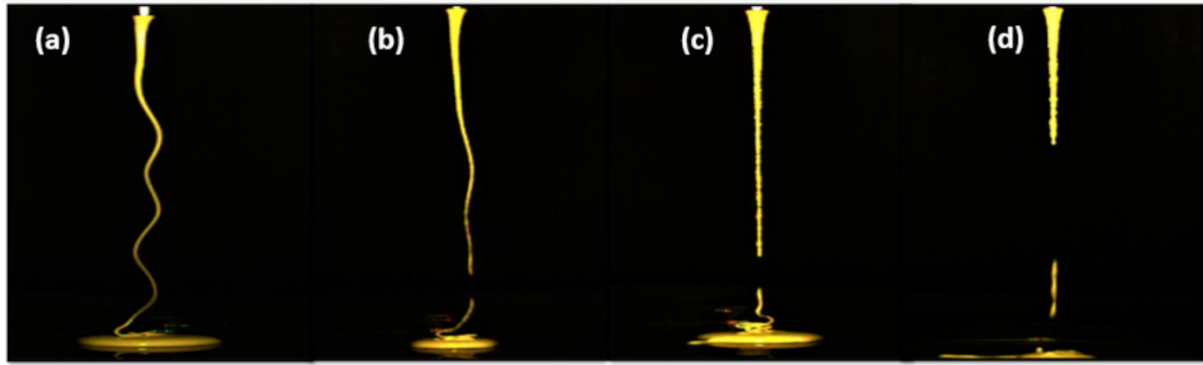


Figure 5.2 Snapshots of the suspension jets at different PA fiber concentrations. (a) CC suspension without PA-fibers. The jet is completely unstable showing a wavy pattern along its length. (b) CC-PA mixture at $\varphi_f = 0.6\%$ vol. The jet is still unstable and presents some fractures in the bottom section. (c) CC-PA mixture at $\varphi_f = 1.6\%$ vol. The jet is stable against lateral oscillations with frequent fractures occurring at the bottom section of the jet. (d) CC-PA mixture at $\varphi_f = 2\%$ vol. The jet is completely stable against lateral oscillations with frequent fractures all along the jet length.

5.2 Quantitative analyses of jet dynamics

We analyze in this section, the dynamics of the jets of CC-PA mixtures through different quantitative features, such as the jet diameter, lateral drift, Fourier spectra, dispersion relation, wave speed.

5.2.1 Variation of the jet diameter

The suspension jet shows some fluctuations of its diameter along its length and during time. For quantitative analysis of these fluctuations, we evaluated first the mean jet diameter, $\langle d \rangle = f(z)$ averaged over time as function of the axial position, as plotted in Figure 5.3a for the CC-PA mixtures at $\varphi_f = 0, 0.6, 1.2$ and 2% vol, with $\varphi_f = 0$ corresponding to the CC suspension without fibers. The average jet diameter was evaluated excluding zero values of the instantaneous jet diameter during possible jet ruptures. For all the curves, we observe an initial rather strong decrease of the diameter in the downstream direction attributed to gravitational stretching, as typically observed for free falling jets [182]. This decrease is followed by a slight increase of the average diameter at the bottom part of the jet due to jet flow deceleration near the point where the jet hits the experimental table. We also notice that the average jet diameter is a growing function of the fiber volume fraction. This is expected from higher viscosity of the CC-PA mixtures with higher φ_f values; the jet of a more viscous fluid exhibits less thinning diameter when stretched by gravity. For example, in viscous regime at short axial distances, the Newtonian jet radius scales as $R \sim u^{-1/2} \sim \eta_0 (\rho g)^{-1/2} z^{-1}$ (with u being the jet speed at a given axial position z) – see, for instance [185]. To quantify jet break-up events that happen at some conditions, we introduce the break-up probability Π at a given axial position z as a ratio of the

time $T_{d=0}$ interval, for which zero instantaneous jet diameter was detected, to the observation time interval T , namely $\Pi = (T_{d=0}/T) \times 100$ (%). Experimental $\Pi(z)$ -dependency is plotted in Figure 5.3b for various φ_f values. As inferred from this figure, the break-up probability is zero all along the jet of the CC suspension without fibers, in agreement with observations of the jets with the length $L < 15$ cm, cf. section 5.1.1. The break-up probability increases dramatically with the fiber volume fraction and achieves 80% at the jet lower section at $\varphi_f = 2$ % vol. The axial probability profile has a sigmodal shape at $\varphi_f = 1.2$ and 2 % vol, with zero break-up probability until some critical break-up length L_b , followed by a gradual increase at $z > L_b$. The effect of the PA fiber volume fraction on the break-up length will be inspected in section 5.3.3 in conjunction with theoretical estimations.

Then, we evaluated the deviation $\Delta d(t, z) = d(t, z) - \langle d \rangle(z)$ of the instantaneous jet diameter $d(t, z)$ from its average value; the spatiotemporal maps (colormaps) of the $\Delta d(t, z)$ function are plotted in Figure 5.4 a, c, e, g for the observation time lapse of 5 s and for the same range of the fiber volume fraction φ_f as in Figure 5.3. The colormaps at $\varphi_f = 0$ and 0.6 %vol clearly show a periodic sequence of the yellow (thicker diameter) and blue (thinner diameter) bands corresponding to the blobs and necks along the jet length. The amplitude of these surface undulations is relatively small (± 0.3 mm) with respect to the wavelengths $\sim 10 - 150$ mm and the jet mean diameter of 1-5 mm. Such surface undulations have not been detected in jet instability experiments of Liard et al. [127] likely because of space resolution limits, as opposed to relatively strong undulation of the filament surface in pinch-off experiments of Roché et al. [123]. A negative slope of the color bands in the (t, z) -space [Figure 5.4] points out to the downstream propagation of the blobs-and-necks sequence along the jet flow direction. An enlarged view of the colormap in Figure 5.4a is provided in the inset of Figure 5.4 and reveals complex dynamics of the surface undulations with two kinds of blobs. On the one hand, thick bands clearly visible in non-zoomed views correspond to relatively long blobs travelling along the jet with a relatively low speed gradually increasing in downward direction. On the other hand, in the lower half of the jet, we detect a sequence of thin yellow and blue bands, corresponding to shorter and faster blobs and necks, each travelling at a high constant speed of about 0.9 m/s, as inferred from the slope of the thin yellow bands – one of these slopes being shown in Figure 5.4a. The speed of two kinds of blobs appears to be much higher than the jet speed, which increases from $\sim 8 \times 10^{-4}$ m/s to ~ 0.02 m/s along the jet. In addition to it, one can easily observe the jet ruptures designated by black colored sections. The ruptures are absent at $\varphi_f = 0$ %vol; some rare break-up events appear at the jet lower section for $\varphi_f = 0.6$ %vol;

the ruptures become frequent and appear closer to the tube outlet for $\varphi_f = 1.2$ and 2 %vol, in agreement with observations in section 5.1.2 and with the break-up probability plotted in Figure 5.3b.

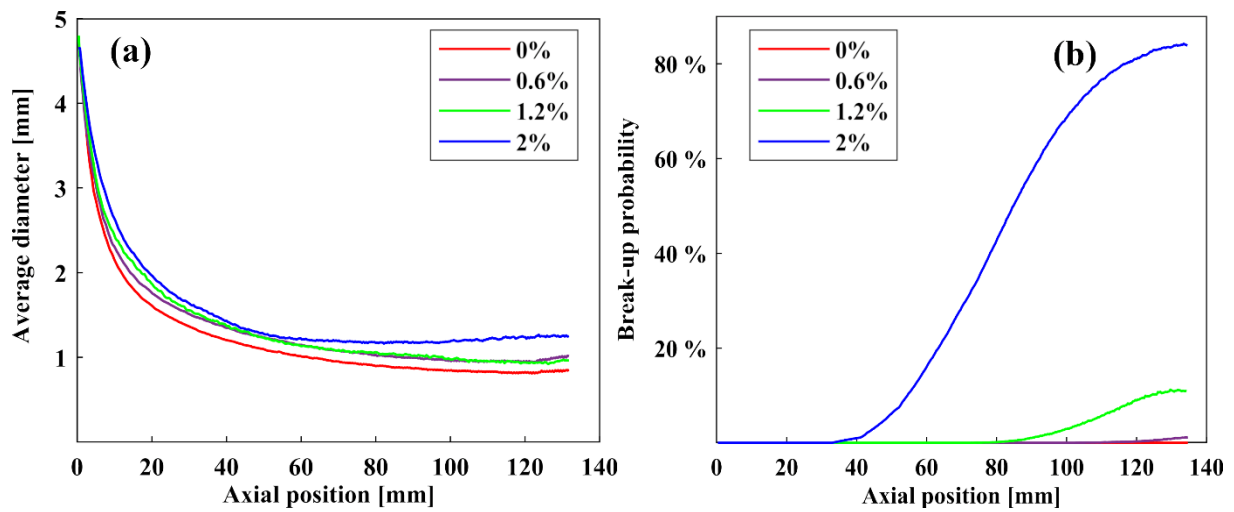


Figure 5.3 Jet diameter (d) averaged over observation time (a) and the jet break-up probability (b) as function of the axial position z for CC-PA mixtures at different PA volume fractions listed in the figure legend.

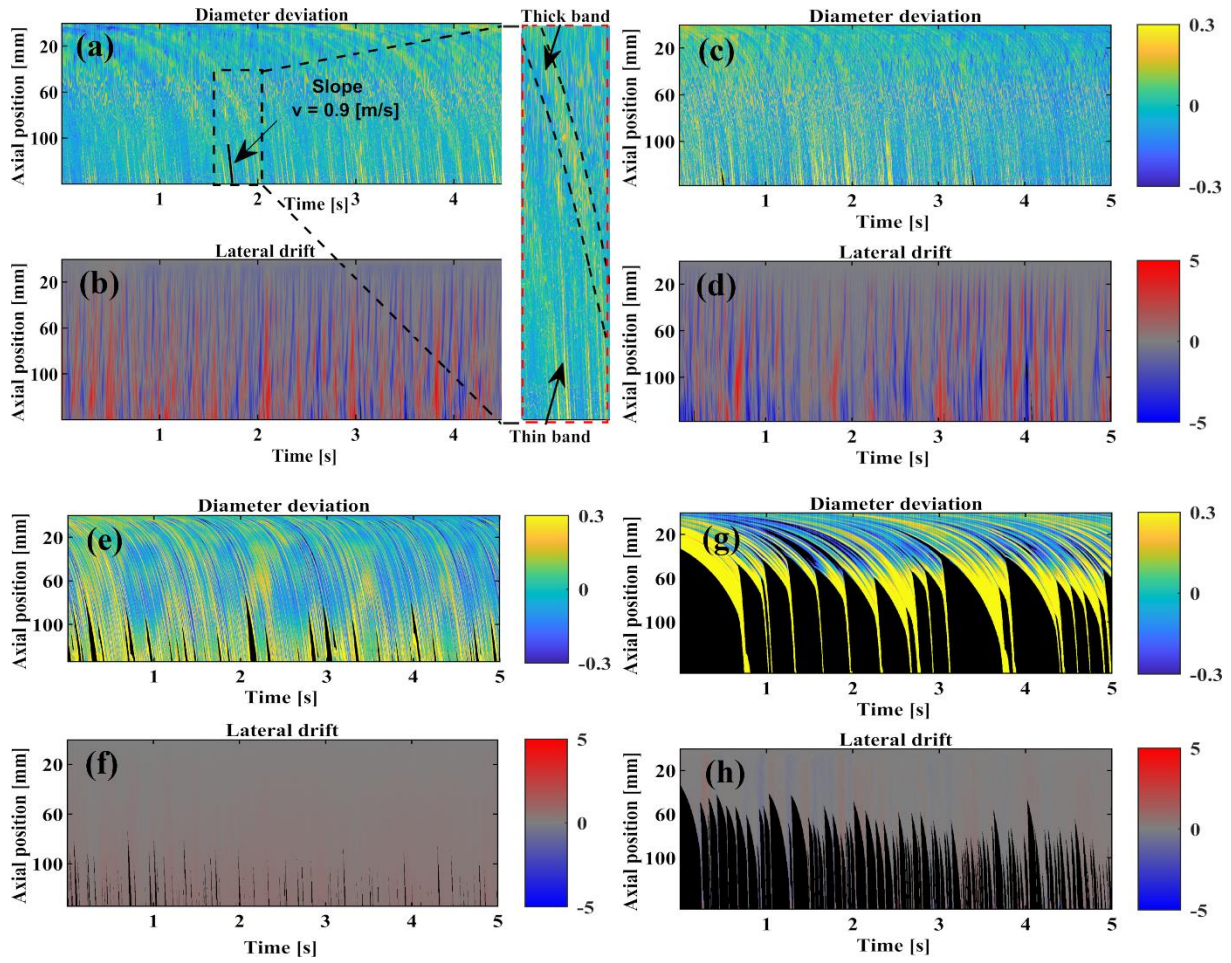


Figure 5.4 Spatiotemporal diagrams of the jet diameter deviation $\Delta d(t, z)$ (in mm, parts (a), (c), (e), (g)) and jet lateral drift $x(t, z)$ (in mm, parts (b), (d), (f), (h)) for CC-PA mixtures at different PA fiber volume fractions: $\varphi_f = 0$ (CC suspension in absence of fibers) (a) and (b); 0.6% vol (c) and (d), 1.2 % vol (e) and (f), 2% vol (g) and (h). The inset on the right of (a) and (b) shows an enlarged view of a rectangular region of the $\Delta d(t, z)$ -map (a) delimited by the dashed line. Thin yellow bands and thick bands delimited by inclined dashed curves are distinguished on this inset.

For a deeper analysis of the blob-and-neck propagation, we perform a 2D DFT analysis of the jet diameter $d(t, z)$, as specified in section 2.2.3 of chapter 2. The contour plots of the amplitude $\mathfrak{D}(\omega, k)$ of the Fourier spectrum in the frequency domain (ω, k) are presented in Figure 5.5 for the CC-PA mixtures at different fiber volume fractions. At $\varphi_f = 0$ and 0.2 %vol, we observe an elongated pattern extended from the second to the fourth quadrant [Figure 5.5 (a,b)], which looks like a mountain crest in a surface 3D plot (not shown here for brevity). This crest corresponds to surface undulation waves propagating downstream the flow. In general, the projection of the crest onto the horizontal (ω, k) -plane is described by some function $\omega = f(k)$, which is nothing but a wave dispersion relation. In Figure 5.5 (a,b), the crests have a linear shape (denoted by a dashed line in Figure 5.5a) corresponding to non-dispersive waves on the jet surface with a linear dispersion relation $\omega = v_s k$. The wave speed v_s is defined as an average slope of experimental $\omega = f(k)$ dependencies.

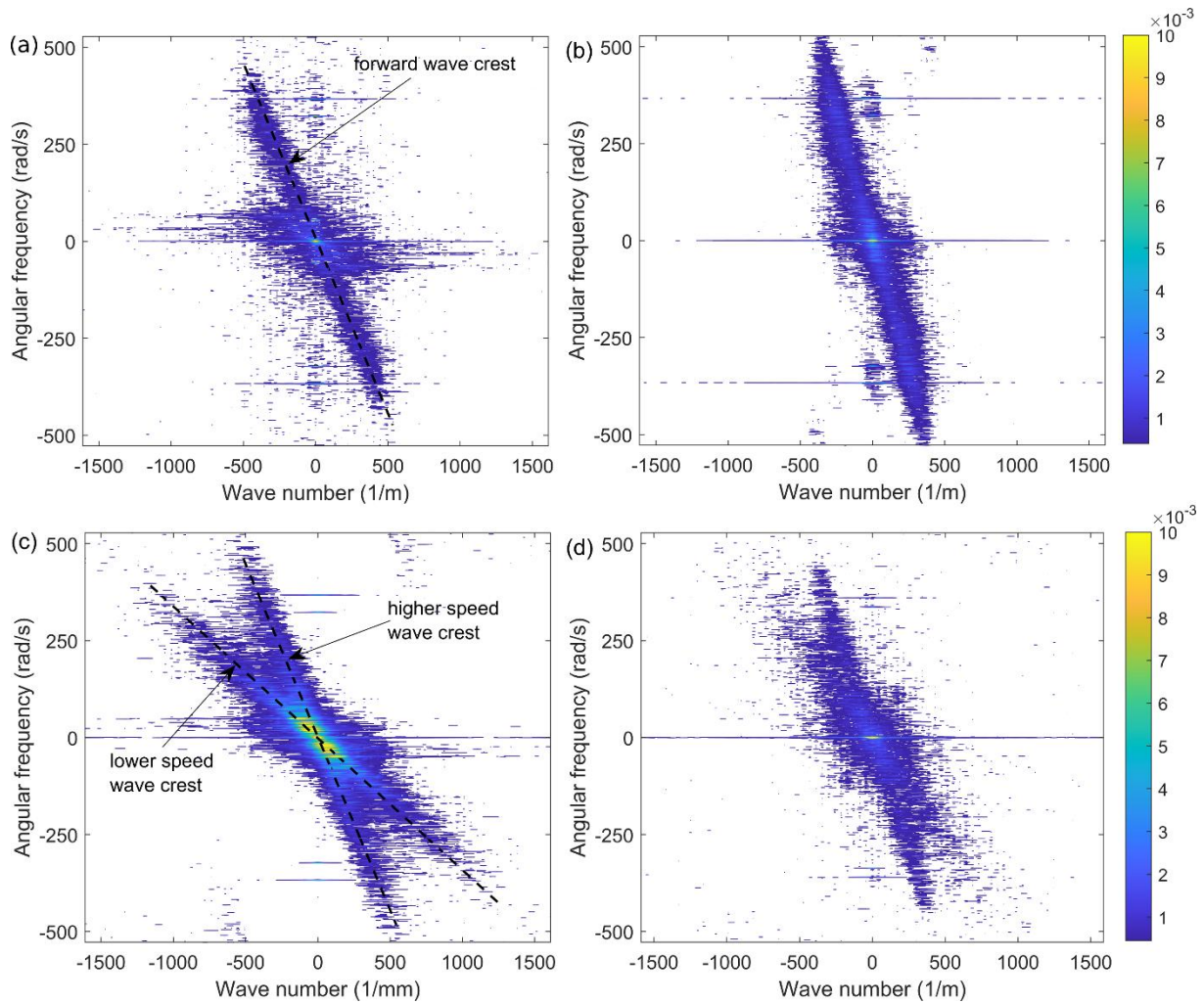


Figure 5.5 Contour plots of the Fourier amplitude $D(\omega, k)$ (in mm) of the jet instantaneous diameter $d(t, z)$ of the CC-PA mixtures at different PA volume fractions: $\varphi_f = 0\%$ vol (a), 0.2% vol (b), 0.5% vol (c) and 0.7% vol (d). The dashed lines in (a) and (c) are guides for eye to follow either a single wave speed (a) or two different wave speeds (c). The color bars of (a) and (c) are similar to those of (b) and (d). The sampling rates were fixed to the values $\omega_{up} \approx 1060 \text{ rad/s}$ and $k_{up} \approx 3200 \text{ m}^{-1}$ slightly larger than twice the highest observable ω and k values (cf. section 2.2.3). The lowest non-zero ω and k values are fixed by the film duration (14.86 s) and the observed jet length ($\sim 145 \text{ mm}$) that gives $\omega_{down} \approx 0.423 \text{ rad/s}$ and $k_{down} \approx 43.3 \text{ m}^{-1}$.

Interestingly, for $\varphi_f \geq 0.5\%$ vol we observe two separate amplitude crests (highlighted by dashed lines in Figure 5.5c), still having a linear shape associated to two different wave speeds for the same propagation direction. This situation is expected to reflect a more complex dispersion relation that may physically correspond to the wave propagation through heterogeneous and/or anisotropic media, which may admit different wave speeds, as often reported for elastic waves in granular media [186], porous media [187] or fibrous materials [188]. In our case, addition of PA fibers likely brings some anisotropy (in case of non-random orientation distribution of fibers along the jet flow) and/or large-scale heterogeneity (in case of formation of flocs perceived at the rough jet surface – see Figure 5.2 (c,d); this probably results in two wave speeds. Further investigations are required to clarify this point. Notice however

that two crests visible in Figure 5.5 (c,d) should not be confounded with the “slow” and “fast” blobs detected in the spatiotemporal maps in Figure 5.4 (a,c) because the “slow” blobs propagated with a speed varying along the jet, while the wave speeds assigned to the wave crests in Figure 5.5 (c,d) are constant and therefore more relevant for “fast” blobs. The “slow” blobs dynamics is likely masked by relatively broad central spot of the Fourier spectra in Figure 5.5. In addition to it, we do not have a clear explanation for the thin horizontal bands appearing at $\omega \approx \pm 370 \text{ rad/s}^{-1}$ in all contour plots of Figure 5.5. It is not expected to come from acoustic wave resonance of the suspension-filled tube (with fundamental frequency $\sim 2 \times 10^4 \text{ s}^{-1}$) but is probably caused by the resonance with the mechanical support of the fluid tank [Figure 2.15].

In what concerns the wavelength range, for all fiber volume fractions, the Fourier amplitude is significant at relatively small wavenumbers and decays above $k_{max} \approx 500 \text{ m}^{-1}$. This corresponds to the surface undulation wavelengths ranging between $\lambda_{min} = 2\pi/k_{max} \sim 10 \text{ mm}$ and the observable jet length $\lambda_{max} \sim L \approx 145 \text{ mm}$. Let us now evaluate two characteristic wavelengths of the Rayleigh-Plateau (RP) instability, which are the critical wavelength of the instability onset [182], $\lambda_c = 2\pi R_0 \approx 15 \text{ mm}$ and the most amplified wavelength [182], $\lambda_m = 2\pi R_0 [2 + 3\eta_0(\rho\gamma R_0/2)^{-1/2}]^{1/2}$, which is equal to 96 – 124 mm for our CC-PA samples, where $\gamma \approx 0.072 \text{ N/m}$ is the surface tension. As we see, both RP wavelengths enter the interval of the surface undulation wavelengths observed in our experiments. However, as we will see in section 5.2.2, the wave speed in our case is much larger than that of the RP instability, which is equal to the jet speed.

As it will be seen in section 5.2.2, the blob-and-neck propagation along the jet at $\varphi_f < 0.8 \text{ \%vol}$ is accompanied by lateral oscillations of the jet centerline. So, the fluctuations of the jet diameter and jet centerline seem to be governed by the same physics related to the DST transition in extensional flow along the jet, as will be inspected in section 5.3.

5.2.2 Lateral oscillations

The spatiotemporal maps of the jet lateral drift are presented in Figures 5.6 (b-h). It is well observed that the jet of CC-suspension without PA fibers is continuous and represents no ruptures [Figure 5.6b], as has been shown in the same figure in the diameter deviation colormaps [Figures 5.4a] and agrees with zero break-up probability shown by the red line in Figure 5.3b. The sequence of blue and red bands in the lateral drift colormaps corresponds to negative (to the left from the tube axis) and positive (to the right from the tube axis) drift of the jet during time, thus indicates that the jet is strongly oscillating. The color bands appear to be

nearly vertical meaning that mostly the whole jet displaces to the left or to the right with respect to the tube axis. We also note that the color intensity varies (and sometimes fluctuates) vertically along the bands becoming more intense in downstream direction. This means that, as expected, the lateral drift is more pronounced at higher axial positions, while color intensity fluctuations reflect jet centerline undulations along the jet, as observed in the experimental snapshots [Figure 5.2 (a, b)].

The jet is not totally continuous and the ruptures along its length sometimes occur when adding PA fibers at 0.6% vol [Figure 5.4d], but the rupture events are still seldom at this PA volume fraction, in agreement with weak (a few %) values of the break-up probability – see the purple line in Figure 5.3b. In the lateral drift colormap, the rare rupture events appear as a few relatively thin black bands or spots. The ruptures become more pronounced when increasing the PA fiber concentration, as inferred from increasing number of black bands in colormaps for $\varphi_f = 1.2\%$ vol [Figure 5.4f] and 2% vol [Figure 5.4h]. This correlates with the increasing break-up probability revealed from Figure 5.3b. However, the jet becomes completely stable at fiber volume fraction $\varphi_f \geq 0.8\%$ vol and lateral oscillations disappear. For example, the lateral drift colormaps for $\varphi_f = 1.2\%$ vol [Figure 5.4f] and 2% vol [Figure 5.4h] are rather homogeneous (with nearly zero lateral drift), except for the black bands at the lower part of the jet standing for the jet ruptures.

For a finer analysis of the jet lateral drift $x(t, z)$, 2D DFT analysis was performed on $x(t, z)$ signal, as detailed in section 2.2.3. The obtained surface plot of the Fourier spectrum $X(\omega, k)$ at $\varphi_f = 0\%$ vol is shown in Figure 5.6a and the contour plots $X(\omega, k)$ for different PA fiber volume fractions are shown in Figure 5.6 (c-f). We observe two main crests in the surface plot of Figure 5.6a, one spanning the odd quadrants and corresponding to the forward propagation of the jet lateral drift, and another one spanning the even quadrants and assigned to the backward wave propagation. A secondary crest at the middle plane of the surface plot (perceived in the contour plots as a horizontal band centered at $\omega = 0$) likely corresponds to some slow dynamics occurring at the jet speed $u \approx 8 \times 10^{-4} - 0.02$ m/s. The contour plots in Figure 5.6 (c-f) allow one to appreciate the “width” of the crests, their extension through the (ω, k) domain and the difference between the forward and backward wave crests. The shape and the height of the crests deserve a detailed analysis.

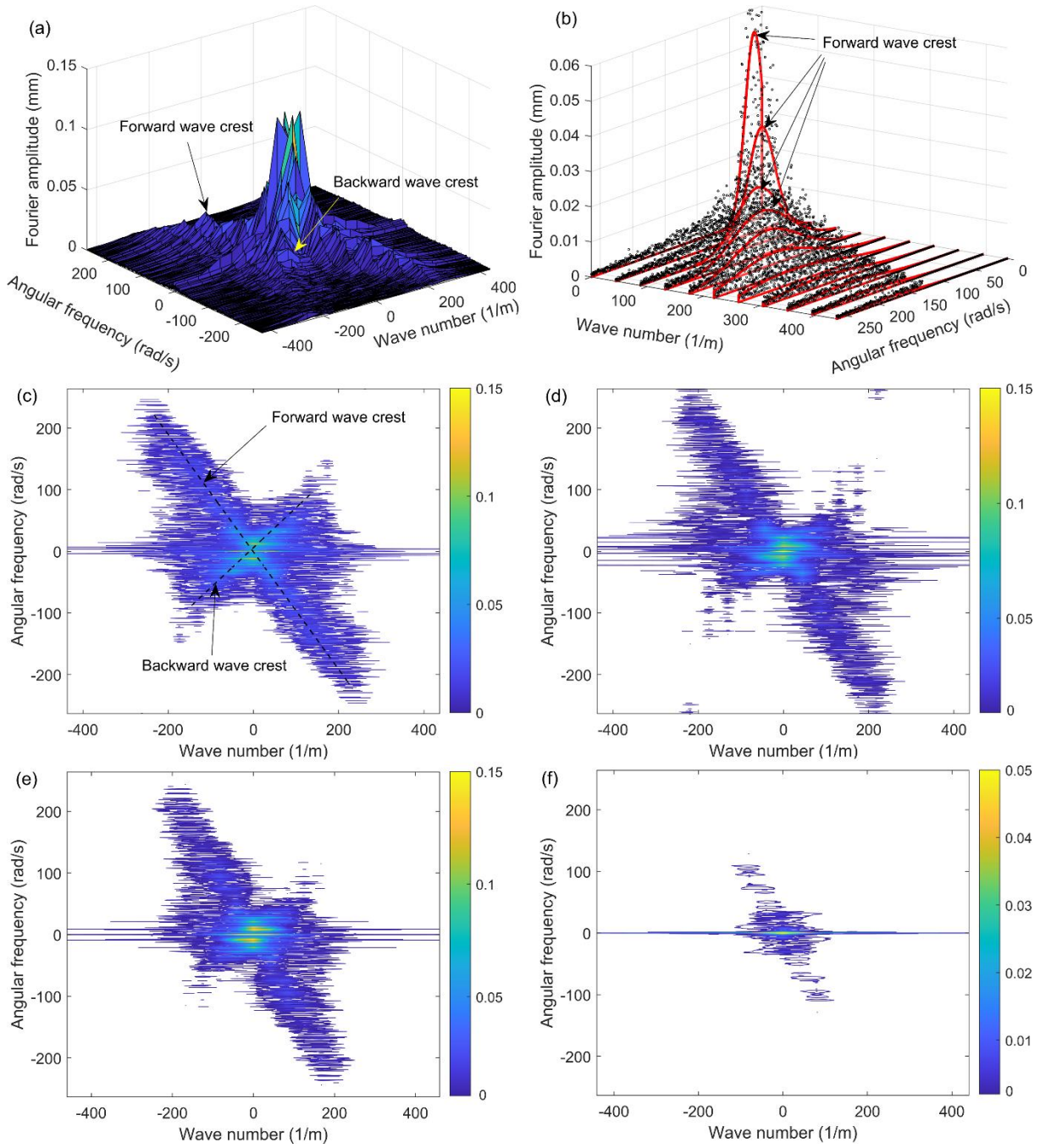


Figure 5.6 Fourier amplitude $X(\omega, k)$ (in mm) of the jet lateral drift $x(z, t)$ of the CC-PA mixtures at different PA volume fractions: surface plot (a), 3D scatter plot of the second quadrant ($\omega \leq 0, k \geq 0$) after sign inversion of ω (b) and contour plot (c) for $\varphi_f = 0$ (CC suspension without PA fibers); contour plots for $\varphi_f = 0.6\%$ vol (d), 0.7% vol (e) and 0.8% vol (f). The red lines in (b) correspond to the gaussian fit of each vertical slice (along the lines $k = \cos nt$) of the 3D scatter plot. The black dashed lines in (c) are guides for eye helping one to follow the forward and backward wave crests. The sampling rates were fixed to the values $\omega_{up} \approx 530 \text{ rad/s}$ and $k_{up} \approx 860 \text{ m}^{-1}$ slightly larger than twice the highest observable ω and k values (cf. section 2.2.3). The lowest non-zero ω and k values are fixed by the film duration (14.86 s) and the observed jet length ($\sim 145 \text{ mm}$) that gives $\omega_{down} \approx 0.423 \text{ rad/s}$ and $k_{down} \approx 43.3 \text{ m}^{-1}$.

The projection of crests [Figure 8a] onto a horizontal (ω, k) - plane, gives a dispersion relation $\omega = f(k)$ corresponding to the wave propagation of lateral oscillations. The dashed lines in Figure 8c indicate an approximate position of both main wave crests. Strictly speaking, the

dispersion relation can be exactly established for infinitely thin (and infinitely high) crests with the Fourier amplitude along the crests respecting the Dirac delta function – a hypothetical case of zero damping (e.g. inviscid fluid) and infinitely long jet. In our case of highly viscous suspension, the crests are much more diffuse, so, we have defined the dispersion relation in the following way. First, we isolated a single quadrant of the Fourier spectrum corresponding to either the forward or backward wave. Second, the residual amplitudes corresponding to the secondary (low frequency) crest were manually eliminated, and the rest of the $X(\omega, k)$ data lower than some threshold were set to zero (filtered) in order to reduce the noise. Third, the 3D scatter plot of the pre-treated $X(\omega, k)$ -signal was generated [Figure 5.6b] and sliced by vertical planes parallel to the ω -axis and corresponding to fixed discrete values of the wavenumber k . Each slice contained a point cloud $X_k(\omega)$ that was fitted by a gaussian function shown by red solid lines in Figure 5.6b. The location of peaks of each gaussian curve was assigned to the crest position in the (ω, k) -plane that allows a clear definition of the dispersion relation. Remarkably, the discrete points of the dispersion relation always gathered along a straight line and therefore were fitted by a linear function $\omega = v_l k$. Such a linear dispersion relation (found for forward and backward waves at all fiber volume fractions) corresponds to non-dispersive waves and the slope v_l stands for the wave speed. Notice that for the present case of non-dispersive waves, the phase speed $\omega/k = v_l$ is the same as the group speed $d\omega/dk = v_l$.

From the theoretical perspective, Liard et al. [127] has supposed that the wave propagation along the shear thickening jet is equivalent to vibration of a solid taut string with the gravity playing the role of the tensile force. Following this idea, the wave speed squared is given by $v_l^2 = \tau/\rho$, where τ is the tensile force by unit jet cross-section. In ideal string model, the tensile force is constant along the string, while in our case of the gravitational stretching, it varies linearly with the axial position: $\tau = \rho g z$, resulting in $v_l^2(z) = g z$. It can be shown that the last expression is valid in a short-wave limit $\lambda \ll L$ and under assumptions of nearly constant jet cross-section and high wave speeds $v_l \gg u$. Notice that our Fourier analysis provides some effective wave speed likely related to the RMS value of $v_l(z)$, which, in the frames of the vibrating string model, is given by

$$v_l = \sqrt{\frac{1}{L} \int_0^L v_l^2(z) dz} = \sqrt{\frac{gL}{2}} \quad (5.1)$$

recalling that $L \approx 0.15$ m is the total jet length.

Experimental and theoretical [Eq. (5.1)] dependencies of the wave speed on the fiber volume fraction are shown in Figure 5.7 for forward (black squares) and backward (blue triangles) waves. The error bars correspond to the confidence interval of the linear fit of the gaussian peak locations (cf. Figure 5.6b). Experimental values show some fluctuation with the fiber volume fraction without deserving any clear tendency. One can observe near similar (within experimental errors) speeds of the forward and backward waves. This suggests the single dispersion relation for both propagation directions. Noteworthy, the wave speed v_s of the blob-and-neck propagation (green diamonds) is the same (within the error bars) as the wave speed v_l of the lateral oscillations. For the CC-PA samples with two blob-and-neck wave speeds [Figure 5.5 (c,d)] we use the highest of two v_s values for comparison with v_l . Quantitatively, we find the average value of these speeds $v_l \approx v_s \approx 0.9 \pm 0.2$ m/s independent of the fiber volume fraction. This value is in excellent agreement with the speed propagation of the “fast” blobs, ~ 0.9 m/s, directly revealed from the spatiotemporal maps in Figure 5.4. The similarity between v_l and v_s -values could point out to the same origin of both instabilities coming from fluctuating stresses above DST transition. On the other hand, the jet surface undulations are typically observed for the RP instability, occurring due to capillary forces. However, the speed of the surface undulation propagation is about the jet speed for the RP instability. In our experiments the jet speed varies from $\sim 8 \times 10^{-4}$ m/s at the tube outlet to ~ 0.02 m/s at the jet lower extremity and remains much lower than the wave speed $v_s \sim 1$ m/s. This could be an argument for ruling out the RP instability in our case.

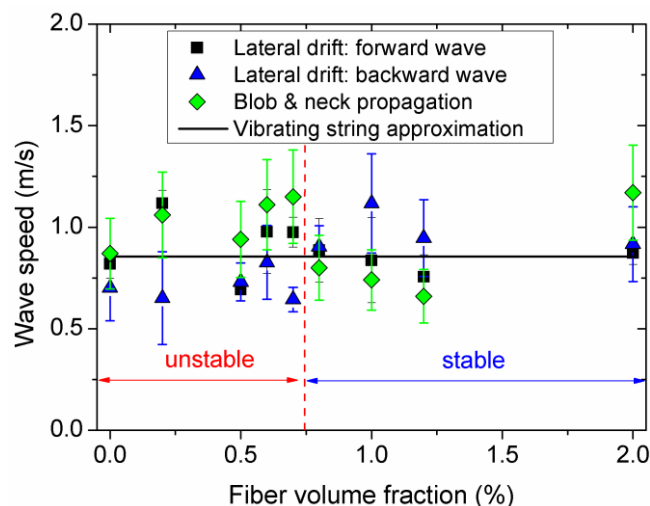


Figure 5.7 Effect of the fiber volume fraction on the forward/backward wave speeds v_l of the jet lateral oscillation and on the blob-and-neck propagation speed v_s . Here, we use the highest of two v_s values for comparison with v_l .

The “vibrating string” model does not distinguish between the jets with and without fibers and provides a single wave speed $v_l \approx 0.87$ m/s independently of the fiber volume fraction

(horizontal black line in Figure 5.7), provided that the jet is in the “solid” state above the DST critical stress. Despite data dispersion, our experiments seem to confirm this tendency and show a very good quantitative agreement with the model (0.9 ± 0.2 m/s in experiments vs 0.87 m/s in theory). Ignoring the tensile force variation along the jet, Liard et al. [127] has obtained the expression $v_l = \sqrt{gL}$ for the wave speed, which differs from our one [Equation. (5.1)] by a factor of $\sqrt{2} \approx 1.4$. In their experiments, they used a completely different DST fluid (concentrated suspension of silica particles) at a different jet length $L \approx 0.08$ m as compared to our experimental value $L \approx 0.15$ m. They have found similar average values of the forward and backward wave speeds, both about half of their theoretical value. They attribute this difference to the phase lag between the forward and upward waves. However, their experimental value $v_l \approx 0.45$ m/s is relatively close (within large statistical errors) to the prediction of Equation. (5.1) that gives $v_l \approx 0.63$ m/s. More data have to be collected for establishing exact scaling of the wave speed as function of the jet length. At this stage, we can constate that the vibrating string model [Equation. (5.1)] provides a good wave speed prediction for two different experimental systems.

Surprisingly, the wave speeds v_l and v_s are also similar for unstable (at $\varphi_f < 0.8$ %vol) and stable (at $\varphi_f \geq 0.8$ %vol) jets. This correlates with the vibrating string model: both kind of jets exhibit the same wave speeds independently of the origin of their vibration, whether it comes from self-excitation in unstable jets or external random vibrations (sound, small mechanical shocks) of stable jets. The difference is in the oscillation amplitude, which is of course significantly lower (if not vanishing) for stable jets, as it will be shown below.

It is instructive to inspect now the intensity of different harmonics of the jet lateral drift. The most relevant magnitude for this purpose is the Fourier amplitude measured along the crests of the Fourier spectra, hereinafter called “crest height”. We defined it experimentally as the height $X_c(k)$ of the gaussian peaks associated to each discrete value of the wavenumber k (red curves in Figure 5.6b). The confidence interval of the gaussian fit was assigned to the uncertainty (error bar) of the crest height determination. The magnitude $L_c(k) = \sqrt{\omega^2(k) + (v_l k)^2} = v_l k \sqrt{2}$ is considered as a dimensionally correct measure of the “crest length”, with the wave speed v_l -values being taken from experiments [Figure 5.7] for each distinct CC-PA mixture. Experimental $X_c(L_c)$ -dependencies obtained in a parametric form $[L_c(k), X_c(k)]$ are shown on Figure 5.8 (a,b) for forward and backward waves, respectively and for different PA fiber volume fractions. Zero frequency values $X_c(0)$ of the crest height corresponds to a lateral offset

of the jet centerline are excluded from the plots because they may change between different experimental runs and must vanish when averaged over a large number of runs.

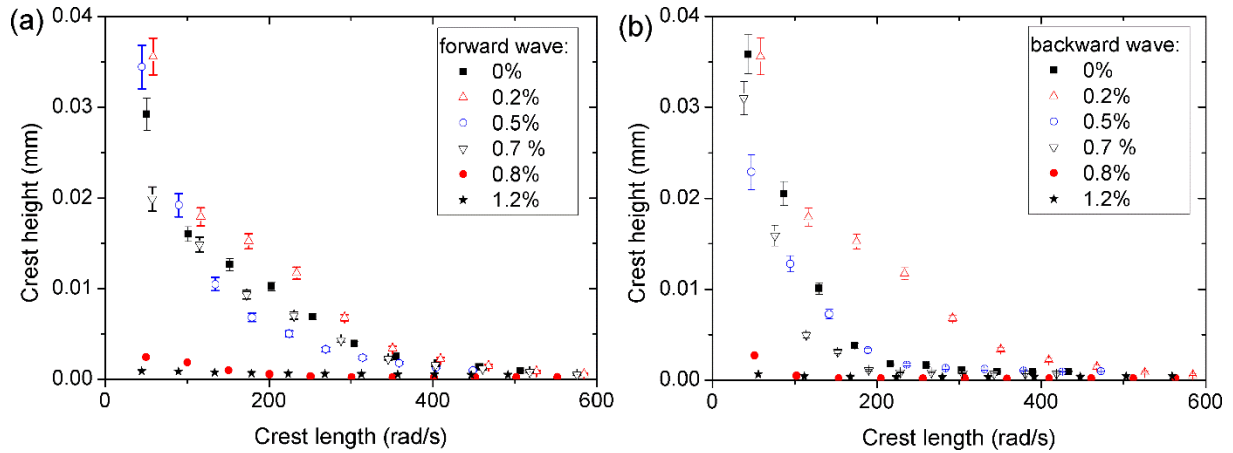


Figure 5.8 Dependency of the crest height on the crest length for the lateral oscillations at different PA fibers volume fractions (indicated in the legends) and for forward waves (a) or backward waves (b).

We see that, the crest height gradually decreases with the crest length. The maximal X_c -value (excluding zero frequency) corresponds to the lowest non-zero discrete wavenumber value $k_{down} \approx 43.3 \text{ m}^{-1}$ imposed by the observable jet length. Thus, for both propagation directions, the dominant wavelength corresponds to the jet length: $\lambda_{max} = 2\pi/k_{down} \approx L \approx 0.15 \text{ m}$. On the opposite limit, the shortest distinguishable wavelength can be arbitrarily assigned to that having an amplitude about 10% of the maximal amplitude at $k = k_{down}$. This gives $k_{max} \approx 280 \text{ m}^{-1}$, $\lambda_{min} = 2\pi/k_{max} \approx 20 \text{ mm}$ for the forward waves and $k_{max} \approx 140 \text{ m}^{-1}$, $\lambda_{min} \approx 40 \text{ mm}$ for backward waves. This corroborates with a shorter extension of the backward wave crests observed in the contour plots of Figure 5.6. In general, the crest height of the backward waves is lower than that of the forward ones. On the other hand, we can conclude that the jet surface undulation and forward waves of jet lateral oscillations exhibit near similar wavelength range, $\lambda = 0.01(0.02) - 0.15 \text{ m}$. It can also be seen that the oscillation amplitude is high for CC-PA mixtures at the fiber volume fractions $\varphi_f \leq 0.7 \text{ \% vol}$ but abruptly decreases at $\varphi_f = 0.8 \text{ \% vol}$, in agreement with the direct observations showing that jet lateral oscillations disappear at $\varphi_f \gtrsim 0.8 \text{ \% vol}$ [section 5.1.2]. Thus, at higher fiber concentrations, $\varphi_f = 1$ and 1.2 \% vol , the Fourier amplitudes are no longer discernable from the errors of the data processing, especially taking into account strong artefacts related to the jet break-up.

The possible reasons for the jet lateral oscillations, stabilization by fibers and for the transition from lateral oscillation regime to jet break-up with increasing fiber content will be inspected in the next section 5.3 in conjunction with theoretical evaluations.

5.3 Theoretical insight

In this section we try to give the responses on the two main questions of the present chapter through a few theoretical evaluations employing the jet's momentum balance. The two questions are: (a) Does the jet transverse oscillation come from the DST transition? (b) What is the effect of the fibers on the qualitative and quantitative changes of the jet dynamics?

5.3.1 Stress profile along the jet

We restrict our analysis to the steady state flow inside the jet and a straight vertical shape of the jet. This is expected to suffice for the analysis of the instability onset and the effect of the fiber addition on the instability threshold. In this section, we consider only the jets of CC suspensions without PA fibers. We follow Sauter and Buggisch [189] who derived the momentum balance equation from the force balance acting on a jet horizontal slice under inertia, capillary, gravity and viscous forces. The flow is classically assumed to be purely extensional with the axial velocity u depending only on the axial z coordinate, as schematically presented in Figure 2.15b in chapter 2. The original derivation covering only Newtonian fluids is easily extended to non-Newtonian rheology and gives the following set of steady-state equations for the evolution of the velocity u , the jet radius R and the tensile stress $\sigma_E = \sigma_{zz} - \sigma_{rr}$ with the axial position z (here, σ_{zz} and σ_{rr} are the axial and radial normal stresses, respectively):

$$\rho u \frac{du}{dz} = \frac{1}{R^2} \frac{d}{dz} (\sigma_E R^2 + \gamma R) + \rho g \quad (5.2)$$

$$uR^2 = u_0 R_0^2 \quad (5.3)$$

$$\frac{du}{dz} = \dot{\epsilon}(\sigma_E) = \frac{\sigma_E}{3\eta_0 \eta_{E,r}(\sigma_E)} \quad (5.4)$$

where $\gamma \approx 0.07$ N/m is the suspension surface tension, $\dot{\epsilon}(\sigma_E)$ is the extension rate at a given axial position z , η_0 is the low-shear viscosity of the CC suspension corresponding to quasi-Newtonian regime well below the DST transition [cf. Figure 3.2c in chapter 3 with h_0 corresponding to the slope of the green line], the factor 3 in Eq. (5.4) corresponds to the Trouton ratio [154]; $\eta_{E,r}(\sigma_E) = \eta_E(\sigma_E)/(3\eta_0)$ is the relative extensional viscosity of the non-Newtonian CC suspension defined as a ratio of the extensional suspension viscosity $\eta_E(\sigma_E)$ to its extensional viscosity $3\eta_0$ at low extension rate. The equation (5.3) is nothing but the flow rate conservation along the jet, with the jet speed at the tube outlet ($z = 0$) given by Eq. (2.26) in chapter 2, while the equation (5.4) is the rheological relationship for the extensional flow along the jet.

Let us now introduce the following scaling factors for the velocity, the jet radius, the axial position and the tensile stress:

$$[u] = u_0 = \frac{\rho g R_0^2}{32\eta_0}, [R] = [z] = R_0; [\sigma_E] = \rho g R_0 \quad (5.5)$$

The dimensionless quantities, $\tilde{u}, \tilde{R}, \tilde{z}, \tilde{\sigma}_E$ are obtained by dividing the respective dimensional quantities by the appropriate scaling factors. Combining Eqs. (5.2), (5.3) and (5.4), we arrive to the single differential equation for $\tilde{\sigma}_E(\tilde{u})$ taking the following dimensionless form:

$$\tilde{u} \frac{d}{d\tilde{u}} \left(\frac{\tilde{\sigma}_E}{\tilde{u}} + \frac{\beta}{\sqrt{\tilde{u}}} - \varepsilon \tilde{u} \right) = -\frac{3\eta_{E,r}(\tilde{\sigma}_E)}{32\tilde{\sigma}_E} \quad (5.6)$$

where $\beta = (L_c/R_0)^2 = \gamma/(\rho g R_0^2)$, $\varepsilon = u_0^2/(gR_0) = \rho^2 g R_0^3/(1024\eta_0^2)$, and $L_c = \sqrt{\gamma/(\rho g)}$ is the capillary length. To get the speed dependency on the axial position, we use Eq. (5.4) in the dimensionless form as follows;

$$\frac{d\tilde{u}}{d\tilde{z}} = \frac{32\tilde{\sigma}_E}{3\eta_{E,r}(\tilde{\sigma}_E)} \quad (5.7)$$

It is known that the forward integration of Eq. (5.6) at an arbitrary initial value of $\tilde{\sigma}_E(1)$ leads to the solution divergence at large speeds \tilde{u} [185]. This problem is commonly handled by backward integration with the initial condition physically corresponding to the inertial regime at infinite speed far below the tube outlet. This corresponds to the free fall speed $u_\infty = \sqrt{2gz_\infty}$, the extensional rate $\dot{\varepsilon}_\infty = \sqrt{g/(2z_\infty)} = g/u_\infty$ and the tensile stress at vanishing extensional rate $\sigma_E(u_\infty) = 3\eta_0\dot{\varepsilon}_\infty = 3\eta_0g/u_\infty$ or in dimensionless form:

$$\tilde{\sigma}_E(\tilde{u}_\infty) = \frac{3\eta_0g}{\rho g R_0 u_0 \tilde{u}_\infty} = \frac{3}{32\varepsilon \tilde{u}_\infty} \quad (5.8)$$

Thus, choosing the initial point at $\tilde{u}_\infty = 10^4 - 10^5$ and the terminal point at $\tilde{u} = 1$ (tube outlet), we obtain numerical solution of the initial value problem [Eq. (5.6), (5.8)] in terms of $\tilde{\sigma}_E(\tilde{u})$ -dependency, which, in the case of the Newtonian rheology, is equivalent to the common representation in coordinates $d\tilde{u}/d\tilde{z} = f(\tilde{u})$. The dependency of the flow speed on the axial position can further be obtained in inverse form by the forward integration of Eq. (5.7):

$$\tilde{z}(\tilde{u}) = \frac{3}{32} \int_1^{\tilde{u}} \frac{\eta_{E,r}(\tilde{\sigma}_E(\tilde{u}))}{\tilde{\sigma}_E(\tilde{u})} d\tilde{u} \quad (5.9)$$

Thus, varying the dimensionless speed in the interval $1 \leq \tilde{u} \leq \tilde{u}_\infty$, we get the axial position as a function of speed with the help of Eq. (5.9), while the $\tilde{\sigma}_E(\tilde{z})$ -dependency is obtained in the parametric form $[\tilde{z}(\tilde{u}); \tilde{\sigma}_E(\tilde{u})]$.

First, we apply this calculation procedure to the Newtonian limit, which is usually appropriate for the shear thickening suspension below the DST transition. To this purpose, we put $\eta_{E,r}(\tilde{\sigma}_E) = 1$ in Eqs. (5.6) and (5.9) and plot in Figure 5.10a the $\tilde{\sigma}_E(\tilde{u})$ theoretical dependency (solid red line) for the typical values $\beta = 0.66$ and $\varepsilon = 2.44 \times 10^{-5}$ of the parameters in our experiments. This dependency has a typical non-monotonic shape of the $d\tilde{u}/d\tilde{z} = f(\tilde{u})$ dependencies reported in literature for Newtonian jets [186,190]. The initial increase of the tensile stress with the speed corresponds to the viscous regime with the stress $\tilde{\sigma}_E(\tilde{z}) \sim \tilde{z} \sim \sqrt{\tilde{u}}$ and the final decrease stands for the inertial regime with $\tilde{\sigma}_E \sim 1/\tilde{u}$ [cf. Eq. (5.8)].

The basic assumption of this work is that the onset of the jet oscillation corresponds to the onset of the DST regime at some lower DST threshold stress, which should from now be distinguished from the upper DST threshold stress above which the stress again exhibits a smooth variation with the shear (or extension) rate. To check this point, we need to introduce a constitutive rheological equation for a DST fluid under extensional flow within the jet. As it follows from particle level simulations [124], the S-shape of the flow curves (typically observed under shear [chapters 3 and 4]) is also expected under extension. At such condition, the Wyart and Cates (WC) model [107] (originally developed for shear flows) could be extended to extensional flow. Recall that the WC model is based on the assumption of a continuous transition between fully lubricated contacts between particles at low stresses and fully frictional contacts at high stresses with a built-up of a dense contact network [chapter 3, Appendix E]. The conceptual basis of this model seems to hold in extensional flow, as inferred from the simulations of the suspension microstructure [124]. We have to bear in mind that the WC model describes only steady-state flows. It anticipates the stress range of the unstable flow but is unable to describe the flow fluctuations. However, as stated above, the assumption of the steady-state condition should still be adequate for finding, at least semi-quantitatively, the onset of the jet instability. Thus, extending the steady-state WC model to extensional flow, we get the following expression for the relative extensional viscosity, $\eta_{E,r} = \eta_E/(3\eta_0)$:

$$\eta_{E,r}(\tilde{\sigma}_E) = \left(\frac{1 - \varphi_p / \varphi_{Lub}}{1 - \varphi_p / \varphi_J(\tilde{\sigma}_E)} \right)^2 \quad (5.10)$$

$$\varphi_J(\tilde{\sigma}_E) = \varphi_{Fr} f(\tilde{\sigma}_E) + \varphi_L (1 - f(\tilde{\sigma}_E)) \quad (5.11)$$

$$f(\tilde{\sigma}_E) = \exp\left(-\left(\frac{\tilde{\sigma}_{E,c}}{\tilde{\sigma}_E}\right)^\Lambda\right) \quad (5.12)$$

where $\varphi_p = 0.68$ (corresponding to 68 % vol) is the CC particle volume fraction; $\varphi_J(\tilde{\sigma}_E)$ is the so-called jamming volume fraction of the suspension particles depending on the proportion $f(\tilde{\sigma}_E)$ of frictional versus lubricated contacts between particles; φ_{Fr} and φ_{Lub} are two limiting values of φ_J , corresponding to fully frictional or fully lubricated contacts; $\tilde{\sigma}_{E,c}$ is the characteristic stress of the DST transition in extension, normalized by $[\sigma_E] = \rho g R_0$; $\tilde{\sigma}_{E,c}$ approaches the DST threshold $\tilde{\sigma}_{E,l}$ at high values of the stretching exponent L . The factor $(1 - \varphi_p/\varphi_{Lub})$ in the numerator of Eq. (5.10) appears because the relative viscosity was not introduced with respect to the viscosity of the suspending liquid (water) of the CC suspension but with respect to the Newtonian suspension viscosity $\sim(1 - \varphi_p/\varphi_{Lub})^{-2}$ at low extensional rates. The equation (5.12) is one of the simplest empirical laws for the fraction of frictional contacts used in the literature and is slightly different from Eq. (3.28) used in chapter 3.

For the case of the DST fluid, we conducted the backward integration of Eq. (5.6) replacing $\eta_{E,r}$ by Eq. (5.10). The theoretical flow curves in extension are plotted in dimensionless form in Figure 5.9b, where the dimensionless extensional rate on the abscissa axis is the function of $\tilde{\sigma}_E$ calculated as $\tilde{\epsilon} = \tilde{\sigma}_E / \eta_{E,r}(\tilde{\sigma}_E)$. All the flow curves were simulated at the CC particle volume fraction $\varphi_p = 0.68$, used in experiments, the packing fractions $\varphi_{Fr} = 0.72$ and $\varphi_{Lub} = 0.69$ found in chapter 3, Appendix E, and at two values $L=5$ and 50 of the stretching exponent.

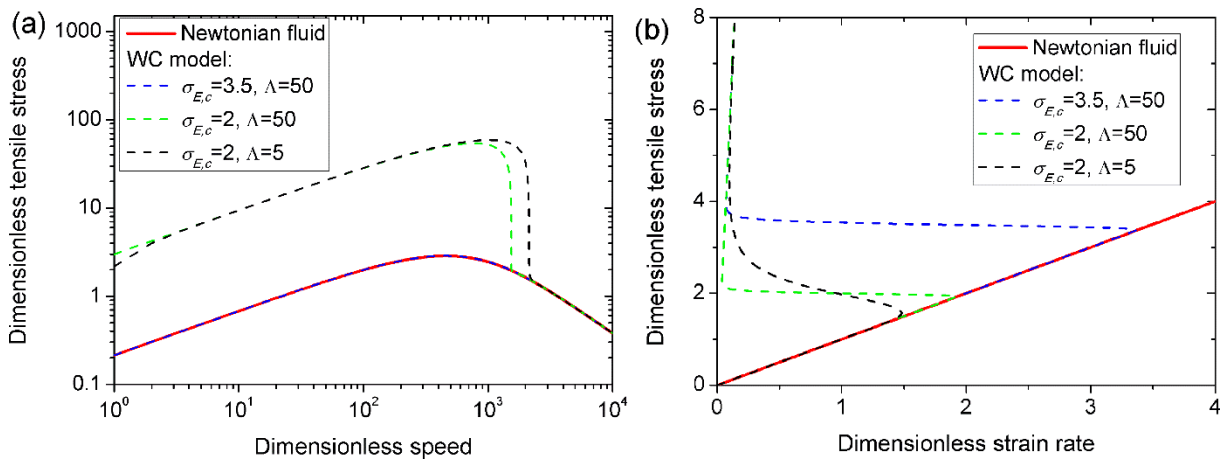


Figure 5.9 Theoretical stress profile (in log-log scale) along the jet of the CC particle suspension in terms of the dimensionless tensile stress as function of the dimensionless jet speed (a). Theoretical flow curves for the extensional rheology of the CC particle suspension (b). Both plots (a) and (b) are made for the Newtonian jet (red solid line) and for the DST WC rheological model (dashed lines) with different values of $\tilde{\sigma}_{E,c}$ and Λ parameters.

The shape of the simulated flow curves in extension is qualitatively similar to the shape of the shear flow curves [cf. chapters 3 and 4] at a relatively high value $\Lambda = 50$ of the stretching exponent (green and blue dashed lines in Figure 5.9b). Furthermore, the value $\Lambda = 50$ provides

the DST threshold stress $\tilde{\sigma}_{E,l}$ very close to the characteristic stress $\tilde{\sigma}_{E,c}$ intervening into Eq. (5.12). Anyway, both values of $\Lambda = 5$ and 50 provide a linear initial section of the flow curve extending up to the DST threshold. This linear section has the same slope at both Λ values corresponding to the relative extensional viscosity $\eta_{E,r}(\tilde{\sigma}_E) = 1$, as expected for the Newtonian regime below the DST transition.

For calculation of the tensile stress profile along the jet, we have chosen two characteristic values of the characteristic stress, the first one $\tilde{\sigma}_{E,c} = 2$ being lower than the peak value $\tilde{\sigma}_{E,m} \approx 2.85$ of the Newtonian $\tilde{\sigma}_E(\tilde{u})$ curve (red solid line in Figure 5.9a), and the second one, $\tilde{\sigma}_{E,c} = 3.5$ being higher than $\tilde{\sigma}_{E,m}$. The value $\tilde{\sigma}_{E,c} = 3.5 > \tilde{\sigma}_{E,m}$ at $\Lambda = 50$ provides the tensile stress profile perfectly collapsing to the Newtonian profile (compare blue dash and red solid lines in Figure 5.9a). This is expected because at $\tilde{\sigma}_{E,c} = 3.5$, the tensile stress does not achieve the lower DST threshold all along the jet and the suspension rheology remains perfectly Newtonian, as inferred from Figure 5.9b. On the other hand, the value $\tilde{\sigma}_{E,c} = 2 < \tilde{\sigma}_{E,m}$ at $\Lambda = 50$ provides a strong change in the tensile stress profile (green dashed line in Figure 5.9a). Recalling that the profile is obtained by the backward integration, the $\tilde{\sigma}_E(\tilde{u})$ curve follows the Newtonian profile (red solid line) when the speed decreases from its terminal value $\tilde{u}_\infty = 10^4$ up to some critical value \tilde{u}_c and the tensile stress increases from $\tilde{\sigma}_E(\tilde{u}_\infty) = 3/(32\varepsilon\tilde{u}_\infty)$ [Eq. (5.8)] up to a value of the lower DST threshold $\tilde{\sigma}_{E,l} \approx \tilde{\sigma}_{E,c} = 2$. At lower speeds, $\tilde{u} < \tilde{u}_c$, the tensile stress experiences a sharp (but mathematically continuous) increase until reaching a peak value $\tilde{\sigma}_{E,m} \approx 50$ being an order of magnitude higher than the peak value $\tilde{\sigma}_{E,m} \approx 2.85$ of the Newtonian profile. It is quite intuitive to suppose that the surface of the tensile stress jump cannot sustain steady-state and likely moves along the jet with some speed. This surface is likely subject to corrugation instability by analogy with propagation of the shock wave front, when initially flat horizontal front develops growing wavy patterns [190]. This could lead to asymmetric shear stresses that are expected to bend initially straight jet. However, at this moment, we have not managed to formulate the linear stability analysis proving this hypothesis. Notice that decreasing the value of the stretching exponent to $\Lambda = 5$ allows a slightly broader region of the tensile stress profile above the DST transition (black dashed line in Figure 5.9a) with the stress jump always occurring at the lower DST threshold $\tilde{\sigma}_{E,l} \approx 1.6$ which is somewhat lower to the imposed value $\tilde{\sigma}_{E,c} = 2$ of the characteristic DST stress in WC model [cf. black dashed curve in Figure 5.9b]. In summary, whatever Λ and $\tilde{\sigma}_{E,c}$ values chosen in simulations, the tensile stress jump and, presumably, the jet instability occur only if the lower DST threshold

stress $\tilde{\sigma}_{E,l}$ is lower than the peak value $\tilde{\sigma}_{E,m} \approx 2.85$ of the Newtonian stress profile. In terms of dimensional magnitudes, this gives the DST tensile stress $\sigma_{E,l} \lesssim 143$ Pa comparable to the DST shear stress $\sigma_c \approx 20 - 50$ Pa measured in plate-plate or mixer type shear rheometry [Figure 3.2c].

Notice finally that the slender jet approximation used in the present study along with the backward integration scheme are not valid for initial part of the jet, $z \lesssim R_0$ and lead to incorrect values of the tensile stress at the tube outlet ($z = 0$) for both Newtonian and shear thickening jets (cf. non-zero $\tilde{\sigma}_E$ values at the ordinate axis in Figure 5.9a). However, this artefact has a minor influence on the shape of the stress profile at $z \gtrsim R_0$.

5.3.2 Effect of fibers on jet stability

Let us now inspect the effect of fiber addition to the tensile stress profile along the jet. From now, we will restrict our analysis to the Newtonian case below DST in order to compare the threshold stress $\sigma_{E,l}$ with the peak value $\sigma_{E,m}$ of the Newtonian stress profile. The addition of fibers impacts the relative extensional viscosity $\eta_{E,r}$ in Eqs. (5.6) and (5.9) and the parameter e , in which the low-shear viscosity η_0 of the shear thickening matrix (CC suspension) should be replaced by the shear viscosity $\eta = \eta_0 \eta_r$ of the CC-PA mixture: $\varepsilon = \rho^2 g R_0^3 / (1024 (\eta_0 \eta_r)^2)$ with η_r being the relative shear viscosity of the PA fiber suspension with respect to the low-shear viscosity of the shear thickening matrix. In the Newtonian regime below DST, both relative viscosities $\eta_{E,r}$ and η_r are stress-independent but depend on the volume fraction φ_f of fibers and on their orientation. As in experiments we do not have access to fiber orientation, we will consider two limiting cases of isotropic orientation and fully aligned orientation when all the fibers are parallel to the extension axis (jet axis z in Figure 2.15b in chapter 2). The values of $\eta_{E,r}$ and η_r are obtained using the rheological model of Phan-Tien and Graham (PTG) model [167] developed for a wide concentration range of fiber suspensions and slightly modified in chapter 3, Appendix A:

$$\eta_r = \frac{\eta}{\eta_0} = 1 + 2\varphi_f + G\psi_S \quad (5.13)$$

$$\eta_{E,r} = \frac{\eta_E}{3\eta_0} = 1 + 2\varphi_f + \frac{1}{3}G\psi_E \quad (5.14)$$

$$G = \frac{\varphi_f(2-\varphi_f/\varphi_m) r^2 f^{\parallel}(r)}{3(1-\varphi_f/\varphi_m)^2 \ln(2r)}, \quad f^{\parallel}(r) = \frac{1+0.64/\ln(2r)}{1-1.5/\ln(2r)} + 1.659/(\ln(2r))^2 \quad (5.15)$$

where $\psi_S = A_{1212}$ and $\psi_E = A_{1111}$ are the shear and extensional components of the 4th rank fiber orientation tensor \mathbf{A} (the subscripts 1 and 2 stand for the velocity and the velocity gradient directions, respectively), whose values are summarized in Table 5.1 for two chosen fiber orientations; $\varphi_m = 5.4/r$ is the maximum packing fraction of the fiber suspension taken at the upper limit of the granular suspension of rods [12]. Notice that the relative shear and extensional viscosities take the same value for the isotropic fiber orientation.

Table 5.1 Parameters of the CC-PA mixtures related to the tensile stress calculations.

Fiber volume fraction/ orientation	ψ_S	ψ_E	z_m (mm)	$\sigma_{E,m}$ (Pa)
$\varphi_f = 0$ (no fibers)	N/A	N/A	53.4	143
$\varphi_f = 1$ % vol (isotropic)	$\frac{1}{15}$	$\frac{1}{5}$	77.7	253
$\varphi_f = 1$ % vol (aligned)	$\frac{0.315}{r_e} \approx 0.011^*$, $r_e = \frac{1.24r}{\ln^{1/2} r}$	1	87.3	394

* The ψ_S parameter for the aligned orientation in a shear flow through the tube (from which the jet flows out) corresponds to the solution of Leal and Hinch [168] for the tumbling rods at vanishing Brownian or hydrodynamic rotary diffusivity

The stress profile in terms of the dimensional $\sigma_E(z)$ -dependency is plotted in Figure 5.10 for the CC suspension without PA fibers (red line) and CC-PA mixture at $\varphi_f = 1$ % vol for isotropic (blue line) and aligned (green line) fiber orientations. Addition of fibers leads to a substantial increase of the stress level along the jet and shifts the stress maximum to higher z values. This is easily explained by a larger viscosity of the mixture, which results to a steeper initial increase of the tensile stress and allows extension of the viscous regime to higher axial positions. Furthermore, the aligned fiber orientation promotes a higher extensional viscosity [129] and, consequently, the higher stress level in the jet than the isotropic orientation. For quantitative comparison, the peak values of the tensile stress $\sigma_{E,m}$ and corresponding axial position z_m are provided in Table 5.2.

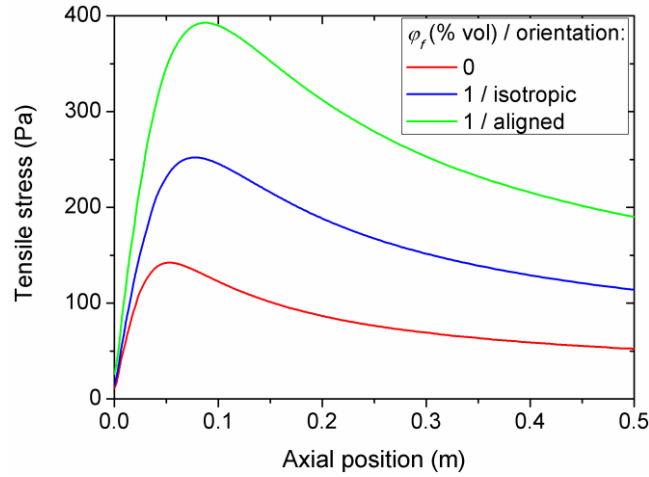


Figure 5.10 Theoretical stress profiles along the jet in terms of the tensile stress as a function of the axial position along the jet for the CC suspension without fibers and CC-PA mixtures at $\varphi_f = 1\%$ vol and two different fiber orientations.

Increasing $\sigma_{E,m}$ values with addition of fibers presumably increases the stress range $\Delta\sigma_E = \sigma_{E,m} - \sigma_{E,l}$ of the DST regime within the jet. However, the lower DST threshold stress in the CC-PA mixture is expected to increase with the fiber volume fraction that could reduce the DST interval $\Delta\sigma_E$. The increasing $\sigma_{E,l}(\varphi_f)$ -dependency is expected to have a similar physics as the increasing $\sigma_c(\varphi_f)$ -dependency revealed in shear flows [Figures 3.7b, 4.5b]. As discussed in chapter 3, this effect is related to local shear rates and local stress levels in the pores of the fiber network filled with a shear thickening matrix (CC suspension). This effect is captured semi-quantitatively by the homogenization approach of Chateau et al. [158] extended to the controlled stress shear rheology in [chapter 3, Appendix A]. Extrapolation to the axisymmetric extension within the jet is straightforward and gives the following expression for the lower DST threshold stress $\sigma_{E,l}(\varphi_f)$ in the CC-PA mixture as function of the DST threshold stress $\sigma_{E,l}(0)$ in the CC matrix:

$$\sigma_{E,l}(\varphi_f) = \sigma_{E,l}(0)\sqrt{(1 - \varphi_f)\eta_{E,r}(\varphi_f)} \quad (5.16)$$

It is important to stress that equation (5.16) is a mixture of the three following theoretical models: (a) the WC model [107] capturing the DST transition in spherical particle suspensions; (b) the PTG model [167] developed for the Newtonian fiber suspensions, and (c) the homogenization approach [158] developed for particle dispersions in non-Newtonian solvents. Such a combination needs justification. The WC model (typically applied to suspensions of spheres) is believed to apply to the sphere-fibers mixtures as long as the four following conditions are accomplished: (i) the size of CC particles is a few times smaller than the minor size (diameter) of PA fibers (scale separation condition); (ii) DST is generated in the CC

particles suspension (shear thickening matrix) filling the space between PA fibers; (iii) the fibers are added at concentrations below the percolation limit, so that they enhance the mixture viscosity but do not generate DST themselves; (iv) there is no specific interactions between CC particles and PA fibers. At these conditions, verified in our experiments, both WC and PTG models can be extended to the sphere-fiber mixtures upon appropriate rescaling of the shear rate and the shear stress, provided by the homogenization approach. In its original form, this approach postulates that the viscosity η of the mixture is equal to the product of the matrix viscosity $\eta_m(\dot{\gamma}_{loc})$ evaluated at some local shear rate $\dot{\gamma}_{loc}$ by the relative viscosity η_r of a fiber suspension dispersed in a Newtonian solvent. In the present case of the controlled stress extensional flow, the matrix extensional viscosity $\eta_{E,m}(\sigma_{E,loc})$ should be considered at a local tensile stress $\sigma_{E,loc}$, by analogy with Eq. (3.8), which results in Eq. (5.16) for the lower DST threshold.

To get quantitative evaluation of the $\sigma_{E,l}(\varphi_f)$ -dependency using Eq. (5.16), we need to know the lower DST threshold $\sigma_{E,l}(0)$ of the pure CC suspension. It can be evaluated from the minimal jet length, $L_{min} \approx 60$ mm, above which the jet exhibits the lateral drift instability [section 5.1.1]. In theory, the lower DST threshold corresponds to the stress level σ_E of the stress profile curve (red line in Figure 5.10) taken at $z = L_{min}$. In practice, we have to take into account fringing effects related to the jet deceleration near the point where it hits the Petri dish. It seems more reasonable to replace the full jet length L_{min} by the axial distance $L_{eff} \approx 35$ mm between the tube outlet and the point of the narrowest jet diameter. The lower DST threshold is then estimated to be about $\sigma_{E,l}(0) = \sigma_E(z = L_{eff}) \approx 133$ Pa. We have to bear in mind that this a very rough estimation subject to the uncertainty of the considered fringing effect and to possible errors of the theoretical evaluation of the stress profile. Injecting the $\sigma_{E,l}(0)$ -value to Eq. (5.16), we are able to plot the $\sigma_{E,l}(\varphi_f)$ -dependency and compare it to previously evaluated $\sigma_{E,m}(\varphi_f)$ -dependency for a particular case of the isotropic fiber orientation – see Figure 5.11a.

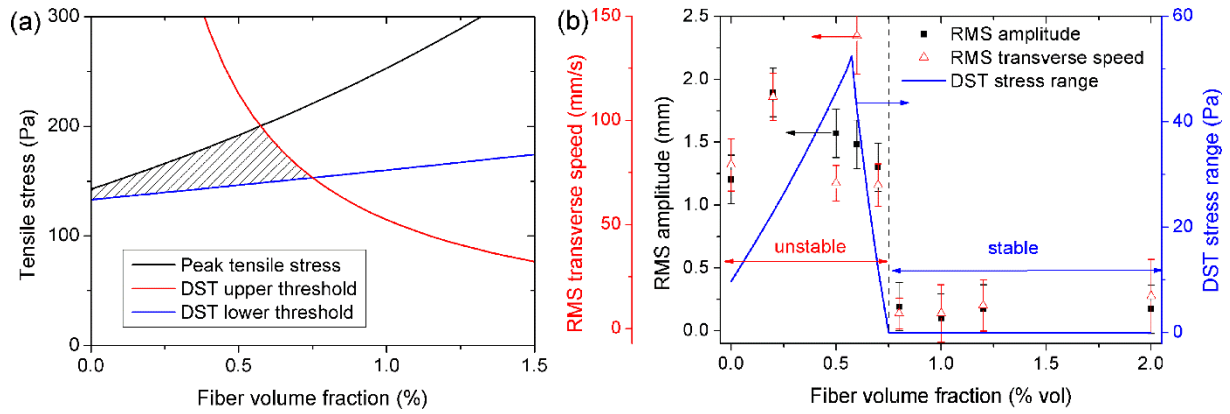


Figure 5.11 Theoretical phase diagram of the jet stability with the hatched region indicating jet instability against lateral oscillations (DST regime) and non-hatched regions standing for stable jets (stable steady-state flow) (a). Experimental dependencies of the RMS amplitude and RMS transverse speed (left ordinate axes) on the fiber volume fraction compared to the semi-empirical dependency of the DST stress range (right ordinate axis) on the fiber volume fraction (b).

Evaluation shows that the peak tensile stress $\sigma_{E,m}(\varphi_f)$ exhibits a stronger increase with the fiber volume fraction, as compared to the lower DST threshold stress $\sigma_{E,l}(\varphi_f)$. This holds for the whole experimental range of φ_f and also for the aligned fiber orientation (curves not shown for brevity). This implies that, as already supposed, the stress range $\Delta\sigma_E = \sigma_{E,m} - \sigma_{E,l}$ of the DST regime within the jet progressively increases with the fiber volume fraction. Thus, the fiber addition is expected to amplify the jet lateral oscillations in contrast to experimental observations showing a full stabilization at $\varphi_f \geq 0.8$ %vol.

However, the DST regime can be bounded above by some upper DST threshold stress, $\sigma_{E,u}$, which is commonly ascribed to the capillary stress in the case of shear flows with free surface [100] (as in plate-plate or cylindrical Couette geometries). In that case, through frictional particle network, the applied shear stress induces a strong normal stress, which is no longer balanced by the ambient air pressure at the free surface but pushes the particles through the surface. The fluid menisci between poking particles at the free surface build a capillary pressure (stress), evaluated empirically as $p_c \approx \gamma/D_c$, with D_c being a characteristic size of the menisci between poking particles ($D_c \approx 10D_p$ for spherical particles of a diameter D_p). It has been experimentally confirmed that the applied shear stress, $\sigma \approx p_c$ corresponds to the end of the DST regime and the stress shows a modest increase with the shear rate above p_c [100]. Somewhat similar physics is supposed to hold in the present case of the extensional flow within the jet. The radial compressive stress σ_{rr} pushes the suspending liquid towards the jet centerline through a quasi-solid particle frictional network; this can “bare” the peripheral particles at the jet surface and create menisci between them resulting in a strong capillary pressure. By analogy

with shear flows with a free surface, the capillary pressure is expected to prevent particles from escaping the surface until the stress level in the suspension overcomes the characteristic capillary pressure. It is therefore reasonable to assign the capillary pressure to the upper DST threshold stress in extensional jet flows: $\sigma_{E,u} \sim p_c \sim \gamma/D_c$.

Since the fibers are much larger than the CC particles, the characteristic size D_c of the menisci is expected to be defined by some effective size of the fibers. This size should depend on their orientation and possibly the volume fraction and agglomeration state. Visual inspection of Figure 5.2 reveals appearance of short-scale ($\lesssim 1$ mm) irregularities on the jet surface of CC-PA mixtures, different from blob-and-necks reported in section 5.2.1 and having wavelengths $\lambda \gtrsim 10$ mm. These irregularities seem to reflect poking of PA fibers through the jet surface; they are absent (or undistinguishable at the current image resolution) for suspensions of CC particles without fibers and their size increases with the PA fiber volume fraction. This could be attributed to existence of sparse fiber flocs whose size likely increases with the fiber volume fraction. Notice that formation of pulp fiber flocs within the free jets of the papermaking furnish is a common phenomenon in the papermaking industry [191]. Unfortunately, space resolution of our CCD camera was too poor to get reliable measurements of the floc size distribution. We can tentatively suppose that the floc size and consequently the characteristic menisci size D_c linearly increases with the fiber volume fraction $D_c \propto \varphi_f$, in qualitative agreement with pulp flocs behavior [191]. This leads to the following semi-empirical scaling for the upper DST threshold stress:

$$\sigma_{E,u} = \frac{\gamma}{D_{c,1}\varphi_f} \quad (5.17)$$

where $D_{c,1}$ is a size scale that should be determined from experiments. In practice we can determine $D_{c,0}$ by matching the lower and the upper DST thresholds at the fiber volume fraction $\varphi_{f,c} \approx 0.75$ % vol, above which the jet becomes stable. Equalizing the right-hand sides of Eqs. (5.16) and (5.17) at $\varphi_f = \varphi_{f,c}$, we get $D_{c,1} \approx 63$ mm.

The upper DST threshold stress appears to be inversely proportional to the fiber volume fraction [Eq. (5.17)], as a direct consequence of our hypothesis on the characteristic size, $D_c \propto \varphi_f$. Of course, this scaling fails at very low fiber volume fractions $\varphi_f \ll \varphi_{f,c} \approx 0.75$ % vol when D_c is expected to scale with the CC particle size $D_p \approx 5.5$ μm . The semi-empirical dependency $\sigma_{E,u}(\varphi_f)$ -dependency is shown in Figure 5.11a by a red line. We see that the upper DST threshold stress $\sigma_{E,u}(\varphi_f)$ becomes lower than the lower DST stress $\sigma_{E,l}(\varphi_f)$ above a critical

fiber volume fraction, $\varphi_{f,c} \approx 0.75$ % vol. Such a crossover means that DST cannot occur above $\varphi_{f,c}$ that likely results in stable jets at $\varphi_f > \varphi_{f,c}$ in agreement with experiments. Thus, the DST regime within the jet is bounded from above by either the peak tensile stress (black curve in Figure 5.11a) or the upper DST threshold (red curve) and is bounded from below by the lower DST threshold (blue curve). The hatched zone in Figure 5.11a represents a DST region, which is likely equivalent to the region of the jet instability against lateral oscillations. In this context, the whole Figure 5.11a can be considered as a phase diagram of the jet stability, with the non-hatched region corresponding to stable jets.

Once the upper DST threshold is taken into account, the stress range of the DST regime within the jet can be evaluated as a vertical distance between the upper and lower bounds of the hatched zone in Figure 5.11a giving the following expression:

$$\Delta\sigma_E(\varphi_f) = \begin{cases} \min(\sigma_{E,m}, \sigma_{E,u}) - \sigma_{E,l}, & \text{at } \varphi_f \lesssim \varphi_{f,c} \\ 0, & \text{at } \varphi_f \gtrsim \varphi_{f,c} \end{cases} \quad (5.18)$$

It is quite intuitive to expect that the intensity of the jet lateral oscillations at $\varphi_f \lesssim \varphi_{f,c}$ is somehow correlated to the DST stress range $\Delta\sigma_E$. To check this point, we evaluated the RMS values of the lateral drift amplitude, x_{RMS} and of the transverse jet speed, v_{RMS} , as adequate integral parameters describing the intensity of jet oscillations [cf. section 2.2.3]. Notice that the kinetic energy (by unit jet volume) of lateral oscillations can be simply evaluated as $e_{cin} = (1/2)\rho v_{RMS}^2$. The $x_{RMS}(\varphi_f)$ and $v_{RMS}(\varphi_f)$ experimental dependencies are shown in Figure 5.11b and compared with the theoretical $\Delta\sigma_E(\varphi_f)$ -dependency (blue line) with $\Delta\sigma_E$ assigned to the right ordinate axis. Both x_{RMS} and v_{RMS} seem to show an initial increase with the fiber volume fraction φ_f followed by a decrease and drastically fall at $\varphi_f = 0.7 - 0.8$ % vol, as the jet becomes visually stable. Figure 5.11b confirms that non-monotonic dependencies $x_{RMS}(\varphi_f)$ and $v_{RMS}(\varphi_f)$ dependencies correlate qualitatively with the concentration dependency of the stress range $\Delta\sigma_E(\varphi_f)$ of the DST regime. This is quite logical issue: larger the DST stress interval, higher is the intensity of the jet lateral fluctuations. We consider it as another argument supporting the basic hypothesis on the rheological (DST) origin of the observed jet instability.

5.3.3 Break-up length

Jet stabilization above the critical fiber volume fraction still cannot explain why the jet breaks up at relatively short lengths without any transverse oscillation. To inspect this behavior, we evaluate the experimental break-up length, L_b as the axial distance from the tube outlet

above which the rupture probability in Figure 5.3b departs from zero. The experimental $L_b(\varphi_f)$ -dependency is plotted in Figure 5.12 and confirms a progressive decrease of the rupture length with fiber volume fraction stated in section 5.3.2.1.

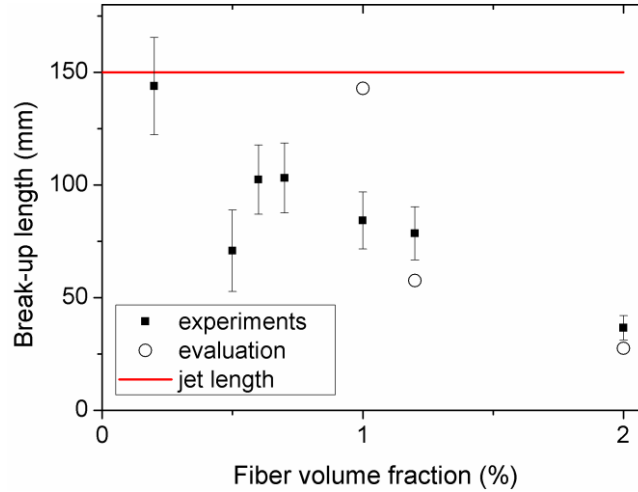


Figure 5.12 Experimental and evaluated break-up length as function of the fiber volume fraction. The red horizontal line stands for the jet length.

Firstly, we can compare our experimental L_b - values with the break-up length of the RP instability. The gravity stretching of jets is known to considerably increase the break-up length and physically relevant expression for L_b has been provided by Javadi et al. [192]: $L_b \approx 172(gu_0^2R_0^4\eta_0^4/\gamma^4)^{1/3}$, valid in the limit of high Ohnesorge numbers $Oh = \eta_0(\rho\gamma R_0)^{-1/2} \gg 1$, respected in our experiments. Taking into account the scaling $u_0 \propto 1/\eta_0$ [Eq. (2.26) in chapter 2] for the jet velocity at the tube outlet, one finds $L_b \propto \eta_0^{2/3}$ that contradicts to our observations of decreasing break-up length with increasing low-shear viscosity η_0 of the CC-PA mixtures at increasing fiber volume fractions. Quantitatively, the last expression gives the theoretical break-up length ranging between about 300 mm and 430 mm, which is much larger than the experimental jet height $L \approx 150$ mm. This discrepancy, along with the wave speed $v_s \gg u$ [section 5.2.2] allows us to definitely rule out the RP instability as a possible reason of the jet break-up.

A similar break-up is usually observed for the jet of Newtonian concentrated suspensions of spherical particles and is attributed to finite size effect when the jet diameter thins under gravity up to a size equal to ten particle diameters [184]. The factor of 10 has been confirmed for several datasets at different particle diameters and suspending liquid viscosities. In our case of CC-PA mixtures, fibers are much larger than the CC particles and the characteristic size $D_c \propto \varphi_f$ of the fiber flocs is by far an appropriate scale of the jet diameter corresponding to the jet break-up.

We can therefore determine the theoretical jet break-up length L_b as an axial position at which the jet average diameter is:

$$\langle d \rangle = D_c = D_{c2} \varphi_f \quad (5.19)$$

where D_{c2} is a size scale that should be determined from experiments. We evaluated the break-up length using experimental dependencies $\langle d \rangle (z)$ of the jet diameter on the axial distance [Figure 5.3a]. Equalizing $\langle d \rangle (z)$ from Figure 5.3a to the right-hand part of Eq. (5.19), we get semi-empirical L_b values for each fiber volume fraction φ_f at different D_{c2} values. The final semi-empirical $L_b(\varphi_f)$ -dependency (corresponding to the finite particle size scenario of the jet break-up) is obtained by choosing a D_{c2} value that provides the closest agreement with experimental $L_b(\varphi_f)$ curve. This value is $D_{c2} \approx 1$ mm under condition that φ_f in Eq. (5.19) is substituted in (% vol) units. Such evaluation gives discrete values of L_b at each experimental value of the fiber volume fraction. These discrete values are added to Figure 5.12 as open circle symbols. We observe a qualitative agreement between experiments and evaluation, both showing the decrease of the break-up length with the fiber volume fraction that is ascribed to increasing critical jet diameter [Eq. (5.19)] corresponding to the jet rupture. Notice that at relatively weak fiber volume fractions $\varphi_f \leq 0.7$ %vol, the jet does not thin down the theoretical critical diameter [Eq. (5.19)], and the model does not predict jet rupture at $\varphi_f \leq 0.7$ %vol in contrast to experiments. This discrepancy is likely related to very rough evaluation of the fiber floc size $D_c \propto \varphi_f$ whose scaling should be checked by recording the jet flow at higher space resolution. At this stage, we can claim that an increasing size of the jet surface roughness (fiber floc size) gives a good explanation for the experimental concentration dependencies of the oscillation amplitude ($x_{RMS}(\varphi_f)$ and $v_{RMS}(\varphi_f)$, Figure 5.11b) and break-up length ($L_b(\varphi_f)$, Figure 5.12).

5.4 Conclusion

This chapter is devoted to the detailed study of the jet instability occurring in concentrated non-Brownian sphere-fiber mixtures presumably above the DST transition in extensional flow. In experiments, we employed either an aqueous suspension of CC isotropic-shaped particles or aqueous mixtures of CC particles with PA fibers at CC and PA volume fractions, respectively, $\varphi_p = const = 68$ % vol and $\varphi_f = 0 - 2$ % vol. The jets of these fluids were subjected to a free fall under gravitational stretching at a constant flow rate. The jets were filmed with a high-speed camera and the stacks of the frames were processed with the MATLAB software in order to extract several quantitative characteristics of the jet dynamics. Evaluations of the tensile

stress profile along the jet allowed us to shed more light to the origin of the observed instability and to propose explanations of the effect of the fiber addition on the observed oscillation-to-break-up transition. The main results can be summarized as follows:

1. In the absence of PA fibers, direct visualization of falling jets of CC suspension reveals relatively strong lateral oscillations occurring for the jet lengths $L \gtrsim 6$ cm. Spatiotemporal diagrams show that the jet lateral drift $x(t, z)$ is accompanied by small but distinguishable undulations $\Delta d(t, z)$ of the jet diameter. 2D DFT analysis of $x(t, z)$ and $\Delta d(t, z)$ reveals approximately linear dispersion relations for propagation of lateral oscillations ($\omega \approx v_l k$) and diameter undulation ($\omega \approx v_s k$) reminiscent for non-dispersive waves. The wave speeds are (within experimental errors) similar for both wave types, $v_l \approx v_s \approx 0.9$ m/s, being much larger than the jet speed. Moreover, both $x(t, z)$ and $\Delta d(t, z)$ oscillations are observed within nearly similar wavelength range $\lambda \sim 0.01 - 0.15$ m bounded above by the jet length. This allows supposing both waves types to be of the same origin related to stress fluctuations above the DST transition, while the Rayleigh-Plateau instability for $\Delta d(t, z)$ is ruled out. The difference is that the diameter undulation propagates only downstream the jet, while the lateral oscillations propagate both downstream at $v_l \approx 0.9$ m/s and upstream at $v_l \approx -0.9$ m/s. The lateral drift amplitude (wave crest height) X_c decreases with the wave crest length $L_c \propto \omega \propto k$, with the dominant wavelength being equal to the jet length.
2. Adapting the WC model [107] to extensional flows, we predict abrupt (but mathematically continuous) increase of the tensile stress σ_E along the jet, at a location corresponding to the lower threshold stress $\sigma_{E,l}$ of the DST transition. Such a tensile stress jump is believed to be responsible for the jet instability by analogy with shock waves behaviors [190]. Above the DST transition, tensile stress fluctuations are expected to lead to fluctuation of the longitudinal and transverse velocity fields within the jet; the former being manifested through undulation of the jet diameter and the latter being perceived as jet transverse oscillations. Hence, linear and non-linear stability analysis is required to validate these hypotheses.
3. Addition of PA fibers to the CC suspension damps lateral oscillations at fiber volume fraction $\varphi_f \gtrsim 0.75$ %vol but favors ruptures along the jet at a critical break-up length L_b decreasing with φ_f . Such oscillation-to-break up transition is tentatively explained by the interplay between growing lower ($\sigma_{E,l}$) and decreasing upper ($\sigma_{E,u}$) DST threshold stress with increasing φ_f along with the jet thinning down the size of fiber flocs poking through the jet surface when the tensile stress overcomes the capillary pressure. The upper concentration limit, $\varphi_{f,c} \approx 0.75$ %vol, of the jet instability is fixed by the crossover of the two DST thresholds $\sigma_{E,l}$

and $\sigma_{E,u}$. The lower concentration limit is simply $\varphi_f = 0$ for any jet length $L \gtrsim 60$ mm because the tensile stress σ_E along the jet overcomes the lower DST threshold stress $\sigma_{E,l}$ at $\varphi_f = 0$. Our theoretical model allows plotting a (σ_E, φ_f) phase diagram of the jet stability and qualitatively captures the shapes of the concentration dependencies of the break-up length $L_b(\varphi_f)$, RMS oscillation amplitude $x_{RMS}(\varphi_f)$ and RMS transverse speed $v_{RMS}(\varphi_f)$. On the other hand, within statistical errors, the wave speeds are poorly affected by addition of fibers. This agrees with the model of vibrating solid string under gravitational stretching predicting the wave speed $v_l = \sqrt{gL/2}$ independent of any rheological parameters including the particle volume fraction. Surprisingly, experimental wave speed values $v_l = 0.9 \pm 0.2$ m/s are in a good quantitative agreement with the vibrating string model, $v_l \approx 0.87$ m/s, as already reported by Liard et al. [127]. Such agreement likely suggests solid-like behavior of the unstable jet above the DST transition.

4. Because of the jet opacity, we were unable to establish the effect of fiber orientation on the jet behavior. However, from evaluations of $\sigma_E(z)$ and $\sigma_{E,l}(\varphi_f)$, we could anticipate that the flow-aligned fibers provide distinguishable increase of the peak stress $\sigma_{E,m}$ and the lower DST threshold $\sigma_{E,l}$ with respect to the random orientation. However, random orientation better correlates with the particle poking scenario of the upper DST threshold and jet break-up (the fibers aligned along the jet surface would not result in significant jet surface “roughness” observed in experiments). In addition to it, in our previous study, the random fiber orientation gave better flow curve predictions in shear flows as compared to aligned orientation.

The results of this chapter are believed to be useful for both practical applications of shear thickening jets (in cement jet grouting, shear thickening polishing, abrasive jet cutting, mortar spraying, cement pumping, etc.) and academic research through detailed characterization of the new type of jet instability and alternative testing of the extensional rheology of DST fluids, as briefly outlined in Appendix (section 5.5). A separate study is needed to develop this rheometric method.

5.5 Appendix: a concept of the jet extensional rheometry

In experiments with free falling jets, one can record the flowing jet and using an image calculator measure the radius profile along the jet, $R(z)$. Knowing the jet velocity at the tube outlet u_0 , one has a direct access to the extension rate along the jet:

$$\dot{\epsilon}(z) = du/dz = u_0 R_0^2 d(R^{-2})/dz \quad (5.20)$$

The tensile stress profile can be obtained by rearranging Eqs. (5.2) - (5.4) and integrating along the jet length:

$$\sigma_E(z) \approx \rho(u_0 R_0^2)^2 R^{-4} (1 - (R/R_m)^2) - \rho g R^{-2} \int_{z_m}^z R^2 dz - \gamma R^{-1} (1 - R_m/R) \quad (5.21)$$

where z_m is the axial position of the minimal jet radius R_m (when the extension is cancelled by the compression some distance above the point where the jet hits the bottom surface). Then, the flow curve $\sigma_E = f(\dot{\epsilon})$ can be plotted in a parametric form $[\dot{\epsilon}(z); \sigma_E(z)]$, with the axial distance z being a parameter.

Conclusion and perspectives

A. Conclusion

This thesis work is an experimental and theoretical study on the discontinuous shear thickening (DST) in concentrated non-Brownian suspensions containing isotropic shaped particles and fibers. Our studied system consists of calcium carbonate (CC) suspension loaded with polyamide or glass fibers. This shear thickening mixture represents a model for fiber-reinforced cementitious materials broadly used in industrial applications. The main objective of this work is to study the DST phenomenon in the sphere-fiber mixtures and to analyze the effect of the fiber addition on the suspension rheology. In particular, we have studied the DST phenomenon in the context of mixing and pumping of cementitious materials loaded with fibers.

To simulate the mixing process, we conducted shear rheological experiments in a rotational rheometer using the mixture of CC-suspension with polyamide (PA) or glass rigid fibers and either conventional plate-plate geometry or a customized mixer type geometry with a double helix rotor tool. The results of the shear tests for the two geometries employed were remarkably different particularly on the critical stresses and the critical shear rates of the DST onset, which were much lower for the mixer type geometry. The addition of fibers to the shear thickening CC suspension also has a major impact to its rheology; at increasing fiber volume fractions, the DST threshold shifted to lower critical shear rates, which is obviously explained by the increase in the viscosity of the mixture, so that the shear rate to reach the DST onset stress decreased. Models based on the homogenization approach of Chateau et al. [158] and the reduced shear rate approach of Ohl and Gleissle [114] also validated the experimental observations satisfactorily. An approach adapted from the frictional particle contact model of Wyart and Cates [107] was also applied for our mixture but the predictions of the model above the DST transition revealed a considerable difference with the conducted shear experiments.

In order to simulate the effects of DST during the pumping of fiber-reinforced concrete in a construction site, a home-made pressure-controlled capillary rheometer was used for pressure-driven flows of the CC-suspension with PA-fibers at different fiber volume fractions. The results of the capillary rheometry were then compared with those of the rotational rheometry using the conventional cylindrical Couette geometry. Quantitatively, the flow curves obtained in capillary rheometry and cylindrical Couette geometry were relatively close to each other for low fiber volume fraction $\varphi_f \leq 1\%$ vol, However, for higher volume fractions, $\varphi_f \geq 2\%$ vol, the flow curves of the capillary rheometry showed much higher suspension viscosity (lower shear rates for a given shear stress) than those of the shear rheometry with cylindrical Couette geometry. We have explained this difference by the fact that starting from a fiber volume fraction $\varphi_f = 2\%$ vol, the microstructure of the suspension likely becomes significantly different in the capillary flow compared to the simple shear flow. The capillary rheometry results were also compared with the H-model predictions based on the homogenization approach of Château et al. [158]. The prediction came in agreement with experiments at $\varphi_f \leq 1\%$ vol, while the H-model fails to reproduce the experimental flow curves at $\varphi_f \geq 2\%$ vol.

Finally, in order to characterize the DST in extensional flows, encountered when the fiber-reinforced concrete exits the pumping line, we conducted experiments on the jet of CC-suspension with PA-fibers. The suspension jet was subject to tensile forces due to gravitational stretching. We characterized the instabilities of the jet both in its diameter variation and the lateral drift of the jet centerline from the vertical axis of the flow. For the first time and differently from the reported works in the literature, a two-dimensional Fourier analysis of the spatiotemporal maps of the jet instantaneous diameter and lateral drift was conducted. The Fourier analysis revealed propagation of non-dispersive waves associated to the jet centerline fluctuations and jet surface undulations and allowed us to obtain the wave speeds and amplitudes of these fluctuations. It was concluded that the CC- suspension jet, depending on its height, transits from a stable to an unstable state with viscoelastic instabilities occurring at the tensile stresses presumably above the DST threshold stress. On the other hand, the addition of PA-fibers with increasing volume fractions remarkably stabilizes the jet by modifying the viscosity of the mixture and thus influencing the threshold of the DST onset. However, the addition of fibers at high concentrations favors fractures in the jet giving a new form of instability, which can be explained by the thinning of the jet diameter down to the size of flow-induced fiber flocs visible on the jet surface.

B. Perspectives

The experimental and theoretical work carried out during this thesis has provided original results on the rheological behavior of shear thickening suspensions concentrated by fibers, we were able to characterize the phenomenon of DST and to describe its effects in different geometries and different flow types. However, it would be very interesting to complete our study with a deep analysis of the shear-induced microstructure of sphere-fiber mixtures using X-ray micro-tomography technique. It would also be interesting to conduct dynamic simulations at particles and fibers scale, as the simulations provide considerable insight into the microscopic physics of the DST transition. X-ray micro-tomography and particle level simulations will allow evaluating the spatial and orientational distributions of fibers orientation in the shear thickening matrix, as well as the spatial distribution of the contact network between the isotropic-shaped particles and will validate (or not) the fiber percolation scenario of the flow blockage above the fiber percolation threshold. Finally, the extrapolation of our results to the fiber-reinforced cement paste is believed to advance the cement production industry.

References

- [1] R. B. Bird, R. C. Armstrong, and O. Hassager, “Dynamics of polymeric liquids”, Fluid mechanics, second edition, Wiley, New York, vol. 1, p. 672, 1987.
- [2] F. A. Morrison, “Understanding rheology”, Oxford University Press, p.545, 2001.
- [3] H. A. Barnes, “Shear-thickening ("dilatancy") in suspensions of nonaggregating solid particles dispersed in Newtonian liquids”, Journal of Rheology, vol. 33, p. 329, 1989.
- [4] A. Einstein, “Eine neue Bestimmung der Moleküldimensionen”, Annalen der Physik, vol. 324, no.2, p. 289-306, 1906.
- [5] G. K. Batchelor et J. T. Green, “The hydrodynamic interaction of two small freely-moving spheres in a linear flow field”, Journal of Fluid Mechanics, vol. 56, no. 2, p. 375-400, 1972.
- [6] S. Gallier, E. Lemaire, F. Peters, et L. Lobry, “Rheology of sheared suspensions of rough frictional particles”, Journal of Fluid Mechanics, vol. 757, p. 514-549, 2014.
- [7] G. Y. Onoda and E. G. Liniger, “Random loose packings of uniform spheres and the dilatancy onset”, Physical Review Letters, vol. 64, no.22, p. 2727-2730, 1990.
- [8] G. D. Scott et D. M. Kilgour, “The density of random close packing of spheres”, Journal of Physics D: Applied Physics, vol. 2, no.6, p. 863-866, 1969.
- [9] H. Eilers, “Die Viskosität von Emulsionen hochviskoser Stoffe als Funktion der Konzentration”, Kolloid-Zeitschrift, vol. 97, no3, p. 313-321, 1941.
- [10] S. H. Maron and P. E. Pierce, “Application of ree-eyring generalized flow theory to suspensions of spherical particles”, Journal of Colloid Science, vol. 11, no.1, p.80-95, 1956.
- [11] I. M. Krieger and T. J. Dougherty, “A Mechanism for Non-Newtonian Flow in Suspensions of Rigid Spheres”, Transactions of The Society of Rheology, vol. 3, no. 1, p. 137–152, 1959.
- [12] M. J. Solomon and P. T. Spicer, “Microstructural regimes of colloidal rod suspensions, gels, and glasses”, Soft Matter, vol. 6, no. 7, p. 1391-1400, 2010.
- [13] J. F. Morris and F. Boulay, “Curvilinear flows of noncolloidal suspensions: The role of normal stresses”, Journal of Rheology, vol. 43, no.5, p. 1213, 1999.
- [14] É. Guazzelli and O. Pouliquen, “Rheology of dense granular suspensions,” Journal of fluid mechanics, vol. 852, p. 11-173, 2018.
- [15] F. G. Maria and A. Acrivos, “Shear-induced structure in a concentrated suspension of solid spheres”, Journal of Rheology, vol. 24, p.799, 1980.

-
- [16] D. Leighton and A. Acrivos, “The shear-induced migration of particles in concentrated suspensions”, *Journal of Fluid Mech*, vol. 181, p.415, 1987.
- [17] R. J. Phillips, R. C. Armstrong, R. A. Brown, A. L. Graham, and J. R. Abbott, “A constitutive equation for concentrated suspensions that accounts for shear-induced particle migration”, *Physics of Fluids A: Fluid Dynamics*, vol. 4, p.30, 1992.
- [18] A. Acrivos, “Bingham award lecture - 1994 shear-induced particle diffusion in concentrated suspensions on noncolloidal particles”, *Journal of Rheology*, vol. 39, p.813, 1995.
- [19] A. Shauly, A. Wachs, and A. Nir, “Shear-induced particle migration in a polydisperse concentrated suspension”, *Journal of Rheology*, vol. 42, p.1329, 1998.
- [20] U. Schaflinger, A. Acrivos, and H. Stibi, “An experimental study of viscous resuspension in a pressure-driven plane channel flow”, *International Journal of Multiphase Flow*, vol. 21, no.4, p.693–704, 1995.
- [21] J. T. Norman, H. V. Nayak, and R. T. Bonnecaze, “Migration of buoyant particles in low-Reynolds-number pressure-driven flows”, *Journal of Fluid Mechanics*, vol. 523, p.1–35, 2005.
- [22] A. Kumar and M. D. Graham, “Mechanism of Margination in Confined Flows of Blood and Other Multicomponent Suspensions”, *Physical Review Letters*, vol. 109, no. 10, p. 108102, 2012.
- [23] P. V. Lagrée, and D. Lhuillier, “The Couette flow of dense and fluid-saturated granular media”. *European Journal of Mechanics-B/Fluids*, vol. 25, no. 6, p. 960-970, 2006, Elsevier Masson SAS. All rights reserved.
- [24] O. Reynolds, “LVII. On the dilatancy of media composed of rigid particles in contact. With experimental illustrations”, *The London, Edinburgh, and Dublin Philosophical Magazine and Journal of Science*, vol. 20, no. 127, p. 469-481, 1885.
- [25] M. K. Lyon, and L. G. Leal, “An experimental study of the motion of concentrated suspensions in two-dimensional channel flow. Part 1. Monodisperse systems”, *Journal of fluid mechanics*, vol. 363, p. 25-56. 1998.
- [26] M. Frank, D. Anderson, E. R. Weeks and J. F. Morris, “Particle migration in pressure-driven flow of a Brownian suspension”, *Journal of Fluid Mechanics*, vol. 493, p. 363-378, 2003.
- [27] G. K. Batchelor, “Sedimentation in a dilute dispersion of spheres”. *Journal of fluid mechanics*, vol. 52, no. 2, p. 245-268, 1972.
-

-
- [28] J. F. Richardson, and W. N. Zaki, "The sedimentation of a suspension of uniform spheres under conditions of viscous flow", *Chemical Engineering Science*, vol. 3, no. 2, p. 65-73, 1954.
- [29] B. D. Marsh, and J. R. A. Pearson, "The measurement of normal-stress differences using a cone-and-plate total thrust apparatus". *Rheologica Acta*, vol. 7, no. 4, p. 326-331, 1968.
- [30] I. E. Zarraga, D. A. Hill and D. T. Leighton JR, "The characterization of the total stress of concentrated suspensions of noncolloidal spheres in Newtonian fluids". *Journal of Rheology*, vol. 44, no. 2, p. 185-220, 2000.
- [31] É. Couturier, F. Boyer, O. Pouliquen, and É. Guazzelli, "Suspensions in a tilted trough: second normal stress difference", *Journal of Fluid Mechanics*, vol. 686, p. 26-39, 2011.
- [32] S. Garland, G. Gauthier, J. Martin, and J. F. Morris, "Normal stress measurements in sheared non-Brownian suspensions", *Journal of Rheology*, vol. 57, no. 1, p. 71-88, 2013.
- [33] C. Gamonpilas, J. F. Morris, and M. M. Denn, "Shear and normal stress measurements in non-Brownian monodisperse and bidisperse suspensions", *Journal of Rheology*, vol. 60, no. 2, p. 289-296, 2016.
- [34] O. Maklad and R. J. Poole, "A review of the second normal-stress difference; its importance in various flows, measurement techniques, results for various complex fluids and theoretical predictions", *Journal of Non-Newtonian Fluid Mechanics*, vol. 292, p. 104522, 2021.
- [35] T. Dbouk, L. Lobry, and E. Lemaire, "Normal stresses in concentrated non-Brownian suspensions", *Journal of Fluid Mechanics*, vol. 715, p. 239-272, 2013.
- [36] A. Singh, and P. R. Nott, "Experimental measurements of the normal stresses in sheared Stokesian suspensions", *Journal of Fluid Mechanics*, vol. 490, p. 293-320, 2003.
- [37] F. Boyer, O. Pouliquen, and É. Guazzelli, "Dense suspensions in rotating-rod flows: normal stresses and particle migration", *Journal of Fluid Mechanics*, vol. 686, p. 5-25, 2011.
- [38] S. C. Dai, E. Bertevas, F. Qi and R. I. Tanner, "Viscometric functions for noncolloidal sphere suspensions with Newtonian matrices", *Journal of Rheology*, vol. 57, no. 2, p. 493-510, 2013.
- [39] R. L. Hoffman, "Discontinuous and dilatant viscosity behavior in concentrated suspensions. II. Theory and experimental tests", *Journal of Colloid and Interface Science*, vol. 46, no. 3, p. 491-506, 1974.
- [40] R. L. Hoffman, "Discontinuous and dilatant viscosity behavior in concentrated suspensions: III. Necessary conditions for their occurrence in viscometric flows", *Advances in Colloid and Interface Science*, Vol.17, no. 1, p. 161-184, 1982.

-
- [41] A. Fall, A. Lemaître, F. Bertrand, D. Bonn, and G. Ovarlez, “Shear Thickening and Migration in Granular Suspensions”, *Physical Review Letters*, vol. 105, no. 26, p. 268303, 2010.
- [42] A. Fall, H. de Cagny, D. Bonn, G. Ovarlez, E. Wandersman, J. A. Dijksman, and M. van Hecke, “Rheology of sedimenting particle pastes”, *Journal of Rheology*, vol. 57, no. 4, p.1237–1246, 2013.
- [43] NO. Y. C. Lin, B. M. Guy, M. Hermes, C. Ness, J. Sun, W. C. K. Poon, and I. Cohen, “Hydrodynamic and Contact Contributions to Continuous Shear Thickening in Colloidal Suspensions”. *Physical Review Letters*, vol. 115, no. 22, p. 1–5, 2015.
- [44] S. Khandavalli, J.P. Rothstein, “Large amplitude oscillatory shear rheology of three different shear-thickening particle dispersions”. *Rheologica. Acta*, vol. 54, p. 601–618, 2015.
- [45] R. Mari, R. Seto, J.F. Morris and M.M. Denn, “Discontinuous shear thickening in Brownian suspensions by dynamic simulation”, *PNAS* ,vol. 112, no. 50, p. 15326-15330, 2015.
- [46] V. Rathee, D. L. Blair and J.S. Urbach, “Localized stress fluctuations drive shear thickening in dense suspensions”, vol. 114, no. 33, p. 8740-8745, 2017.
- [47] C. Ness, J. Sun, “Shear thickening regimes of dense non-Brownian suspensions”, *Soft Matter*, vol. 12, p.914–924, 2016.
- [48] A.K. Townsend, H.J. Wilson, “Frictional shear thickening in suspensions: the effect of rigid asperities”, *Physics of Fluids*, vol. 29, p.121607, 2017.
- [49] G. Bossis, Y. Grasselli, O. Volkova, “Capillary flow of a suspension in the presence of discontinuous shear thickening”, *Rheologica Acta*, vol.61, p. 1–12, 2022.
- [50] B. J. Maranzano and NO. J. Wagner, “Flow-small angle neutron scattering measurements of colloidal dispersion microstructure evolution through the shear thickening transition” *The Journal of Chemical Physics*, vol. 117, p. 10291, 2002.
- [51] NO. Fernandez, R. Mani, D. Rinaldi, D. Kadau, M. Mosquet, H. Lombois -Burger, J. Cayer-Barrioz, H. J. Herrmann, NO. D. Spencer and L. Isa, “Microscopic mechanism for the shear-thickening of non-Brownian suspensions” *Physical Review Letters*, vol. 111, p. 108301, 2013.
- [52] S. R. Waitukaitis, L. K. Roth, V. Vitelli and H. M. Jaeger, “Dynamic jamming fronts”, *Europhysics Letters*, vol. 102, p.44001, 2013.
- [53] R. D. Deegan, “Stress hysteresis as the cause of persistent holes in particulate suspensions”, *Physical Review. E*, vol. 81, no. 3, p. 036319, 2010.
-

- [54] J. Bergenholtz, J. F. Brady and M. Vacic, “The non-Newtonian rheology of dilute colloidal suspensions *Journal of Fluid Mechanics*, vol. 456, p. 239-275, 2002.
- [55] R. S. Farr, J. R. Melrose and R. C. Ball, “Kinetic theory of jamming in hard-sphere startup flows”, *Physical Review. E*, vol. 55, no. 6, p. 7203-7211, 1997.
- [56] J. F. Morris, “Lubricated-to-frictional shear thickening scenario in dense suspensions”, *Physical Review Fluids*, vol. 3, no. 3, p. 110508, 2018.
- [57] R. Seto, R. Mari, J. F. Morris, and M. M. Denn, “Discontinuous shear thickening of frictional hard-sphere suspensions”, *Physical Review Letters*, vol. 111, no. 21, p.1–5, 2013.
- [58] Z. Pan, H. de Cagny, B. Weber and D. Bonn, “S-shaped flow curves of shear thickening suspensions: direct observation of frictional rheology”. *Physical Review. E*, vol. 92, no. 3, p.032202, 2015.
- [59] J. Mewis and NO. J. Wagner, “Colloidal suspension rheology”. Cambridge series in chemical engineering, Cambridge: Cambridge University Press, 2012.
- [60] J. Maybury, J. Ho, S. Binhowimal, “Fillers to lessen shear thickening of cement powder paste”, *Construction and Building Materials*, vol. 142, p. 268–279, 2017.
- [61] A. A. Tracton, “Coatings technology handbook”, CRC press, 2005.
- [62] Y. Lee, E.D. Wetzel, and NO. J. Wagner, “The ballistic impact characteristics of Kevlar® woven fabrics impregnated with a colloidal shear thickening fluid”, *Journal of Materials Science*, Vol. 38, No. 13, p.2825–2833, 2003.
- [63] G. Bettin, “Energy Absorption of Reticulated Foams Filled with Shear-Thickening Silica Suspensions”, Master of Science in Mechanical Engineering, Massachusetts Institute of Technology, 2005.
- [64] D. P. Kalman, J. B. Schein, J. M. Houghton , C. H. NO. Laufer, E. D. Wetzel, and NO. J. Wagner, “Polymer dispersion based shear thickening fluid-fabrics for protective applications”, *International SAMPE Symposium and Exhibition (Proceedings)*, 2007.
- [65] X. Li, H. L. Cao, S. Gao, F. Y. Pan, L. Q. Weng, S. H. Song and Y. D. Huang, “Preparation of body armour material of Kevlar fabric treated with colloidal silica nanocomposite”, *Plastics, Rubber and Composites*, Vol. 37, no. 5–6, p.223–226, 2008.
- [66] V. K. Rangari, T. A. Hassan, and S. Jeelani, “Synthesis and mechanical properties of shear thickening fluid/Kevlar composite for body armor application”, *International SAMPE Symposium and Exhibition (Proceedings)*, 2008.
- [67] O. E. Petel, S. Ouellet, J. Loiseau, B. J. Marr, Frost, D. L. and Higgins, A. J. “The effect of particle strength on the ballistic resistance of shear thickening fluids”, *Applied Physics Letters*, Vol. 102, no. 6, p.064103–064104, 2013.

- [68] M. B. Stauffer, “Chocolate behavior-What influences your selection?,” *The Manufacturing Confectioner*, vol. 78, p. 75–80, 1998.
- [69] E. B. Bagley, F. R. Dintzis, “Shear thickening and flow induced structures in foods and biopolymer systems”, *Rheology Series*, vol.8, p. 63-86, 1999.
- [70] C. Fischer, A. Bennani, V. Michaud, E. Jacquelin, and J. A. E. Månson, “Structural damping of model sandwich structures using tailored shear thickening fluid compositions”, *Smart Materials and Structures*, Vol. 19, no. 3, p. 035017, (2010).
- [71] Z. H. Tan, L. Zuo, W. H. Li, L. S. Liu, and P. C. Zhai, 2016 “Dynamic response of symmetrical and asymmetrical sandwich plates with shear thickening fluid core subjected to penetration loading”, *Materials & Design*, Vol. 94, p.105–110, 2016.
- [72] T. Tian and M. Nakano, “Design and testing of a rotational brake with shear thickening fluids”, *Smart Materials and Structures*, Vol. 26, no. 3, p.035038, 2017.
- [73] A. Yahia, “Shear-thickening behavior of high-performance cement grouts—Influencing mix-design parameters”, *Cement and Concrete Research*, vol. 41 no. 3, p. 230–235, 2011.
- [74] B. Felekoglu, “Rheological behaviour of self-compacting micro-concrete”, *Sadhana*, vol. 39, no. 6, p. 1471–1495, 2014.
- [75] D. A. Williams, A. W. Saak, H. M. Jennings, “The influence of mixing on the rheology of fresh cement paste”, *Cement and Concrete Research*. Vol, 29, no.9, p.1491–1496, 1999.
- [76] NO. Roussel, “Steady and transient flow behaviour of fresh cement pastes”, *Cement and Concrete Research*”, Vol. 35, no. 9, pp1656–1664, 2005.
- [77] S. Amziane, C. F. Ferraris, E. P. Koehler, “Measurement of workability of fresh concrete using a mixing truck”, *Journal of Research of the National Institute of Standards and Technology*, Vol.110, no. 1, p. 55, 2005.
- [78] M. Sahmaran, A. Yurtseven, I. O. Yaman, “Workability of hybrid fiber reinforced self-compacting concrete”, *Building and Environment*, vol. 40, no.12, p. 1672-1677, 2005.
- [79] S. Sha, M. Wang, C. Shi, Y. Xiao, “Influence of the structures of polycarboxylate superplasticizer on its performance in cement-based materials-A review”, *Construction and Building Materials*, vol. 233, p. 117257, 2020.
- [80] H. Freundlich and H. L. Röder, “Dilatancy and its relation to thixotropy”, *Transactions of the Faraday Society*, vol. 34, p. 308-316, 1938.
- [81] A. B. Metzner and M. Whitlock, “Flow behavior of concentrated (dilatant) suspensions”, *Transactions of the Society of Rheology*, vol. 2, no 1, p. 239-254, 1958.

-
- [82] H. A. Barnes, “Shear-thickening (“Dilatancy”) in suspensions of nonaggregating solid particles dispersed in Newtonian liquids”, *Journal of Rheology*, vol. 33, no. 2, p. 329-366, 1989.
- [83] V. T. O'Brien, and M. E. Mackay, “Stress components and shear thickening of concentrated hard sphere suspensions”, *Langmuir*, vol. 16, no. 21, p. 7931-7938, 2000.
- [84] D. Lootens, H. VAN DAMME and P. Hébraud, “Giant stress fluctuations at the jamming transition”, *Physical review letters*, vol. 90, no. 17, p. 178301, 2003.
- [85] C. B. Holmes, M. E. Cates, M. FUCHS, and P. Sollich, “Glass transitions and shear thickening suspension rheology”, *Journal of Rheology*, vol. 49, no. 1, p. 237-269, 2005.
- [86] D. Lootens, H. Van Damme, Y. Hémar, and P. Hébraud, “Dilatant flow of concentrated suspensions of rough particles”, *Physical review letters*, vol. 95, no. 26, p. 268302, 2005.
- [87] M. E. Cates, M. D. HAW, and C. B. HOLMES, “Dilatancy, jamming, and the physics of granulation”, *Journal of Physics: Condensed Matter*, vol. 17, no. 24, p. S2517, 2005.
- [88] A. Fall, N. Huang, F. Bertrand, G. Ovarlez and D. Bonn, “Shear thickening of cornstarch suspensions as a reentrant jamming transition”, *Physical review letters*, vol. 100, no. 1, p. 018301, 2008.
- [89] E. Brown, and H. M. Jaeger, “The role of dilation and confining stresses in shear thickening of dense suspensions”, *Journal of Rheology*, vol. 56, no. 4, p. 875-923, 2012.
- [90] J. F. Brady and G. Bossis, “The rheology of concentrated suspensions of spheres in simple shear flow by numerical simulation”, *Journal of Fluid Mechanics*, vol. 155, p. 105-129, 1985.
- [91] J. F. Brady and G. Bossis, “Stokesian dynamics”, *Annual review of fluid mechanics*, vol. 20, p. 111-157, 1988.
- [92] J. R. Melrose and R. C. Ball, “Continuous shear thickening transitions in model concentrated colloids—The role of interparticle forces”, *Journal of Rheology*, vol. 48, no. 5, p. 937-960, 2004.
- [93] N. J. Wagner and J. F. Brady, “Shear thickening in colloidal dispersions”, *Physics Today*, vol. 62, no. 10, p. 27-32, 2009.
- [94] E. Nazockdast and J. F. Morris, “Microstructural theory and the rheology of concentrated colloidal suspensions”, *Journal of Fluid Mechanics*, vol. 713, p. 420-452, 2012.
- [95] X. Cheng, J. H. McCoy, J. N. Israelachvili, I. Cohen, “Imaging the microscopic structure of shear thinning and thickening colloidal suspensions”, *Science*, vol. 333, no. 6047, p. 1276-1279, 2011.
-

- [96] A. A. Catherall, J. R. Melrose and R. C. Ball, “Shear thickening and order-disorder effects in concentrated colloids at high shear rates”, *Journal of Rheology*, Vol. 44, no. 1, p. 1–25, 2000.
- [97] H. Laun, R. Bung, S. Hess, W. Loose, O. Hess, K. Hahn and P. Lindner, “Rheological and small angle neutron scattering investigation of shear-induced particle structures of concentrated polymer dispersions submitted to plane Poiseuille and Couette flow a”, *Journal of Rheology*, vol. 36, no. 4, p. 743-787, 1992.
- [98] R. G. Egres and N. J. Wagner, “The rheology and microstructure of acicular precipitated calcium carbonate colloidal suspensions through the shear thickening transition”, *Journal of rheology*, vol. 49, no. 3, p. 719-746, 2005.
- [99] R. G. Egres, F. Nettekoven and N. J. Wagner, “Rheo-SANS investigation of acicular-precipitated calcium carbonate colloidal suspensions through the shear thickening transition”, *Journal of Rheology*, vol. 50, no. 5, p. 685-709, 2006.
- [100] E. Brown, and H. M. Jaeger, “Shear thickening in concentrated suspensions: phenomenology, mechanisms and relations to jamming”, *Reports on Progress in Physics*, vol. 77, no. 4, p. 046602, 2014.
- [101] F. Blanc, F. Peters, and E. Lemaire, “Experimental signature of the pair trajectories of rough spheres in the shear-induced microstructure in noncolloidal suspensions”, *Physical review letters*, vol. 107, no. 20, p. 208302, 2011.
- [102] F. Peters, G. Ghigliotti, S. Gallier, F. Blanc, E. Lemaire and L. Lobry, “Rheology of non-Brownian suspensions of rough frictional particles under shear reversal: A numerical study”, *Journal of rheology*, vol. 60, no. 4, p. 715-732, 2016.
- [103] R. Mari, R. Seto, J. F. Morris and M. M. Denn, “Shear thickening, frictionless and frictional rheologies in non-Brownian suspensions”, *Journal of Rheology*, vol. 58, no. 6, p. 1693-1724, 2014.
- [104] P. Pham, B. Metzger, and J. E. Butler, “Particle dispersion in sheared suspensions: Crucial role of solid-solid contacts”, *Physics of Fluids*, vol. 27, no. 5, p. 051701, 2015.
- [105] C. Clavaud, A. Bérut, B. Metzger and Y. Forterre, “Revealing the frictional transition in shear-thickening suspensions”, *Proceedings of the National Academy of Sciences*, vol. 114, no. 20, p. 5147-5152, 2017.
- [106] A. Singh, R. Mari, M. M. Denn and J. F. Morris, “A constitutive model for simple shear of dense frictional suspensions”, *Journal of Rheology*, vol. 62, no. 2, p. 457-468, 2018.
- [107] M. Wyart and M. E. Cates, “Discontinuous shear thickening without inertia in dense non-Brownian suspensions”, *Physical review letters*, vol. 112, no. 9, p. 098302, 2014.

- [108] M. Neuville, G. Bossis, J. Persello, O. Volkova, P. Boustingorry, and M. Mosquet, “Rheology of a gypsum suspension in the presence of different superplasticizers”, *Journal of rheology*, vol. 56, no. 2, p. 435-451, 2012.
- [109] C. Clavaud, “ Rhéoépaississement des suspensions denses: mise en évidence de la transition frictionnelle ”, PhD thesis, University of Aix-Marseille (2018).
- [110] M. Hermes, B. Guy and W. Poon, “A unified description of the rheology of hard particles”, *APS March Meeting Abstracts*, Vol. 2016, pp. K34-008, 2016.
- [111] M. Hermes, B. M. Guy, W. C. Poon, G. Poy, M. E. Cates, and M. Wyart, “Unsteady flow and particle migration in dense, non-Brownian suspensions”. *Journal of Rheology*, vol. 60, no. 5, p. 905-916, 2016.
- [112] Y. Madraki, S. Hormozi, G. Ovarlez, E. Guazzelli, and O. Pouliquen, “Enhancing shear thickening”, *Physical Review Fluids*, vol. 2, no. 3, p. 033301, 2017.
- [113] Y. Madraki, G. Ovarlez and S. Hormozi, “Transition from continuous to discontinuous shear thickening: An excluded-volume effect”, *Physical review letters*, vol. 121, no. 10, p. 108001, 2018.
- [114] N. Ohl and W. Gleissle, “The characterization of the steady-state shear and normal stress functions of highly concentrated suspensions formulated with viscoelastic liquids”, *Journal of Rheology*, vol. 37, no. 2, p. 381-406, 1993.
- [115] C. D. Cwalina and N. J. Wagner, “Rheology of non-Brownian particles suspended in concentrated colloidal dispersions at low particle Reynolds number”, *Journal of Rheology*, vol. 60, no. 1, p. 47-59, 2016.
- [116] C. D. Cwalina, K. J. Harrison and N. J. Wagner, “Rheology of cubic particles in a concentrated colloidal dispersion suspending medium”, *AIChE Journal*, vol. 63, no. 3, p. 1091-1101, 2017.
- [117] R. G. Larson, “The Structure and Rheology of Complex Fluids”, Oxford University, New York, vol. 150, 1999.
- [118] C. J. S. Petrie, “The rheology of fibre suspensions. *Journal of Non-Newtonian Fluid Mechanics*”, vol. 87, no. 2-3, p. 369-402, 1999.
- [119] J. E. Butler, and B. Snook. “Microstructural dynamics and rheology of suspensions of rigid fibers”, *Annual Review of Fluid Mechanics*, vol. 50, p. 299-318, 2018.
- [120] E. Brown, H. Zhang, N. A. Forman, B. W. Maynor, D. E. Betts, J. M. DeSimone, and H. M. Jaeger, “Shear thickening and jamming in densely packed suspensions of different particle shapes”, *Physical Review E*, vol. 84, no. 3, p. 031408 , 2011.

- [121] E. E. B. White, M. Chellamuthu and J. P. Rothstein, “Extensional rheology of a shear-thickening cornstarch and water suspension”, *Rheologica acta*, vol. 49, no. 2, p. 119-129, 2010.
- [122] R. J. Andrade, A. R. Jacob, F. J. Galindo-Rosales, L. Campo-Deaño, Q. Huang, O. Hassager and G. Petekidis, “Dilatancy in dense suspensions of model hard-sphere-like colloids under shear and extensional flow”, *Journal of Rheology*, vol. 64, no. 5, p. 1179-1196, 2020.
- [123] M. Roché, H. Kellay and H. A. Stone, “Heterogeneity and the role of normal stresses during the extensional thinning of non-Brownian shear-thickening fluids”, *Physical review letters*, vol. 107, no. 13, p. 134503, 2011.
- [124] R. Seto, G. G. Giusteri and A. Martiniello, “Microstructure and thickening of dense suspensions under extensional and shear flows”, *Journal of Fluid Mechanics*, vol. 825, 2017.
- [125] M.I. Smith, R. Besseling, M.E. Cates, and V. Bertola, “Dilatancy in the flow and fracture of stretched colloidal suspensions”, *Nature communications*, vol.1, no.114, 2010.
- [126] B. Darbois Texier, H. Lhuissier, Y. Forterre and B. Metzger, “Surface-wave instability without inertia in shear-thickening suspensions”, *Communications Physics*, vol. 3, no. 1, p. 1-7, 2020.
- [127] M. Liard, A. Sato, J. Sautel, D. Lootens and P. Hébraud, “Jet instability of a shear-thickening concentrated suspension”, *The European Physical Journal E*, vol. 43, no. 11, p. 1-6, 2020.
- [128] Z. Y. Wang, H. Zhao, W. F. Li, J. L. Xu and H. F. Liu, “Primary breakup of shear-thickening suspension jet by an annular air jet”, *AIChE Journal*, vol. 68, no. 4, p. e17579, 2022.
- [129] Z. Y. Wang, H. Zhao, W. F. Li, J. L. Xu and H. F. Liu, “Secondary breakup of shear thickening suspension drop”, *Physics of Fluids*, vol. 33, no. 9, p. 093103, 2021.
- [130] P. Soroushian,; A. Khan,; J.W. Hsu, “Mechanical properties of concrete materials reinforced with polypropylene or polyethylene fibers”, *American Concrete Institute*, vol. 89, no. 6, P. 535–540, 1992.
- [131] B. Mobasher, S.P. Shah, “Interaction between fibers and the matrix in glass fiber reinforced concrete. In *Thin-Section Fiber Reinforced Concrete and Ferrocement*”, *American Concrete Institute*, vol SP-124, no.20, p. 137–156, 1991.

- [132] A.B. Kizilkanat, NO. Kabay, V. Akyüncü, S. Chowdhury and A. H. Akçad, “Mechanical properties and fracture behavior of basalt and glass fiber reinforced concrete: An experimental study”, *Construction and Building Materials*, vol. 100, p. 218-224, 2015.
- [133] R. Morini, “Rheology of concentrated suspensions of calcium carbonate in the presence of superplasticizer”. PhD thesis, University of Nice-Sophia Antipolis (2013) (in French).
- [134] G. Bossis, P. Boustingorry, Y. Grasselli, A. Meunier, R. Morini, A. Zubarev and O. Volkova, “Discontinuous shear thickening in the presence of polymers adsorbed on the surface of calcium carbonate particles”, *Rheologica Acta*, vol. 56, no.5, P.415–430, 2017.
- [135] L. NO. Plummer, E. Busenberg, “The solubilities of calcite, aragonite and vaterite in CO₂-H₂O solutions between 0 and 90°C, and an evaluation of the aqueous model for the system CaCO₃-CO₂-H₂O”, *Geochimica et Cosmochimica Acta*, vol 46, no. 6, p. 1011-1040, 1982.
- [136] R. B. B. Kammoe, “Synthese de nanoparticules de carbonate de calcium”, PHD thesis, Laval university-Québec, 2010.
- [137] C. Geffroy, A. Foissy, J. Persello, and B. Cabane, “Surface Complexation of Calcite by Carboxylates in Water”, *Journal of Colloid and Interface Science*, vol. 211, no. 1, p. 45–53, 1999.
- [138] M. Mosquet, Y. Chevalier, S. Brunel, J. P. Guicquero, and P. Le Percec, “Polyoxyethylene di-phosphonates as efficient dispersing polymers for aqueous suspensions”, *Journal of applied polymer science*, vol. 65, no. 12, p. 2545–2555, 1997.
- [139] Y. Chevalier, P. Le Percec, and A. Foissy, “The mechanism of fluidization of concentrated calcium carbonate slurries by poly(oxyethylene) diphosphonates”, *Colloid and Polymer Science*, vol. 1171, p. 1162–1171, 1999.
- [140] F. Dalas, A. Nonat, S. Pourchet, M. Mosquet, D. Rinaldi, and S. Sabio, “Cement and Concrete Research Tailoring the anionic function and the side chains of comb-like superplasticizers to improve their adsorption”, *Cement and Concrete Research*, vol. 67, p. 21–30, 2015.
- [141] S. Pourchet, S. Liautaud, D. Rinaldi, and I. Pochard, “Effect of the repartition of the PEG side chains on the adsorption and dispersion behaviors of PCP in presence of sulfate”, *Cement and Concrete Research*, vol. 42, no. 2, p. 431–439, 2012.
- [142] L. Ferrari, J. Kaufmann, F. Winnefeld, and J. Plank, “Multi-method approach to study influence of superplasticizers on cement suspensions”, *Cement and Concrete Research*, vol. 41, no. 10, p. 1058–1066, 2011.

- [143] L. Ferrari, J. Kaufmann, F. Winnefeld, and J. Plank, “Interaction of cement model systems with superplasticizers investigated by atomic force microscopy, zeta potential, and adsorption measurements”, *Journal of Colloid and Interface Science*, vol. 347, no. 1, p. 15–24, 2010.
- [144] NO. Mikanovic, K. Khayat, M. Pagé, and C. Jolicoeur, “Aqueous CaCO₃ dispersions as reference systems for early-age cementitious materials,” *Colloids and Surfaces A: Physicochemical and Engineering Aspects*, vol. 291, no. 1-3, p. 202-211, 2006.
- [145] DY. Yoo, HO. Shin, JM. Yang and YS. Yoon, “Material and bond properties of ultra high performance fiber reinforced concrete with micro steel fibers”, *Composites Part B: Engineering*, vol. 58, p. 122-133, 2014.
- [146] P.W. Chen and D.D.L. Chung, “Carbon fiber reinforced concrete for smart structures capable of non-destructive flaw detection”, *Smart Materials and Structures*, vol. 2, no.1, pp 22, 1993.
- [147] S. Guler, “The effect of polyamide fibers on the strength and toughness properties of structural lightweight aggregate concrete”, *Construction and Building Materials*, vol. 173, p. 394-402, 2018.
- [148] JK. Jeon, WS. Kim, CK. Jeon, JC. Kim, “Processing and mechanical properties of macro polyamide fiber reinforced concrete”, *Materials*, vol. 7, p. 7634-7652, 2014.
- [149] P.S. Song, S. Hwang, B.C. Sheub, “Strength properties of nylon-and polypropylene-fiber-reinforced concretes”, *Cement and Concrete Research*. Vol. 35, no. 8, p. 1546– 1550, 2005.
- [150] O.B. Ozger, F. Girardi, G.M. Giannuzzi, V.A. Salomoni, C.E. Majorana, L. Fambri, NO. Baldassino, R.D. Maggio, “Effect of polyamide fibres on mechanical and thermal properties of hardened concrete for energy storage systems”, *Materials & Design*, vol. 51, p. 989–997, 2013.
- [151] S. Spadea, I. Farina, A. Carrafiello, F. Fraternali, “Recycled polyamide fibers as cement mortar reinforcement”, *Construction and Building Materials*, Vol. 80, p. 200–209, 2015.
- [152] L. E. Becker and M. J. Shelley, “Instability of elastic filaments in shear flow yields first-normal-stress differences”, *Physical Review Letters*. Vol. 87, p.198301, 2001.
- [153] S. N. Bounoua, , P. Kuzhir, and E. Lemaire, “Shear reversal experiments on concentrated rigid fiber suspensions”, *Jornal of Rheology*, vol. 63, p.785–798, 2019.
- [154] C. W. Macosko, “Rheology : principles, measurements, and applications”. Wiley-vch, 1994.

- [155] A. Ait-Kadi, P. Marchal, L. Choplin, A. S. Chrissemant and M. Bousmina, “Quantitative analysis of mixer-type rheometers using the couette analogy”. *The Canadian Journal of Chemical Engineering*, Vol. 80, p. 1166-1174, 2002.
- [156] G. Bossis, O. Volkova, Y. Grasselli and A. Cifreio, "The Role of Volume Fraction and Additives on the Rheology of Suspensions of Micron Sized Iron Particles", *Frontiers in Materials*, vol.6, 2019.
- [157] G. Bossis, Y. Grasselli, A. Cifreio and O. Volkova, “Tunable discontinuous shear thickening in Capillary flow of MR suspensions” *Journal of Intelligent Material Systems and Structures*, vol. 32, no.12, p. 1349–1357, 2021.
- [158] X. Château, G. Ovarlez, and K. L. Trung, “Homogenization approach to the behavior of suspensions of noncolloidal particles in yield stress fluids”, *Journal of Rheology*, vol. 52, no. 2, p. 489-506, 2008.
- [159] J. Comtet, G. Chatté, A. Niguès, L. Bocquet, A. Siria, and A. Colin, “Pairwise frictional profile between particles determines discontinuous shear thickening transition in non-colloidal suspensions”, *Nature communications*, vol. 8, no. 1, p. 1-7, 2017.
- [160] G. Bossis, O. Volkova, Y. Grasselli, O. Gueye, “Discontinuous shear thickening in concentrated suspensions”, *Philosophical Transactions of the Royal Society A*, vol. 377, no. 2143, p. 20180211, 2019.
- [161] R. Mari and R. Seto, “Force transmission and the order parameter of shear thickening”, *Soft matter*, vol. 15, no. 33, p. 6650-6659, 2019.
- [162] D. Merhi, E. Lemaire, G. Bossis, and F. Moukalled, “Particle migration in a concentrated suspension flowing between rotating parallel plates: Investigation of diffusion flux coefficients”, *Journal of Rheology*, vol. 49, no. 6, p. 1429-1448, 2005.
- [163] R. N. Chacko, R. Mari, M. E. Cates, and S. M. Fielding, “Dynamic vorticity banding in discontinuously shear thickening suspensions”, *Physical review letters*, vol. 121, no. 10, p. 108003, 2018.
- [164] S. M. Dinh and R. C. Armstrong, “A rheological equation of state for semiconcentrated fiber suspensions”, *Journal of Rheology*, vol. 28, no. 3, p. 207-227, 1984.
- [165] A. P. Chatterjee, “Nonuniform fiber networks and fiber-based composites: Pore size distributions and elastic moduli”, *Journal of Applied Physics*, vol. 108, no. 6, p. 063513, 2010.
- [166] X. Bian, S. Litvinov, M. Ellero, and N. J. Wagner, “Hydrodynamic shear thickening of particulate suspension under confinement”, *Journal of Non-Newtonian Fluid Mechanics*, vol. 213, p. 39-49, 2014.

-
- [167] N. Phan-Thien and A. L. Graham, , “A new constitutive model for fibre suspensions: flow past a sphere”, *Rheologica acta*, vol. 30, no. 1, p. 44-57, 1991.
- [168] L. G. Leal and E. J. Hinch, , “The effect of weak Brownian rotations on particles in shear flow”, *Journal of Fluid Mechanics*, vol. 46, no. 4, p. 685-703, 1971.
- [169] T. S. Majmudar and R. P. Behringer, “Contact force measurements and stress-induced anisotropy in granular materials”, *nature*, vol. 435, no. 7045, p. 1079-1082, 2005.
- [170] G. Bossis, Y. Grasselli, A. Meunier, and O. Volkova, “Tunable discontinuous shear thickening with magnetorheological suspensions”, *Journal of Intelligent Material Systems and Structures*, vol. 29, no. 1, p. 5-11, 2018.
- [171] G. Ovarlez, F. Mahaut, S. Deboeuf, N. Lenoir, S. Hormozi, and X. Chateau, “Flows of suspensions of particles in yield stress fluids”, *Journal of rheology*, vol. 59, no. 6, p. 1449-1486, 2015.
- [172] G. K. Batchelor, “Slender-body theory for particles of arbitrary cross-section in Stokes flow”, *Journal of Fluid Mechanics*, vol. 44, no. 3, p. 419-440, 1970.
- [173] H. Brenner, “Rheology of a dilute suspension of axisymmetric Brownian particles”, *International journal of multiphase flow*, vol. 1, no. 2, p. 195-341, 1974.
- [174] L. Martinie, “Rheological behavior and casting of fiber reinforced materials”, PhD thesis, University Paris-Est, 2010. (In French).
- [175] I. Balberg, C. H. Anderson, S. Alexander and N. Wagner, “Excluded volume and its relation to the onset of percolation”, *Physical review B*, vol. 30, no. 7, p. 3933, 1984.
- [176] S. Toll, “Note: On the tube model for fiber suspensions”, *Journal of Rheology*, vol. 37, no. 1, p. 123-125, 1993.
- [177] A. P. Philipse and A. M. Wierenga, “On the density and structure formation in gels and clusters of colloidal rods and fibers. *Langmuir*, vol. 14, no. 1, p. 49-54, 1998.
- [178] R. Mari, R. Seto, J. F. Morris and M. M. Denn, “Nonmonotonic flow curves of shear thickening suspensions”, *Physical Review E*, vol. 91, no. 5, p. 052302, 2015.
- [179] J. M. Nouri, J. H. Whitelaw, and M. Yianneskis, “Particle motion and turbulence in dense two-phase flows”, *International journal of multiphase flow*, vol. 13, no. 6, p. 729-739, 1987.
- [180] B. N. Persson, “Sliding friction: physical principles and applications”, Springer Science & Business Media.,2013
- [181] H. Nakanishi, S. I. Nagahiro and N. Mitarai, “Fluid dynamics of dilatant fluids”, *Physical Review E*, vol. 85, no. 1, p. 011401, 2012.
-

- [182] J. Eggers and E. Villermaux, “Physics of liquid jets. Reports on progress in physics”, vol. 71, no. 3, p. 036601, 2008.
- [183] F. Ianni, D. Lasne, R. Sarcia and P. Hébraud, “Relaxation of jammed colloidal suspensions after shear cessation”, *Physical Review E*, vol. 74, no. 1, p. 011401, 2006.
- [184] J. Château and H. Lhuissier, “Breakup of a particulate suspension jet”, *Physical Review Fluids*, vol. 4, no. 1, p. 012001, 2019.
- [185] S. Senchenko and T. Bohr, “Shape and stability of a viscous thread”, *Physical review E*, vol. 71, no. 5, p. 056301, 2005.
- [186] M. C. Koenders, “Wave propagation through elastic granular and granular auxetic materials”, *physica status solidi (b)*, vol. 246, no. 9, p. 2083-2088, 2009.
- [187] P. Puri and S. C. Cowin, “Plane waves in linear elastic materials with voids”, *Journal of Elasticity*, vol. 15, no. 2, p. 167-183, 1985.
- [188] Z. Hou, R. J. Okamoto and P. V. Bayly, “Shear wave propagation and estimation of material parameters in a nonlinear, fibrous material”, *Journal of biomechanical engineering*, vol. 142, no. 5, 2020.
- [189] U. S. Sauter and H. W. Buggisch, “Stability of initially slow viscous jets driven by gravity”, *Journal of Fluid Mechanics*, vol. 533, p. 237-257, 2005.
- [190] L. D. Landau and E. M. Lifshitz, “A Course in Theoretical Physics—Fluid Mechanics”, Vol. 6, Pergamon-NewYork, 1987.
- [191] M. A. Hubbe, “Flocculation and redispersion of cellulosic fiber suspensions: A review of effects of hydrodynamic shear and polyelectrolytes”, *BioResources*, vol. 2, no. 2, p. 296-331, 2007.
- [192] A. Javadi, J. Eggers, D. Bonn, M. Habibi and N. M. Ribe, “Delayed capillary breakup of falling viscous jets”, *Physical review letters*, vol. 110, no.14, p.144501, 2013.